UNIVERSITY OF Southampton

University of Southampton Research Repository
ePrints Soton

Copyright © and Moral Rights for this thesis are retained by the author and/or other copyright owners. A copy can be downloaded for personal non-commercial research or study, without prior permission or charge. This thesis cannot be reproduced or quoted extensively from without first obtaining permission in writing from the copyright holder/s. The content must not be changed in any way or sold commercially in any format or medium without the formal permission of the copyright holders.

When referring to this work, full bibliographic details including the author, title, awarding institution and date of the thesis must be given e.g.

AUTHOR (year of submission) "Full thesis title", University of Southampton, name of the University School or Department, PhD Thesis, pagination

http://eprints.soton.ac.uk

UNIVERSITY OF SOUTHAMPTON

FACULTY OF ENGINEERING
AND THE ENVIRONMENT

Institute of Sound and Vibration Research

A High-Order Finite Element Model for Acoustic Propagation

by

Karim Hamiche

Thesis for the degree of Doctor of Philosophy

July 2016

UNIVERSITY OF SOUTHAMPTON

ABSTRACT

FACULTY OF ENGINEERING AND THE ENVIRONMENT

Institute of Sound and Vibration Research

Doctor of Philosophy

A HIGH-ORDER FINITE ELEMENT MODEL FOR ACOUSTIC PROPAGATION

by Karim Hamiche

Sound propagation in complex non-uniform mean flows is an important research area for transport, building and power generation industries. Unsteady flows are responsible for noise generation in rotating and pulsating machines. Sound propagates in ducts and radiates through their openings. Duct discontinuities and complex flow effects on acoustic propagation need to be investigated. Although it provides accurate results, the most commonly used Computational AeroAcoustics propagation method, the full potential theory, does not describe the whole physics. Turbofan exhaust noise radiation involves strong refraction of the sound field occurring through jet shear layer, as well as interaction between the acoustic field and the vorticity/entropy waves. The Linearised Euler Equations are able to represent these effects. Solving these equations with time-domain solvers presents shortcomings such as linear instabilities and impedance modelling, which can be avoided by solving in the frequency domain. Nevertheless the classical Finite Element Method in frequency domain suffers from dispersion error and high memory requirements. These drawbacks are particularly critical at high frequencies and with the Linearised Euler Equations, which involve up to five unknowns. To circumvent these obstacles a novel approach is developed in this thesis, using a high-order Finite Element Method to solve the Linearised Euler Equations in the frequency domain. The model involves high-order polynomial shape functions with unstructured triangular meshes, numerical stabilisation and Perfectly Matched Layers. The computational effort is further optimised by coupling the Linearised Euler Equations in the regions of complex sheared mean flow with the Linearised Potential Equation in the regions of irrotational mean flow. The numerical model is applied to aeroengine acoustic propagation either by an intake or by an exhaust. Comparisons with analytic solutions demonstrate the method accuracy which properly represents the acoustic and vorticity waves, as well as the refraction of the sound field across the jet shear layer. The benefits in terms of memory requirements and computation time are significant in comparison to the standard low-order Finite Element Method, even more so with the coupling technique.

Contents

List of Figures

List of Tables

Declaration of Authorship

I, Karim Hamiche, declare that this thesis and the work presented in it are my own and have been generated by me as the result of my own original research.

A High-Order Finite Element Model for Acoustic Propagation

I confirm that:

1. This work was done wholly or mainly while in candidature for a research degree at this University;

2. Where any part of this thesis has previously been submitted for a degree or any other qualification at this University or any other institution, this has been clearly stated;

3. Where I have consulted the published work of others, this is always clearly attributed;

4. Where I have quoted from the work of others, the source is always given. With the exception of such quotations, this thesis is entirely my own work;

5. I have acknowledged all main sources of help;

6. Where the thesis is based on work done by myself jointly with others, I have made clear exactly what was done by others and what I have contributed myself;

7. Either none of this work has been published before submission, or parts of this work have been published as: [1–5].

Signed:

Date:

"The education of a man is never completed until he dies."

Robert Edward Lee

Acknowledgements

This research has been financially supported from the European Commission through the FP7-PEOPLE-ITN-2011 FlowAirS project, grant agreement 289352, coordinated by Y. Aurégan from the Laboratoire d'Acoustique de l'Université du Maine (France). The work has been carried out partly in the offices of Siemens Industry Software in Leuven, Belgium, and at the Institute of Sound and Vibration Research (ISVR), University of Southampton, United Kingdom.

Some of the geometry/flow test cases used in this work were provided by the European TURNEX project and its industrial partners (Airbus, Rolls-Royce, Dassault and AVIO) who provided financial support for the experiment.

I would particularly like to acknowledge my supervisors for this project, Dr. Gwénaël Gabard and Dr. Hadrien Bériot, who constantly supported me and helped me in bringing this research to a successful ending. I am also grateful to my friends and colleagues in Leuven and Southampton, and within the FlowAirS project, with whom I have shared strong moments in this three-and-a-half-year project. Amongst them I would like to give a special thank to Jonathan, Alessandra, Simone, Marco, Alice, Thomas, Jayanth, Vincent... Finally my recognition goes to my family, especially to my parents, my sisters and my brother, who have always encouraged me during my work abroad and provided me with wise advices.

Abbreviations

APE	**A**coustic **P**erturbations **E**quations
ASGS	**A**lgebraic **S**ub**G**rid **S**cale
BEM	**B**oundary **E**lement **M**ethod
BPF	**B**lade **P**ass **F**requency
CAA	**C**omputational **A**ero**A**coustics
CFD	**C**omputational **F**luid **D**ynamics
DEM	**D**iscontinuous **E**nrichment **M**ethod
DGM	**D**iscontinuous **G**alerkin **M**ethod
DNS	**D**irect **N**umerical **S**imulation
DOF	**D**egree **O**f **F**reedom
DRP	**D**ispersion-**R**elation-**P**reserving
EPNdB	**E**ffective **P**erceived **N**oise level in **dB**
FD	**F**inite **D**ifference
FEM	**F**inite **E**lement **M**ethod
FMBEM	**F**ast-**M**ultipole **B**oundary **E**lement **M**ethod
GIE	**G**eometry **I**nduced **E**rror
GLS	**G**alerkin/**L**east-**S**quares
HVAC	**H**eating, **V**entilation and **A**ir **C**onditioning
ICAO	**I**nternational **C**ivil **A**viation **O**rganisation
ICE	**I**nternal **C**ombustion **E**ngine
LEE	**L**inearised **E**uler **E**quations
LES	**L**arge **E**ddy **S**imulation
LNSE	**L**inearised **N**avier-**S**tokes **E**quations
LPE	**L**inearised **P**otential **E**quation
NRBC	**N**on-**R**eflecting **B**oundary **C**ondition
OGV	**O**utlet **G**uide **V**ane
PML	**P**erfectly **M**atched **L**ayer

PUFEM	**P**artition of **U**nity **F**inite **E**lement **M**ethod
RANS	**R**eynolds **A**veraged **N**avier-**S**tokes
SEA	**S**tatistical **E**nergy **A**nalysis
SGS	**S**ub**G**rid-**S**cale
SNGR	**S**tochastic **N**oise **G**eneration and **R**adiation
SPL	**S**ound **P**ressure **L**evel
SUPG	**S**treamline-**U**pwind **P**etrov-**G**alerkin
UWVF	**U**ltra-**W**eak **V**ariational **F**ormulation

Physical Constants

Acoustic reference pressure	p_{ref}	=	$20\,\mu\text{Pa}$
Specific heats ratio at constant pressure and volume	γ	=	1.4

Symbols

Roman		
a_i	imaginary part constant coefficient	-
a_r	real part constant coefficient	-
$\boldsymbol{A}$	left-hand side mean flow properties matrix	-
$\boldsymbol{A}_\bullet$	flux matrix	-
$A^{\bullet}_{\bullet}$	field constant amplitude	-
$\boldsymbol{B}$	right-hand side mean flow properties matrix	-
c	isentropic sound speed	$\mathrm{m\,s^{-1}}$
C_1	error bound constant	-
C_2	error bound constant	-
d	Perfectly Matched Layer length	m
d_λ	number of degrees of freedom per wavelength	-
$\boldsymbol{d}$	vector of degrees of freedom	-
$\mathfrak{D}$	stabilisation operator	-
$\boldsymbol{D}_1$	first-order derivative differential matrix with respect to y	-
e	specific internal energy	$\mathrm{J\,kg^{-1}}$
$\boldsymbol{e}_x$	x-axis	-
E_d	dispersion error	%
E_{H^1}	H^1-norm error	%
E_{L^2}	L^2-norm error	%
f	frequency	Hz
f_c	cut-off frequency	Hz
f_r	velocity profile in the r-direction	-
f_x	Perfectly Matched Layer stretching function	-
f_y	velocity profile in the y-direction	-
$\boldsymbol{f}$	external force density vector	$\mathrm{N\,m^{-3}}$

$\boldsymbol{F}$	flux matrix	-
$g_{n_{1\to2}}$	transmission source term	-
h	characteristic mesh size	m
h_r	discrete spacing in r-direction	m
h_y	discrete spacing in y-direction	m
H	duct height	m
$\Im$	imaginary part	-
$\boldsymbol{I}$	identity matrix	-
j	unit imaginary number ($\mathrm{j}^2 + 1 = 0$)	-
$\boldsymbol{J}$	Jacobian matrix	-
J_m	m^{th}-order Bessel function of the 1^{st} kind	-
k	wavenumber	m^{-1}
k_0	standard wavenumber	m^{-1}
k_x	longitudinal or axial wavenumber	m^{-1}
k^{c}	characteristic wavenumber	m^{-1}
$\boldsymbol{k}$	wavenumber vector	m^{-1}
K	cut-off ratio	m^{-1}
$\boldsymbol{K}$	system matrix	-
l	number of imposed boundary conditions	-
L	domain length	m
L_x	length in the x-direction	m
L_y	length in the y-direction	m
L_z	length in the z-direction	m
$\mathfrak{L}$	Linearised Euler Equations differential operator	-
(m, n)	mode numbers	-
M	Mach number	-
$\boldsymbol{M}$	coefficient matrix	-
$\hat{\boldsymbol{M}}$	modified coefficient matrix	-
$\boldsymbol{n}$	unit normal vector	-
n_{dof}	number of degrees of freedom	-
n_{e}	number of elements	-
$\boldsymbol{N}$	shape functions vector	-
$\mathrm{nnz}_{\boldsymbol{K}}$	number of non-zero entries	-
$\boldsymbol{o}$	n_{dof}-length vector	-
p	polynomial order or pressure	- or Pa

p_c	modified pressure	-
p_∞	reference pressure	Pa
Pe	Péclet number	-
q	scalar quantity	-
$\boldsymbol{q}$	perturbations variable vector	-
Q	Floquet multiplier	-
$\boldsymbol{Q}$	outgoing heat flux vector	$\mathrm{W\,m^{-2}}$
$\hat{\boldsymbol{q}}$	characteristic amplitude vector	-
$\boldsymbol{q}_\mathrm{d}$	discretised perturbations variable vector	-
$\boldsymbol{q}_\bullet$	discretised perturbations vectors for the field variables	-
r	r-cylindrical coordinate	m
r_e	intake exterior radius	m
r_o	duct outer radius	m
r_i	duct inner radius	m
R	Perfectly Matched Layer reflection coefficient	-
$\boldsymbol{r}$	reflection matrix	-
$\boldsymbol{R}$	coefficient matrix	-
$\mathfrak{R}$	residual	-
$\Re$	real part	-
s	specific entropy	$\mathrm{J\,kg^{-1}\,K^{-1}}$
$\boldsymbol{s}$	source vector	-
$\hat{\boldsymbol{s}}$	modified source vector	-
S	polynomial shape functions	-
$\boldsymbol{S}$	polynomial shape functions matrix	-
St	Strouhal number	-
t	time	s
T	thermodynamic temperature	K
u	velocity	$\mathrm{m\,s^{-1}}$
$\boldsymbol{u}$	velocity vector	$\mathrm{m\,s^{-1}}$
$U_{m,n}$	mode amplitude function in the radial direction	-
$\boldsymbol{U}_{1\to2}$	operator matrix	-
$\boldsymbol{U}_{2\to1}$	operator matrix	-
$\boldsymbol{w}$	test functions vector	-
$\boldsymbol{W}$	eigenvectors matrix	-
x	x-Cartesian coordinate	m

x_i	coordinates	m
$\boldsymbol{x}$	position vector in space	m
y	y-Cartesian coordinate	m
y_1	first discretisation point in generalised eigenvalue problem	m
y_n	last discretisation point in generalised eigenvalue problem	m
Y_m	m^{th}-order Bessel function of the 2^{nd} kind	-
z	z-Cartesian coordinate	m
Z	acoustic impedance	$\mathrm{kg\,m^{-2}}$

Greek

α	plane wave direction of propagation	$^\circ$
α_0	mean flow velocity direction of propagation	$^\circ$
$\alpha_{m,n}$	characteristic equation n^{th} non-trivial zero	$\mathrm{s^{-1}}$
β	shear layer spreading angle	$^\circ$
γ	specific heats ratio	-
γ_{x_i}	Perfectly Matched Layer complex coordinates derivatives	-
Γ	domain boundary	-
δ	shear layer thickness	m
ε	coefficient	-
ζ	constant of proportionality in the equation of state	-
η	η-reference coordinate	-
θ	θ-cylindrical coordinate	$^\circ$
κ	matrix condition number	-
λ	wavelength	m
$\boldsymbol{\Lambda}$	eigenvalues matrix	$\mathrm{m\,s^{-1}}$
μ	fluid shear viscosity	Pa s
μ_x	Perfectly Matched Layer correction coefficient	$\mathrm{m^{-1}}$
ν	diffusivity coefficient	$\mathrm{m^2\,s^{-1}}$
ξ	ξ-reference coordinate	-
ρ	mass density	$\mathrm{kg\,m^{-3}}$
σ	Perfectly Matched Layer absorption function	-
$\boldsymbol{\sigma}$	stress tensor	Pa
τ	stabilisation parameter	s
$\boldsymbol{\tau}$	shear stress tensor or stabilisation parameter matrix	Pa or s
ϕ	velocity potential	$\mathrm{m^2\,s^-1}$

Φ	measure angle	$^\circ$
$\mathbf{\Phi}$	complex amplitude vector	-
χ	field variable	-
ω	angular frequency	$\mathrm{rad\,s^{-1}}$
Ω	computational domain	-

Subscripts

$\bullet_0$	mean flow component	-
$\bullet_\mathrm{a}$	acoustic	-
$\bullet_\mathrm{bl}$	boundary layer	-
$\bullet_\mathrm{d}$	downstream	-
$\bullet_\mathrm{e}$	entropy	-
$\bullet_i$	index	-
$\bullet_\mathrm{i}$	incident	-
$\bullet_\mathrm{int}$	interface	-
$\bullet_\mathrm{l}$	linear mean flow profile	-
$\bullet_\mathrm{n}$	numerical solution	-
$\bullet_\mathrm{p}$	parabolic mean flow profile	-
$\bullet_\mathrm{r}$	reflected	-
$\bullet_\mathrm{u}$	upstream	-
$\bullet_\mathrm{v}$	vorticity	-

Superscripts

$\bullet'$	perturbation component or first-order derivative	-
$\bullet^+$	towards positive direction	-
$\bullet^-$	towards negative direction	-
$\bullet^\pm$	towards positive or negative direction	-
$\hat{\bullet}$	modified variable	-
$\tilde{\bullet}$	Perfectly Matched Layer complex transformation	-
$\bullet^{(j)}$	index	-
$\bullet^\mathrm{env}$	envelope	-
$\bullet^\mathrm{mem}$	memory	-
$\bullet^\mathrm{osc}$	oscillation	-
$\bullet^\mathrm{opt}$	optimal	-
$\bullet^\mathrm{phys}$	physical domain	-

$\bullet^{\mathrm{PML}}$	Perfectly Matched Layer	-
$\bullet^{\mathrm{ref}}$	reference domain	-
$\bullet^{\mathrm{t}}$	vector transpose	-
$\bullet^{\mathrm{T}}$	Hermitian transpose	-

Chapter 1

Introduction

The generation, propagation and absorption of sound in flow ducts are critical issues for many industries. The European Marie-Curie project FlowAirS (Silent Air Flows) focuses on these problems for transport, building and power generation. The general purpose of this project is to investigate new, efficient methodologies to circumvent current limitations of Computational AeroAcoustics (CAA).

Many processes involve air flows for heat transfer and mechanical work: cooling and ventilation systems, internal combustion engines (ICEs), gas turbines, power plants, aeroengines, etc. The unsteady flow and complex geometries constituting these systems lead to pressure perturbations and sound generation. Flow induced noise can be divided into three topics: noise sources, noise reduction and noise propagation. Noise sources are mainly rotating and pulsating machines, whereas secondary sources occur by flow instabilities like turbulence noise. Sound can be emitted directly by radiation through duct openings, but also through wall vibrations. Noise reduction mostly relies on reactive and dissipative silencers. Noise propagation is rather well understood in straight ducts, but duct discontinuities and complex flow effects on near- and far-field propagation are still to be investigated.

In air transport, noise pollution has a significant environmental impact on living beings in the surrounding areas of airports. Aircraft take-off and landing are responsible for community noise whose high levels may cause negative effects on health [6]. The International Civil Aviation Organisation (ICAO) recommendations for the noise produced by aircraft on the ground are becoming more restrictive. For example, at aircraft service locations, the overall Sound Pressure Level (SPL) must not exceed 85 dBA, and a maximum of 90 dBA must be respected along a perimeter of 20 meters around the airplane (recommendations

from the ICAO, Annex 16, Attachment C [7]). Optimised acoustic treatments are thus necessary for auxiliary power units, for air conditioning systems and for turbofan engines, which mainly contribute to sound generation. Also, aircraft interior noise is a challenging key point for passenger comfort. Still in the transport industry, the noise emitted by the cooling systems in trains and cars also creates serious nuisance both for passenger comfort and for exterior environment. In new electric cars, ICE-generated noise reduction is such that its masking effect on other sound sources is less important. As a consequence, these sources become more significant, in particular the noise induced by HVAC (Heating, Ventilation and Air Conditioning) flow and by battery cooling systems.

In buildings, HVAC systems produce excessive noise and vibration that have significant impact on people, making work environment uncomfortable and leading to concentration loss. Loud low-frequency noise can also affect health. For power generation systems, flow noise induces reliability and safety problems. High-vibration levels linked to flow acoustic feedback mechanisms induce fatigue of high-pressure ducts and can lead to mechanical failure.

1.1 Context

The issues associated with noisy air flows are complex and combine different disciplines such as fluid dynamics, structural dynamics and acoustics. Existing techniques for understanding flow induced noise problems are based on experiments, for instance in wind tunnels or anechoic chambers. Because of the complexity for setting up reliable real-scale experiments, these methods can often be expensive both in terms of cost and time. Therefore, using computational methods to model acoustic problems is becoming more attractive, especially on a financial level. However, computer-aided techniques also suffer from drawbacks and computational costs can become prohibitive in some cases. This thesis focuses on the study of efficient approaches to address the existing limitations of CAA methods in the presence of flow due to high computational effort. The continuous increase in computing power makes these methods even more interesting.

Several numerical methods are presently used in industry for modelling acoustic propagation. Accurate results are obtained for low-frequency problems, but these are limited in mid- and high- frequency range. For acoustic simulations, the Finite Element Method (FEM) is one of the most established computational tools for industrial applications in flow duct systems. However, this method faces some issues and improvements are necessary in

order to eliminate existing numerical problems such as dispersion error, pollution effect and convection-dominated instabilities. In addition, there is a need for more general models which take into account, for instance, the mean flow heterogeneities (temperature and density gradients, velocity profile) and the use of porous materials. The improvement of FEM accuracy at high frequencies can rely on stabilised methods, domain decomposition methods, multi-scale or multi-grid methods. The main motivation of this work is therefore to develop a general numerical method that goes beyond the current limitations of the commercial aeroacoustic prediction codes.

The few obstacles to efficient acoustic numerical models are key points in CAA. The numerical methods for complex physical models deal with multiple wavelengths or length scales, and they should be able to solve both short and large wavelengths with appropriate efficiency, i.e. acoustic, vorticity and entropy waves. The wide range of frequencies involved in aeroacoustics is challenging: accurate numerical simulations for the extremely short wavelengths associated with high frequencies are laborious to obtain. Furthermore, aeroacoustic problems generally involve propagation over long distances and interest is given to sound waves radiation in far field. The numerical solution should thus be valid from the source region to the measurement point, located at many acoustic wavelengths away. Therefore, numerical dispersion and dissipation have to be minimal. In addition, the numerical model must cope with spurious oscillations in convection-dominated problems: dedicated formulations should help in addressing these issues. Finally, a general requirement for efficient numerical methods is to provide accurate results with reduced computational time and memory requirements.

This work aims at confronting FEM current limitations for acoustic propagation in the presence of complex flow and geometry. The investigation leads to a new efficient methodology to deal with large-scale problems. The standard FEM is limited by pollution error problems which render that approach very expensive for high frequencies. A technique based on high-order polynomial finite elements (p-FEM, where p is the polynomial order) will reduce these pollution effects and improve the computational costs for a given accuracy. Here, the p-FEM is applied to the Linearised Euler Equations (LEE) operator in order to account for the flow and geometry complexity, and for the acoustic, vorticity and entropy waves. This work is performed in collaboration with the industrial sponsor Siemens Industry Software located in Leuven (Belgium), specialised in developing software and programming model-based system engineering.

1.2 Original Contributions

The final contribution of this thesis is the implementation of a novel accurate efficient prediction tool for acoustic propagation with non-uniform flows. First, a high-order finite element method is developed to solving the Linearised Euler Equations in the frequency domain for multi-dimensional applications. The code is verified with plane wave propagation in free field and duct mode propagation, for acoustic, vorticity and entropy waves, with mean flow.

Second, an analytic study of the Perfectly Matched Layer is performed both in one and two dimensions. A modified stretching function is proposed with an imaginary part to improve wave damping in the PML. This results in the exact absorption of the waves in one dimension and better performance in two dimensions, with respect to classical logarithmic stretching functions.

Third, a detailed analysis of the dispersion problem and of the convection-related spurious oscillations is carried out and numerical stabilisation is investigated. Optimal stabilisation parameters are found analytically for low polynomial orders, which are able to cancel out the dispersion error. The effects of high orders show that even orders introduce artificial diffusion in the numerical model which is responsible for a lower convergence rate of the dispersion error. Stabilisation corrects the asymptotic convergence for these orders.

Fourth, a novel coupling technique is developed in order to optimise the numerical model by accounting for the heterogeneous character of the mean flow for aeroengine exhaust applications. In the computational domain, the Linearised Euler Equations, which are solved in the rotational flow regions, are coupled with the Linearised Potential Equation, which is solved in the potential flow regions. The procedure is based on characteristic transmission conditions at the coupling interfaces. This coupling technique produces accurate results similar to the full Linearised Euler Equations solution, with lower memory requirements and computational time.

Fifth, the numerical model is applied to several test cases such as an aeroengine intake with potential mean flow, a straight duct with several mean flow configurations, and a realistic aeroengine exhaust with complex heterogeneous mean flow. The mean flow effects are assessed, as well as the impact of the mean flow interpolation on the sound field. These effects are significant in strong shear layer regions, but are limited outside these regions.

1.3 Thesis Outline

In the scope of numerical methods for acoustic propagation, the aim of this thesis is to develop a novel computational model accounting for the effects of complex mean flow and geometry on the sound field. The objectives are to develop a novel approach solving the Linearised Euler Equations in the frequency domain with a high-order finite element code. The procedure used in this thesis is based on the following structure. In Chapter 2, the literature review provides a general overview on existing numerical methods for aeroacoustics. The physical model described in Chapter 3 introduces the governing equations for wave propagation in non-uniform media and provides reference solutions for further verification of the numerical method. In Chapter 4, the high-order finite element model is detailed as well as the boundary conditions. Several verification results for the numerical model are thus developed in Chapter 5, which validate the main features of the code for further application to realistic test cases. Some model improvements are developed in the following two chapters. In Chapter 6, the numerical stabilisation problem is discussed in terms of dispersion error and convection-related instabilities. A coupling method between two mathematical models is then proposed in Chapter 7. The application cases are detailed in Chapter 8 with engine intake, simplified exhaust and realistic exhaust problems. The conclusions of this work are enumerated in Chapter 9, and directions for future work are suggested.

Chapter 2

Literature Review

This work aims at developing a high-order finite element model to compute acoustic propagation in a heterogeneous mean flow, by solving the Linearised Euler Equations. To that purpose, the following literature review analyses several aspects which are relevant for this study. In this chapter, the targeted applications for this project are first introduced, as well as the noise problem in transport industry. A discussion of Computational AeroAcoustics is then presented in the second section. The third section focuses on existing mathematical models and their description. Next, aeroacoustic models are described, including comments on time/frequency domain, grids and computational schemes. The subsequent section is dedicated to boundary conditions, and the final part explains features related to numerical accuracy.

2.1 Targeted Applications

In the transport industry, commercial aviation experiences a continuous growth. Reducing travel times over large distances and providing numerous employment opportunities, aviation presents several benefits. Nonetheless, various effects of this industry have negative impact on the environment, particularly on climate change, air quality and noise. Besides climate pollution through heat, particulates and gases emissions from fossil energy fuels, aviation noise is a major concern for civilian populations. Effects on health can be caused by aircraft noise at take-off and landing stages, creating high levels of stress and annoyance [6, 8, 9]. In addition, aircraft noise can also have aesthetic and affective impact on natural landscape assessment [10]. Negative effects are not only limited to humans but more generally extend to wildlife in terrestrial environments [11].

Worldwide, aircraft-traffic control organisations have imposed more and more restrictive conditions in order to reduce aircraft noise impact. Although present-days aircraft are 75 % quieter than those manufactured in the 1960's [12], achieved principally via an increase in bypass ratio, reducing the environmental footprint of aircraft noise is a key goal for the ICAO. The organisation defined noise reduction technology goals, whose long-term objectives expect a diminution of about 20 EPNdB in 2028 with respect to the effective perceived noise levels EPNdB (in decibels) in 2010. Similarly, the European Commission have indicated their objectives for aircraft perceived noise emissions: these should be reduced by 65 % in 2050 with respect to typical new aircraft capabilities in 2000 [13].

Modern turbofan-powered aircraft generate sound through the engine and the airframe. The aeroengine noise is produced by different mechanisms [14]. The fan and compressor are responsible for noise propagating through the intake duct and radiating to the far field in the forward arc region. The fan also contributes to noise propagation through the bypass duct, which radiates through the bypass shear layer. The turbine and combustor generate core noise which propagate through the exhaust streams and radiate to the far field in the rear arc region. Finally, the so-called jet noise is produced by the unsteady mixing exhaust shear layers. The reduction of aircraft engine noise over the years has made airframe noise comparable with engine noise during the approach to landing [15]. The airframe major noise sources are caused by flow interacting with the landing gear, the slats and the flaps [16].

In the framework of duct systems which are present in turbofans, silencers or liners are used to reduce the sound during propagation. These silencers can use different types of dissipative materials such as porous materials. Several research projects are ongoing to better understand the benefits of such materials for sound absorption, using heterogeneous materials with for instance two different microscales [17] or investigating complex porous structures [18]. Some studies also assess the mean flow effects on sound propagation [19].

Within turbofan aircraft, this work focuses on the sound propagating by the aeroengine. In particular, the application test cases developed in Chapter 8 concentrate on the sound propagation from the aeroengine intake and from the aeroengine exhaust. The mechanisms of sound generation and absorption are not studied here, and the numerical model described in this work focuses on sound propagation aspects. However, the model is also suitable for applications such as installation effects of fan/OGV (Outlet Guide Vane) interaction noise.

2.2 Computational AeroAcoustics

Computational AeroAcoustics (CAA) develops numerical methods to predict aerodynamic noise generation and propagation. Since the mid 1980's, CAA has been identified as a discipline different from Computational Fluid Dynamics (CFD). Hardin and Lamkin first introduced computational aeroacoustics for sound calculations with low Mach number and low Reynolds number [20]. The traditional approaches used by the CFD community were not suitable for modelling noise propagation. A major reason for this rests on the difference in length scales and amplitudes between the flow and acoustic fields. Although they provide insight into fundamental mechanisms in fluid mechanisms, high-resolution schemes such as Direct Numerical Simulation (DNS) require enormous computational resources for solving simultaneously both length scales [21]. Those are therefore not adequate for full-scale industrial design. In practice, hybrid approaches combining CFD and acoustic propagation models are largely used: the CFD results provide the mean flow field and characterise the noise sources, which are generally located in small regions where non-linear effects prevail; the aeroacoustic model computes the far-field radiated noise, whilst taking into account the background flow [22]. Hardin and Lamkin were at the origin of this hybrid technique with the aeroacoustic computation of cylinder wake flow in 1984 [23].

In 1993, Tam and Webb listed CAA special requirements for finite difference schemes [24]. These particular challenges were also highlighted in a more recent review on advances in computational aeroacoustics by Tam in 2006 [25]. For instance aerodynamics implicates low-frequency unsteadiness, whereas aeroacoustic problems are time dependent and involve large frequency ranges. High-frequency waves with very short wavelengths also restrain numerical simulation accuracy since they require finer discretisation [26]. In the framework of aeroengine noise, the sound radiated to the far field is of interest and the solution needs to be valid from the source region all the way to the microphone at many acoustic wavelengths away. Because waves are very sensitive to numerical dissipation and dispersion which accumulate along the way, these must therefore be reduced to the minimum [27]. Another critical aspect of CAA lies in the fact that the waves reaching the computational domain boundaries may be reflected back into the domain and pollute the solution. Designing proper boundary conditions which help the waves in exiting the computational domain without spurious reflections is therefore crucial [28].

Aeroacoustic models face several problems which ongoing research tends to circumvent [29]. Amongst these issues, the multiple length scales involved in aeroacoustic problems

are such that the acoustic source is usually very different from the acoustic wavelength. This dependency naturally follows on from the underlying physics. As a consequence, necessary long time integration to capture the full problem physics leads to expensive computational costs for high accuracy requirements. The computational accuracy and efficiency of the numerical method are therefore of primary importance. In addition, high-frequency waves can have spatial scales which are many orders of magnitude smaller than the far-field propagation distance. Fine spatial domain discretisation is thus required for these small scales. Another concern with aeroacoustic simulations is the presence of vorticity and entropy perturbations in the model, which length scales may be very different from the acoustic wavelengths. The numerical models should be highly accurate to describe the coupling between the different physical phenomena which may combine these different types of waves. Furthermore, complex geometries in aeroacoustic problems require sufficiently detailed representation of the boundaries to maintain high accuracy levels [30]. These features in CAA are further discussed in the following paragraphs.

2.3 Physical Models

The mathematical models used to model aeroacoustic problems must represent the physics carried by the background mean flow under specific approximation levels, amongst which: the convection effects on the acoustics, vorticity and entropy waves, the refraction of the sound field through shear layers, the interaction between the acoustic waves and the hydrodynamic/entropy waves, the non-linear or viscous effects. In CAA, two different approaches can be used: the direct and hybrid techniques. The full compressible Navier-Stokes equations solution contains both the base flow and the perturbations, whose orders of magnitude differ significantly [31]. Direct methods such as DNS consider the totality of the problem scales, which vary from the smallest turbulent fluctuations to the largest convective features [21]. DNS is therefore a high computational cost method which is mainly used to help in flow dynamics understanding [32]. To avoid computing all length scales, Large Eddy Simulation (LES) offers an alternative approach by applying a filtering operator which separates the smallest scales via a subgrid-scale model [33]. Kolmogorov formulated relevant assumptions to remove the high-frequency structures [34]: the large scales characterise the flow, are sensitive to boundary conditions, are anisotropic, and contain the main part of the total fluctuating kinetic energy; the small scales are isotropic, are responsible for the viscous dissipation, and contain only a few percent of the total fluctuating kinetic energy.

Though, applying LES to solve aeroacoustic problems still remains prohibitive for far-field propagation and large Reynolds numbers.

To reduce the computational cost, hybrid methods decouple the sound propagation from the sound generation. In a first stage, the sound sources can be computed in a small region using DNS or LES [35]. Then, the sound propagation to the far-field can be performed with an acoustic analogy such as Lighthill's [36]. Alternately since DNS and LES are still expensive for practical engineering applications, Reynolds Averaged Navier-Stokes (RANS) solution can be used to compute the mean flow field and to construct the acoustic sources through analytic means or stochastic methods [37]. To compute the sound propagation, different aeroacoustic models can be used. These are discussed in the following paragraphs.

In linear acoustic problems the fluid density, pressure and velocity fluctuations are in general very small with respect to the respective mean flow quantities. This observation justifies the fluid motion to be described by linear approximations of the governing equations, neglecting non-linear effects [31]. First, problems where viscosity effects on the perturbations may be significant could be solved using the Linearised Navier-Stokes Equations (LNSE) [38]. These equations are suitable to solve sound propagation near solid-wall geometries where viscosity gives rise to boundary layer effects. Since acoustic boundary layers may play a major role in sound wave damping for duct propagation, viscosity should not be neglected for applications such as in-duct orifice propagation [39, 40].

A second physical model is derived from the LNSE: by neglecting viscosity and heat transfer, the Linearised Euler Equations (LEE) are obtained [41, 42]. They represent the linearised form of the compressible Euler equations, which constitute a simplification of the Navier-Stokes equations. The LEE solutions are composed of acoustic, vorticity and entropy waves [24, 30]. In addition, the LEE support Kelvin-Helmholtz instabilities which may develop in non-uniform mean flows. In real flow, these unstable spatial effects are attenuated by viscous and non-linear effects. Since the LEE do not conserve the non-linear terms, instabilities may not be damped by non-linearities, resulting in the growth of these instabilities in the numerical model which would pollute the numerical solution. Some techniques have been developed to limit these instabilities. For instance, the Acoustic Perturbation Equations (APE) have been proposed as a variant of the LEE but their accuracy at low frequency is limited [43]. Also, rewriting and solving the LEE in the frequency domain is considered a way to avoid the frequency range in which these instabilities grow [44, 45]. Other ways for removing instabilities have been developed such as a saturation method [41] and the suppression of the mean flow derivatives in the formulation [42]. In

this work, the LEE are solved and more details on these equations are given in Chapter 3.

Other physical models have been used in the literature to solve aeroacoustic problems. The most common assumption is that the temperature gradients are null in the flow region, meaning that the flow is homentropic [31]. In the linearised potential theory, the mean flow is irrotational and the velocity is expressed in terms of a potential [46]. The subsequent Linearised Potential Equation (LPE) presents the advantage of involving only a scalar variable, the velocity potential, while up to five unknowns are solved for the LEE. Although the assumption limits this model to irrotational flows, Pierce has shown that this formulation also holds for arbitrary unsteady flows, but for sufficiently small wavelengths [47]. Prinn *et al.* have applied the LPE to noise radiation by an aeroengine exhaust: in this model a shear layer makes the transition between the jet mean flow velocity and the exterior mean flow velocity, and vorticity waves develop from the duct outlet lip. The pressure and displacement continuity is ensured across the vortex sheet and by implementing the Kutta condition at the nozzle lip, resulting in the noise refraction through the shear layer [48].

In the case of parallel sheared flows, acoustic propagation has been described by Pridmore-Brown for constant flow properties in the streamwise direction [49]. This equation supports both acoustic and hydrodynamic waves, but is limited to very specific flows. Another mathematical model is the convected Helmholtz equation which considers uniform mean flows [50, 51]. This equation relates the Laplacian operator and the second material derivative in the mean flow of the pressure field perturbations. Although it describes the acoustic field, the main drawback of this model, which is also the one of the LPE, is that it does not support the hydrodynamic and entropy perturbations. Finally, the standard Helmholtz equation can be used if the flow is at rest or can be neglected, which is often possible for low Mach number M applications ($M < 0.1$) [52].

2.4 Aeroacoustic Models

Solving the physical models described in the previous section may be achieved through a number of computational methods. Such numerical methods predict sound propagation in mean flows, based on frequency- or time-domain models, using structured or unstructured grids. These aspects are discussed in the following paragraphs, as well as existing computational schemes.

2.4.1 Frequency and Time Domain

Solving aeroacoustic problems can be performed either in the frequency domain or in the time domain, and both approaches have advantages and drawbacks [45]. By definition, a frequency-domain approach is particularly suitable for tonal noise aeroacoustic problems, since only a few frequencies have to be solved for. In addition, frequency-based computations are often considered a way to avoid linear instabilities [44]. However, frequency-domain solutions require solving global system matrices which can involve large memory requirements. This issue increases rapidly with the problem size, the frequency and the number of variables to solve for instance with the LEE. In order to minimise these memory requirements and decrease the computational time, coupling methods can be considered. The basic idea is to optimise the simulation by using appropriate mathematical models in different regions of the computational domain where the LEE may not be needed. A similar approach has been applied to a CFD/CAA coupling method for jet noise prediction [53]. In this work a novel technique coupling the LEE and the LPE is developed and discussed in Chapter 7.

In the time domain a single computation can provide a solution over a wide frequency range. Time-domain solutions may therefore be more convenient for broadband noise investigation. One main advantage over frequency-domain methods is the relative low memory requirements resulting from explicit time-stepping schemes. Nonetheless, impedance boundary conditions modelling is not straightforward and its accurate description is an issue in the presence of mean flow [54]. The numerical instability associated with the Myers condition, which describes the impedance condition and the flow effects over an acoustic liner, is likely to appear with fine grids and to deteriorate the numerical solution [55]. Furthermore, time-domain solutions are also known to suffer from linear instabilities which would deteriorate the numerical solution [44]. In the presence of thin mean flow shear layers, the Kelvin-Helmholtz instabilities develop below a critical frequency. While in the frequency domain the frequency is well defined, time-domain solutions support the complete frequency range and the frequencies responsible for the Kelvin-Helmholtz instabilities may indeed be triggered, resulting in inaccurate solutions [30, 56]. In the following, existing LEE models are reviewed both in frequency and time domain.

LEE Models in Frequency Domain

Several numerical methods have been applied to solving the LEE in the frequency domain, ranging from the high-order finite difference [57, 58] to the finite element [59] schemes or

the discontinuous Galerkin method [60]. In the early 1980's, Astley and Eversman have first solved sound propagation using the two-dimensional LEE with weighted residual or finite element methods [61, 62]. For sound transmission through non-uniform ducts carrying high speed subsonic compressible flows, the authors have observed that the finite element approach compares favorably with the weighted residual method. Iob *et al.* have solved these equations through two-dimensional and axisymmetric formulations on an unstructured mesh using triangular and quadrangular elements, with a linear finite element method based on a continuous Galerkin discretisation [59]. In a complementary study by Iob *et al.* [60], a high-order discontinuous Galerkin method has been applied instead of using a continuous Galerkin approach. Both models have been validated for the Munt problem [63]. To reduce the memory requirements, a parallel distribution has been applied with the finite element model while static condensation has been used with the discontinuous Galerkin method. The latter allows to express the interior degrees of freedom in terms of the boundary ones before assembling the system matrix (see Section 4.3.5). Also to reduce computational time and memory requirements, the authors neglected the pressure gradients in the momentum equations which allowed to decouple the continuity equation and to solve only the momentum and energy equations. With such an approach the number of total unknowns is therefore reduced by a factor of 5/4.

Studies solving the LEE in the frequency domain may be motivated to avoid instability waves to deteriorate the numerical solution. In 2004, Agarwal *et al.* have suggested that the instabilities may be avoided for a time-harmonic response if the governing equations are solved with a direct method in the frequency domain [44]. Several authors have solved the LEE in the frequency domain to cancel these instabilities [58, 60, 64]. In particular, Özyörük and Tester show that the instabilities completely disappear from the solution when the gradient terms are excluded from the LEE [58].

Solving in frequency domain may also generate spurious oscillations in convection-dominated problems, which would compromise the numerical solution. Specific details on this issue are given in Chapter 6, as well as ways to avoid these oscillations such as the Streamline-Upwind Petrov-Galerkin (SUPG) method. In 2006, Rao and Morris have compared this method with the Discontinuous Galerkin Method (DGM) to solve the two-dimensional LEE in the frequency domain for a general mean flow configuration with unstructured grid [64]. A crucial point in the SUPG method is the stabilisation parameter which is decisive for the suppression of the aforementioned spurious oscillations which may occur in convection-dominated problems. The authors conclude that, in terms of computational cost, the SUPG method is less expensive than the DGM for practical aeroacoustics applications in

the frequency domain.

LEE Models in Time Domain

An important issue with time-domain LEE models is the suppression of the linear instabilities which may grow in the numerical solution. Different techniques have been applied in that purpose. In 2000 Bailly and Juvé have developed a two-dimensional LEE solution by using a Dispersion-Relation-Preserving (DRP) finite difference scheme in space, combined with a fourth-order Runge-Kutta algorithm in time [41]. In order to suppress the instabilities, the authors have proposed a modified formulation of the time-domain LEE. A non-linear formulation has been developed to saturate the instability waves growth, by adding the flux vectors containing the non-linear terms. As suggested by the authors, the time-domain LEE model provides accurate solutions for sound propagation and good performance is achieved in terms of stability, storage and computational time. The artificial non-linear terms limit the growth of the instability waves supported by the LEE, without significantly altering the computation of the acoustic waves. Another way of preventing the growth of instability waves has been proposed by Bogey *et al.* in 2002 [42]. The sound field generated by a subsonic mixing layer has been investigated by solving the LEE. In this purpose, the terms responsible for linear instabilities have been removed in the formulation. These terms contain the mean flow derivatives. The results indicate that such a modification of the LEE gives a good approximation for high-frequency sound propagation. For low-frequency cases the numerical solution is slightly inaccurate.

The LEE have been studied in the time domain for the formulation of acoustic source terms. Billson *et al.* have computed jet noise acoustic solutions using the Stochastic Noise Generation and Radiation (SNGR) method [65]. In this method, the LEE written in conservative form have been derived to build an acoustic analogy together with source terms. The simulations have been performed using a fourth-order DRP scheme in space and a fourth-step fourth-order Runge-Kutta time marching technique. This acoustic analogy based on the conservative form of the LEE provides results in good agreement with direct simulation solutions.

Other authors have solved the Linearised Euler Equations in time domain for acoustic propagation. For instance, Richards *et al.* [66] have developed a computational model of fan noise radiation through an engine exhaust geometry with flow. Acoustic wave propagation is calculated for the axisymmetric LEE. The LEE model uses a sixth-order prefactored compact scheme to calculate spatial derivatives and a fourth-order Runge-Kutta scheme for time integration. The computed solution has been compared to a semi-analytic multiple-

scale solution, and the agreement is good until near the by-pass duct exit, where the duct geometry changes. Besides, some solutions are present in industry to solve the LEE in time domain. The commercial software Actran DGM based on the discontinuous Galerkin method has been used to solve large three-dimensional problems with arbitrary mean flows [67]. In terms of computational cost this time-domain model developed in Actran significantly reduces the memory requirements in comparison with a similar approach in the frequency domain, whereas it increases the computational time [45].

2.4.2 Structured and Unstructured Grids

In computational methods, domain discretisation is crucial to properly describe the geometry and to solve accurately the problem [68]. Structured grids are generally more convenient to achieve high accuracy, since they limit dispersion and dissipation phenomena. They also generate simpler data structures which lead to better optimisation and usage of computational resources. However, designing structured meshes may be time consuming for complex geometries and requires special care to preserve grid quality. On the other hand, less time is usually required for users to generate unstructured meshes. Another benefit of unstructured grids is their high potential for automated mesh generation, which is important for design optimisation. Nonetheless, unstructured grids involve more complex data structures which makes it more difficult to optimise the usage of computational resources. Several methods for mesh generation exist and differ in terms of speed, robustness and quality [69]. Conformal meshes are such that nodes, edges and faces are perfectly matched between two neighbouring elements. On the contrary, non-conformal meshes have interfaces between cell zones in which the mesh node locations are not identical. Furthermore, curved elements may be used: such high-order approximations allow to use larger elements by guaranteeing an accurate geometry representation [70]. In this work, conformal unstructured meshes are used.

2.4.3 Computational Schemes

In the following, an overview of several methods is proposed, amongst which the Finite Difference (FD) method, the Discontinuous Galerkin Method (DGM), the Boundary Element Method (BEM), the Statistical Energy Analysis (SEA) method, ray acoustics and the Finite Element Method (FEM).

Finite Difference Method

CAA problems have been solved with the Finite Difference method. Commonly, this method has been used to solve the LEE and the Navier-Stokes equations in the time domain because of the high accuracy level required to solve the acoustic and vorticity perturbations. The development of high-order low-dispersion schemes have made this method more efficient [24, 57, 58]. The major issue with the FD method is that it relies on structured grids which restrain its use to problems with limited geometrical complexity [71].

Discontinuous Galerkin Method

The Discontinuous Galerkin Method uses an approximation which is continuous only inside each element, while the continuity between elements is ensured through the definition of numerical fluxes. Unstructured grids can be used with this method. The DGM is often considered a spectral method since the solution is generally interpolated with high-order polynomials. Non-polynomial bases have also been considered for time-dependent problems [72]. Over the past fifteen years, the DGM scheme has been used for solving aeroacoustic problems in the time domain [67, 73–75] and in the frequency domain [64]. Though, some issues for practical engineering applications are still to be investigated: for instance, the usual quadrature-free formulation is efficient but suffers to represent accurately curved boundaries [38, 67, 76]. Another disadvantage of the DGM is its computational cost due to the discontinuous character of the method: the extra degrees of freedom at cell boundaries demand more computational resources.

Boundary Element Method

Unlike the previous methods, the Boundary Element Method solves the acoustic problem on the domain boundary [77, 78]. The solution inside the acoustic domain is determined based on the boundary solution, such that the variables inside the domain are expressed as a surface integral over the domain boundary. The BEM can be computationally expensive in models with a large number of degrees of freedom [79, 80]. The model construction itself is quite demanding, since the matrices are fully populated, frequency dependent, complex and non-symmetric. To overcome the high memory requirements,the Fast Multipole BEM (FMBEM) [81] and the hierarchical matrix approach (data-sparse approximation of non-sparse matrices) [82, 83] have been developed. In the FMBEM, the traditional BEM is solved using high-speed iterative techniques where the model is split up into several domains which are then split up again and again. This results in a gain in memory. The BEM is usually limited to homogeneous propagation media. Some extensions to slowly varying

mean flows [84] and weakly non-uniform potential flows [85] have been proposed.

Statistical Energy Analysis and Ray Acoustics

High-frequency modelling can be supported by two alternative prediction techniques, Statistical Energy Analysis (SEA) and ray acoustics. As a probabilistic technique, the SEA provides averaged approximations of a dynamic system global response, which is subdivided into subsystems [86]. The frequency range is also split into frequency bands. For each subsystem, an energy balance is written and the resulting equations are solved for the averaged subsystem energy levels. The SEA is mainly interesting because of its low computational efforts, since only average energy levels have to be determined. Also for high-frequency problems, ray acoustics is based on the ray tracing technique [87]. The acoustic domain and the scattering object dimensions are large compared to the acoustic wavelength. The hypotheses of this technique permit however to obtain good indicative prediction results, notably for the acoustic modelling in large spaces, both indoor (factory floors, churches, concert halls) and outdoor (urban areas, airports).

Finite Element Method

For solving engineering problems in acoustics, the Finite Element Method is currently one of the most frequently used computation techniques in industry. The governing equations are associated with appropriate boundary conditions to predict acoustic propagation in a continuum domain [88–90]. Details on the method are given in Chapter 4. Finite elements for acoustics has first been introduced introduced by Gladwell in 1965 [91]. From an engineering viewpoint, Donea and Huerta have detailed the fundamentals of stabilised finite element methods for the analysis of steady and time dependent fluid dynamics problems [92]. Harari provides a survey on finite element methods for time harmonic acoustics, and reviews the current related issues and methodologies [93]. In 2006 Thompson has focused on time-harmonic acoustics governed by the Helmholtz equation [94]. He reviewed the state of the art and the challenges of the finite element methods, the main issues being the memory requirements, the treatment of acoustic scattering in unbounded domains and the numerical dispersion error at high frequencies.

The FEM has been extensively used to solve the convected wave equation in the frequency domain [93, 95–97]. However, this method suffers from dispersion error: the wavenumber obtained for the numerical solution differs from the exact wavenumber. The subsequent pollution effect, which corresponds to the accumulation of the dispersion error over the domain, is significant for low-resolution problems [27, 98], which renders this technique

particularly expensive for high frequencies or large problems. The classical FEM, when applied to wave propagation, suffers from the accumulation of dispersion error and the pollution effect. Babuska and Sauter have discussed it for the Helmholtz equation at high wavenumber [99]. Finer mesh grids are therefore required in order to limit this error and obtain an acceptable accuracy. Consequently, the classical first-order FEM is usually limited to low frequency applications.

A few alternative methods have been proposed to bypass this drawback: the Partition of Unity Finite Element Method (PUFEM) [100], the Ultra-Weak Variational Formulation (UWVF) method [101, 102] and the Discontinuous Enrichment Method (DEM) [103]. The latter suffers from prohibitive computational assembly procedures and the difficulty to apply them to problems with inhomogeneous media. A suitable and efficient alternative for most wave propagation problems is the adaptive finite element method. Three different types of that technique are present in the literature: the h- (spatial refinement), p- (polynomial order) and hp-versions of the finite element methods. In the h-FEM, the mesh is generally constructed by an adaptive procedure with local refinement based on error estimators. In the p-FEM, the convergence is ensured by the polynomial order p of the shape functions while the mesh is already defined. These two techniques are associated in the hp-FEM. In 1992 Babuska and Guo have produced a comparative study of these three adaptive strategies for finite elements [104]. The p-FEM is one of the best approaches for practical engineering computations of problems in structural mechanics. In 1997 the h- and hp-versions of the FEM have been treated by Ihlenburg and Babuska for the Helmholtz equation with high wavenumber [98, 105]. More recently in 2006, Rachowicz *et al.* have presented a three dimensional implementation of the fully automatic hp-adaptive mesh refinement with positive results, especially in terms of convergence both with respect to problem size and computational time [106].

For practical problems, enriching the polynomial basis with high-order shape functions in the p-FEM leads to improved accuracy and lower memory requirements, including in the presence of mean flow [51, 52]. High-order approximations allow to solve high-frequency problems [107]. The nodal shape functions have the advantage of the δ-property: their value is one at a certain node and zero at the others. Therefore, the corresponding unknown degree of freedom directly relates to the solution at a specific point of the element. The other family of polynomials refers to the modal shape functions, which do not have the δ-property. In some cases, these polynomials have the hierarchic property, such that the basis of the polynomial space for order p is included in the basis for order $p+1$. This characteristic is an advantage for p- and hp-adaptivity, since the shape functions do not

have to be changed when increasing the polynomial order of the approximation. In this work, the Lobatto hierarchic shape functions are used for their good conditioning properties [108].

One of the concerns when it comes to the p-FEM is the choice of the polynomial basis for high-order approximation [108]. Petersen *et al.* have compared some polynomial bases commonly used in finite element methods [109]: Lagrange polynomials, Legendre polynomials and Bernstein polynomials. They found that high-order polynomial bases increase the efficiency of direct solvers, whereas high-order polynomial bases generally decrease the stability and the efficiency when using iterative solvers . However, Biermann *et al.* have shown the improved performance and robustness of a Bernstein polynomial base finite element formulation with iterative solver for solving Helmholtz problems [110]. Bériot *et al.* have discussed the performance of a high order finite element method for solving Helmholtz problems at high frequencies, for practical engineering applications [107]. They have assessed the performance of a three dimensional p-FEM model for solving a Helmholtz problem for intermediate wavenumbers. Prinn has also used the p-FEM for aircraft engine noise prediction [46]. Very high orders may become inefficient for more complex geometry problems which would require a thinner refinement to properly describe the geometry. This calls for adaptive techniques with specific orders with respect to each element size.

2.5 Non-Reflecting Boundary Conditions

Boundary conditions are very important in CAA in order to make the acoustic problem well posed, stable and accurate. The physical domain is often truncated because of the limitation of the finite computational domain. Thus, non-reflecting boundary conditions (NRBCs) must be applied so that outgoing waves are not reflected back inside the domain and do not pollute the solution. Such techniques include Infinite Element Method (IFEM) [111], Absorbing Boundary Condition (ABC) [112] and Perfectly Matched Layer (PML) [113]. In addition, far-field reconstruction methods are necessary to predict the sound distribution outside the computational domain [114]. Kreiss has examined the mathematical theory for boundary value problems in order for hyperbolic systems to be well posed [115]. A few years later, Engquist and Majda have first specified the theoretical basis for non-reflecting boundary conditions [112]. Higdon [116] has then given a physical interpretation of this theory by discussing boundary conditions for linear hyperbolic partial differential equations in one or more spatial dimensions. These theoretical studies form the basis for

the definition of suitable non-reflecting boundary conditions for numerical simulations. The most commonly used non-reflecting boundary conditions for the Euler equations are the method of characteristics, the far field asymptotic boundary conditions and the buffer zone techniques.

The method of characteristics applied to the Euler equations has been presented by several authors for formulating non-reflecting boundary conditions. Thompson has developed a general formalism for all types of boundary conditions involving hyperbolic systems, including non-reflecting boundaries [28, 117]. Giles [118] has also contributed to this work and formulated the mathematical theory in a simpler form for engineering applications. In this method, the value of the characteristics associated to waves entering the domain at the boundary is directly assigned. This technique applies the splitting of one-dimensional characteristics variables in the normal direction to the boundary. This approach is practical but one limitation is that the reflections are theoretically prevented only in the normal direction to the boundary, and some non-negligible reflections may occur for waves hitting the boundary with non-normal incidence. This method has been used for the prediction of supersonic jet noise using the LEE [119]. Further details on the method implementation are given in Section 4.2.

Another class of non-reflecting boundary conditions are the radiation boundary conditions [120]. They are based on asymptotic solutions of the governing equations. The wave equations in the far field are replaced by analytic solutions which are obtained by imposing an asymptotic behaviour to the system [24, 121]. These boundary conditions have been shown to be accurate in some specific cases. However, obtaining asymptotic solutions can be complex in many problems and the applicability of this technique may be limited.

The buffer zone technique is another family of non-reflecting boundary conditions,[122, 123]. The computational domain is extended in order to create an additional zone in which the solution is damped by application of low-pass filters, grid stretching or numerical damping. A first absorbing zone is based on the modification of the governing equations in order to mimic physical dissipation mechanisms through artificial dissipation and damping coefficients [124]. The reflection coefficient at the outlet boundary depends on these additional parameters. Ta'asan and Nark have also proposed another method consisting in accelerating the mean flow to supersonic speed at the end of the buffer zone [125]. The main advantage of these buffer zone techniques is the simplicity of implementation. Nevertheless, adjoining buffer zones generates additional degrees of freedom and increases the computational cost. Richards *et al.* have studied the performances of buffer techniques

based on numerical damping [126]. They concluded that a buffer zone boundary condition that uses explicit damping provides the best performance. Nonetheless, it is also observed that higher outgoing wave angles deteriorate the efficiency.

As an alternative to the previous damping techniques, the Perfectly Matched Layer (PML) is also gaining popularity in the CAA community. First introduced by Bérenger in 1994 , the PML was developed for electromagnetic waves absorption [113]. In practice, the outgoing waves are damped in an extra zone created around the computational domain. The PML is based on the modification of the coordinates system in the additional layer, transforming the coordinate in the direction of absorption into the complex plane. In practice, this transformation turns propagative waves into evanescent waves with artificial damping. The main advantage of the PML as an absorbing boundary condition over classical buffer zones stands in the equations formulation, which is theoretically able to damp any kind of waves, regardless of the direction or the frequency. In 1996 Hu has first proposed a PML formulation for absorbing waves from the LEE [127]: the outgoing acoustic, vorticity and entropy waves are damped without reflection. Nevertheless, Tam *et al.* have stressed that, for open domains, the PML equations support instabilities with the LEE and subsonic mean flow normal to the layer [128]. Abarbanel has applied the PML to the Euler equations and noticed exponentially growing solutions at the interface between the computational domain and the PML under specific flow conditions [129]. Hu has further developed a stable time-domain PML formulation for the LEE in the presence of mean flow in order to cancel the exponentially growing instabilities that appear for inverse upstream waves [130]. These waves have a positive group velocity but a negative phase velocity in the direction of the mean flow, which become amplified in a classical PML formulation. Bécache *et al.* have also developed an approach to damp these inverse upstream waves in the frequency domain [50]. This work has been extended to a parallel non-uniform mean flow [131]. The PML is studied in this work and more details on the technique and its implementation are provided in Section 4.4.

2.6 Numerical Accuracy

Computational methods provide approximated solutions of real problems under specific assumptions. Their accuracy is therefore subject to several parameters which are discussed in this section. Amongst these parameters governing the accuracy of a numerical model, the geometric description must necessarily be accurate in order to represent the relevant

geometrical features without introducing spurious scattering. Curved and complex boundaries are badly represented by coarse linear interpolation, and mesh refinement helps in improving the geometric representation for finite elements. However, such a solution increases the computational cost. As an alternative, the geometric interpolation order could be incremented, resulting in a more accurate description of the problem boundaries: for instance a classical triangular element with three nodes can be improved to a six-node triangular element. This geometric enhancement improves the geometric description but the geometry may still not be exactly described, and some geometric error still exists. This translates into a difference between the numerical solution solved for the approximated geometry and the analytic solution of the original problem [132]. The difference between these two solutions is the Geometry Induced Error. High-order curvilinear mesh [133] and NURBS-enhanced method [134, 135] are examples of ongoing research to improve geometry representation for finite elements.

Another relevant aspect in numerical accuracy is given by the mean flow interpolation. For practical applications, CFD simulations generally provide the mean flow, typically using RANS solvers. The resulting CFD data on the CFD mesh are then mapped onto the acoustic mesh used for solving the acoustic problem. The mesh resolution requirements are generally very different for CAA and CFD simulations, since the acoustic and hydrodynamic length scales are usually significantly disparate. Using coarse mesh with high-order models for acoustic propagation makes this difference notably more relevant. The mean flow interpolation onto the acoustic grid is responsible for significant errors, in particular in regions with high gradients such as shear layers or boundary layers. A poorly accurate description of strong mean flow gradients in the acoustic computation may lead to inaccurate solutions and spurious reflections for small acoustic wavelengths. To overcome these interpolation errors, locally refining the acoustic mesh is one possibility. For high-order methods, a mean flow interpolation directly at the Gauss points of the numerical quadrature also lead to a more accurate representation of the CFD data. The mean flow representation effects are discussed in Chapter 8 for the application test cases. Introducing smarter mapping methods is also an approach to improve the mean flow interpolation. For instance, Gracia *et al.* have developed a least-squares mapping procedure combined with an anti-aliasing filter [136, 137].

The FEM has been widely studied in the literature for wave propagation problems [98, 105, 138, 139]. Ihlenburg and Babuška have shown that upper bounds for the global error in the H^1-norm can be found for the Helmholtz equation solved with the *hp*-version

of finite elements [105]. While an algebraic convergence is observed when increasing the mesh resolution (h-refinement), an exponential convergence is obtained when increasing the interpolation order (p-refinement). This shows how advantageous can the p-FEM be with respect to the linear FEM. Though, this is only valid for smooth solutions. The p-refinement also converges algebraically for problems involving weakly singular solutions. Such results have motivated the development of the hp-automatic adaptivity to automatically define the optimal h- and p-refinement at a given location in a computational domain [52]. The FEM evaluation has shown that the numerical error can be decomposed into two contributions, the interpolation error and the dispersion error. The interpolation error depends on the Helmholtz number kh (where k is the wavenumber) with an order p. It can be controlled by the number of elements per wavelength $\lambda = 2\pi/(kh)$. This error tends to zero with mesh refinement or polynomial order increase. On the other hand, the dispersion error dominates in the low-resolution regime. It expresses the difference between the numerical wavenumber and the actual wavenumber. Approximations of the dispersion error have been found for well-resolved models ($kh \ll 1$) [140], showing that the dispersion error increases with a faster rate than the interpolation error. The accumulation of dispersion error over many wavelengths represents the so-called pollution effect. In practice the dispersion error dominates the overall error for poorly resolved models, while the interpolation error is relatively more significant for over-resolved problems or small domain size models where the phase error does not build-up. Dispersion analyses have provided supplementary information to understand the dispersion properties of numerical models. Studies have been made to evaluate the stability and accuracy of finite elements based on the convected Helmholtz equation and on the Galbrun equation [51, 141, 142]. Some stabilisation techniques have been developed to treat the dispersion problem [143]. In Chapter 6, further details are given on numerical accuracy and sources of error, as well as on stabilisation procedures.

2.7 Summary

The main issues in CAA have been discussed in this literature review. On that basis, a strategy has been elaborated in this work to develop a novel numerical model for acoustic propagation. In the framework of aeroengine exhaust noise, complex shear layers may be present and have a strong effect on the sound field. This impact is supported by the Linearised Euler Equations, which are, for this reason, chosen to be solved in this work.

Moreover, not only the acoustic waves are supported by the LEE, but also the vorticity and entropy waves. The latter develop from the aeroengine exit plane and are carried along the shear layer. To limit the issues arising from linear instabilities, the LEE are solved in the frequency domain. The high-order Finite Element Method is applied to compute the solution in order to reduce the computational cost with respect to the classical linear FEM. To further reduce the final global matrix size, an innovative coupling procedure between the Linearised Euler Equations and the Linearised Potential Equation is developed, considering the fact that, in most practical problems, the LEE is only required in a small portion of the computational domain. This technique will allow to optimise the numerical cost by solving the vector-based LEE in strong gradient regions and the scalar LPE in irrotational flow regions.

Chapter 3

Wave Propagation in Non-Uniform Media

In this chapter, the problem of wave propagation in non-uniform media is introduced. The first section focuses on the physical model description through the governing equations. The derivation of the Linearised Euler Equations leads to the definition of acoustic, vorticity and entropy waves, which are presented in the second section. This physical model is solved through the numerical method described in Chapter 4. In the third section analytic solutions for wave propagation in infinite straight ducts with uniform mean flow are provided. Modal solutions of similar problems with non-uniform mean flow are then considered in the fourth section: these solutions are valid for two-dimensional and axisymmetric problems. They constitute reference results for the numerical model verification in Chapter 5.

3.1 Physical Model

The physical model is described in this section. The conservation equations for mass, momentum and energy are first introduced. Additional equations such as thermodynamics equations, the constitutive equation and the equation of state, are also presented. They provide extra information in order to close the system of equations. The combination of these sets of equations, together with specific assumptions, thus provides the Linearised Euler Equations.

3.1.1 Conservation Equations

The conservation equations are specific expressions of the balance of volumetric quantities in a continuum medium. This balance indicates that the time variations of a volumetric quantity are equal to the sum of the relative production (or destruction) of this quantity and of its convective flux through the boundary surface. Three equations of that type, written for quantities such as mass density, momentum and energy, govern fluid motion in a continuum medium [144]. The following equations are local partial differential equations, in opposition to volumetric macroscopic equations, less suitable for solving fluid mechanics problems.

Mass Conservation

The mass conservation stipulates that a fixed fluid volume in space can accumulate matter or exchange it with the outside, but neither create nor destroy matter [145, 146]. The mass flux through the boundary surface exactly compensates the mass variation in the volume. Equation 3.1 shows the mass conservation without mass source term:

$$\frac{\partial \rho}{\partial t} + \boldsymbol{\nabla} \cdot (\rho \boldsymbol{u}) = 0, \tag{3.1}$$

where ρ is the fluid mass density, $\boldsymbol{u}$ is the flow velocity vector and t is the time variable. The momentum vector $\rho\boldsymbol{u}$ represents the mass flux.

Momentum Conservation

The momentum conservation indicates the effects of forces on a fluid: a force applied on a fluid corresponds to a fluid momentum increase, whereas a force exerted by a fluid corresponds to a fluid momentum decrease [147]. Put differently, the sum of the momentum flux through the boundary surface and of the stresses on this same boundary surface counterbalances the momentum variation in the fluid volume. This translates into the momentum conservation, as seen in Equation 3.2:

$$\frac{\partial (\rho \boldsymbol{u})}{\partial t} + \boldsymbol{\nabla} \cdot (\rho \boldsymbol{u} \otimes \boldsymbol{u}) - \boldsymbol{\nabla} \cdot \boldsymbol{\sigma} = \boldsymbol{f}, \tag{3.2}$$

where $\boldsymbol{\sigma}$ is the stress tensor and $\boldsymbol{f}$ is an external force density (for instance, the gravitational force). The convective momentum flux tensor product $\rho\boldsymbol{u} \otimes \boldsymbol{u} = \rho\boldsymbol{u}\boldsymbol{u}^{\mathrm{t}}$ of the momentum vector by the flow velocity vector is an outer product (the superscript $^{\mathrm{t}}$ denotes the vector transpose) [148]. The momentum conservation equation is vectorial and involves the flow

velocity vector components. This equation is also known as the Navier-Stokes equation [144].

Energy Conservation

The energy conservation is an application of the first law of thermodynamics for fluid particles. The considered total energy is the sum of the specific internal energy e and of the specific kinetic energy $\boldsymbol{u} \cdot \boldsymbol{u}/2 = u^2/2$ [149]. The law states that the sum of the power generated by external forces and of the heat power exchanged by conduction evens out the variation of total energy in the fluid volume. Equation 3.3 illustrates that principle:

$$\frac{\partial \rho \left(e + u^2/2\right)}{\partial t} + \boldsymbol{\nabla} \cdot \left(\rho \left(e + u^2/2\right) \boldsymbol{u}\right) - \boldsymbol{\nabla} \cdot (\boldsymbol{\sigma} \boldsymbol{u}) = \boldsymbol{f} \cdot \boldsymbol{u} - \boldsymbol{\nabla} \cdot \boldsymbol{Q}, \tag{3.3}$$

where $\boldsymbol{Q}$ is the outgoing heat flux, which refers to the energy transfer across the boundary caused by temperature gradients at the boundary [150].

3.1.2 Additional Equations

At this stage, the conservation equations include one scalar equation for the mass density, three scalar equations for the momentum (in three dimensions), and one scalar equation for the energy. But, these five equations involve six unknowns: the mass density, the three components of the flow velocity vector, the pressure (through the stress tensor) and the internal energy. Additional equations must complete the system as closure conditions for the problem [31]. In the following, four extra equations are introduced: two thermodynamics equations, the constitutive equation and the equation of state for an ideal gas.

First Thermodynamics Equation

During a reversible process, the first law of thermodynamics relates the total differentials of the specific internal energy, of the specific entropy and of the mass density, so that [150]:

$$\mathrm{d}e = T\mathrm{d}s - \frac{p}{\rho^2}\mathrm{d}\rho, \tag{3.4}$$

where T is the thermodynamic temperature, s is the specific entropy and p is the pressure.

Second Thermodynamics Equation

The fundamental thermodynamic equation associates the total differentials of the pressure,

of the mass density and of the entropy [151]:

$$\mathrm{d}p = c^2 \mathrm{d}\rho + \left(\frac{\partial p}{\partial s}\right)_\rho \mathrm{d}s, \tag{3.5}$$

where $c^2 = (\partial p/\partial \rho)_s$ is the isentropic sound speed.

Constitutive Equation

The stress tensor $\boldsymbol{\sigma}$ is the sum of a normal component (pressure), and of a tangential component (shear stress $\boldsymbol{\tau}$), proportionally to the element surface [144]:

$$\boldsymbol{\sigma} = \boldsymbol{\tau} - p\boldsymbol{I}, \tag{3.6}$$

where $\boldsymbol{I}$ is the unit tensor. For a Newtonian fluid the shear stress depends linearly on the rate-of-strain tensor, and the proportionality constant is the fluid shear viscosity μ.
The combination of these equations with the conservation laws (Equations 3.1, 3.2, 3.3) gives the entropy equation:

$$\rho T \frac{\mathrm{d}s}{\mathrm{d}t} - \boldsymbol{\tau} : \boldsymbol{\nabla u} = -\boldsymbol{\nabla} \cdot \boldsymbol{Q}, \tag{3.7}$$

where $\mathrm{d}/\mathrm{d}t = \partial/\partial t + \boldsymbol{u} \cdot \boldsymbol{\nabla}$ is the material derivative, which represents the rate of change of the quantity along with the moving fluid element. The double dot product ':' represents the tensor inner product. Appendix A gives details on the mathematical procedure to obtain the entropy equation.

Equation of State

Assuming an isentropic process (inviscid and adiabatic), the equation of state defines the properties of a perfect gas with constant specific heats. The relation between pressure and density is [148]:

$$p = \zeta \rho^\gamma, \tag{3.8}$$

where ζ is a constant and γ is the specific heats ratio at constant pressure and volume respectively. Under the isentropy assumption, the entropy equation 3.7 reduces to: $\mathrm{d}s/\mathrm{d}t = 0$. This perfect fluid model is suitable for high Reynolds numbers but does not describe dissipation phenomena in the flow. From Equation 3.5, the pressure material derivative

for an isentropic process reduces to:

$$\frac{\mathrm{d}p}{\mathrm{d}t} = c^2 \frac{\mathrm{d}\rho}{\mathrm{d}t}. \tag{3.9}$$

The combination of Equation 3.8 with Equation 3.9 then gives the expression of the sound speed:

$$c^2 = \frac{\gamma p}{\rho}. \tag{3.10}$$

3.1.3 Linearised Euler Equations

The Linearised Euler Equations result from a three-step procedure. First, the flow decomposition expresses each variable as the sum of mean flow components and of perturbations. Second, the assumptions on the perturbations define the nature of the mathematical model as explained in Section 2.3. Finally, the linearisation stage provides the governing equations for the perturbations. The phases are described in the following paragraphs.

Flow Decomposition

The first step consists in expressing the flow into the sum of time-invariant mean flow components and of small perturbations [31]. This decomposition translates into the following equations:

$$\begin{cases} \rho(\boldsymbol{x},t) &= \rho_0(\boldsymbol{x}) &+ \rho'(\boldsymbol{x},t) \\ \boldsymbol{u}(\boldsymbol{x},t) &= \boldsymbol{u}_0(\boldsymbol{x}) &+ \boldsymbol{u}'(\boldsymbol{x},t) \\ p(\boldsymbol{x},t) &= p_0(\boldsymbol{x}) &+ p'(\boldsymbol{x},t) \end{cases}, \tag{3.11}$$

where $\boldsymbol{x}$ is the position in space, the subscript $_0$ denotes the mean flow components and the superscript $'$ refers to the perturbations. The mean flow has arbitrary amplitude, is viscous and transfers heat. It satisfies the general steady conservation equations and does not account for any potential feedback effects from the perturbations. The perturbations are unsteady and have small amplitude ($|\rho'| \ll |\rho_0|$, $\|\boldsymbol{u}'\| \ll \|\boldsymbol{u}_0\|$, $|p'| \ll |p_0|$).

Assumptions on Perturbations

As discussed in Section 2.3, each aeroacoustic propagation model corresponds to some hypotheses. Regarding the Linearised Euler Equations, the assumptions on the unsteady perturbations are the following:

- The fluid is inviscid: there is no viscous dissipation $\boldsymbol{\tau} : \boldsymbol{\nabla u}$ since the viscosity is zero.

- The process is adiabatic: there is no heat conduction $\boldsymbol{\nabla} \cdot \boldsymbol{Q}$.
- There is no external force: $\boldsymbol{f} = \mathbf{0}$.

These assumptions leave us with three simplified equations, namely the Euler equation (i.e. the Navier-Stokes equation, simplified with the aforementioned hypotheses) combined with the mass conservation and pressure equations. By extension, the Euler equations refer to the whole system 3.12 where the third equation, combination of the mass conservation 3.1 with Equation 3.9, expresses the pressure instead of the energy:

$$\begin{cases} \dfrac{\partial \rho}{\partial t} + \boldsymbol{\nabla} \cdot (\rho \boldsymbol{u}) & = & 0 \\ \dfrac{\partial (\rho \boldsymbol{u})}{\partial t} + \boldsymbol{\nabla} \cdot (\rho \boldsymbol{u} \otimes \boldsymbol{u}) + \boldsymbol{\nabla} p & = & \mathbf{0} \\ \dfrac{\partial p}{\partial t} + \boldsymbol{u} \cdot \boldsymbol{\nabla} p + \rho c^2 \boldsymbol{\nabla} \cdot \boldsymbol{u} & = & 0 \end{cases} . \tag{3.12}$$

Linearisation

Considering the flow decomposition and the assumptions, the Euler equations 3.12 simplify. Three types of terms appear in the equations: the leading-order terms which only contain mean flow properties (such as $\rho_0 \boldsymbol{u}_0$), the linear terms which are the products of perturbations with mean flow components (such as $\rho_0 \boldsymbol{u}' + \rho' \boldsymbol{u}_0$), and the non-linear terms which involve products of perturbations components (such as $\rho' \boldsymbol{u}'$). Retaining only the leading order terms provides the steady Euler equations which govern the mean flow properties. These equations are non-linear and do not account for any feedback from the perturbations on the mean flow. Then neglecting the non-linear terms, the unsteady Linearised Euler Equations are obtained, where the mean flow has an influence but is assumed to be known:

$$\begin{cases} \dfrac{\partial \rho'}{\partial t} + \boldsymbol{\nabla} \cdot (\rho_0 \boldsymbol{u}' + \rho' \boldsymbol{u}_0) & = & 0 \\ \rho_0 \dfrac{\partial \boldsymbol{u}'}{\partial t} + \dfrac{\partial \rho'}{\partial t} \boldsymbol{u}_0 + \boldsymbol{\nabla} \cdot (\rho_0 \boldsymbol{u}_0 \otimes \boldsymbol{u}' + \rho_0 \boldsymbol{u}' \otimes \boldsymbol{u}_0 + \rho' \boldsymbol{u}_0 \otimes \boldsymbol{u}_0) + \boldsymbol{\nabla} p' & = & \mathbf{0} \\ \dfrac{\partial p'}{\partial t} + \boldsymbol{u}_0 \cdot \boldsymbol{\nabla} p' + \boldsymbol{u}' \cdot \boldsymbol{\nabla} p_0 + \rho_0 c_0^2 \boldsymbol{\nabla} \cdot \boldsymbol{u}' + \dfrac{\rho_0 c_0^2}{p_0} p' \boldsymbol{\nabla} \cdot \boldsymbol{u}_0 & = & 0 \end{cases} . \tag{3.13}$$

The assumptions indicate that, for this physical model, the perturbations are inviscid, isentropic and linear. Therefore, the Linearised Euler Equations do not account for viscosity, heat transfer, non-linearities and possible effects of the perturbations on the mean flow. In particular, the omission of the non-linear terms and of the viscosity implies that the physical Kelvin-Helmholtz instabilities which are encountered in the presence of thin flow

shear layers are not saturated [30, 45]. This is a clear limitation of the Linearised Euler Equations model, although non-linear effects are negligible for sound propagation.

Conservative Form of the Linearised Euler Equations

It is useful to introduce the conservative form of the Linearised Euler Equations. Written in matrix form for the Cartesian coordinates, the two-dimensional Linearised Euler Equations can be written:

$$\frac{\partial \boldsymbol{q}}{\partial t} + \frac{\partial \boldsymbol{A}_x \boldsymbol{q}}{\partial x} + \frac{\partial \boldsymbol{A}_y \boldsymbol{q}}{\partial y} = \boldsymbol{0}, \tag{3.14}$$

where the flux matrices $\boldsymbol{A}_x$ and $\boldsymbol{A}_y$ contain the mean flow properties. In two dimensions, the perturbations variable vector $\boldsymbol{q}$ reads:

$$\boldsymbol{q} = \left\{ \begin{array}{c} \rho' \\ (\rho u_x)' \\ (\rho u_y)' \\ p'_{\mathrm{c}} \end{array} \right\}, \tag{3.15}$$

where the momentum perturbations are used instead of the velocity. The momentum vector perturbations read: $(\rho \boldsymbol{u})' = \rho_0 \boldsymbol{u'} + \rho' \boldsymbol{u}_0$.

In addition, p'_{c} is the perturbation of the modified pressure defined by Goldstein [152]. This pressure reads:

$$p_{\mathrm{c}} = (p/p_\infty)^{1/\gamma}, \tag{3.16}$$

where p_∞ is a reference pressure. The corresponding mean flow component p_{c_0} and perturbations p'_{c} relate to the pressure by:

$$p_{\mathrm{c}_0} = (p_0/p_\infty)^{1/\gamma} \text{ and } p'_{\mathrm{c}} = p_{\mathrm{c}_0}/(\rho_0 c_0^2) p'. \tag{3.17}$$

The conservative form of the Linearised Euler Equations given in Equation 3.14 for the density, the momentum and the modified pressure is attractive since it does not directly depend on any matrix of the mean flow properties derivatives. Such matrix would be present in a formulation with the classical variables (density, velocity, pressure). Assuming time-harmonic solutions, a Fourier decomposition of any field variable χ' of the acoustic perturbations gives:

$$\chi'(\boldsymbol{x}, t) = \chi'(\boldsymbol{x}, \omega) \mathrm{e}^{\mathrm{j}\omega t}, \tag{3.18}$$

where the angular frequency ω relates to the frequency f by $\omega = 2\pi f$.

By inserting this decomposition into Equation 3.14 and factoring out the term $\mathrm{e}^{\mathrm{j}\omega t}$, the two-dimensional Linearised Euler Equations are obtained in the frequency domain without external source:

$$\mathrm{j}\omega \boldsymbol{q} + \frac{\partial \boldsymbol{A}_x \boldsymbol{q}}{\partial x} + \frac{\partial \boldsymbol{A}_y \boldsymbol{q}}{\partial y} = \boldsymbol{0}, \tag{3.19}$$

where the left-hand side differential operator is noted $\mathfrak{L}(\boldsymbol{q})$. From this point onwards, the superscript notation is dropped, unless otherwise stated: unscripted variables represent small amplitude perturbations of the mean flow.

The flux matrices read:

$$\boldsymbol{A}_x = \begin{bmatrix} 0 & 1 & 0 & 0 \\ -u_{0_x}^2 & 2u_{0_x} & 0 & \dfrac{\rho_0 c_0^2}{p_{\mathrm{c}_0}} \\ -u_{0_x}u_{0_y} & u_{0_y} & u_{0_x} & 0 \\ -\dfrac{p_{\mathrm{c}_0}}{\rho_0}u_{0_x} & \dfrac{p_{\mathrm{c}_0}}{\rho_0} & 0 & u_{0_x} \end{bmatrix} \text{ and } \boldsymbol{A}_y = \begin{bmatrix} 0 & 0 & 1 & 0 \\ -u_{0_x}u_{0_y} & u_{0_y} & u_{0_x} & 0 \\ -u_{0_y}^2 & 0 & 2u_{0_y} & \dfrac{\rho_0 c_0^2}{p_{\mathrm{c}_0}} \\ -\dfrac{p_{\mathrm{c}_0}}{\rho_0}u_{0_y} & 0 & \dfrac{p_{\mathrm{c}_0}}{\rho_0} & u_{0_y} \end{bmatrix}. \tag{3.20}$$

For the sake of completeness, Appendix B contains additional forms of the Linearised Euler Equations, in three dimensions and in cylindrical coordinates with the corresponding expressions of the flux matrices.

3.2 Acoustic, Vorticity and Entropy Waves

Within this mathematical model, the time-harmonic perturbations described by the Linearised Euler Equations do not only contain acoustic waves but also include vorticity and entropy waves. In this section, these different types of waves are described through a two-dimensional test case study. Acoustic plane wave propagation is considered in free field, in the presence of a uniform mean flow. First, the Linearised Euler Equations are simplified with the aforementioned assumptions. Then, the test case is described. Finally, an analytic solution provides details on the acoustic, vorticity and entropy waves.

Equations

Written for the classical variables ρ, $\boldsymbol{u}$ and p, in a uniform mean flow, the Linearised Euler

Equations given in Equation 3.19 simplify to:

$$\left\{\begin{array}{rcrcl} \dfrac{\mathrm{d}_0\rho}{\mathrm{d}t} & + & \rho_0\boldsymbol{\nabla}\cdot\boldsymbol{u} & = & 0 \\ \dfrac{\mathrm{d}_0\boldsymbol{u}}{\mathrm{d}t} & + & \dfrac{1}{\rho_0}\boldsymbol{\nabla}p & = & \mathbf{0} \\ \dfrac{\mathrm{d}_0 p}{\mathrm{d}t} & + & \rho_0 c_0^2\boldsymbol{\nabla}\cdot\boldsymbol{u} & = & 0 \end{array}\right. , \tag{3.21}$$

where $\mathrm{d}_0/\mathrm{d}t = \mathrm{j}\omega + \boldsymbol{u}_0\cdot\boldsymbol{\nabla}$ denotes the mean flow material derivative. By taking the divergence of the velocity equation and the mean flow material derivative of the pressure equation, the velocity field cancels out and the classical wave equation is obtained for the pressure:

$$\frac{\mathrm{d}_0}{\mathrm{d}t}\left(\frac{\mathrm{d}_0 p}{\mathrm{d}t}\right) - c_0^2\boldsymbol{\Delta}p = 0. \tag{3.22}$$

The velocity is then obtained from the second equation:

$$\frac{\mathrm{d}_0\boldsymbol{u}}{\mathrm{d}t} = -\frac{1}{\rho_0}\boldsymbol{\nabla}p. \tag{3.23}$$

Multiplying the first equation by c_0^2 and subtracting the third equation, the density can be obtained by solving the following equation:

$$\frac{\mathrm{d}_0\left(p - c_0^2\rho\right)}{\mathrm{d}t} = 0. \tag{3.24}$$

Test Case

At large distance from a sound source such as aeroengines, plane waves can be seen as approximations for spherical waves. Waves propagating at low frequencies may also behave like plane waves [31]. The field of plane waves only depends on the propagation direction and on its spatial coordinate. Moreover, plane waves form a basis of the total field. A plane wave decomposition can be used to describe any admissible field of perturbations. Let us consider a plane wave of direction α propagating in free field with a uniform mean flow velocity of direction α_0. In two dimensions, the wavenumber $\boldsymbol{k}$, which characterises the wave propagation direction, and the mean flow velocity vector $\boldsymbol{u}_0$ read:

$$\boldsymbol{k} = k\left\{\begin{array}{c}\cos\alpha\\ \sin\alpha\end{array}\right\} \text{ and } \boldsymbol{u}_0 = u_0\left\{\begin{array}{c}\cos\alpha_0\\ \sin\alpha_0\end{array}\right\}, \tag{3.25}$$

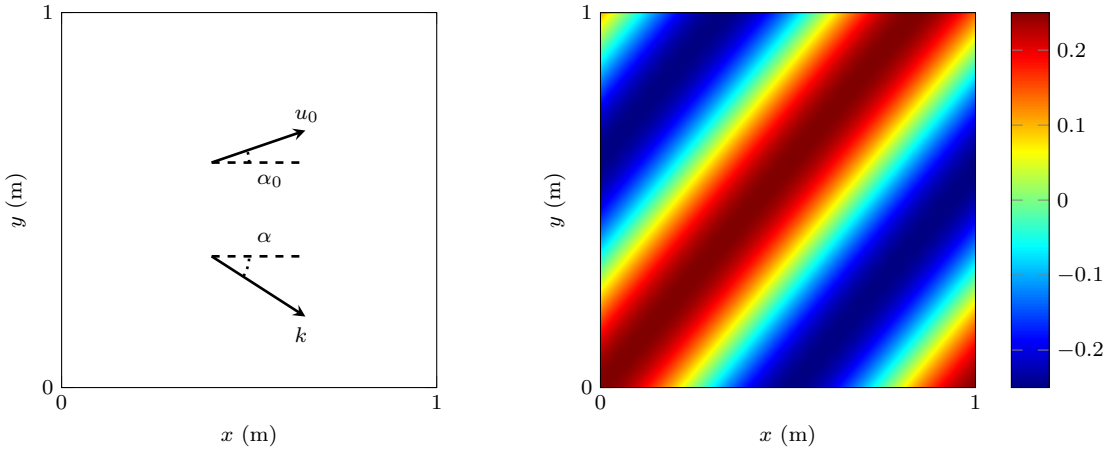

(a) Sketch. (b) $\Re(p_c)$ (-).

Figure 3.1: Two-dimensional free field sound propagation problem with $k_0 = 10\,\mathrm{m}^{-1}$, $\alpha = -40°$, $\alpha_0 = 20°$, $\|\boldsymbol{u}_0\| = 0.5c_0$.

where $k = \|\boldsymbol{k}\|$ and $u_0 = \|\boldsymbol{u}_0\|$ are the norms of the wavenumber and mean flow velocity vectors, respectively. The standard wavenumber is defined by $k_0 = \omega/c_0$. Figure 3.1 shows the two-dimensional configuration of the test case on the left-hand side. On the right-hand side, an example of acoustic plane wave propagation in free field represents the real part of the non-dimensional acoustic pressure field.

Analytic Solutions

Exact solutions of acoustic plane wave type are sought, i.e. $p_\mathrm{a} = A_\mathrm{a}^p \mathrm{e}^{-\mathrm{j}\boldsymbol{k}_\mathrm{a}\cdot\boldsymbol{x}}$ where A_a^p is the constant amplitude of the pressure field. By introducing this expression into Equation 3.22, the dispersion relation for the acoustic wavenumber k_a is obtained:

$$\left(c_0^2 - u_0^2\cos^2(\alpha-\alpha_0)\right)k_\mathrm{a}^2 + 2\omega u_0\cos(\alpha-\alpha_0)k_\mathrm{a} - \omega^2 = 0. \tag{3.26}$$

Solving the dispersion relation gives two possible values of the acoustic wavenumber:

$$k_\mathrm{a}^{\pm} = \frac{\omega}{\pm c_0 + u_0\cos(\alpha-\alpha_0)}. \tag{3.27}$$

The only admissible value is $k_\mathrm{a} = k_\mathrm{a}^+ > 0$. By introducing the pressure expression into Equation 3.23 and 3.24, the velocity and the density are obtained. Those are first-order linear differential equations whose particular solutions provide the acoustic components. The homogeneous equations give the vorticity/entropy solutions. Table 3.1 summarises these contributions. The amplitudes $A_\mathrm{a}^\bullet$, $A_\mathrm{v}^\bullet$ and $A_\mathrm{e}^\bullet$ are constant. $\boldsymbol{k}_\mathrm{v}$ and $\boldsymbol{k}_\mathrm{e}$ are the vorticity/entropy wavenumbers, respectively. The acoustic amplitudes $A_\mathrm{a}^{u_x}$, $A_\mathrm{a}^{u_y}$ and A_a^ρ

	Acoustic	Vorticity	Entropy
p	$A_{\mathrm{a}}^{p}\mathrm{e}^{-\mathrm{j}\boldsymbol{k}_{\mathrm{a}}\cdot\boldsymbol{x}}$	0	0
u_x	$A_{\mathrm{a}}^{u_x}\mathrm{e}^{-\mathrm{j}\boldsymbol{k}_{\mathrm{a}}\cdot\boldsymbol{x}}$	$A_{\mathrm{v}}^{u_x}\mathrm{e}^{-\mathrm{j}\boldsymbol{k}_{\mathrm{v}}\cdot\boldsymbol{x}}$	0
u_y	$A_{\mathrm{a}}^{u_y}\mathrm{e}^{-\mathrm{j}\boldsymbol{k}_{\mathrm{a}}\cdot\boldsymbol{x}}$	$A_{\mathrm{v}}^{u_x}\mathrm{e}^{-\mathrm{j}\boldsymbol{k}_{\mathrm{v}}\cdot\boldsymbol{x}}$	0
ρ	$A_{\mathrm{a}}^{\rho}\mathrm{e}^{-\mathrm{j}\boldsymbol{k}_{\mathrm{a}}\cdot\boldsymbol{x}}$	0	$A_{\mathrm{e}}^{\rho}\mathrm{e}^{-\mathrm{j}\boldsymbol{k}_{\mathrm{e}}\cdot\boldsymbol{x}}$

TABLE 3.1: Acoustic, vorticity and entropy contributions in the two-dimensional analytic expressions of p, u_x, u_y and ρ, for plane wave propagation in free field.

relate to A_{a}^{p} like:

$$A_{\mathrm{a}}^{u_x} = \frac{A_{\mathrm{a}}^{p}}{\rho_0}\frac{k_{\mathrm{a}}\cos(\alpha_{\mathrm{a}})}{\omega - \boldsymbol{k}_{\mathrm{a}}\cdot\boldsymbol{u}_0},\ A_{\mathrm{a}}^{u_y} = \frac{A_{\mathrm{a}}^{p}}{\rho_0}\frac{k_{\mathrm{a}}\sin(\alpha_{\mathrm{a}})}{\omega - \boldsymbol{k}_{\mathrm{a}}\cdot\boldsymbol{u}_0} \text{ and } A_{\mathrm{a}}^{\rho} = \frac{A_{\mathrm{a}}^{p}}{c_0^2}, \tag{3.28}$$

where α_{a} is the acoustic wave angle. All variables contribute to the acoustic field with the wavenumber $\boldsymbol{k}_{\mathrm{a}}$. The rotational of the acoustic velocity vector $\boldsymbol{u}_{\mathrm{a}} = \{u_{x_{\mathrm{a}}}, u_{y_{\mathrm{a}}}\}^{\mathrm{t}}$ is zero: $\boldsymbol{\nabla}\times\boldsymbol{u}_{\mathrm{a}} = \boldsymbol{0}$. Therefore, the acoustic field is purely divergent. Table 3.1 shows that only the velocity field supports vorticity waves. The vorticity wavenumber norm reads:

$$k_{\mathrm{v}} = \frac{\omega}{u_0\cos(\alpha_{\mathrm{v}} - \alpha_0)}, \tag{3.29}$$

where α_{v} is the vorticity wave angle. Seeing that k_{v}, u_0 and ω are positive, $\cos(\alpha_{\mathrm{v}} - \alpha_0)$ is also positive and $|\alpha_{\mathrm{v}} - \alpha_0| < \pi/2$: this means that vorticity waves propagate with the mean flow. The divergence of the vorticity components velocity vector $\boldsymbol{u}_{\mathrm{v}} = \{u_{x_{\mathrm{v}}}, u_{y_{\mathrm{v}}}\}^{\mathrm{t}}$ is zero: $\boldsymbol{\nabla}\cdot\boldsymbol{u}_{\mathrm{v}} = 0$. Thus, unlike the acoustic field, the vorticity field is purely rotational. A relation between the vorticity velocity components is found:

$$\cos(\alpha_{\mathrm{v}})A_{\mathrm{v}}^{u_x} + \sin(\alpha_{\mathrm{v}})A_{\mathrm{v}}^{u_y} = 0. \tag{3.30}$$

Finally, only the density field contains entropy waves. The entropy wavenumber norm k_{e} is identical to the vorticity wavenumber k_{v} (see Equation 3.29). Like vorticity waves, entropy waves propagate with the mean flow. The density expression holds for isentropic disturbances. In the case of homentropic perturbations, the entropy field is zero ($A_{\mathrm{e}}^{\rho} = 0$) and it is found that $p = c_0^2\rho$.

This example of wave propagation in free field, in the presence of uniform mean flow, shows the particularity of the Linearised Euler Equations. They carry acoustic waves, as well as vorticity and entropy waves. These waves propagate at different speeds and the vorticity/entropy waves only exist in a mean flow in motion.

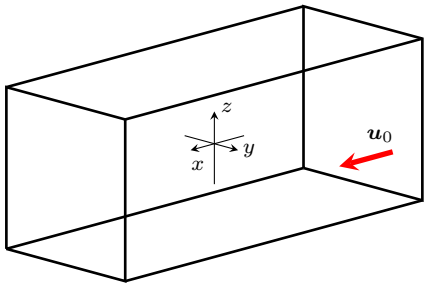

Figure 3.2: Rectangular cross-section straight duct with uniform axial mean flow.

3.3 Analytic Solutions for Uniform Mean Flow Velocity

Analytic solutions, which will serve for numerical results verification, especially in Chapter 5, are now presented. This work focuses on noise propagation in ducts, with some application in turbomachinery and aeroengine noise. The sound generated within aeroengines propagates through the inlet and exhaust ducts of turbofans, and radiates to the far field in the surrounding mean flow. Two typical problems arise: plane wave propagation in free field and ducted wave propagation. Analytic solutions in free field have already been obtained in Section 3.2.

In this section, analytic solutions for wave propagation in straight infinite ducts with hard walls are provided. The mean flow properties are uniform and the constant subsonic mean flow velocity vector follows the duct axis $\boldsymbol{e}_x$: $\boldsymbol{u}_0 = u_{0_x}\boldsymbol{e}_x$. The choice of the coordinates system should align with the duct cross-section: Cartesian coordinates (x, y, z) for rectangular ducts and cylindrical coordinates (r, θ, x) for annular/circular ducts. Equations 3.21 and 3.22 hold for this test case, and further simplify with the assumption that $\boldsymbol{u}_0 = u_{0_x}\boldsymbol{e}_x$. Depending on the coordinates system, they develop in different ways.

Rectangular Cross-Section Duct

Let us consider an infinite straight duct with rectangular cross-section, as depicted in Figure 3.2. Waves propagate inside the duct in the x-direction, and hard-wall boundary conditions are applied on the lateral faces at $y = \pm L_y/2$ and $z = \pm L_z/2$ such that:

$$\frac{\partial p}{\partial y} = 0 \ \forall y \in \left\{-\frac{L_y}{2}, \frac{L_y}{2}\right\} \text{ and } \frac{\partial p}{\partial z} = 0 \ \forall z \in \left\{-\frac{L_z}{2}, \frac{L_z}{2}\right\}, \tag{3.31}$$

where L_y and L_z are the dimensions of the duct in the y- and z-direction, respectively.

In Cartesian coordinates, Equation 3.22 reduces to:

$$\left(c_0^2 - u_{0_x}^2\right)\frac{\partial^2 p}{\partial x^2} + c_0^2\frac{\partial^2 p}{\partial y^2} + c_0^2\frac{\partial^2 p}{\partial z^2} - 2\mathrm{j}\omega u_{0_x}\frac{\partial p}{\partial x} + \omega^2 p = 0. \tag{3.32}$$

By means of separation of variable, solutions of modal type which are linear combinations of left- and right-propagating waves are found:

$$p^{\pm}_{m,n}(x,y,z) = A^{\pm}_{p_{m,n}}\cos(k_{y_m}y)\cos(k_{z_n}z)\mathrm{e}^{-\mathrm{j}k^{\pm}_{x_{m,n}}x}, \tag{3.33}$$

where $A^{\pm}_{p_{m,n}}$ and $(k^{\pm}_{x_{m,n}}, k_{y_m}, k_{z_n})$ are respectively the amplitudes and the wavenumbers of the modes. The mode numbers $(m,n) \in \mathbb{N}^2$ characterise the propagating wave, whose general solution is:

$$p(x,y,z) = \sum_{m=0}^{\infty}\sum_{n=0}^{\infty}\left(p^{-}_{m,n}(x,y,z) + p^{+}_{m,n}(x,y,z)\right). \tag{3.34}$$

The transverse wavenumbers are $k_{y_m} = m\pi/L_y$ and $k_{z_n} = n\pi/L_z$. The longitudinal wavenumber reads:

$$k^{\pm}_{x_{m,n}} = \frac{-k_0 M_x \pm \sqrt{k_0^2 - (1-M_x^2)\left({k_{y_{m,n}}}^2 + {k_{z_{m,n}}}^2\right)}}{1-M_x^2}, \tag{3.35}$$

where $M_x = u_{0_x}/c_0$ is the Mach number. From the simplified Linearised Euler Equations 3.21 and the modal pressure found in Equation 3.33, the expressions of the velocity vector and of the density are obtained for each mode couple (m,n) (see Appendix C). These solutions contain acoustic and vorticity/entropy contributions, as seen in Section 3.2. The analytic solution presented here is three-dimensional: the two-dimensional solution follows on from setting the z-coordinate to 0.

Circular and Annular Cross-Section Ducts

For cylindrical ducts, the solutions are different since they are expressed in cylindrical coordinates. Figure 3.3 shows the geometries for circular and annular cross-sections. In this system of coordinates, the convected Helmholtz equation 3.22 reads:

$$c_0^2\frac{\partial^2 p}{\partial r^2} + \frac{c_0^2}{r^2}\frac{\partial^2 p}{\partial \theta^2} + \left(c_0^2 - u_{0_x}^2\right)\frac{\partial^2 p}{\partial x^2} + \frac{c_0^2}{r}\frac{\partial p}{\partial r} - 2\mathrm{j}\omega u_{0_x}\frac{\partial p}{\partial x} + \omega^2 p = 0. \tag{3.36}$$

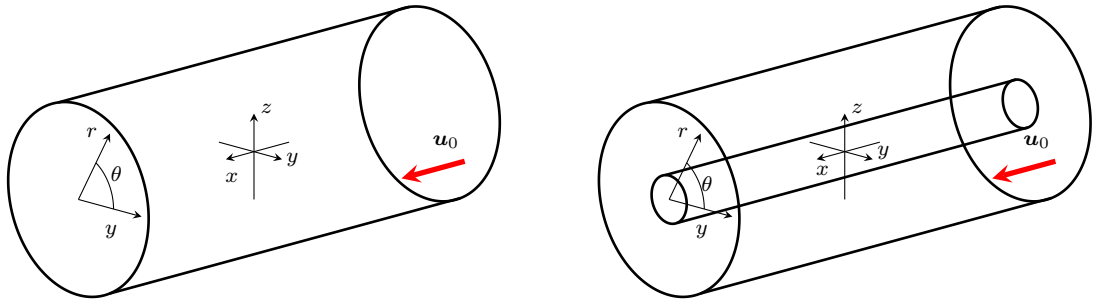

(a) Circular cross-section. (b) Annular cross-section.

Figure 3.3: Cylindrical straight ducts with uniform axial mean flow.

Hard wall boundary conditions are set at the outer wall of the duct, and at the inner wall for annular ducts:

$$\frac{\partial p}{\partial r} = 0, \forall r \in \{r_\mathrm{o}, r_\mathrm{i}\}, \tag{3.37}$$

where r_o and r_i are the outer and inner radii of the ducts. Separation of variable provides three equations, one for each coordinate. The left- and right-propagating modal solutions read:

$$p^{\pm}_{m,n}(r,\theta,x) = A^{\pm}_{p_{m,n}} U_{m,n}(r) \mathrm{e}^{-\mathrm{j}k^{\pm}_x x} \mathrm{e}^{-\mathrm{j}m\theta}, \tag{3.38}$$

where $m \in \mathbb{Z}$ is the azimuthal mode number, $n \in \mathbb{N}^*$ is the radial mode number, $k^{\pm}_x$ is the axial wavenumber and $U_{m,n}(r)$ is the mode amplitude function in the radial direction. Since they do not depend on θ, modes with $m = 0$ are called axisymmetric, whereas those with $m \neq 0$ are spinning modes. The expression of the axial wavenumber is:

$$k^{\pm}_x = \frac{-k_0 M_x \pm \sqrt{k_0^2 - (1 - M_x^2)\, k^2_{r_{m,n}}}}{1 - M_x^2}, \tag{3.39}$$

where $k_{r_{m,n}} = \alpha_{m,n}/c_0$ is the radial wavenumber. In practice, $\alpha_{m,n}$ is the n^{th} non-trivial zero of the characteristic equation of the duct to satisfy the hard-wall boundary condition given in Equation 3.37. Admissible values of $\alpha_{m,n}$ can be found numerically. Note that this expression of $k^{\pm}_x$ is analogous to the one found in Equation 3.35 for a rectangular cross-section duct, with $k^2_{r_{m,n}} \equiv k^2_{y_{m,n}} + k^2_{z_{m,n}}$. The amplitude in the radial direction is solution of the Bessel equation [153, 154]:

$$\frac{\mathrm{d}^2 U_{m,n}}{\mathrm{d}\hat{r}^2} + \frac{1}{\hat{r}} \frac{\mathrm{d}U_{m,n}}{\mathrm{d}\hat{r}} + \left(1 - \frac{m^2}{\hat{r}^2}\right) U_{m,n} = 0, \tag{3.40}$$

where $\hat{r} = k_{r_{m,n}} r$ is a modified coordinate. It yields:

$$U_{m,n}(r) = \begin{cases} J_m(k_{r_{m,n}} r) & \text{for circular ducts} \\ Y'_m(k_{r_{m,n}} r_\mathrm{i}) J_m(k_{r_{m,n}} r) - J'_m(k_{r_{m,n}} r_\mathrm{i}) Y_m(k_{r_{m,n}} r) & \text{for annular ducts} \end{cases}, \tag{3.41}$$

where J_m and Y_m are the m^{th}-order Bessel functions of the 1^{st} and 2^{nd} kind respectively, and the prime denotes the derivative with respect to the argument. The characteristic equations satisfied by $\alpha_{m,n}$ are therefore:

$$\begin{cases} J'_m(k_{r_{m,n}} r_\mathrm{o}) = 0 & \text{for circular ducts} \\ Y'_m(k_{r_{m,n}} r_\mathrm{i}) J'_m(k_{r_{m,n}} r_\mathrm{o}) - J'_m(k_{r_{m,n}} r_\mathrm{i}) Y'_m(k_{r_{m,n}} r_\mathrm{o}) = 0 & \text{for annular ducts} \end{cases}. \tag{3.42}$$

Finally, the general solution is:

$$p(r, \theta, x) = \sum_{m=0}^{\infty} \sum_{n=0}^{\infty} \left(p^-_{m,n}(r, \theta, x) + p^+_{m,n}(r, \theta, x) \right). \tag{3.43}$$

The solutions for the density and the velocity vector follow on from the simplified Linearised Euler Equations and from the expression of the pressure. Appendix C contains details on these solutions, which support acoustic, vorticity and entropy contributions.

Duct Modes

The duct modes longitudinal wavenumbers contain a fundamental property which characterises wave propagation: duct modes may be either propagating or evanescent. A perturbation of angular frequency ω and radial wavenumber $k_{r_{m,n}}$ propagates if $k_{r_{m,n}} \in \mathbb{R}$, i.e. if:

$$k_0 \geq \sqrt{1 - M_x^2} k_{r_{m,n}}, \tag{3.44}$$

which simply expresses that the term in the square root in the expression of the axial wavenumber is positive (see Equations 3.35 and 3.39). Outside this regime, the longitudinal wavenumber is complex with a non-zero imaginary part which is responsible for an exponentially decaying behaviour: such modes are evanescent. The cut-off frequency f_c defines the limit between the two regimes:

$$f_\mathrm{c} = \frac{c_0}{2\pi} \sqrt{1 - M_x^2} k_{r_{m,n}}. \tag{3.45}$$

The dependency of the cut-off frequency in the mean flow velocity shows that high-velocity mean flows create more propagating modes, since f_c is reduced. Propagating (or cut-on)

modes carry acoustic energy all along the duct, whereas evanescent (or cut-off) modes do not contribute to the sound field far from the source.

The phase and group velocities also give some insight on duct wave propagation. The phase velocity $k_0/k_x^{\pm}$ defines the rate at which the wave phase propagates in space, whereas the group velocity $\partial k_0/\partial k_x^{\pm}$ refers to the velocity with which the wave packets (characterised by the modulation or envelope) travel through space [155]. They read:

$$\frac{k_0}{k_x^{\pm}} = \frac{\left(1-M_x^2\right)k_0}{-M_x k_0 \pm \sqrt{k_0^2-(1-M_x^2)\,k_{r_{m,n}}^2}} \text{ and } \frac{\partial k_0}{\partial k_x^{\pm}} = \frac{\pm\left(1-M_x^2\right)\sqrt{k_0^2-(1-M_x^2)k_{r_{m,n}}^2}}{k_0 \mp M_x\sqrt{k_0^2-(1-M_x^2)k_{r_{m,n}}^2}}. \tag{3.46}$$

Since the mean flow is subsonic, the group velocity is negative for left-propagating modes and positive for right-propagating modes. There exist right-propagating modes with positive group velocity and negative phase velocity [50]. Such modes are referred to as inverse upstream modes and verify the following condition:

$$\sqrt{1-M_x^2}k_{r_{m,n}} < k_0 < k_{r_{m,n}}. \tag{3.47}$$

3.4 Modal Solutions for Non-Uniform Mean Flow Velocity

In this section, a modal analysis of the Linearised Euler Equations is performed in order to provide a reference solution for the numerical model verification in the presence of non-uniform mean flow. Infinite straight ducts are considered in the x-direction. The mean flow velocity is axial and may vary along the direction transverse to the propagation direction (i.e. the y-direction in Cartesian coordinates and the r-direction in cylindrical coordinates): $\boldsymbol{u}_0 = u_{0_x} f_y(y)\boldsymbol{e}_x$ or $\boldsymbol{u}_0 = u_{0_x} f_r(r)\boldsymbol{e}_x$, with $f_\bullet$ functions describing the velocity profile in the transverse direction. Assuming time-harmonic waves in the axial x-direction, the solution vector behaves like: $\boldsymbol{q} \equiv \mathrm{e}^{-\mathrm{j}k_x x}$. This condition implies that any derivative of the solution vector with respect to x is such that: $\partial/\partial x \equiv -\mathrm{j}k_x$. The system of equations is discretised in the transverse direction by means of a finite difference method [156]. The discrete form of the equations translates into a generalised eigenvalue problem of the form [157]:

$$k_x \boldsymbol{A}\boldsymbol{q}_\mathrm{d} = \boldsymbol{B}\boldsymbol{q}_\mathrm{d}, \tag{3.48}$$

where $\boldsymbol{A}$ and $\boldsymbol{B}$ are matrices containing the mean flow properties, and $\boldsymbol{q}_\mathrm{d}$ is the discretised vector of variables. Imposing proper boundary conditions closes the problem.

The solution of the generalised eigenvalue problem provides eigenvectors (or modes) and their corresponding eigenvalues k_x. A total of $4n$ modes are found in two dimensions, where n is the number of discretisation nodes: n acoustic right-propagating modes, n acoustic left-propagating modes, n vorticity modes and n entropy modes. The total solution is a linear combination of these modes. In the next two paragraphs, modal solutions are derived for two-dimensional and axisymmetric ducts.

3.4.1 Wave Propagation in Two-Dimensional Duct

Let us consider a two-dimensional infinite straight duct in the x-direction, of height H in the y-direction. For a time-harmonic solution and a mean flow velocity varying in the y-direction, Equation 3.19 simplifies to:

$$\mathrm{j}\omega \boldsymbol{q}_\mathrm{d} - \mathrm{j}k_x \boldsymbol{A}_x \boldsymbol{q}_\mathrm{d} + \frac{\partial \boldsymbol{A}_y}{\partial y}\boldsymbol{q}_\mathrm{d} + \boldsymbol{A}_y \frac{\partial \boldsymbol{q}_\mathrm{d}}{\partial y} = \boldsymbol{0}, \tag{3.49}$$

with $\boldsymbol{q}(x,y) = \boldsymbol{q}_\mathrm{d}(y)\mathrm{e}^{-\mathrm{j}k_x x}$. The derivative of $\boldsymbol{A}_x$ with respect to x is zero since the mean flow is uniform in the axial direction.

Generalised Eigenvalue Problem

The system is discretised in the y-direction by taking n equally spaced points. The first point y_1 is taken at the lower wall of the duct ($y_1 = 0$) and the last point y_n at the upper wall ($y_n = H$). The spacing between two consecutive points is $h_y = H/(n-1)$. The generalised eigenvalue problem 3.48 is obtained, with: $\boldsymbol{q}_\mathrm{d} = \left\{\boldsymbol{q}_\rho; \boldsymbol{q}_{\rho u_x}; \boldsymbol{q}_{\rho u_y}; \boldsymbol{q}_{p_\mathrm{c}}\right\}$, where $\boldsymbol{q}_\rho$, $\boldsymbol{q}_{\rho u_x}$, $\boldsymbol{q}_{\rho u_y}$ and $\boldsymbol{q}_{p_\mathrm{c}}$ are column vectors of size n, respectively discretisations of the density, x-momentum, y-momentum and modified pressure perturbations. The system matrices $\boldsymbol{A}$ and $\boldsymbol{B}$ from Equation 3.48 have the following expressions:

$$\boldsymbol{A} = \mathrm{j}\begin{bmatrix} \boldsymbol{0} & \boldsymbol{I} & \boldsymbol{0} & \boldsymbol{0} \\ -u_{0_x}^2\boldsymbol{F}^2 & 2u_{0_x}\boldsymbol{F} & \boldsymbol{0} & \dfrac{\rho_0 c_0^2}{p_{\mathrm{c}_0}}\boldsymbol{I} \\ \boldsymbol{0} & \boldsymbol{0} & u_{0_x}\boldsymbol{F} & \boldsymbol{0} \\ -\dfrac{p_{\mathrm{c}_0}}{\rho_0}u_{0_x}\boldsymbol{F} & \dfrac{p_{\mathrm{c}_0}}{\rho_0}\boldsymbol{I} & \boldsymbol{0} & u_{0_x}\boldsymbol{F} \end{bmatrix}, \boldsymbol{B} = \begin{bmatrix} \mathrm{j}\omega\boldsymbol{I} & \boldsymbol{0} & \boldsymbol{D}_1 & \boldsymbol{0} \\ \boldsymbol{0} & \mathrm{j}\omega\boldsymbol{I} & u_{0_x}\left(\boldsymbol{F}' + \boldsymbol{F}D_1\right) & \boldsymbol{0} \\ \boldsymbol{0} & \boldsymbol{0} & \mathrm{j}\omega\boldsymbol{I} & \dfrac{\rho_0 c_0^2}{p_{\mathrm{c}_0}}\boldsymbol{D}_1 \\ \boldsymbol{0} & \boldsymbol{0} & \dfrac{p_{\mathrm{c}_0}}{\rho_0}\boldsymbol{D}_1 & \mathrm{j}\omega\boldsymbol{I} \end{bmatrix}, \tag{3.50}$$

where $\boldsymbol{I}$ is the identity matrix. $\boldsymbol{F}$ is the diagonal matrix of the mean flow profile at the discretisation points. $\boldsymbol{F}'$ is the diagonal matrix of the first derivative of the mean

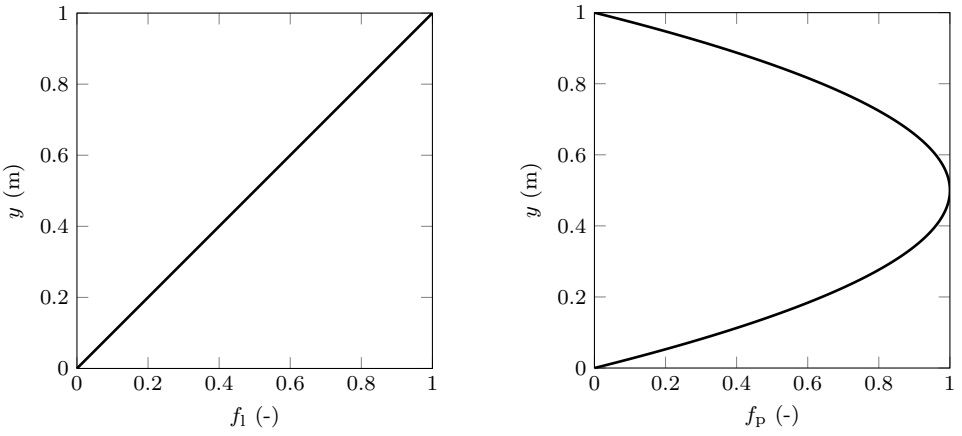

(a) Linear. (b) Parabolic.

Figure 3.4: Non-uniform mean flow profiles in two-dimensional duct.

flow profile at the discretisation points. $\boldsymbol{D}_1$ is the differential matrix for the first-order derivative with respect to y. The hard wall boundary condition $(\rho\boldsymbol{u})\cdot\boldsymbol{n}=0$ is enforced at $y=0$ and at $y=H$: $V_1=V_n=0$. In practice, the rows and columns corresponding to the positions of V_1 and V_n in $\boldsymbol{A}$ and $\boldsymbol{B}$ are set to zero. Only the diagonal terms corresponding to the positions of V_1 and V_n in $\boldsymbol{B}$ are set to 1.

Mean Flow Profiles

Two non-uniform mean flow profiles are investigated, as shown in Figure 3.4. The first profile is linear: the mean flow velocity is zero along the lower duct wall and has a constant value $u_{0_x}\neq 0$ along the upper duct wall. The second profile is parabolic: the mean flow velocity is zero along both duct walls and has a maximum value along the duct axis. These profiles are such that the mean flow velocity field $\boldsymbol{u}_0=u_{0_x}f_\bullet(y)\boldsymbol{e}_x$ verify the steady Euler equations, with ρ_0 and p_0 constant: $\boldsymbol{\nabla}\cdot\boldsymbol{u}_0=0$. The analytic expressions of the mean flow velocity profiles are:

$$\begin{cases} f_{\mathrm{l}}(y) &= \dfrac{y}{H} & \text{for the linear mean flow profile} \\ f_{\mathrm{p}}(y) &= 4\dfrac{y}{H}\left(1-\dfrac{y}{H}\right) & \text{for the parabolic mean flow profile} \end{cases} . \tag{3.51}$$

In the following, some results of the modal analysis are shown for both mean flow profiles: Figures 3.5 and 3.6 represent the real parts of the modified pressure field in the two-dimensional duct for $k_0=10\,\mathrm{m}^{-1}$, for the linear and parabolic profiles respectively. The first five right-propagating acoustic duct modes are plotted, for downstream ($u_{0_x}=0.5c_0$) and upstream ($u_{0_x}=-0.5c_0$) propagation. The duct extends for x from 0 to 2.5 m, and

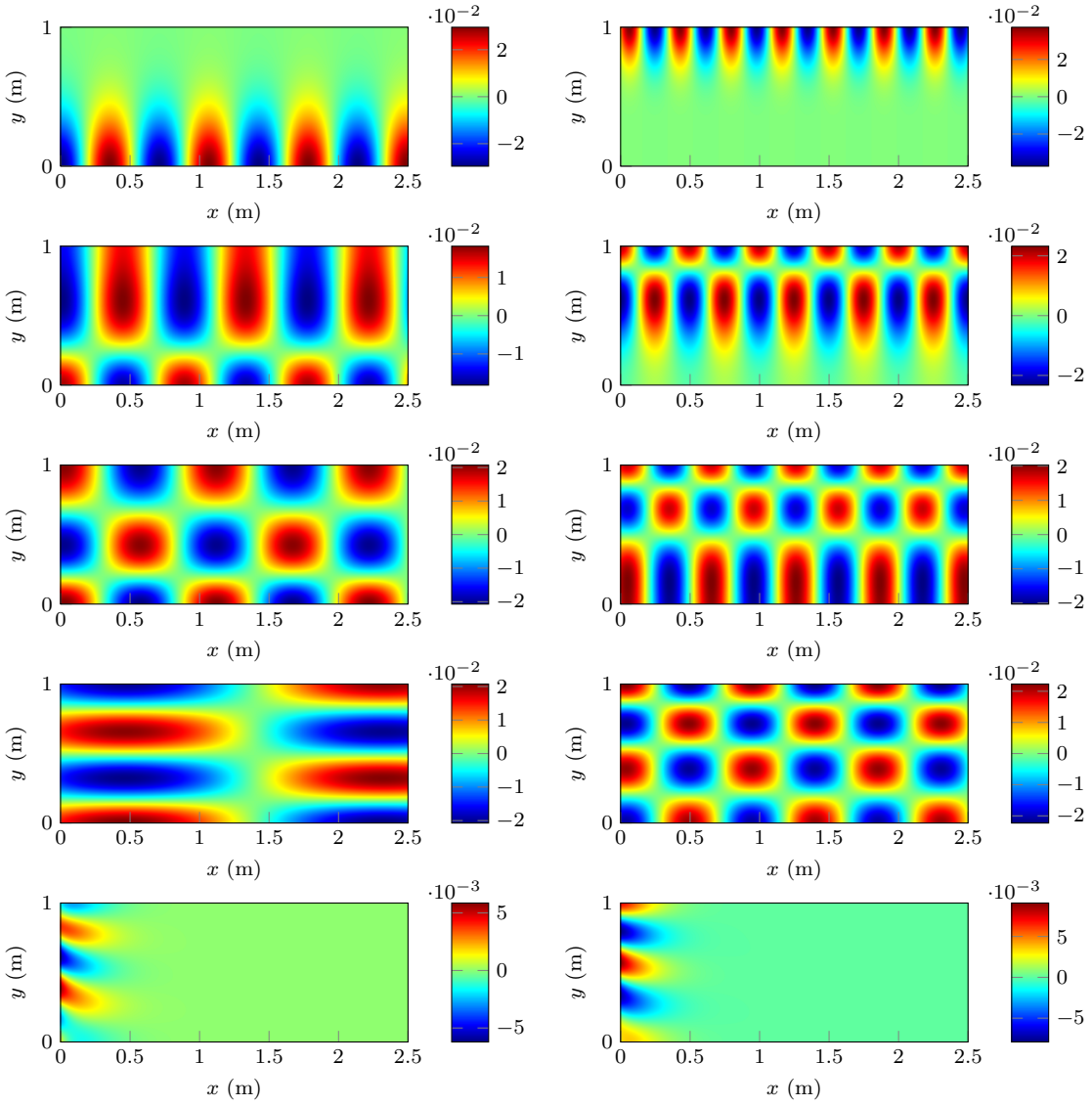

Figure 3.5: Real part of the modified pressure for the first five right-propagating acoustic modes, in a two-dimensional duct with a linear velocity profile. Left: $u_{0_x} = 0.5c_0$. Right: $u_{0_x} = -0.5c_0$.

$H = 1\,\text{m}$. The discretisation uses $n = 5000$ points. A first general observation is that the downstream propagating waves have increased wavelengths, in opposition to the waves propagating upstream which have shorter wavelengths. Moreover, the wavelength increases with the mode number, as long as the cut-off frequency is not reached. From the mode $m = 5$, evanescent waves are obtained which amplitudes decrease exponentially inside the duct. The mean flow profile has an effect on the axial wavenumber and on the modes amplitude: with the linear profile, the plane wave amplitude is the highest where the mean flow Mach number is the smallest. With the parabolic profile, the profile symmetry is conserved in the acoustic solution and the same conclusions as those observed for the linear profile can be drawn.

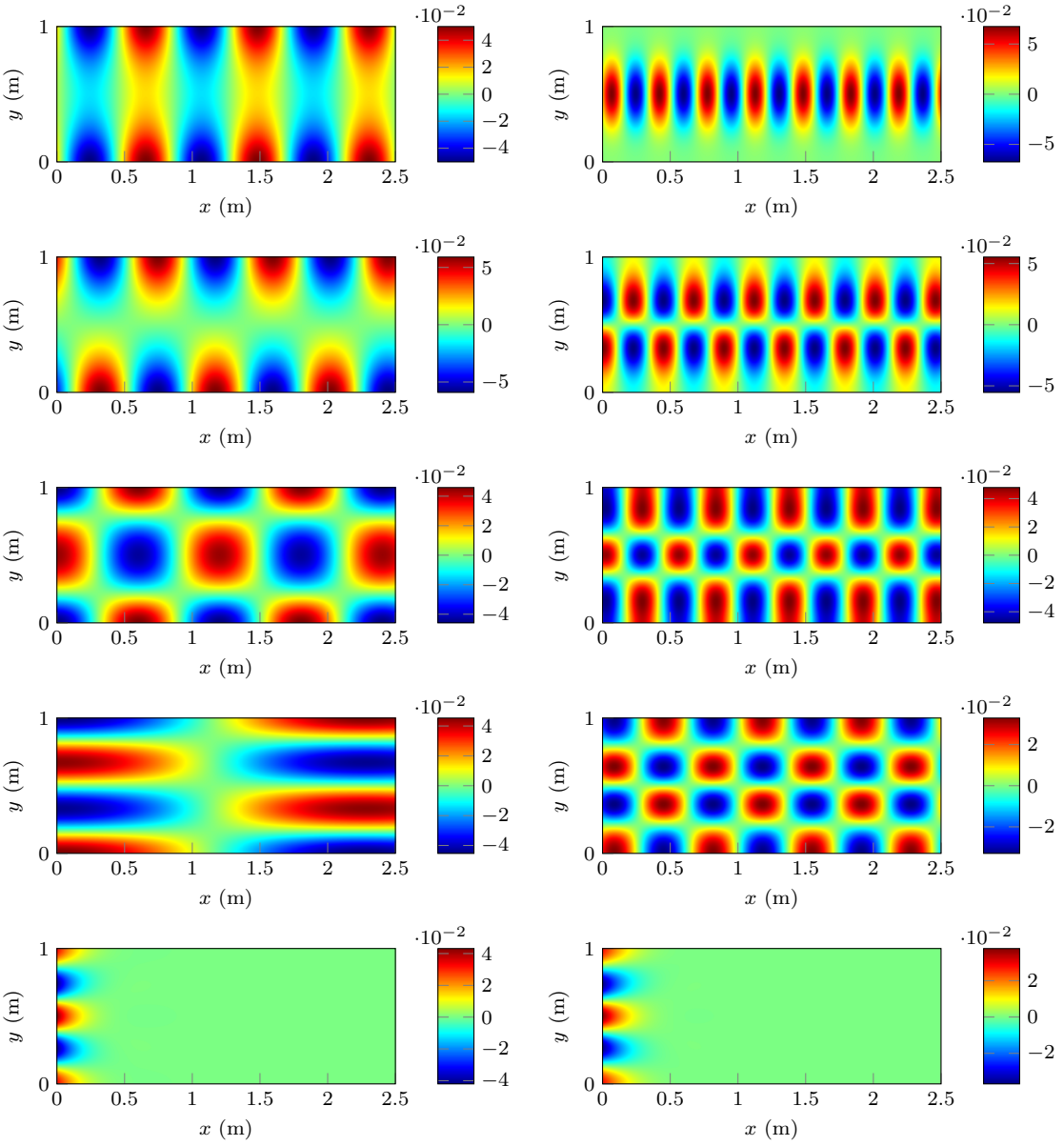

Figure 3.6: Real part of the modified pressure for the first five right-propagating acoustic modes, in a two-dimensional duct with a parabolic velocity profile. Left: $u_{0_x} = 0.5c_0$. Right: $u_{0_x} = -0.5c_0$.

3.4.2 Wave Propagation in Axisymmetric Duct

Let us now consider a cylindrical infinite straight duct in the x-direction, with outer radius r_o. The mean flow velocity varies in the radial direction r. The mean flow and the geometry are axisymmetric, and the fluid properties do not depend on θ. A Fourier decomposition of the fields yields azimuthal contributions of the form:

$$\boldsymbol{q}(r,\theta,x) = \boldsymbol{q}_r(r)\mathrm{e}^{-\mathrm{j}m\theta}\mathrm{e}^{-\mathrm{j}k_x x}. \tag{3.52}$$

For a time-harmonic solution, Equation B.3 simplifies to:

$$\mathrm{j}\omega \boldsymbol{q}_r + \frac{1}{r}\left(\boldsymbol{A}_r - \mathrm{j}m\boldsymbol{A}_\theta + \boldsymbol{A}_\mathrm{c}\right)\boldsymbol{q}_r + \frac{\partial \boldsymbol{A}_r}{\partial r}\boldsymbol{q}_r + \boldsymbol{A}_r\frac{\partial \boldsymbol{q}_r}{\partial r} - \mathrm{j}k_x\boldsymbol{A}_x\boldsymbol{q}_r = \boldsymbol{0}, \tag{3.53}$$

where the derivatives of $\boldsymbol{A}_x$ with respect to x and of $\boldsymbol{A}_\theta$ with respect to θ are zero since the mean flow is longitudinally uniform and axisymmetric. Since the problem is axisymmetric, it is solved in the two-dimensional plane (x, r) where θ is fixed. Only half of the corresponding section of the duct is considered, and appropriate boundary conditions are applied. The hard wall is enforced at $r = r_\mathrm{o}$. Along the axis, the fields must be continuous. Depending on the azimuthal mode m, the boundary conditions at $r = 0$ impose the perturbations values along the axis such that [158]:

$$\begin{cases} u_r = u_\theta = 0 & \text{, if } m = 0, \\ \rho = 0;\ u_r = \pm\mathrm{j}u_\theta;\ u_z = 0;\ p = 0 & \text{, if } m = \pm 1, \\ \rho = 0;\ u_r = u_\theta = u_z = 0;\ p = 0 & \text{, if } |m| > 1. \end{cases} \tag{3.54}$$

The system is discretised in the r-coordinate with n equally spaced points, between $r_1 = 0$ and $r_n = r_\mathrm{o}$. The spacing between the points is $h_r = r_\mathrm{o}/(n-1)$. The generalised eigenvalue problem 3.48 is such that: $\boldsymbol{q}_\mathrm{d} = \left\{\boldsymbol{q}_\rho;\ \boldsymbol{q}_{\rho u_r};\ \boldsymbol{q}_{\rho u_\theta};\ \boldsymbol{q}_{\rho u_x};\ \boldsymbol{q}_{p_\mathrm{c}}\right\}$, where $\boldsymbol{q}_\rho$, $\boldsymbol{q}_{\rho u_r}$, $\boldsymbol{q}_{\rho u_\theta}$, $\boldsymbol{q}_{\rho u_x}$ and $\boldsymbol{q}_{p_\mathrm{c}}$ are column vectors of size n, respectively discretisations of the density, r-momentum, θ-momentum, x-momentum and modified pressure perturbations. The matrices $\boldsymbol{A}$ and $\boldsymbol{B}$ are obtained like in Section 3.4.1, and the generalised eigenvalue problem is solved similarly. Moreover, the colormaps of the pressure field are of the same type as those found in Figures 3.5 and 3.6, and are not shown here.

Chapter 4

High-Order Finite Element Model

In this chapter, we present the numerical method used for solving the problem of wave propagation in non-uniform media. The chosen physical model is the Linearised Euler Equations described in Chapter 3. For turbomachinery applications, the numerical method solving the Linearised Euler Equations must account for complex geometries and inhomogeneous media. As explained in Chapter 2, the high-order Finite Element Method is used. The first section introduces the formulation. The boundary conditions are explained in the second section. The finite element model features are described in the third section. The final section introduces the Perfectly Matched Layers.

4.1 Weighted Residual Formulation

The Finite Element Method rests on the transformation of the physical problem into an equivalent integral formulation [90]. In the absence of external source, the differential operator $\mathfrak{L}(\boldsymbol{q})$ given by the numerical model (see Equation 3.19) gives the so-called residual $\mathfrak{R}$: $\mathfrak{L}(\boldsymbol{q}) = \mathfrak{R}$. Requiring that the residual is orthogonal to all test functions $\boldsymbol{w}$, it yields [159]:

$$\int_{\Omega} \boldsymbol{w}^{\mathrm{T}} \mathfrak{R} \mathrm{d}\Omega = 0, \tag{4.1}$$

where Ω is the domain and the superscript $^{\mathrm{T}}$ denotes the Hermitian transpose. The test functions $\boldsymbol{w}$ are bounded, and uniquely defined within the domain Ω and its boundary surface Γ. This orthogonality condition states that the residual weighted average over the problem has to be zero in order to find the best approximate solution.

4.1.1 Formulation in Cartesian Coordinates

An integration by parts provides the weak variational formulation for the Linearised Euler Equations in Cartesian coordinates:

$$\int_\Omega \left(\mathrm{j}\omega \boldsymbol{w}^\mathrm{T}\boldsymbol{q} - \frac{\partial \boldsymbol{w}^\mathrm{T}}{\partial x}\boldsymbol{A}_x\boldsymbol{q} - \frac{\partial \boldsymbol{w}^\mathrm{T}}{\partial y}\boldsymbol{A}_y\boldsymbol{q} \right) \mathrm{d}\Omega = -\int_\Gamma \boldsymbol{w}^\mathrm{T} \left(n_x\boldsymbol{A}_x + n_y\boldsymbol{A}_y \right) \boldsymbol{q}\mathrm{d}\Gamma. \tag{4.2}$$

The flux matrix $\boldsymbol{F} = n_x\boldsymbol{A}_x + n_y\boldsymbol{A}_y$ along the unit normal direction $\boldsymbol{n}$ to the boundary Γ is crucial for the definition of boundary conditions, as it is seen in Section 4.2. Note that the vector $\boldsymbol{n}$ points toward the domain exterior.

4.1.2 Formulation for an Axisymmetric Problem

For axisymmetric mean flows and geometries, a Fourier decomposition of the solution yields azimuthal contributions such that: $\boldsymbol{q}(r,\theta,x) = \boldsymbol{q}(r,x)\mathrm{e}^{-\mathrm{j}m\theta}$, where $m \in \mathbb{Z}$ is the azimuthal order. The weak variational formulation for the axisymmetric Linearised Euler Equations given in Equation B.5 reads:

$$\begin{aligned}\int_\Omega \left(\mathrm{j}\omega r\boldsymbol{w}^\mathrm{T}\boldsymbol{q} - \mathrm{j}m\boldsymbol{w}^\mathrm{T}\boldsymbol{A}_\theta\boldsymbol{q} + \boldsymbol{w}^\mathrm{T}\boldsymbol{A}_\mathrm{c}\boldsymbol{q} - r\frac{\partial \boldsymbol{w}^\mathrm{T}}{\partial x}\boldsymbol{A}_x\boldsymbol{q} - r\frac{\partial \boldsymbol{w}^\mathrm{T}}{\partial r}\boldsymbol{A}_r\boldsymbol{q} \right) \mathrm{d}x\mathrm{d}r \\ = -\int_\Gamma r\boldsymbol{w}^\mathrm{T} \left(n_x\boldsymbol{A}_x + n_r\boldsymbol{A}_r \right) \boldsymbol{q}\mathrm{d}\Gamma.\end{aligned} \tag{4.3}$$

In cylindrical coordinates, the differential $\mathrm{d}\Omega$ has been replaced by $r\mathrm{d}r\mathrm{d}\theta\mathrm{d}x$. The multiplication of the Linearised Euler Equations by r cancels out any existing singularity (the factors $1/r$ which appear in front of the terms in $\boldsymbol{A}_r$, $\boldsymbol{A}_\theta$ and $\boldsymbol{A}_\mathrm{c}$, in Equation B.5). The integral over θ is constant and factors out, which leaves us with the differentials $\mathrm{d}x\mathrm{d}r$. This problem is then equivalent to a two-dimensional problem in the plane (x,r), where $\boldsymbol{F} = n_x\boldsymbol{A}_x + n_r\boldsymbol{A}_r$ is the flux matrix along the normal direction $\boldsymbol{n} = \{n_x, n_r\}^\mathrm{t}$.

4.2 Boundary Conditions

Within numerical simulations, the computational domain Ω is truncated. Proper non-reflecting boundary conditions must be applied at the domain boundary Γ. The method of characteristics gives a framework to apply the boundary conditions for hyperbolic problems [116, 160].

4.2.1 Characteristic Waves

The Linearised Euler Equations define a hyperbolic system, where each flux matrix $\boldsymbol{A}_{x_i}$ has real eigenvalues and real eigenvectors [161]. In terms of those eigenvalues and eigenvectors, each flux matrix reads: $\boldsymbol{A}_{x_i} = \boldsymbol{W}_{x_i}\boldsymbol{\Lambda}_{x_i}\boldsymbol{W}_{x_i}^{-1}$, where $\boldsymbol{\Lambda}_{x_i}$ is the eigenvalues diagonal matrix and $\boldsymbol{W}_{x_i}$ is the non-singular eigenvectors matrix. For a uniform mean flow, the original system Equation 3.14 is left-multiplied by $\boldsymbol{W}_x^{-1}$. It yields:

$$\frac{\partial \hat{\boldsymbol{q}}_x}{\partial t} + \boldsymbol{\Lambda}_x \frac{\partial \hat{\boldsymbol{q}}_x}{\partial x} + \boldsymbol{W}_x^{-1}\boldsymbol{A}_y\boldsymbol{W}_x \frac{\partial \hat{\boldsymbol{q}}_x}{\partial y} = \boldsymbol{0}, \tag{4.4}$$

where $\hat{\boldsymbol{q}}_x = \boldsymbol{W}_x^{-1}\boldsymbol{q}$ is the amplitude vector of the characteristic wave travelling along the x-axis [28, 117]. Its equation is: $\mathrm{d}x/\mathrm{d}t = \lambda_x^{(i)}$, where $\lambda_x^{(i)}$ are the flux matrix $\boldsymbol{A}_x$ eigenvalues [116]. The components of $\hat{\boldsymbol{q}}_x$ can be seen as travelling waves moving at the phase velocities $\lambda_x^{(i)}$, which define whether a characteristic is incoming or outgoing. It can be shown that these considerations hold with non-uniform mean flows [116].

This approach can be generalised to the flux matrix $\boldsymbol{F} = n_{x_i}\boldsymbol{A}_{x_i}$, which represents the characteristic waves travelling along the direction $\boldsymbol{n}$. The eigenvalues diagonal matrix $\boldsymbol{\Lambda}$ and the eigenvectors matrix $\boldsymbol{W}$ are such that: $\boldsymbol{F} = \boldsymbol{W}\boldsymbol{\Lambda}\boldsymbol{W}^{-1}$. The amplitude vector of the characteristic waves travelling along the direction $\boldsymbol{n}$ is: $\hat{\boldsymbol{q}} = \boldsymbol{W}^{-1}\boldsymbol{q}$. The travelling velocities are: $\boldsymbol{u}_0 \cdot \boldsymbol{n}$, $\boldsymbol{u}_0 \cdot \boldsymbol{n} - c_0$ and $\boldsymbol{u}_0 \cdot \boldsymbol{n} + c_0$. In two-dimensional Cartesian coordinates, the vector of amplitudes reads:

$$\hat{\boldsymbol{q}} = \begin{Bmatrix} \rho_0 \left(n_x u_y' - n_y u_x'\right) \\ \rho' - \dfrac{p'}{c_0^2} \\ \dfrac{\rho_0}{2c_0}\left(-\boldsymbol{u}' \cdot \boldsymbol{n} + \dfrac{1}{\rho_0 c_0} p'\right) \\ \dfrac{\rho_0}{2c_0}\left(\boldsymbol{u}' \cdot \boldsymbol{n} + \dfrac{1}{\rho_0 c_0} p'\right) \end{Bmatrix}. \tag{4.5}$$

This vector exhibits the particularity of the Linearised Euler Equations, in such that they support acoustic, vorticity and entropy waves [160]. The first component corresponds to the hydrodynamic characteristic, which travels along the normal vector $\boldsymbol{n}$ with phase velocity $\lambda_\mathrm{v} = \boldsymbol{u}_0 \cdot \boldsymbol{n}$. The second component is the entropy characteristic. It also travels with phase velocity $\lambda_\mathrm{e} = \boldsymbol{u}_0 \cdot \boldsymbol{n}$. That characteristic only depends on the density and pressure perturbations. The entropy characteristic amplitude vanishes for homentropic perturbations, but it may not be zero for isentropic perturbations. The last two components refer to the acoustic characteristics. These characteristics travel along the normal vector $\boldsymbol{n}$,

with phase velocities $\lambda_{a^-} = \boldsymbol{u}_0 \cdot \boldsymbol{n} - c_0$ for the incoming characteristic and $\lambda_{a^+} = \boldsymbol{u}_0 \cdot \boldsymbol{n} + c_0$ for the outgoing characteristic. That is true for subsonic mean flows since $\|\boldsymbol{u}_0 \cdot \boldsymbol{n}\| \leq \|\boldsymbol{u}_0\| < c_0$.

4.2.2 Implementation

In practice, the boundary conditions implementation through the method of characteristics relies on the knowledge of the incoming and outgoing characteristics. For subsonic mean flows, the acoustic characteristics are already identified with $\lambda_{a^-} < 0$ and $\lambda_{a^+} > 0$. The sign of $\lambda_v = \lambda_e$ indicates whether the hydrodynamic and entropy characteristic waves enter or leave the domain. Three cases arise:

- Without mean flow, the hydrodynamic and entropy waves do not exist.
- If $\boldsymbol{u}_0 \cdot \boldsymbol{n} > 0$, the hydrodynamic and entropy waves leave the domain. Only the incoming acoustic characteristic enters the domain.
- If $\boldsymbol{u}_0 \cdot \boldsymbol{n} < 0$, the hydrodynamic and entropy waves enter the domain together with the incoming acoustic characteristic.

For a well-posed problem, the number l of imposed boundary conditions is equal to the number of incoming characteristics: $l = 1$ for $\boldsymbol{u}_0 \cdot \boldsymbol{n} \geq 0$ and $l = 3$ for $\boldsymbol{u}_0 \cdot \boldsymbol{n} < 0$. In matrix form, the boundary conditions read: $\boldsymbol{M}\boldsymbol{q} = \boldsymbol{s}$, where $\boldsymbol{M}$ is a $(l \times 4)$ coefficient matrix and $\boldsymbol{s}$ is a source vector. Written for the vector of characteristic amplitudes $\hat{\boldsymbol{q}}$, it yields: $\hat{\boldsymbol{M}}\hat{\boldsymbol{q}} = \boldsymbol{s}$, where $\hat{\boldsymbol{M}} = \boldsymbol{M}\boldsymbol{W}$. By separating the characteristics leaving the domain from the characteristics entering the domain, the equation becomes:

$$\begin{bmatrix} \hat{\boldsymbol{M}}^+ & \hat{\boldsymbol{M}}^- \end{bmatrix} \begin{Bmatrix} \hat{\boldsymbol{q}}^+ \\ \hat{\boldsymbol{q}}^- \end{Bmatrix} = \boldsymbol{s}, \tag{4.6}$$

where $\hat{\boldsymbol{M}}^-$ and $\hat{\boldsymbol{q}}^-$ (respectively $\hat{\boldsymbol{M}}^+$ and $\hat{\boldsymbol{q}}^+$) are the restrictions of $\hat{\boldsymbol{M}}$ and $\hat{\boldsymbol{q}}$ associated with the outgoing characteristics (respectively incoming characteristics). That decomposition allows to express the incoming characteristics with respect to the outgoing characteristics in terms of the amplitudes:

$$\hat{\boldsymbol{q}}^- = \left(\hat{\boldsymbol{M}}^-\right)^{-1} \left(\boldsymbol{s} - \hat{\boldsymbol{M}}^+ \hat{\boldsymbol{q}}^+\right). \tag{4.7}$$

The boundary integral transforms into:

$$\int_\Gamma \boldsymbol{w}^{\mathrm{T}} \boldsymbol{F} \boldsymbol{q} \mathrm{d}\Gamma = \int_\Gamma \boldsymbol{w}^{\mathrm{T}} \boldsymbol{W} \boldsymbol{\Lambda} \boldsymbol{R} \boldsymbol{W}^{-1} \boldsymbol{q} \mathrm{d}\Gamma + \int_\Gamma \boldsymbol{w}^{\mathrm{T}} \hat{\boldsymbol{s}} \mathrm{d}\Gamma, \tag{4.8}$$

where the matrix $\boldsymbol{R}$ represents the reflection between the characteristics and the vector $\hat{\boldsymbol{s}}$ is the incoming source term. Their generic expressions are:

$$\boldsymbol{R} = \begin{bmatrix} \boldsymbol{I} & \boldsymbol{0} \\ -\left(\hat{\boldsymbol{M}}^{-}\right)^{-1} \hat{\boldsymbol{M}}^{+} & \boldsymbol{0} \end{bmatrix} \text{ and } \hat{\boldsymbol{s}} = \boldsymbol{W} \boldsymbol{\Lambda} \begin{Bmatrix} \boldsymbol{0} \\ \left(\hat{\boldsymbol{M}}^{-}\right)^{-1} \boldsymbol{s} \end{Bmatrix}. \tag{4.9}$$

In practice, the first integral is computed within the numerical model, whereas the second integral is defined as boundary condition in the right-hand side of the linear system. The full expressions of the different matrices are written in Appendix D.

4.2.3 Imposed Conditions

In this work, sound propagation with rigid-wall ducts is mainly investigated. Duct modes may be injected through the method of characteristics by means of the normal velocity at the boundary. The condition is: $\boldsymbol{u} \cdot \boldsymbol{n} = u_{n_\mathrm{i}}$, where u_{n_i} is the imposed incident normal velocity. Written for the conservative variables, the condition reads:

$$-\boldsymbol{u}_0 \cdot \boldsymbol{n} \rho + (\rho \boldsymbol{u}) \cdot \boldsymbol{n} = \rho_0 u_{n_\mathrm{i}}. \tag{4.10}$$

For the case $\boldsymbol{u}_0 \cdot \boldsymbol{n} < 0$, three characteristics enter the domain: the hydrodynamic, entropy and acoustic characteristics. Each characteristic is specified. The matrix $\boldsymbol{M}$ and the source vector $\boldsymbol{s}$ read:

$$\boldsymbol{M} = \begin{bmatrix} n_y u_{0_x} - n_x u_{0_y} & -n_y & n_x & 0 \\ 1 & 0 & 0 & -\dfrac{\rho_0}{p_{\mathrm{c}_0}} \\ -\boldsymbol{u}_0 \cdot \boldsymbol{n} & n_x & n_y & 0 \end{bmatrix} \text{ and } \boldsymbol{s} = \begin{Bmatrix} \hat{q}_\mathrm{v} \\ \hat{q}_\mathrm{e} \\ \rho_0 u_{n_\mathrm{i}} \end{Bmatrix}, \tag{4.11}$$

where the first row corresponds to the expression of the hydrodynamic characteristic found in Equation 4.5 ($\hat{q}_\mathrm{v}$ is the vorticity characteristic) and the second row defines the entropy characteristic $\hat{q}_\mathrm{e}$. The third row is the condition on the acoustic characteristic, imposed through the normal velocity (see Equation 4.10). The matrices $\hat{\boldsymbol{M}}$, $\hat{\boldsymbol{M}}^{-}$ and $\hat{\boldsymbol{M}}^{+}$ are

obtained:

$$\hat{\boldsymbol{M}} = \begin{bmatrix} 1 & 0 & 0 & 0 \\ 0 & 1 & 0 & 0 \\ 0 & 0 & -c_0 & c_0 \end{bmatrix}, \hat{\boldsymbol{M}}^- = \begin{bmatrix} 1 & 0 & 0 \\ 0 & 1 & 0 \\ 0 & 0 & -c_0 \end{bmatrix} \text{ and } \hat{\boldsymbol{M}}^+ = \begin{bmatrix} 0 \\ 0 \\ c_0 \end{bmatrix}. \tag{4.12}$$

The reflection matrix $\boldsymbol{R}$ and the source vector $\hat{\boldsymbol{s}}$ yield:

$$\boldsymbol{R} = \begin{bmatrix} 0 & 0 & 0 & 0 \\ 0 & 0 & 0 & 0 \\ 0 & 0 & 0 & 1 \\ 0 & 0 & 0 & 1 \end{bmatrix} \text{ and } \hat{\boldsymbol{s}} = \boldsymbol{W}\boldsymbol{\Lambda} \begin{Bmatrix} \hat{q}_\mathrm{v} \\ \hat{q}_\mathrm{e} \\ -\dfrac{\rho_0}{c_0} u_{n_\mathrm{i}} \\ 0 \end{Bmatrix}. \tag{4.13}$$

For the case $\boldsymbol{u}_0 \cdot \boldsymbol{n} \geq 0$, only the incoming acoustic characteristic enters the domain. It is imposed through the normal velocity u_{n_i}. The corresponding reflection matrix and source vector are:

$$\boldsymbol{R} = \begin{bmatrix} 1 & 0 & 0 & 0 \\ 0 & 1 & 0 & 0 \\ 0 & 0 & 0 & 1 \\ 0 & 0 & 0 & 1 \end{bmatrix} \text{ and } \hat{\boldsymbol{s}} = \boldsymbol{W}\boldsymbol{\Lambda} \begin{Bmatrix} 0 \\ 0 \\ -\dfrac{\rho_0}{c_0} u_{n_\mathrm{i}} \\ 0 \end{Bmatrix}. \tag{4.14}$$

A particular case of the imposed normal velocity boundary condition is the hard wall, which can be encountered on aeroengine ducts. For rigid walls, the mean flow and perturbations normal velocities are equal to zero. As a consequence, the corresponding source vector $\hat{\boldsymbol{s}}$ is equal to zero.

For duct walls treated with liners, an impedance boundary condition may be imposed. Without mean flow, that soft-wall condition is [162, 163]: $p = Z\boldsymbol{u} \cdot \boldsymbol{n}$, where Z is the boundary acoustic impedance. In terms of conservative parameters, this condition can be written:

$$\frac{Z}{\rho_0} (\rho \boldsymbol{u}) \cdot \boldsymbol{n} - \frac{\rho_0 c_0^2}{p_{\mathrm{c}_0}} p_\mathrm{c} = 0. \tag{4.15}$$

Like the hard-wall boundary condition, the soft-wall source vector is equal to zero. The reflection matrix involves the impedance reflection coefficient: $(Z - \rho_0 c_0)/(Z + \rho_0 c_0)$. The particular value $Z = \rho_0 c_0$ is such that the reflection coefficient is equal to zero: the acoustic wave is fully transmitted. The particular value $Z = \infty$, which corresponds to the hard wall, is such that the reflection coefficient is equal to one: the acoustic wave is fully reflected. With mean flow, the impedance boundary condition includes the mean flow gradient, which

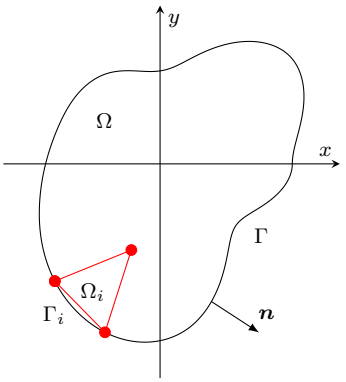

Figure 4.1: Two-dimensional problem domain Ω, boundary Γ, normal vector $\boldsymbol{n}$ and triangular mesh element Ω_i.

makes its definition through the method of characteristics complex [162, 163]. This is not investigated in this work.

4.2.4 Axisymmetric Conditions

For axisymmetric problems, proper conditions verifying the variables continuity are applied along the axis at $r = 0$. For a cylindrical problem, the conditions are described in Equation 3.54 depending on the values of the mode number m. In practice, within the numerical model, these conditions are directly applied through linear relations on the degrees of freedom.

4.3 Finite Element Model

4.3.1 Field Variable Approximation

The next step consists in discretising the continuous domain Ω. Since complex geometries are considered in the application test cases (see Chapter 8), unstructured conformal meshes are preferred. In the following, linear elements are mainly used (unless otherwise stated) and the meshes are generated with Gmsh mesh generator [164]. Figure 4.1 shows an example of a two-dimensional domain Ω, its boundary Γ, the normal vector $\boldsymbol{n}$ to the boundary and a triangular mesh element Ω_i from the discretisation.

The discretisation permits to approximate the integrals element by element, since $\int_\Omega = \sum_{i=1}^{n_\mathrm{e}} \int_{\Omega_i}$ and $\int_\Gamma = \sum_{i=1}^{n_\mathrm{e}} \int_{\Gamma_i}$, with n_e the number of elements in the discretisation. The solution vector $\boldsymbol{q}_i$ on each element expands in terms of high-order polynomial shape functions $S_i^{(j)}$

and of degrees of freedom $\boldsymbol{q}_i^{(j)}$ such that:

$$\boldsymbol{q}_i(\boldsymbol{x}) = \sum_{j=1}^{n_{\text{dof}}} \boldsymbol{q}_i^{(j)} S_i^{(j)}(\boldsymbol{x}) \quad \forall \boldsymbol{x} \in \Omega, \forall i \in \{1, \dots, n_{\text{e}}\}, \tag{4.16}$$

where n_{dof} is the number of degrees of freedom. The same shape functions are used for each variable. The weighting functions in $\boldsymbol{w}$ have the same approximation basis. Written in the matrix form, the vectors expansions read:

$$\left\{ \begin{array}{rcl} \boldsymbol{q} & = & \boldsymbol{S}\boldsymbol{d} \\ \boldsymbol{w} & = & \boldsymbol{S}\boldsymbol{o} \end{array} \right. , \tag{4.17}$$

where $\boldsymbol{S}$ is the shape functions matrix, $\boldsymbol{d}$ is the vector of degrees of freedom and $\boldsymbol{o}$ is an n_{dof}-length vector.

4.3.2 Linear System

Each element integral is then evaluated by means of numerical quadrature, with accuracy order corresponding to the highest polynomial order in the integrand. The standard Gauss-Legendre quadrature is used for two-dimensional elements and the Dunavant quadrature for triangular elements [165]. As an example, the first integral in the formulation 4.2 transforms into:

$$\int_{\Omega} \mathrm{j}\omega \boldsymbol{w}^{\mathrm{T}} \boldsymbol{q} \mathrm{d}\Omega = \boldsymbol{o}^{\mathrm{T}} \left(\sum_{i=1}^{n_{\text{e}}} \int_{\Omega_i} \mathrm{j}\omega \boldsymbol{S}^{\mathrm{T}} \boldsymbol{S} \mathrm{d}\Omega_i \right) \boldsymbol{d}. \tag{4.18}$$

For a single frequency ω, the elementary integrals are computed within each element and then assembled to form the following discrete global system:

$$\boldsymbol{K}\boldsymbol{d} = \boldsymbol{f}, \tag{4.19}$$

where $\boldsymbol{K}$ is a square, sparse, complex matrix of size n_{dof}^2. $\boldsymbol{f}$ is the complex right-hand side vector. Solving that linear system provides the unknown degrees of freedom contained in the vector $\boldsymbol{d}$, by means of the direct LU factorisation method [166]. The finite element model must comply with consistency, such that the numerical solution converges to the correct solution with mesh refinement and/or increase of shape functions polynomial order [167].

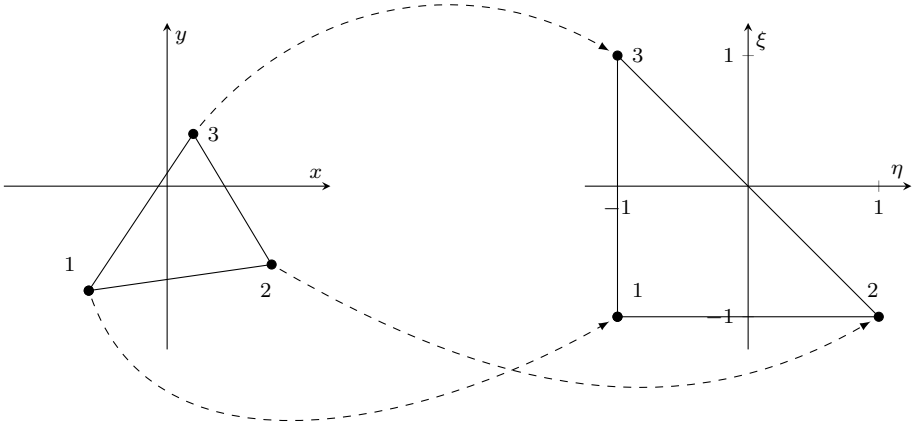

Figure 4.2: Mapping of triangular element from physical domain to reference domain.

4.3.3 Reference Elements

High-order finite elements use large amounts of information, requiring efficient management [108]. Numerical quadrature necessitates many integration points inside each element. The use of reference elements makes the numerical quadrature more convenient. On each element, the coordinates (x, y) in the physical domain transform into the coordinates (η, ξ) in the reference domain by means of a bijective reference map (see Figure 4.2). In practice, this mapping is a change of variable inside the integrals of the formulation. On each two-dimensional element, the integral over Ω_i with differential $\mathrm{d}x\mathrm{d}y$ transforms into an integral over Ω_i^{ref} with differential $\mathrm{d}\eta\mathrm{d}\xi$ which is the triangular element in the reference domain, such that:

$$\mathrm{d}x\mathrm{d}y = \det(\boldsymbol{J})\mathrm{d}\eta\mathrm{d}\xi, \text{ with } \boldsymbol{J} = \begin{bmatrix} \dfrac{\partial x}{\partial \eta} & \dfrac{\partial y}{\partial \eta} \\ \dfrac{\partial x}{\partial \xi} & \dfrac{\partial y}{\partial \xi} \end{bmatrix}. \tag{4.20}$$

The first-order derivatives of the physical coordinates (x, y) with respect to the reference coordinates (η, ξ) are contained in the Jacobian matrix $\boldsymbol{J}$. For linear triangular elements, a Lagrange interpolation expands the physical coordinates in terms of the vertex shape functions $S_{\mathrm{v}}^{(j)}$ such that:

$$\begin{cases} x(\eta,\xi) &= \sum\limits_{j=1}^{3} S_{\mathrm{v}}^{(j)}(\eta,\xi) x_j \\ y(\eta,\xi) &= \sum\limits_{j=1}^{3} S_{\mathrm{v}}^{(j)}(\eta,\xi) y_j \end{cases}, \tag{4.21}$$

where (x_j, y_j) are the three vertices coordinates of the triangular elements. These shape functions read:

$$S_{\mathrm{v}}^{(1)}(\eta,\xi) = -\frac{\eta+\xi}{2},\ S_{\mathrm{v}}^{(2)}(\eta,\xi) = \frac{1+\eta}{2} \text{ and } S_{\mathrm{v}}^{(3)}(\eta,\xi) = \frac{1+\xi}{2}. \tag{4.22}$$

Any variable χ in the formulation is given by: $\chi(x,y) = \chi^{\mathrm{ref}}(\eta,\xi)$. Its gradient in the physical domain reads: $\boldsymbol{\nabla}\chi(x,y) = \boldsymbol{J}^{-1}\boldsymbol{\nabla}^{\mathrm{ref}}\chi^{\mathrm{ref}}(\eta,\xi)$, where $\boldsymbol{\nabla}^{\mathrm{ref}}$ is the gradient in the reference domain and χ^{ref} is the variable in the reference domain. On each physical element, the quadrature evaluates the integral over the reference element for any function f such that:

$$\int_{\Omega_i} f(x,y)\mathrm{d}x\mathrm{d}y = \int_{\Omega_i^{\mathrm{ref}}} \det(\boldsymbol{J}) f(\eta,\xi)\mathrm{d}\eta\mathrm{d}\xi = \sum_{k=1}^{n_{\mathrm{q}}} w_k \det(\boldsymbol{J}) f(\eta_k,\xi_k), \tag{4.23}$$

where the finite sum approximates the integral. The number n_{q} of weighting coefficients w_k and quadrature points (η_k, ξ_k) depends on the quadrature order. For curved elements, the quadrature order increases since the Jacobian may not be constant over the element.

4.3.4 Shape Functions

The standard finite element method uses linear shape functions. As discussed in Section 2.6, that method is known to suffer from dispersion error and high memory requirements limit its applicability to low frequencies. In this work, the polynomial basis is enriched with high-order polynomial shape functions. This leads to lower resolution requirements, smaller number of degrees of freedom and possibility to solve high-frequency problems [107]. Two polynomial shape functions families exist: the nodal shape functions and the modal shape functions. The nodal shape functions have the advantage of the δ-property: their value is one at a given node and zero at the others. Therefore, the corresponding unknown degree of freedom directly relates to the solution at a specific point of the element. The modal shape functions may benefit from the hierarchic property: the polynomial space basis for order p is included in the basis for order $p+1$. This characteristic is an advantage for *p*- and *hp*-adaptivity, since the shape functions do not have to be changed when increasing the polynomial order of the approximation. In this work, the Lobatto hierarchic shape functions are used because of their good conditioning properties [108]. On each element, the approximation basis contains not only vertex functions, but also edge and bubble shape functions. The vertex functions are non-zero at a given node and vanish at the others. The edge functions are non-zero along a given edge and vanish along the others. The bubble

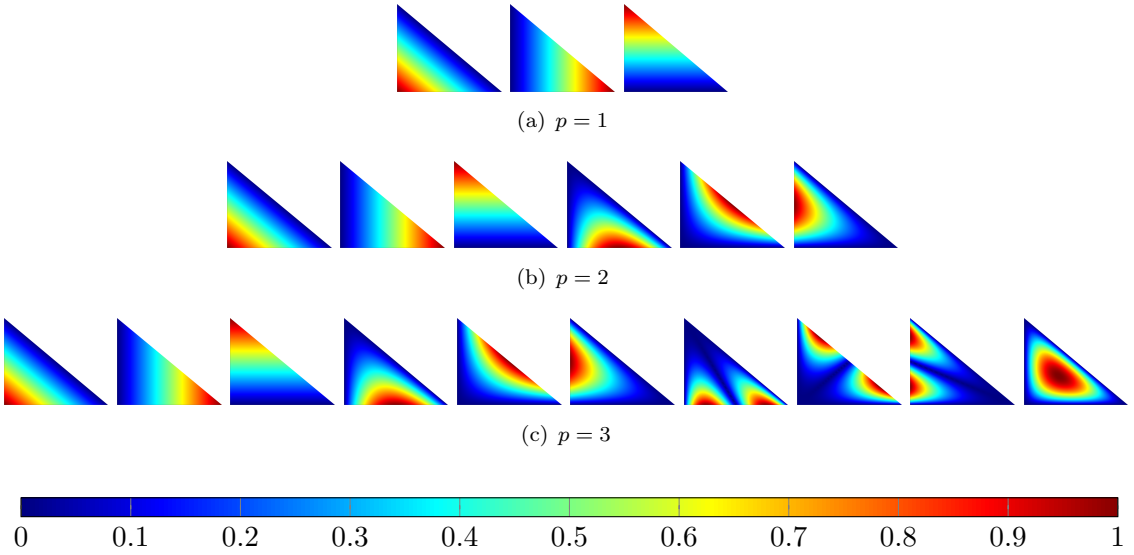

Figure 4.3: Hierarchic Lobatto shape functions on the reference triangular element (absolute values), for p from 1 to 3.

functions are internal and vanish along the edges of the element.

Figure 4.3 shows the Lobatto shape functions on the reference triangular element for p varying from 1 to 3. Their hierarchic property is noticeable. The linear shape functions involve only the vertex functions, as seen in Figure 4.3(a). The quadratic shape functions involve the linear vertex functions plus the first edge functions, as shown in Figure 4.3(b). As depicted in Figure 4.3(c), the cubic shape functions consist of the linear vertex functions and of the quadratic edge functions, plus the cubic edge functions and the first internal bubble function. For a triangular element, the number of vertex shape functions is constant and equal to 3. The number of edge functions linearly depends on the polynomial order p, for $p \geq 2$. The number of bubble functions is a quadratic function of the polynomial order, for $p \geq 3$. That shows the significant impact of high orders on the polynomial basis enrichment through bubble shape functions.

4.3.5 Static Condensation

Since they vanish along the reference element edges, the bubble shape functions are only local and have no connectivity with their neighbouring elements. Static condensation consists in expressing their corresponding degrees of freedom in terms of the remaining ones (vertex and edge degrees of freedom) and to eliminate them from the global system 4.19 [108, 168]. Post-processing permits to recover the internal degrees of freedom of the solution. Static condensation allows to reduce the global system size and the computational cost. In addition, it improves the system conditioning and substantially decreases the mem-

ory requirements [169]. Those effects become more important for higher polynomial orders, since the number of bubble functions increases in p^2. Note that the static condensation technique does not affect the final solution.

4.4 Perfectly Matched Layer

In this part, the Perfectly Matched Layer (PML) properties are discussed. The chapter begins with an introduction on the PML technique. Then, the corresponding variational formulation is described. Finally, an analytic study of the properties of the continuous and the discrete PML is performed.

4.4.1 PML Technique

The PML approach consists in surrounding the computational domain with some artificial domain in which a complex coordinate transformation is applied to absorb the outgoing waves. A propagation domain $[0, x_{\text{int}}]$ is considered. It is terminated by a PML domain $[x_{\text{int}}, x_{\text{int}} + d]$ of length d. x_{int} is the coordinate of the interface between the physical domain and the PML. The complex coordinate $\tilde{x}$ in the PML can be written like:

$$\tilde{x}(x) = x + \frac{f_x(x)}{\mathrm{j}k_0}, \tag{4.24}$$

where f_x is a function of the real physical coordinate x. The designation 'perfectly matched' indicates that the transmission at x_{int} is perfect: no reflection is generated at the interface, for any frequency, and for any incidence angle in multi-dimensional problems [113]. The stretching function f_x is often written as an integral:

$$f_x(x) = \int_{x_{\text{int}}}^{x} \sigma_x(s)\mathrm{d}s, \tag{4.25}$$

where σ_x is the absorption function. In order to ensure absorption in the PML, the stretching function f_x needs to verify a few properties:

- The continuity of both the x-coordinate and the solution at the interface requires that the stretching function vanishes at $x = x_{\text{int}}$. Thus, $f_x(x_{\text{int}}) = 0$, which guarantees that $\tilde{x}(x_{\text{int}}) = x_{\text{int}}$.

- To assure the absorption of the outgoing waves, the stretching function is positive

and increases monotonically in the PML (for the time-harmonic $e^{j\omega t}$ dependence).

- The value $f_x(x_{\text{int}} + d)$ of the stretching function at the PML outlet is large enough to have insignificant reflections in the physical domain.

When dealing with wave propagation in duct with mean flow, inverse upstream modes may propagate (see Section 3.3 and Equation 3.47). A simple classical PML would be inefficient in that case and would make the numerical solution blow up. That issue is addressed for uniform mean flows by applying a translation to wavenumbers into the lower half of the complex plane [50]. In practice, this modification corresponds to a Lorentz transformation by modifying the time coordinate $\tilde{t}$ in the PML:

$$\tilde{t}(x,t) = t - \frac{\mu_x}{\omega}\left(\tilde{x}(x) - x_{\text{int}}\right), \tag{4.26}$$

where μ_x is a constant correction coefficient. Since $\tilde{x}(x_{\text{int}}) = x_{\text{int}}$, the continuity of the time coordinate is verified at the interface: $\tilde{t}(x_{\text{int}}, t) = t$. This transformation has been generalised for non-uniform mean flows [131]. A detailed analytic study of the PML is performed in Section 4.4.3.

4.4.2 Weighted Residual Formulation

In the PML, the change of coordinates leads to a modification of the Linearised Euler Equations. However, the procedure to obtain the weighted residual formulation is identical to the one described in Section 4.1. The formulations in Cartesian coordinates and for an axisymmetric problem are presented hereafter.

PML Formulation in Cartesian Coordinates

In two dimensions, the space-time transformation in the PML converts the real coordinates (x, y, t) in the physical domain into the complex coordinates $(\tilde{x}, \tilde{y}, \tilde{t})$. The two-dimensional Linearised Euler Equations in the PML read:

$$j\omega \boldsymbol{q} + j\mu_x \boldsymbol{A}_x \boldsymbol{q} + \frac{1}{\gamma_x}\frac{\partial \boldsymbol{A}_x \boldsymbol{q}}{\partial x} + \frac{1}{\gamma_y}\frac{\partial \boldsymbol{A}_y \boldsymbol{q}}{\partial y} = \boldsymbol{0}. \tag{4.27}$$

The complex coordinates derivatives γ_{x_i} are defined by:

$$\gamma_{x_i} = \frac{\mathrm{d}\tilde{x}_i(x_i)}{\mathrm{d}x_i} = 1 + \frac{f'_{x_i}(x_i)}{jk_0}, \tag{4.28}$$

where f'_{x_i} is the derivative of f_{x_i} with respect to x_i ($x_i \equiv x$ or y). The weighted residual formulation follows:

$$\int_{\tilde{\Omega}} \left(\mathrm{j}\omega\gamma_x\gamma_y \boldsymbol{w}^{\mathrm{T}}\boldsymbol{q} + \mathrm{j}\gamma_x\gamma_y\mu_x \boldsymbol{w}^{\mathrm{T}}\boldsymbol{A}_x\boldsymbol{q} - \gamma_y \frac{\partial \boldsymbol{w}^{\mathrm{T}}}{\partial x}\boldsymbol{A}_x\boldsymbol{q} - \gamma_x \frac{\partial \boldsymbol{w}^{\mathrm{T}}}{\partial y}\boldsymbol{A}_y\boldsymbol{q} \right) \mathrm{d}x\mathrm{d}y = -\int_{\tilde{\Gamma}} \boldsymbol{w}^{\mathrm{T}} \left(\gamma_y n_x \boldsymbol{A}_x + \gamma_x n_y \boldsymbol{A}_y\right) \boldsymbol{q} \mathrm{d}\tilde{\Gamma}, \quad (4.29)$$

where $\tilde{\Omega}$ is the PML domain and $\tilde{\Gamma}$ its boundary. An infinitesimal element in the PML is such that: $\mathrm{d}\tilde{x}\mathrm{d}\tilde{y} = \gamma_x\gamma_y \mathrm{d}x\mathrm{d}y$, which justifies the integration with respect to the real coordinates. That formulation is actually a generalisation of Equation 4.2, since in the physical domain: $\gamma_{x_i} = 1$ and $\mu_x = 0$.

PML Formulation for an Axisymmetric Problem

For an axisymmetric problem, the space-time transformation in the PML converts the real coordinates (r, θ, x, t) in the physical domain into the complex coordinates $(\tilde{r}, \theta, \tilde{x}, \tilde{t})$. Note that the transformation does not apply to θ. Similarly, the axisymmetric Linearised Euler Equations in the PML read:

$$\mathrm{j}\omega\boldsymbol{q} + \mathrm{j}\mu_x\boldsymbol{A}_x\boldsymbol{q} + \frac{1}{\tilde{r}}\boldsymbol{A}_{\mathrm{c}}\boldsymbol{q} + \frac{1}{\tilde{r}}\frac{1}{\gamma_r}\frac{\partial \tilde{r}\boldsymbol{A}_r\boldsymbol{q}}{\partial r} - \mathrm{j}\frac{m}{\tilde{r}}\boldsymbol{A}_\theta\boldsymbol{q} + \frac{1}{\gamma_x}\frac{\partial \boldsymbol{A}_x\boldsymbol{q}}{\partial x} = \boldsymbol{0}. \quad (4.30)$$

The weighted residual formulation follows:

$$\int_{\tilde{\Omega}} \Big(\mathrm{j}\omega\tilde{r}\gamma_r\gamma_x \boldsymbol{w}^{\mathrm{T}}\boldsymbol{q} + \mathrm{j}\tilde{r}\gamma_r\gamma_x\mu_x \boldsymbol{w}^{\mathrm{T}}\boldsymbol{A}_x\boldsymbol{q} + \gamma_r\gamma_x \boldsymbol{w}^{\mathrm{T}}\boldsymbol{A}_{\mathrm{c}}\boldsymbol{q} - \mathrm{j}m\gamma_r\gamma_x \boldsymbol{w}^{\mathrm{T}}\boldsymbol{A}_\theta\boldsymbol{q} - \tilde{r}\gamma_x \frac{\partial \boldsymbol{w}^{\mathrm{T}}}{\partial r}\boldsymbol{A}_r\boldsymbol{q} - \tilde{r}\gamma_r \frac{\partial \boldsymbol{w}^{\mathrm{T}}}{\partial x}\boldsymbol{A}_x\boldsymbol{q} \Big) \mathrm{d}r\mathrm{d}x = -\int_{\tilde{\Gamma}} \tilde{r}\boldsymbol{w}^{\mathrm{T}} \left(\gamma_x n_r \boldsymbol{A}_r + \gamma_r n_x \boldsymbol{A}_x\right) \boldsymbol{q} \mathrm{d}\tilde{\Gamma}. \quad (4.31)$$

Generalisation of the PML for Mode Injection

The original purpose of the PML is to absorb outgoing waves. The PML is also suitable for injecting incident modes or analytic solutions into the computational domain. The advantage over the method of characteristics is that the reflected waves are absorbed regardless of the incidence angle. The principle lies in applying the PML equations to the reflected field only [57, 59]. Writing the total solution $\boldsymbol{q}$ as the sum of an incident field $\boldsymbol{q}_{\mathrm{i}}$ and of a reflected field $\boldsymbol{q}_{\mathrm{r}}$. The reflected field yields:

$$\boldsymbol{q}_{\mathrm{r}} = \boldsymbol{q} - \boldsymbol{q}_{\mathrm{i}}. \quad (4.32)$$

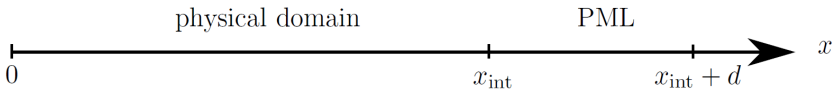

Figure 4.4: One-dimensional PML.

For example, the two-dimensional Linearised Euler Equations written in that 'active' PML read:

$$\mathrm{j}\omega\boldsymbol{q} + \mathrm{j}\mu_x\boldsymbol{A}_x\boldsymbol{q} + \frac{1}{\gamma_x}\frac{\partial\boldsymbol{A}_x\boldsymbol{q}}{\partial x} + \frac{1}{\gamma_y}\frac{\partial\boldsymbol{A}_y\boldsymbol{q}}{\partial y} = \mathrm{j}\omega\boldsymbol{q}_{\mathrm{i}} + \mathrm{j}\mu_x\boldsymbol{A}_x\boldsymbol{q}_{\mathrm{i}} + \frac{1}{\gamma_x}\frac{\partial\boldsymbol{A}_x\boldsymbol{q}_{\mathrm{i}}}{\partial x} + \frac{1}{\gamma_y}\frac{\partial\boldsymbol{A}_y\boldsymbol{q}_{\mathrm{i}}}{\partial y}. \quad (4.33)$$

The weighted residual formulation follows Equation 4.29. In that case, the right-hand side in the formulation contains a source term which is characterised by the incident field $\boldsymbol{q}_{\mathrm{i}}$.

4.4.3 Analytic Study

In this section, some insight is given on the PML behaviour. A simple one-dimensional analysis is first performed to better understand the absorption mechanisms. Then, a two-dimensional study is proposed.

One-Dimensional Perfectly Matched Layer

Let us consider a one-dimensional unbounded domain in the x-direction in which propagates an acoustic wave. The domain is truncated at x_{int} and a PML is applied between x_{int} and $x_{\text{int}} + d$ (see Figure 4.4). The one-dimensional Helmholtz equation for acoustic waves is obtained for the pressure field as the simplification of Equation 3.32 with $u_{0_x} = 0$:

$$c_0^2\frac{\mathrm{d}^2p}{\mathrm{d}x^2} + \omega^2 p = 0 \quad \forall x \in [0, x_{\text{int}}]. \quad (4.34)$$

Given the changes of variables in the PML (see Equation 4.24), this equation is similar in the PML:

$$c_0^2\frac{\mathrm{d}^2\tilde{p}}{\mathrm{d}\tilde{x}^2} + \omega^2\tilde{p} = 0 \quad \forall x \in [x_{\text{int}}, x_{\text{int}} + d]. \quad (4.35)$$

Considering waves propagating in the positive x-direction in the physical domain, the analytic solutions simplify to:

$$\begin{cases} p(x) &= A\mathrm{e}^{-\mathrm{j}k_0x} + B\mathrm{e}^{\mathrm{j}k_0x} & \forall x \in [0, x_{\text{int}}] \\ \tilde{p}(x) &= A\mathrm{e}^{-\mathrm{j}k_0\tilde{x}(x)} + B\mathrm{e}^{\mathrm{j}k_0\tilde{x}(x)} & \forall x \in [x_{\text{int}}, x_{\text{int}} + d] \end{cases}, \quad (4.36)$$

where A is the pressure field amplitude at $x = 0$ and B is the reflected wave amplitude. Since $\tilde{x}(x_{\text{int}}) = x_{\text{int}}$, the continuity of the solution holds at the interface. In practice, numerical solutions are not perfect and residual reflections are present at the PML outlet in $x = x_{\text{int}} + d$. At the PML outlet, we want the total pressure field to vanish, which provides B. It yields:

$$\tilde{p}(x) = A\left(\mathrm{e}^{-\mathrm{j}k_0 x - f_x(x)} - R\mathrm{e}^{\mathrm{j}k_0 x + f_x(x)}\right), \tag{4.37}$$

where $R = \mathrm{e}^{-2\mathrm{j}k_0(x_{\text{int}}+d)}\mathrm{e}^{-2f_x(x_{\text{int}}+d)}$ is the reflection coefficient at the PML outlet. These expressions highlight the first important feature of an efficient PML: a low-value reflection coefficient for minimising reflected waves amplitudes. The second significant aspect in designing the PML is related to its discretisation in the numerical model: an adequate stretching function is necessary for the numerical model to better approximate the solution in the PML. The first requirement indicates that $f_x(x_{\text{int}} + d)$ has to be very large in order to have $|R|$ small enough. Regarding the discrete PML, the second requirement calls for an optimal stretching function such that the profile of the solution in the PML is smooth enough to facilitate its approximation. Bermúdez *et al.* propose a logarithm function [170]:

$$f_x(x) = -\ln\left(1 - \frac{x - x_{\text{int}}}{d}\right). \tag{4.38}$$

This function verifies the different requirements previously set:

$$\begin{cases} f_x(x_{\text{int}}) = 0 \\ f_x(x_{\text{int}} + d) = +\infty \\ f_x'(x) > 0 \quad \forall x \in [x_{\text{int}}, x_{\text{int}} + d] \end{cases}, \tag{4.39}$$

such that it leads to $R = 0$. The pressure field in the PML is:

$$\tilde{p}(x) = A\mathrm{e}^{-\mathrm{j}k_0 x}\left(1 - \frac{x - x_{\text{int}}}{d}\right), \tag{4.40}$$

which induces a linear decay in the PML [171]. The complex exponential is responsible for additional oscillations in the PML, with the same wavelength characteristics as those encountered in the physical domain. These oscillations induce an additional source of error for the approximation of the solution in the PML. Therefore, we propose to cancel these oscillations by adding an imaginary part to the stretching function:

$$f_x^{\text{opt}} = -\ln\left(1 - \frac{x - x_{\text{int}}}{d}\right) - \mathrm{j}k_0\left(x - x_{\text{int}}\right). \tag{4.41}$$

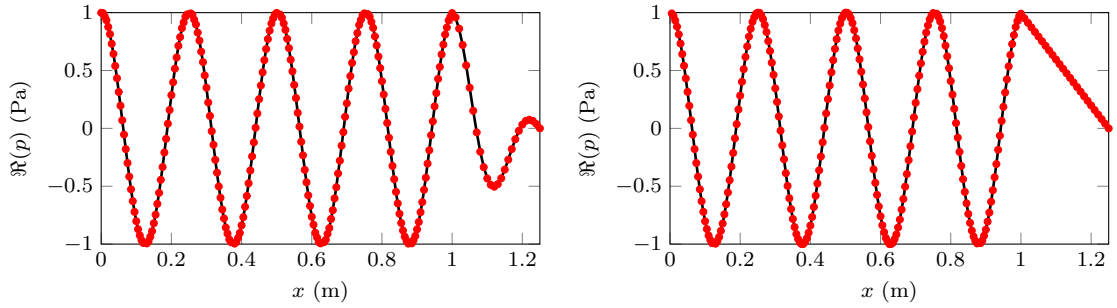

(a) Classical stretching function f_x.

(b) Optimal stretching function f_x^{opt}.

Figure 4.5: Absorption of a one-dimensional acoustic wave through a Perfectly Matched Layer. Black solid line: analytic solution. Red dots: numerical solution.

This new stretching function f_x^{opt} verifies the requirements 4.39 and is such that the pressure in the PML becomes:

$$\tilde{p}^{\text{opt}}(x) = A\mathrm{e}^{-\mathrm{j}k_0 x_{\text{int}}}\left(1 - \frac{x - x_{\text{int}}}{d}\right). \tag{4.42}$$

The natural oscillations in the PML vanish thanks to the imaginary part in the stretching function, while the linear decay behaviour is ensured by the real part. Figure 4.5 illustrates these results with a wave propagating in the physical domain and being damped in the PML for: $x_{\text{int}} = 1$, $d = 0.25$ and $k_0 = 25$. The analytic solution is compared to the numerical solution, for 200 discretisation elements in the physical domain and 25 in the PML (linear shape functions are used). In the left figure, the classical stretching function introduced in Equation 4.38 is used, while in the right figure, the optimal function defined in Equation 4.41 is used. Both stretching functions provide the expected results: they absorb the oscillating wave but, while f_x keeps the natural oscillations in the PML, f_x^{opt} cancels them out. In terms of accuracy, the Euclidean errors in the physical domain and in the PML are:

$$E_{\text{L}^2}^{\text{phys}} = \begin{cases} 0.23\% & \text{with } f_x \\ 0.096\% & \text{with } f_x^{\text{opt}} \end{cases} \quad \text{and} \quad E_{\text{L}^2}^{\text{PML}} = \begin{cases} 0.28\% & \text{with } f_x \\ 0.0036\% & \text{with } f_x^{\text{opt}} \end{cases}.$$

The two-dimensional Euclidean error is defined as:

$$E_{\text{L}^2} = \frac{\|p_{\text{n}} - p_{\text{a}}\|_{\text{L}^2}}{\|p_{\text{a}}\|_{\text{L}^2}} \tag{4.43}$$

where p_{n} is the numerical solution, p_{a} is the analytic solution and $\|p\|_{\text{L}^2} = \sqrt{\int_\Omega |p|^2 \mathrm{d}\Omega}$. These results show the improvement brought by the new stretching function. The proposed discrete PML becomes exact for plane waves of normal incidence. The state of the art function as proposed by Bermúdez *et al.*, is not, since it induces some reflections due

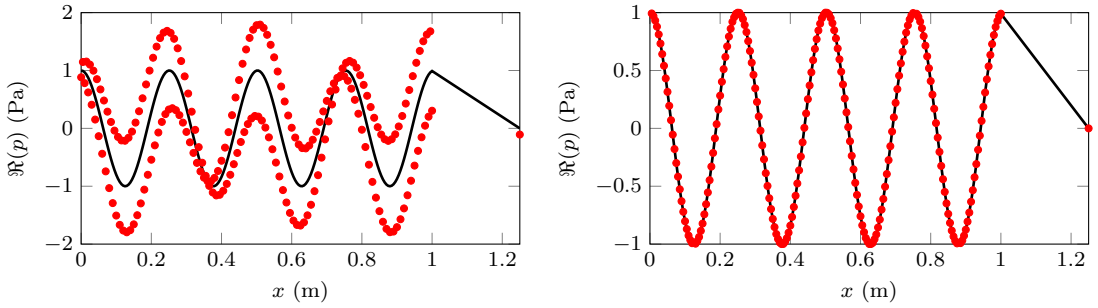

(a) Classical stretching function f_x.

(b) Optimal stretching function f_x^{opt}.

Figure 4.6: Absorption of a one-dimensional acoustic wave through a Perfectly Matched Layer, with one element in the damping region. Black solid line: analytic solution. Red dots: numerical solution.

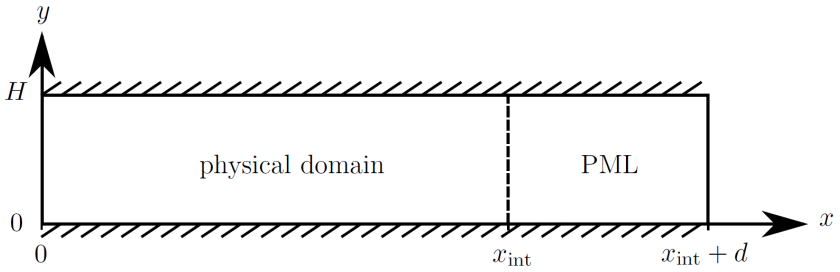

Figure 4.7: Two-dimensional PML.

to the additional oscillations in the layer.

Figure 4.6 shows the results with only one element in the PML. The numerical solution with the classical stretching function does not match the analytic solution. The PML is not able to absorb the outgoing wave which is reflected at the PML outlet and propagates back in the physical domain. By contrast, the proposed stretching function has the exact same accuracy as in the case with 25 elements in the PML. Note that for the classical stretching function, the numerical results become more and more accurate as the PML length is reduced. For $d \ll 1$, the pressure profile tends to a straight line [171].

An optimal stretching function which exactly absorbs propagating waves with normal incidence has been derived. This approach theoretically cancels interpolation errors in discrete PML. Let us now extend the one-dimensional investigation to a two-dimensional case.

Two-Dimensional Perfectly Matched Layer

We consider an infinite straight duct of height H in which waves propagate in the x-direction, carrying a uniform mean flow. After truncation, the physical domain extends for x from 0 to x_{int} and the Perfectly Matched Layer spreads over the length d. Figure 4.7 shows the problem configuration, which is a simplification in two dimensions of the rectangular cross-section duct studied in Section 3.3. In two dimensions, the convected

Helmholtz equation 3.32 holds considering that there is no z-coordinate. The coordinates $(\tilde{x}, \tilde{t})$ in the PML are defined in Equations 4.24 and 4.26. The domain truncation introduces spurious reflections at the PML outlet. For $y \in [0, H]$, the corresponding bounded solutions are:

$$\begin{cases} p(x,y) &= A\cos(k_y y)\left(\mathrm{e}^{-\mathrm{j}k_x^+ x} - R\mathrm{e}^{-\mathrm{j}k_x^- x}\right) & \forall x \in [0, x_{\text{int}}] \\ \tilde{p}(x,y) &= \tilde{A}\cos(k_y y)\mathrm{e}^{-\mathrm{j}\mu_x \tilde{x}(x)}\left(\mathrm{e}^{-\mathrm{j}k_x^+ \tilde{x}(x)} - R\mathrm{e}^{-\mathrm{j}k_x^- \tilde{x}(x)}\right) & \forall x \in [x_{\text{int}}, x_{\text{int}}+d] \end{cases}, \tag{4.44}$$

where the continuity of the solutions at the interface is such that $\tilde{A} = A\mathrm{e}^{\mathrm{j}\mu_x x_{\text{int}}}$. We recall the parameters introduced in previous sections: $k_y = m\pi/H$ for $m \in \mathbb{N}$ is the transverse wavenumber, μ_x is the correction coefficient introduced in the expression of $\tilde{t}$, and R is the reflection coefficient at the PML outlet.

The objective pursued here is to examine the behavior of the PML for guided propagation, more precisely, to examine the ability of the PML to absorb modes close to cut-on and evanescent waves.

Reflection Coefficient

Let us first focus on the reflection coefficient $R = \mathrm{e}^{-2\mathrm{j}K\tilde{x}(x_{\text{int}}+d)}$. It depends on the cut-off ratio K:

$$K = \begin{cases} \dfrac{\sqrt{k_0^2 - (1-M_x^2)\,k_y^2}}{1-M_x^2} & \text{for cut-on modes} \\ -\mathrm{j}\dfrac{\sqrt{(1-M_x^2)\,k_y^2 - k_0^2}}{1-M_x^2} & \text{for cut-off modes} \end{cases}. \tag{4.45}$$

K is a positive real number for propagating modes and purely complex imaginary for evenescent modes. This affects the reflection coefficient:

$$R = \begin{cases} \mathrm{e}^{-2\mathrm{j}K(x_{\text{int}}+d)} & \mathrm{e}^{-2\mathrm{j}\frac{K}{k_0}f_{x_\mathrm{i}}(x_{\text{int}}+d)} & \mathrm{e}^{-2\frac{K}{k_0}f_{x_\mathrm{r}}(x_{\text{int}}+d)} & \text{for cut-on modes} \\ \mathrm{e}^{-2\hat{K}(x_{\text{int}}+d)} & \mathrm{e}^{-2\frac{\hat{K}}{k_0}f_{x_\mathrm{i}}(x_{\text{int}}+d)} & \mathrm{e}^{2\mathrm{j}\frac{\hat{K}}{k_0}f_{x_\mathrm{r}}(x_{\text{int}}+d)} & \text{for cut-off modes} \end{cases}, \tag{4.46}$$

where $\hat{K} = -\Im(K) \in \mathbb{R}^+$. General stretching functions f_x, with real part f_{x_r} and imaginary part f_{x_i}, are considered. From these expressions, we can build conditions on the stretching function and on the domain size in order to limit reflections:

- For cut-on modes, $|R| = \mathrm{e}^{-2\frac{K}{k_0}f_{x_\mathrm{r}}(x_{\text{int}}+d)}$ and reflections are insignificant if $f_{x_\mathrm{r}}(x_{\text{int}} + d) \gg 1$.
- For cut-off modes, $|R| = \mathrm{e}^{-2\hat{K}(x_{\text{int}}+d)}\mathrm{e}^{-2\frac{\hat{K}}{k_0}f_{x_\mathrm{i}}(x_{\text{int}}+d)}$ and reflections are limited if

$f_{x_\mathrm{i}}(x_\mathrm{int}+d) \gg 1$, or if the domain and/or the PML are large enough.

Error Sources

Let us now consider the origins of error introduced through the PML. The relative difference between unbounded and bounded solution can be measured. The subsequent error $E^R_{\mathrm{L}^2}$ is called reflection or truncation error. We find:

$$E^R_{\mathrm{L}^2} = \left\{ \begin{array}{c} |R| \\ \mathrm{e}^{\hat{K}x_\mathrm{int}}|R| \end{array} \right. = \left\{ \begin{array}{cc} \mathrm{e}^{-2\frac{K}{k_0}f_{x_\mathrm{r}}(x_\mathrm{int}+d)} & \text{for cut-on modes} \\ \mathrm{e}^{-\hat{K}(x_\mathrm{int}+2d)}\mathrm{e}^{-2\frac{\hat{K}}{k_0}f_{x_\mathrm{i}}(x_\mathrm{int}+d)} & \text{for cut-off modes} \end{array} \right. . \tag{4.47}$$

This measure indicates the limit accuracy due to the domain truncation: the real part of the stretching function controls the error for cut-on modes, whereas the imaginary part of the stretching function as well as the domain dimensions (x_int and d) command the accuracy for cut-off modes. The conditions for minimising the truncation error are identical to those explained for reflections limitation in the previous paragraph. The second source of error is a discretisation error. The stretching functions should be designed in order to create smooth decays, which are easier to approximate and thereby lead to lower discretisation error. The combination of the truncation error with the discretisation error gives the total error introduced by the PML.

Solution Profile

Let us now have a closer look at the solution in the continuous PML, assuming that reflections are nonexistent. The pressure field expanded expression in the PML is of the form $\tilde{p}(x,y) = A\cos(k_y y)\mathrm{e}^{\mathrm{j}h_\mathrm{osc}(x)}\mathrm{e}^{h_\mathrm{env}(x)}$, where $h_\mathrm{osc}(x)$ and $h_\mathrm{env}(x)$ are functions representing the oscillatory behaviour and the envelope profile in the PML, respectively. They read:

$$\left\{ \begin{array}{rcl} h_\mathrm{osc}(x) & = & -\Im(k_x)\dfrac{f_{x_\mathrm{r}}(x)}{k_0} - (\mu_x + \Re(k_x))\left(x - x_\mathrm{int} + \dfrac{f_{x_\mathrm{i}}(x)}{k_0}\right) - \Re(k_x)x_\mathrm{int} \\ h_\mathrm{env}(x) & = & -(\mu_x + \Re(k_x))\dfrac{f_{x_\mathrm{r}}(x)}{k_0} + \Im(k_x)\left(x - x_\mathrm{int} + \dfrac{f_{x_\mathrm{i}}(x)}{k_0}\right) + \Im(k_x)x_\mathrm{int} \end{array} \right. . \tag{4.48}$$

It is clear from these expressions that the propagative and evanescent waves behave very differently in the PML. We recall the wavenumber for right-propagating acoustic modes:

$$k_x = -\frac{k_0 M_x}{1-M_x^2} + K. \tag{4.49}$$

Since $\mu_x + \Re(k_x) \geq 0$ in order to guarantee the absorption of the propagative modes in the PML, it yields:

$$\mu_x = \frac{k_0 M_x}{1 - M_x^2}, \tag{4.50}$$

which leads to $\mu_x + \Re(k_x) = \Re(K)$. This expression of μ_x is identical to the one proposed by Bécache *et al.* for treating inverse upstream modes [50].

We now propose expressions of f_{x_r} and f_{x_i} which provide an optimal solution in the PML, i.e. with no oscillations and with linear envelope. For cut-on modes, we choose:

$$\left\{ \begin{array}{rcc} f_{x_\mathrm{r}}(x) & = & -k_0 a_\mathrm{r} \ln\left(1 - \dfrac{x - x_\mathrm{int}}{d}\right) \\ f_{x_\mathrm{i}}(x) & = & -k_0 (x - x_\mathrm{int}) \end{array} \right. , \tag{4.51}$$

where a_r is a constant coefficient. By setting $a_\mathrm{r} = 1/K$, f_{x_r} is optimal and the pressure profile is exactly linear in the PML. But this choice depends on the mode order: there exists an optimal stretching function for each cut-on mode. The choice of f_{x_i} cancels out oscillations in the direction of propagation.

For cut-off modes, an optimal choice would be:

$$\left\{ \begin{array}{rcc} f_{x_\mathrm{r}}(x) & = & 0 \\ f_{x_\mathrm{i}}(x) & = & -k_0 (x - x_\mathrm{int}) - k_0 a_\mathrm{i} \ln\left(1 - \dfrac{x - x_\mathrm{int}}{d}\right) \end{array} \right. , \tag{4.52}$$

where a_i is a constant coefficient. Choosing $a_\mathrm{i} = 1/\hat{K}$ theoretically gives the optimal choice for the absorption of evanescent waves, with linear profile and no oscillations in the PML. However, such choice is in contradiction with the stretching functions expressed for cut-on modes in Equation 4.51.

These two examples demonstrate that it is analytically possible to find optimal stretching functions that provide a linear decay and that cancel out axial oscillations in the PML. However, this choice is mode-order dependent and besides, the choice of the optimal stretching function for the evanescent and propagating case is rather contradictory. An intermediate choice should therefore be found. In the rest of our study, unless otherwise stated, the classical Perfectly Matched Layer will be used, i.e. applying the stretching function introduced by Bermúdez *et al.* [170] and the correction coefficient of Bécache *et al.* [50] for inverse upstream modes absorption:

$$\left\{ \begin{array}{rcc} f_x(x) & = & -\ln\left(1 - \dfrac{x - x_\mathrm{int}}{d}\right) \\ \mu_x & = & \dfrac{k_0 M_x}{1 - M_x^2} \end{array} \right. . \tag{4.53}$$

Chapter 5

Verification Results

In this chapter, numerical results are presented for two-dimensional simple test cases in order to verify the high-order finite element model solving the Linearised Euler Equations. The computed solutions are compared with the reference solutions described in Chapter 3. The model performance is studied through solution convergence by means of mesh refinement, increase of shape functions polynomial order and frequency change. The mean flow velocity effects are also considered. A discussion on performance assessment quantities is first performed. The results for plane wave propagation in free field are then presented. Acoustic, vorticity and entropy waves propagation in duct is assessed for high-order modes. The implementation of the Perfectly Matched Layer is also verified.

5.1 Performance Assessment Quantities

As discussed in Section 2.6 of the literature review, numerical accuracy is a global notion that encompasses many different error sources: geometry description, mean flow interpolation, non-reflecting boundary conditions, dispersion and interpolation errors, and acoustic sources description. In addition, several parameters can assess the cost of a numerical model: computational time, memory usage, condition number and number of degrees of freedom per wavelength, among others. These aspects are described in the following sections and the parameters used to evaluate them are introduced.

5.1.1 Numerical Error

In this chapter, the test cases involve simple squared geometries. This allows the geometry to be exactly represented by standard linear triangular or quadrangular elements. In terms of medium properties, the mean flow is uniform in the first two test cases and the mean flow interpolation is exact. On the contrary, a non-uniform mean flow velocity is considered in Section 5.3.2: the mean flow interpolation accuracy is shown to have an impact on the numerical solution.

The physical domain truncation is also a potential source of error for unbounded problems, since it may create spurious reflections inside the computational domain. For this verification, characteristic boundary conditions (see Section 4.2) are used to ensure that outgoing waves leave the computational domain without generating significant reflections. The validation of Perfectly Matched Layer absorbing boundary conditions is also examined in Section 5.4.

The discretisation itself introduces additional numerical errors, as explained in Section 2.6. The numerical wavenumber differs from the exact wavenumber. The difference between these wavenumbers results in the global dispersion error, which accumulates along the computational domain contributing to the so-called pollution effect. Mesh refinement and/or polynomial order increase may reduce this effect (h- and p-refinements). The dispersion error increases with the frequency. The second numerical error is the interpolation error, which represents the asymptotic behaviour of the numerical error.

In practice, for each variable χ of the solution vector $\boldsymbol{q}$, several error measures E between the numerical solution χ_n and the reference solution χ_a are used:

$$E = \frac{\|\chi_\mathrm{n} - \chi_\mathrm{a}\|}{\|\chi_\mathrm{a}\|}. \tag{5.1}$$

- The Euclidean error E_{L^2} is based on the L^2-norm over the computational domain, such that:

$$\|\chi\|_{\mathrm{L}^2} = \sqrt{\int_\Omega |\chi|^2 \,\mathrm{d}\Omega}. \tag{5.2}$$

- The Sobolev-like error E_{H^1} is based on the H^1-norm over the computational domain and involves the solution gradient. It reads:

$$\|\chi\|_{\mathrm{H}^1} = \sqrt{\int_\Omega k_0^2 |\chi|^2 + |\boldsymbol{\nabla}\chi|^2 \,\mathrm{d}\Omega}. \tag{5.3}$$

5.1.2 Performance Measures

Some more parameters are introduced to evaluate the numerical method efficiency. The condition number κ gives some indication on the stability of the final linear system given in Equation 4.19: $\boldsymbol{K}\boldsymbol{d} = \boldsymbol{f}$. It indicates how much a small change of the input $\boldsymbol{f}$ in the system will affect the numerical solution $\boldsymbol{d}$. Low condition numbers characterise well-conditioned problems, whereas ill-conditioned problems have high condition numbers. The condition number is measured on the sparse system matrix $\boldsymbol{K}$:

$$\kappa = \|\boldsymbol{K}\|_{\mathrm{L}^1} \|\boldsymbol{K}^{-1}\|_{\mathrm{L}^1}, \tag{5.4}$$

where the L^1-norm is such that $\|\boldsymbol{K}\|_{\mathrm{L}^1} = \max_j \left(\sum_i |K_{i,j}|\right)$, i and j being the rows and columns of the matrix $\boldsymbol{K}$ respectively [172].

The sparsity of $\boldsymbol{K}$ is another indicator of the computational performance. The number of non-zero entries (noted $\mathrm{nnz}_{\boldsymbol{K}}$) quantifies the matrix sparsity, which is directly correlated with the memory usage to store the matrix. The linear system is solved with the multifrontal massively parallel sparse direct solver MUMPS [173], which provides indicative factorisation and total computational times.

The numerical resolution is characterised by the number of degrees of freedom per wavelength d_λ. That parameter indicates the density of information used to describe one wavelength [174]. It accounts for both the characteristic mesh size and the polynomial order:

$$d_\lambda = \lambda \frac{\sqrt{n_{\mathrm{dof}}} - 1}{\sqrt{S_\Omega}}, \tag{5.5}$$

where $\lambda = 2\pi/k_x$ is the wavelength, n_{dof} is the total number of degrees of freedom and S_Ω is the area of the computational domain Ω. Another definition of that number explicitly expresses d_{λ_a} as a function of h and p, and considers the shortest acoustic wavelength induced by the mean flow [107]:

$$d_{\lambda_\mathrm{a}} = 2\pi \frac{c_0 - u_0}{\omega} \frac{p}{h}. \tag{5.6}$$

That definition is convenient since, in practical problems, upstream and downstream waves may propagate, and a proper mesh grid should be able to resolve both waves. In this way, aliasing issues are also avoided [51].

A few input parameters are varied in order to evaluate their effects on the aforementioned

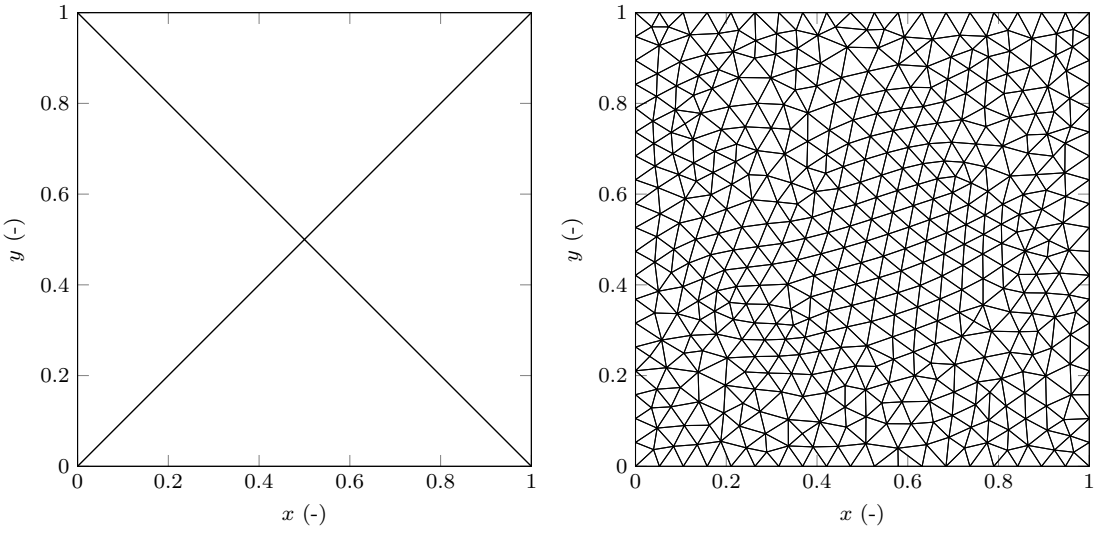

(a) Coarse mesh ($h = 0.5$). (b) Fine mesh ($h = 0.05$).

Figure 5.1: Unstructured triangular meshes.

output performance quantities. The characteristic mesh size h and the angular frequency ω define the number of elements per wavelength. The polynomial order p increases the model accuracy. The mean flow velocity u_0 also affects the numerical results. Depending on the test case, the effects of the wave direction with respect to the mean flow velocity direction (expressed through the angle $\alpha - \alpha_0$) and of the duct mode m are also studied.

5.2 Plane Wave in Free Field

This section focuses on plane wave propagation in free field. The test case is described in Section 3.2: a plane wave of wavenumber $\boldsymbol{k}$ propagates in free field with a direction α. The background flow is characterised by its velocity vector $\boldsymbol{u}_0$ and its direction α_0. Figure 3.1 summarises this configuration. The fluid properties are non-dimensional and equal to one.

5.2.1 Numerical Setup

The numerical simulations use a two-dimensional computational domain Ω of length L and height H. In this study, a unit squared domain is considered: $L = H = 1$. The domain is discretised with unstructured triangular elements. Figure 5.1 shows two examples of coarse mesh and fine mesh, which respective characteristic mesh sizes h are 0.5 and 0.05. Characteristic boundary conditions enforce the plane wave analytic solution along the domain outer limits, as described in Section 4.2. Note that although only acoustic plane

waves are considered in this section, similar results and conclusions could be drawn for vorticity and entropy waves.

5.2.2 Numerical Results

Several inputs may affect the numerical results: the wave angular frequency ω, the mesh size h, the polynomial order p, the mean flow velocity u_0 and the relative wave direction with respect to the mean flow direction $\alpha - \alpha_0$. These parameters are varied in order to produce performance plots.

No Mean Flow Case

At a first stage, acoustic plane waves propagate in a medium at rest ($u_0 = 0$). Some figures compare the error measures E_{L^2} and E_{H^1} on the four variables (ρ, ρu_x, ρu_y, p_c). The wave angle effects are discussed, as well as the resolution parameters impact (h, p, d_{λ_a}) on these errors and on the performance quantities (κ, $\mathrm{nnz}_{\boldsymbol{K}}$).

Comparison of Error Measures

A first comparison of the errors introduced in Section 5.1.1 is performed. An acoustic plane wave propagates with an angle $\alpha = 60°$ in a medium at rest. The errors on each variable are measured for $h = 0.5$. The number of degrees of freedom per shortest acoustic wavelength d_{λ_a} is varied from 2 to 100. Figure 5.2 represents the L^2- and H^1-norm errors against d_{λ_a} for each variable. The curves are shown for $p = 1$ and 2. Three different regimes are identified: a very-low resolution regime where the problem is numerically under-resolved ($d_{\lambda_\mathrm{a}} < 5$), an intermediate regime where the dispersion error dominates ($5 < d_{\lambda_\mathrm{a}} < 10$), and an asymptotic high-resolution regime where the interpolation error prevails ($d_{\lambda_\mathrm{a}} > 10$). The L^2-norm error is lower than the H^1-norm error, which converges with one order less than the L^2-norm error. The Linearised Euler Equations indicate that the velocity field depends on the pressure gradient. For instance, without mean flow the velocity relates to the pressure by:

$$\mathrm{j}\omega\boldsymbol{u} = \frac{1}{\rho_0}\boldsymbol{\nabla} p. \tag{5.7}$$

In the following, the L^2-norm is considered, unless otherwise stated.

Wave Angle Effects

The wave direction effects are now checked. Figure 5.3 represents the L^2-norm error against

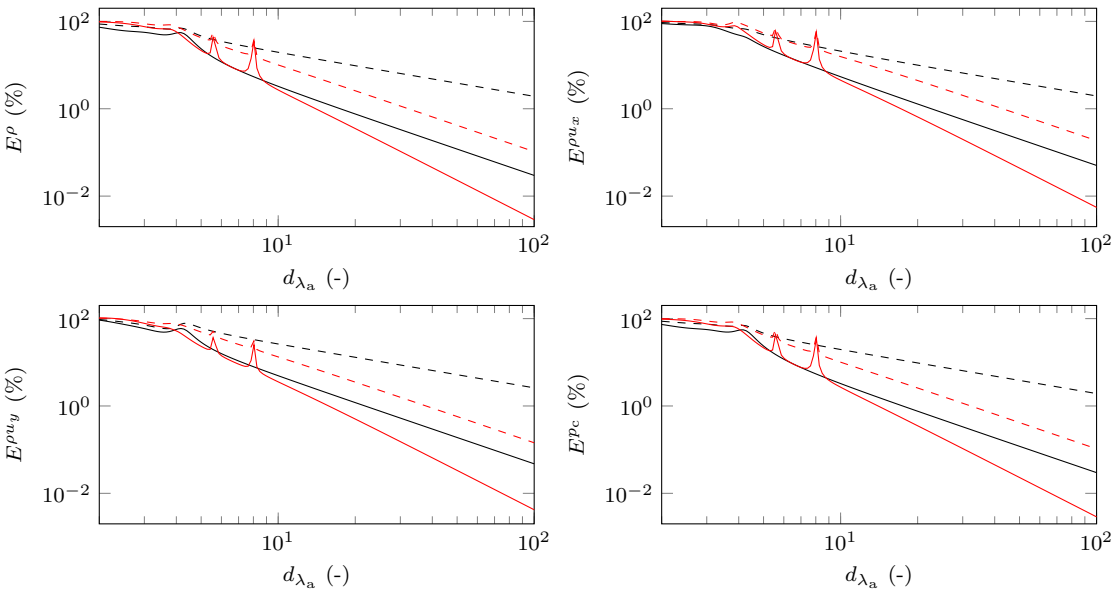

Figure 5.2: Error measures against the number of degrees of freedom per shortest acoustic wavelength, for an acoustic plane wave in free field. $h = 0.5$, $\alpha = 60°$, $u_0 = 0$. Black: $p = 1$. Red: $p = 2$. Solid line: E_{L^2}. Dashed line: E_{H^1}. Top left: ρ. Top right: ρu_x. Bottom left: ρu_y. Bottom right: p_c.

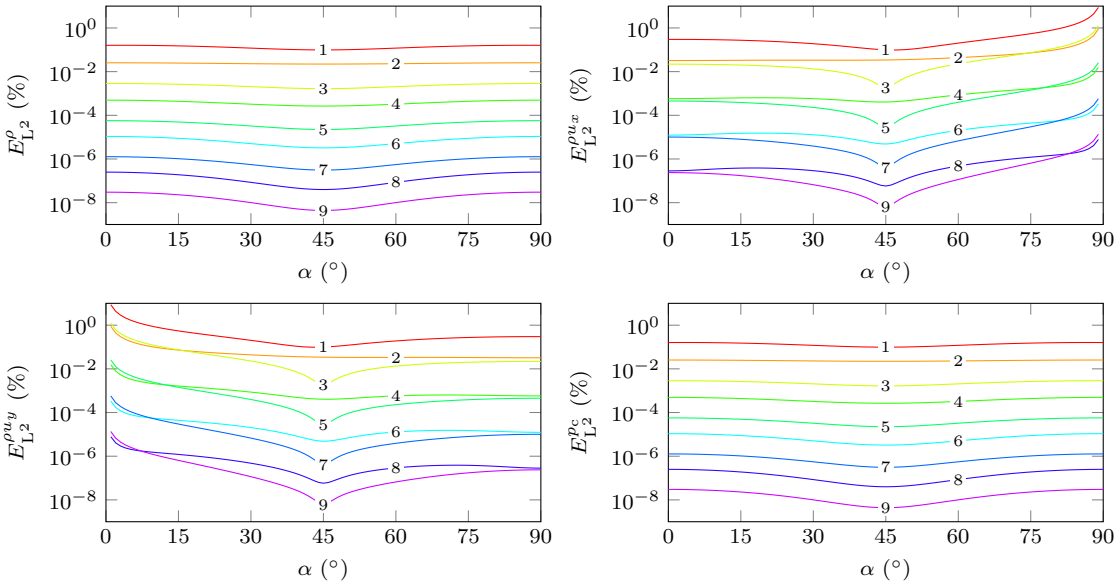

Figure 5.3: L^2-norm error against the wave direction, for an acoustic plane wave in free field. $h = 0.5$, $d_{\lambda_a} = 50$, $u_0 = 0$, $p \in \{1, \cdots, 9\}$. Top left: ρ. Top right: ρu_x. Bottom left: ρu_y. Bottom right: p_c.

the wave direction α for each variable. Because of the problem symmetry, the study is limited to values of α between 0° and 90°. The number of degrees of freedom per shortest acoustic wavelength is chosen large enough to be in the asymptotic high-resolution regime: $d_{\lambda_a} = 50$. The curves are shown for p from 1 to 9. The anisotropic behaviour of the density/pressure differs from the one of the momentum. For the density/pressure, a symmetric behaviour is observed: the lowest error is reached for $\alpha = 45°$, and the error increases to attain its maximum value at $\alpha = 0°$ and 90°. Incrementing p lowers the error

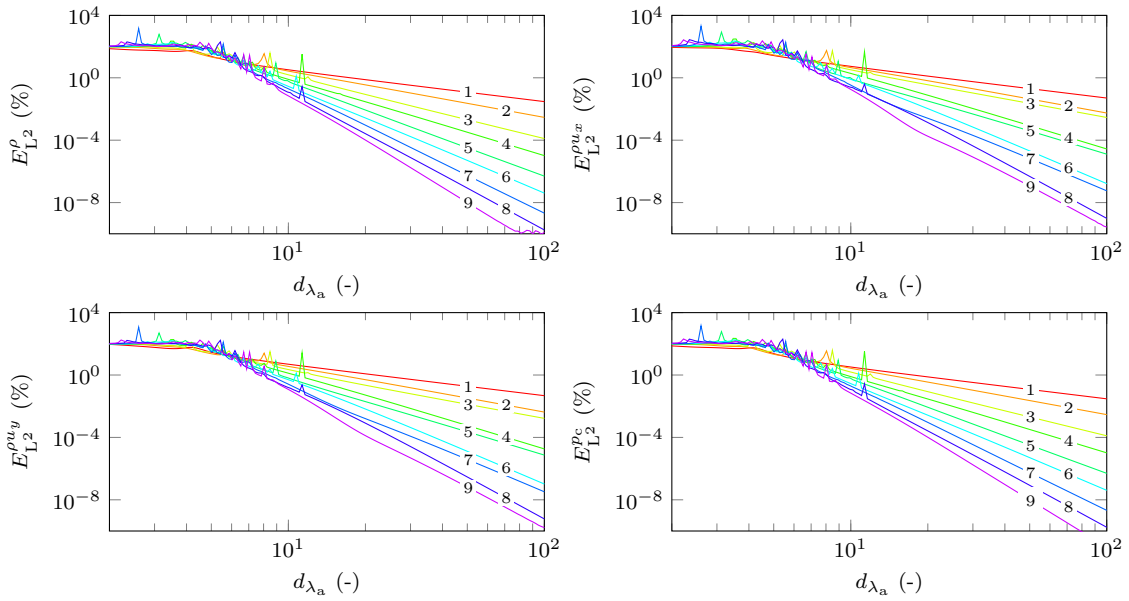

Figure 5.4: L^2-norm error against the number of degrees of freedom per shortest acoustic wavelength, for an acoustic plane wave in free field. $h = 0.5$, $\alpha = 60°$, $u_0 = 0$, $p \in \{1, \cdots, 9\}$. Top left: ρ. Top right: ρu_x. Bottom left: ρu_y. Bottom right: p_c.

level and maintains the same wave direction effects. For the momentum, the smallest error is also reached for $\alpha = 45°$. In the x-direction, the error increases faster for $\alpha > 45°$ than for $\alpha < 45°$. In the y-direction, the situation is reversed. That can be explained by the wave direction which favours one momentum component, depending on the values of $\cos\alpha$ and $\sin\alpha$. Another observation relates to the polynomial order: close to normal directions to the domain ($\alpha = 0°$ and $90°$), incrementing p to $p+1$ (with p even number) does not significantly improve the numerical accuracy.

Polynomial Order Effects

The L^2-norm error is plotted against d_{λ_a}, for each variable, and for polynomial orders from 1 to 9. The results are shown in Figure 5.4. The asymptotic performance gives details on the numerical model convergence: for the density/pressure, the errors behave like $O\left(d_{\lambda_a}^{-(p+1)}\right)$ as expected from the finite element theory described in Section 2.6 [89, 105]. Note that here these two variables relate like $p = c_0^2\rho$ and the errors on those variables are identical. For the momentum, the situation is more complex. Linear shape functions provide an identical behaviour to the density/pressure one. For high-order polynomials, the performance depends on the polynomial order parity. Even orders ($p \geq 2$) follow the same $O\left(d_{\lambda_a}^{-(p+1)}\right)$ rule, with an error level sightly higher than the density/pressure error. However, odd orders ($p \geq 3$) converge in $O\left(d_{\lambda_a}^{-p}\right)$: the high-order finite element looses one accuracy order on the momentum interpolation for odd orders. In terms of performance

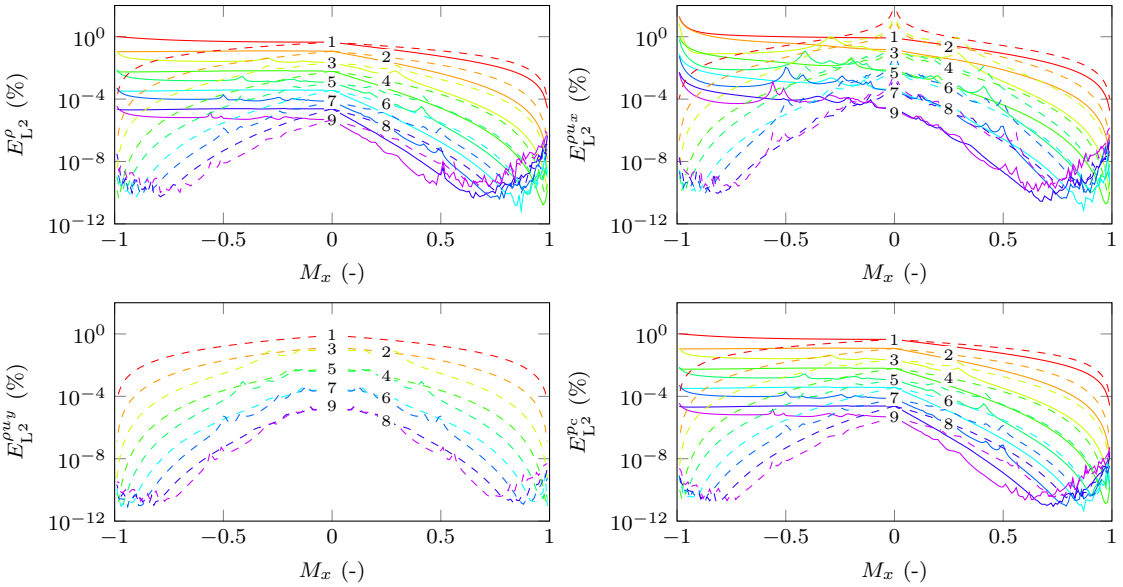

Figure 5.5: L^2-norm error against the mean flow Mach number, for an acoustic plane wave in free field. $h = 0.5$, $d_{\lambda_\mathrm{a}} = 30$, $\alpha_0 = 0°$ or $180°$, $p \in \{1, \cdots, 9\}$. Solid line: $\alpha = 0°$. Dashed line: $\alpha = 90°$. Top left: ρ. Top right: ρu_x. Bottom left: ρu_y. Bottom right: p_c.

of the high-order model, let us compare the resolution needed to obtain a 0.1% L^2-norm error on the density. For linear shape functions, about 55 degrees of freedom per shortest acoustic wavelength are necessary to reach that accuracy, whereas only 10 are sufficient for $p = 9$.

Mean Flow Case

In this paragraph, mean flow effects are considered. At first, the mean flow velocity is varied for a fixed flow direction. Then, the mean flow velocity is fixed and the impact of the flow orientation is assessed.

Mean Flow Velocity Effects

The number of degrees of freedom per shortest acoustic wavelength is fixed to $d_{\lambda_\mathrm{a}} = 30$, which is large enough to guarantee errors lower than 10%. Plane waves of directions $\alpha = 0°$ and $90°$ are studied. The flow direction is either $\alpha_0 = 0°$ or $180°$, which gives $\boldsymbol{u}_0 = u_0\{\pm 1, 0\}^\mathrm{t}$. This means that the wave propagation is downstream/upstream for $\alpha = 0°$, and orthogonal to the mean flow direction for $\alpha = 90°$. Figure 5.5 represents the L^2-norm error against the mean flow Mach number $M_x = u_{0_x}/c_0$ for each variable. For the density/pressure, the mean flow velocity effects on the error are stronger downstream than upstream for a propagation in the flow direction (see solid lines): the longer wavelength makes the error decrease significantly, whereas the shorter wavelength slightly affects the error. For an orthogonal propagation (see dashed lines), the results are symmetric since the

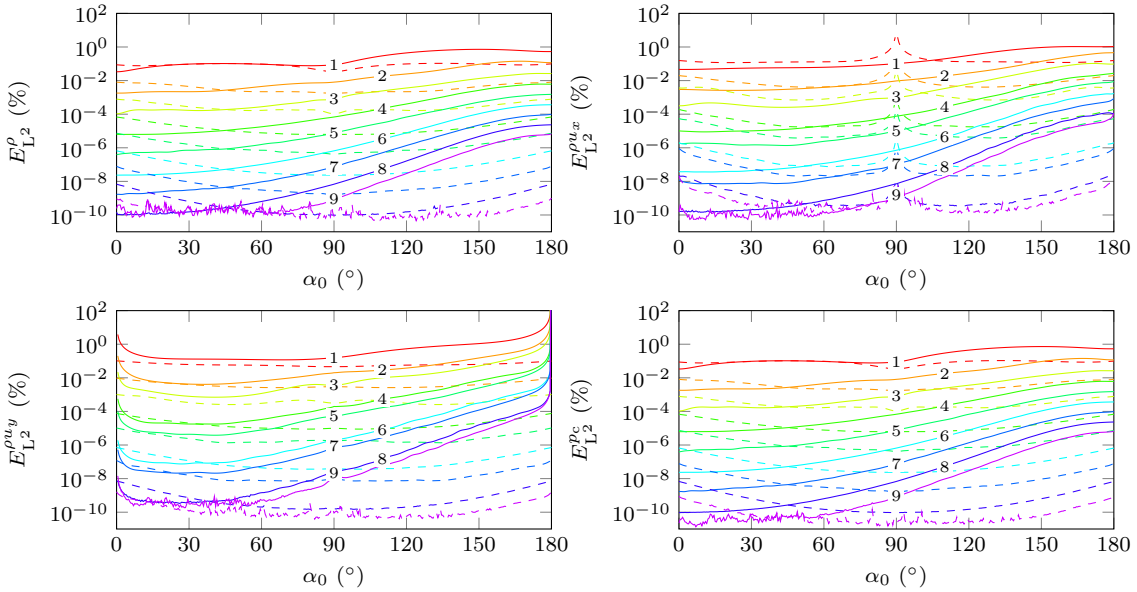

Figure 5.6: L^2-norm error against the mean flow direction, for an acoustic plane wave in free field. $h = 0.5$, $d_{\lambda_a} = 30$, $u_0 = 0.6c_0$, $p \in \{1, \cdots, 9\}$. Solid line: $\alpha = 0°$. Dashed line: $\alpha = 90°$. Top left: ρ. Top right: ρu_x. Bottom left: ρu_y. Bottom right: p_c.

wavenumber k_a is identical for $\alpha_0 = 0°$ and 180°: $k_a = \omega/(c_0 + u_0 \cos(\alpha - \alpha_0)) = \omega/(c_0 + u_0)$ with $\alpha = 90°$. The error decreases when the mean flow velocity increases. Regarding the momentum, the mean flow velocity effects are more complex. For $\alpha = 0°$, the momentum y-component is zero and the influence is seen on the x-momentum which error decreases when the Mach number M_x increases from -1 to 1. The error declines faster for downstream propagation. For an orthogonal propagation ($\alpha = 90°$), the symmetry observed on the density/pressure is also verified on the momentum and the error decreases with a mean flow velocity rise. However, the polynomial order impact is not as obvious: an increment of p to $p + 1$ (p even) does not improve the error for mean flow velocities in a range of values around zero. That range increases with the order. This behaviour is not observed on the density/pressure. The spurious oscillations observed for orders 8 and 9 at very low error indicate that the machine precision has been reached.

Mean Flow Direction Effects

Let us now observe the mean flow direction effects. The mean flow velocity is fixed to $u_0 = 0.6c_0$. The flow angle varies from 0 to 180°. Plane waves of directions $\alpha = 0°$ and 90° are considered. Figure 5.6 shows the L^2-norm error against the flow direction α_0 for each variable. For the right-propagating wave ($\alpha = 0°$), an increase of the mean flow angle amplifies the errors, especially for $\alpha_0 > 90°$ which corresponds to upstream propagation. For the y-propagating wave ($\alpha = 90°$), the error levels are symmetric around $\alpha_0 = 90°$.

The error increases as the flow tends to be orthogonal to the wave propagation ($\alpha_0 = 0°$ or 180°).

5.3 Duct Problem

In this section, the second verification test case is introduced. It considers the wave propagation in infinite two-dimensional straight ducts in the presence of axial mean flow. The computational domain is identical to the one described in Section 5.2.1 for plane wave propagation in free field (length $L = 1$, height $H = 1$, unstructured triangular mesh). Hard wall boundary conditions are enforced to characterise duct walls, at $y = 0$ and H. Characteristics boundary conditions enforce duct modes at $x = 0$, and close the problem at $x = L$. Numerical results are presented first for uniform mean flows, and then for non-uniform mean flows. The comparison is performed with the reference results given in Sections 3.3 and 3.4.

5.3.1 Uniform Mean Flow

The characteristic mesh size h is varied between 0.01 and 0.5. Acoustic and vorticity modes are propagated (results for entropy modes are not shown since they are similar to vorticity modes). The uniform mean flow Mach number is fixed to $M_x = u_{0_x}/c_0 = 0.6$. The mode order effects are assessed.

Acoustic Modes

The first five acoustic duct modes (m from 0 to 4) are propagated at a frequency such that $k_0 = 10$. The modes 0 to 3 are cut-on, whereas the mode 4 is cut-off. A characteristic mesh size Helmholtz number is defined by $k_0 h$. Figure 5.7 shows the L^2-norm error against the Helmholtz number for each variable, with $p = 3$. For each mode, numerical convergence is observed by mesh refinement. Increasing the mode order makes the error rise: although the axial wavenumber k_x decreases, the transverse wavenumber k_y grows with m. That causes a loss of accuracy in the transverse direction. The y-momentum is zero for the acoustic plane wave, since the mean flow velocity is only in the x-direction.

Vorticity Modes

Vorticity modes are now investigated. The characteristic mesh size is fixed to $h = 0.25$

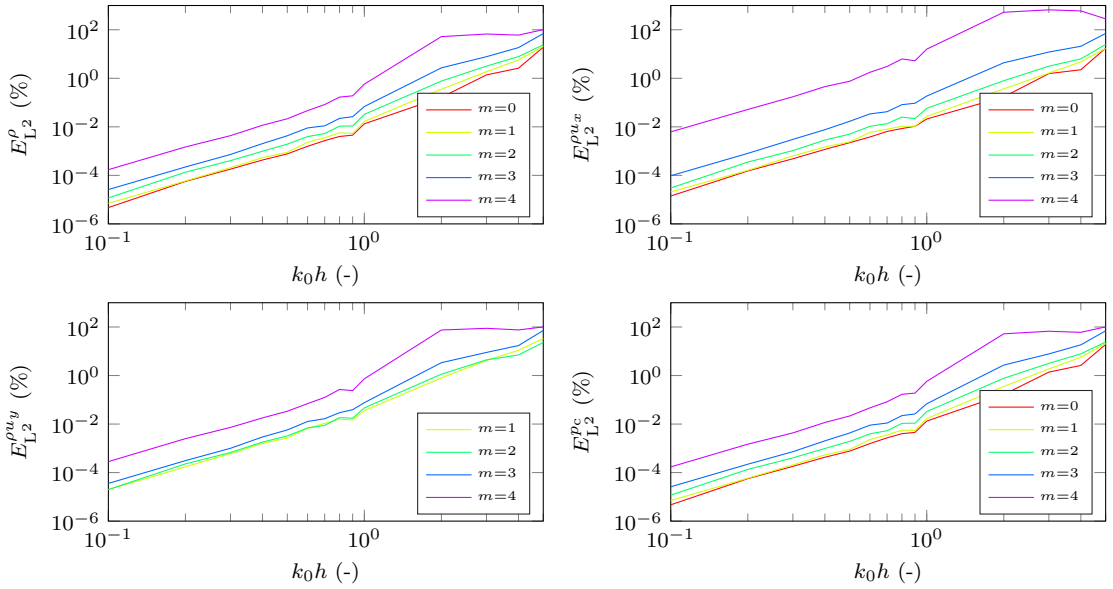

Figure 5.7: L^2-norm error against the characteristic mesh size Helmholtz number, for acoustic duct modes with uniform mean flow. $k_0 = 10$, $M_x = 0.6$, $m \in \{0, \cdots, 4\}$, $p = 3$. Top left: ρ. Top right: ρu_x. Bottom left: ρu_y. Bottom right: p_c.

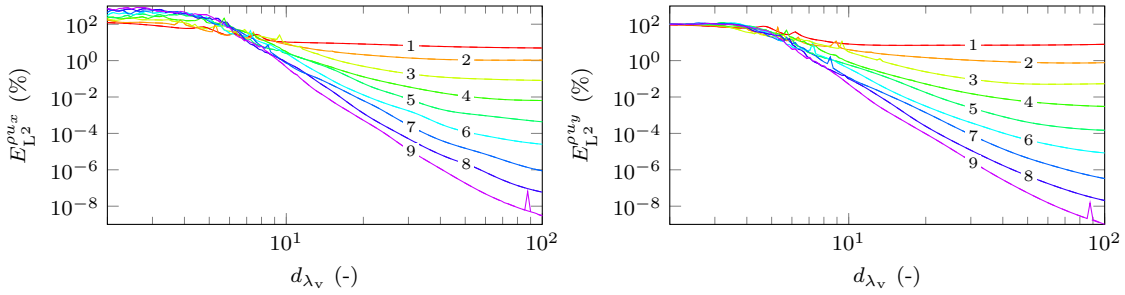

Figure 5.8: L^2-norm error against the number of degrees of freedom per hydrodynamic wavelength, for vorticity duct modes with uniform mean flow. $h = 0.25$, $M_x = 0.6$, $m = 1$. Left: ρu_x. Right: ρu_y.

and the polynomial order varies from 1 to 9. Only the velocity carries information from hydrodynamic modes. Results are shown for the first two modes: Figure 5.8 shows the L^2-norm error on the momentum against the number of degrees of freedom per hydrodynamic wavelength d_{λ_v}. This number is an adaptation of d_{λ_a} to vorticity waves. Let us define:

$$d_{\lambda_v} = 2\pi \frac{|u_{0_x}|}{\omega} \frac{p}{h}. \tag{5.8}$$

On the error plots, the three regimes previously introduced are still visible: the under-resolved region in low-resolution regime ($d_{\lambda_v} < 5$), the intermediate zone where the dispersion error dominates ($5 < d_{\lambda_v} < 10$) and the high-resolution regime governed by the interpolation error ($d_{\lambda_v} > 10$). An error level stagnation is observed after the asymptotic range for high values of d_{λ_v}. The convergence rate in the asymptotic regime is of order p. The condition number κ (see Equation 5.4) and the number of non-zeros $\mathrm{nnz}_{\boldsymbol{K}}$ intro-

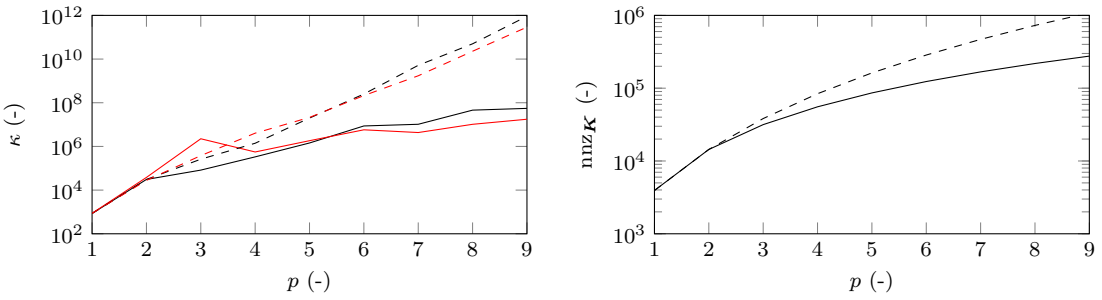

Figure 5.9: Condition number and number of non-zeros against the polynomial order, for vorticity duct modes with uniform mean flow. $h = 0.25$, $M_x = 0.6$, $m = 1$. Black: $d_{\lambda_\mathrm{v}} = 2$. Red: $d_{\lambda_\mathrm{v}} = 100$. Solid line: with condensation. Dashed line: without condensation. Left: κ. Right: $\mathrm{nnz}_{\boldsymbol{K}}$.

duced in Section 5.1.2 are displayed in Figure 5.9. Regarding the system conditioning, it increases with p. Without condensation (dashed curves), the condition number behaves like $\kappa \approx 10^p$. Numerical condensation effects (solid curves) are visible for $p \geq 3$, since bubble functions are present only for these polynomial orders: the condition number is decreased, up to a factor 1.5×10^4 for $p = 9$. The number of degrees of freedom does not have much influence on κ: its values are very similar for $d_{\lambda_\mathrm{v}} = 2$ and 100. Concerning the number of non-zeros in the system matrix, a quadratic dependency is found with p in the presence of condensation in the model: $\mathrm{nnz}_{\boldsymbol{K}} \approx p^2$. Without condensation, the number of non-zeros is higher considering that the numerical model accounts for the internal degrees of freedom. $\mathrm{nnz}_{\boldsymbol{K}}$ does not depend on d_{λ_v}.

5.3.2 Non-Uniform Mean Flow

Non-uniform mean flow effects are now investigated for the two-dimensional infinite straight duct. Linear and parabolic variations of the mean flow velocity are considered in the transverse direction, as introduced in Section 3.4. The velocity is uniform in the x-direction. Only the first acoustic mode is studied. The standard wavenumber is $k_0 = 10$ and the mean flow Mach number maximum value is 0.5.

Figure 5.10 shows the L^2-norm error against the shape functions polynomial order, for each variable. The mesh size is $h = 0.25$. The black and red curves show the results with exact mean flow values in the numerical model for the linear and parabolic flow profiles, respectively. The convergence is nearly of order p: $E_{\mathrm{L}^2} \approx 10^{-p}$. One critical point when dealing with non-uniform mean flows is the mean flow interpolation strategy. For realistic applications, the mean flow data used for acoustic simulations are obtained from separate procedures, by means of measurements, steady Euler computations or RANS

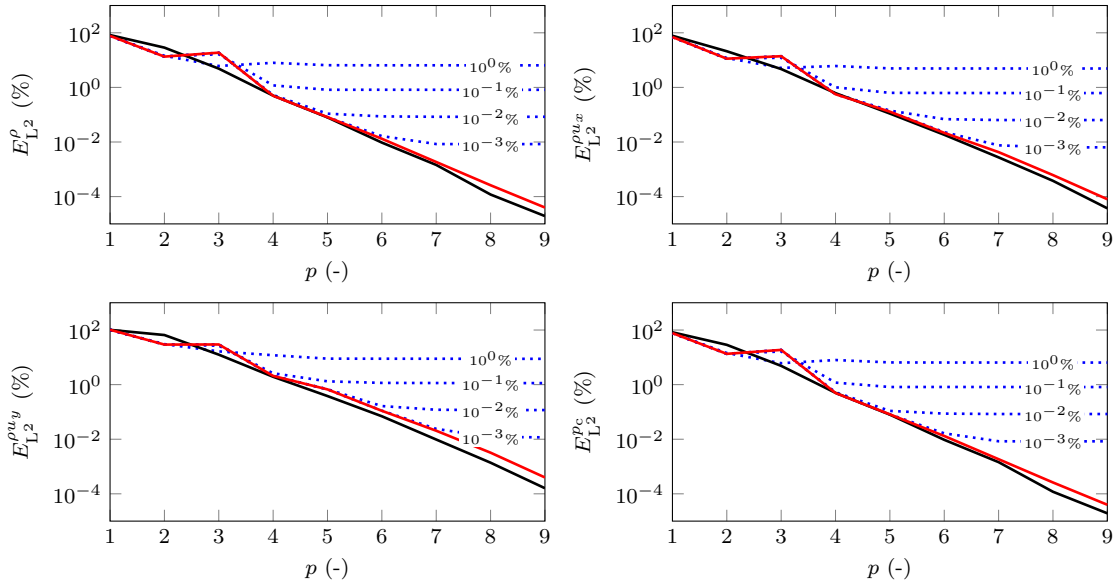

Figure 5.10: L^2-norm error against the polynomial order, for acoustic duct modes with non-uniform mean flow. $h = 0.25$, $M_x = 0.5$, $m = 0$. Black: linear profile. Red: parabolic profile. Solid line: exact mean flow. Dotted blue line: error on mean flow interpolation, for parabolic profile. Top left: ρ. Top right: ρu_x. Bottom left: ρu_y. Bottom right: p_c.

(Reynolds-Averaged Navier-Stokes) simulations for instance. The mean flow values are then interpolated on the acoustic mesh for the acoustic simulation, which may introduce some error. Regarding the linear flow profile, no additional error is introduced since the numerical model is able to exactly interpolate the mean flow. For the parabolic flow profile, the mean flow interpolation effect is evaluated by considering an inaccurate mean flow velocity value at each integration point of the numerical procedure. The corresponding numerical results are shown for relative errors with the exact mean flow velocity of 1, 0.1, 0.01 and 0.001%, on the dotted blue curves. Each numerical error on the mean flow interpolation introduces a stagnation in the error convergence of about one order of magnitude higher than the mean flow velocity error. This result highlights the importance of an accurate mean flow description in order to obtain valid numerical results [175].

5.4 Perfectly Matched Layer

The numerical model has been validated for wave propagation in free field and in ducts, with characteristic boundary conditions. The Perfectly Matched Layer (PML) for outgoing waves absorption is now verified. Results are shown for the two-dimensional problem of wave propagation in duct with axial uniform mean flow. The computational domain is composed of two subdomains, as introduced in Figure 4.7 in Section 4.4.3. The physical

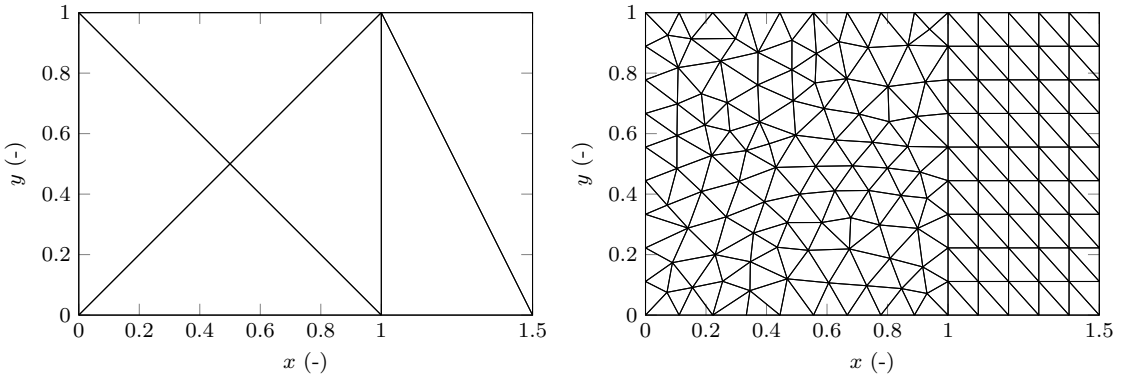

(a) Coarse mesh ($h = 0.5$). (b) Fine mesh ($h = 0.1$).

Figure 5.11: Unstructured and structured triangular meshes, in physical domain and in Perfectly Matched Layer.

waves propagate in the so-called physical domain (for x from 0 to $x_{\text{int}} = 1$) and the PML, where the waves leaving the physical domain are damped, extends over the length $d = 0.5$. The duct height is $H = 1$. Non-dimensional values are used. An unstructured triangular mesh is used in the physical domain, whereas a structured mesh constitutes the PML discretisation, as seen in Figure 5.11. Examples of wave absorption in the PML are studied in the first section, for acoustic, vorticity and entropy modes. Then, the PML performance is discussed.

5.4.1 Wave Absorption in Perfectly Matched Layer

In the following, waves propagate with a frequency such that $k_0 = 20$. The mean flow Mach number is $M_x = 0.6$. The first non-plane acoustic mode (cut-on) and the first vorticity/entropy modes are considered ($m = 1$). The characteristic mesh size is $h = 0.1$ and the PML length is $d = 0.5$. Figure 5.12 shows the real parts of the different variables in the computational domain for those modes. The difference in wavelength scales is visible: the acoustic mode wavenumber is $k_{x_{\text{a}}} \approx 12.25$, which corresponds to an acoustic wavelength of $\lambda_{\text{a}} \approx 0.51$; the vorticity/entropy modes wavenumber is $k_{x_{\text{v}}} = k_{x_{\text{e}}} \approx 33.33$, coinciding with a wavelength of $\lambda_{\text{v}} = \lambda_{\text{e}} \approx 0.19$. The duct modes propagate in the physical domain and are absorbed in the PML. Note that in these results, the PML definition given in Equation 4.53, involving Bermúdez's logarithm stretching function and Bécache's correction coefficient for inverse upstream modes, is used. It is worth noticing that the PML performs well for acoustic modes, but also for vorticity/entropy modes.

For the acoustic mode, the polynomial order is fixed to $p = 6$. The numerical error on the variables is obtained in the L^2-norm, both in the physical domain and in the PML, as seen

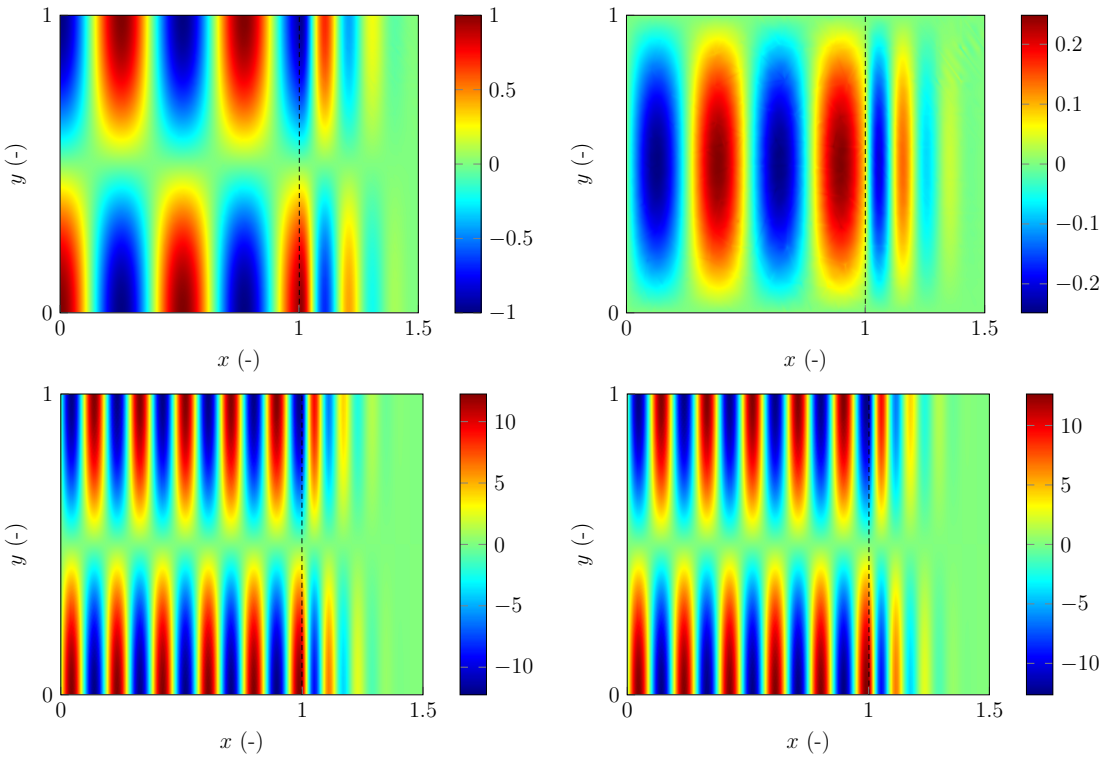

Figure 5.12: Real parts of the variables for the first non-plane acoustic mode and the first vorticity/entropy modes, in a two-dimensional duct with axial uniform mean flow. $k_0 = 20$, $m = 1$, $M_x = 0.6$. Top left: acoustic mode, p_c. Top right: acoustic mode, ρu_y. Bottom left: vorticity mode, ρu_x. Bottom right: entropy mode, ρ.

in Table 5.1. The numerical error in the PML is measured with respect to the analytic

	$E^{\rho}_{\mathrm{L}^2}$	$E^{\rho u_x}_{\mathrm{L}^2}$	$E^{\rho u_y}_{\mathrm{L}^2}$	$E^{p_c}_{\mathrm{L}^2}$
physical domain	0.014%	0.026%	0.088%	0.014%
PML	0.070%	0.046%	0.32%	0.070%

TABLE 5.1: L^2-norm errors in the physical domain and in the PML, for the first non-plane acoustic mode in a two-dimensional duct with uniform axial mean flow velocity. $k_0 = 20$, $m = 1$, $M_x = 0.6$, $h = 0.1$, $d = 0.5$, $p = 6$.

solution described in Section 4.4.3. For the vorticity mode, the polynomial order is fixed to $p = 8$. In the physical domain, the errors on the momentum are: $E^{\rho u_x}_{\mathrm{L}^2} \approx 0.18\%$ and $E^{\rho u_y}_{\mathrm{L}^2} \approx 0.010\%$. In the PML, they are: $E^{\rho u_x}_{\mathrm{L}^2} \approx 0.27\%$ and $E^{\rho u_y}_{\mathrm{L}^2} \approx 0.028\%$. It can be seen that the errors in the PML are slightly higher than the errors in the physical domain.

5.4.2 Perfectly Matched Layer Performance

The performance of the Perfectly Matched Layer is investigated in this section. The L^2-norm errors are plotted against the number of degrees of freedom per wavelength for each

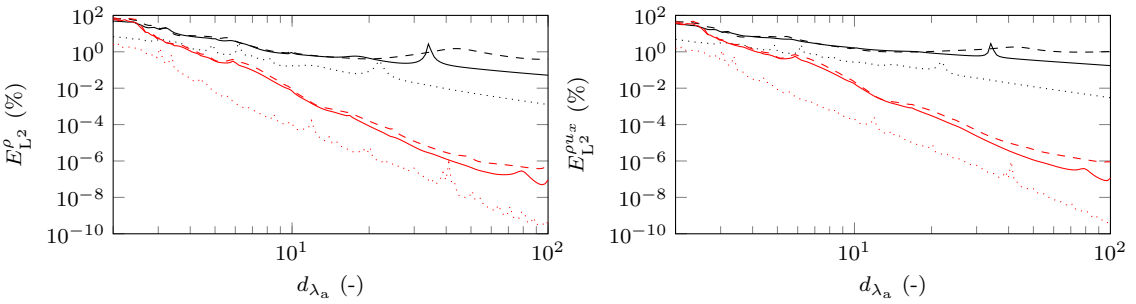

Figure 5.13: L^2-norm error in the physical domain against the number of degrees of freedom per shortest acoustic wavelength, for the duct acoustic plane wave. $h = 0.1$, $d = 0.5$, $M_x = 0.6$. Solid line: Bermúdez. Dashed line: Modave. Dotted line: proposed stretching function. Black: $p = 1$. Red: $p = 5$. Left: ρ. Right: ρu_x.

variable. Three types of PML are compared, depending on the stretching function.

- The logarithm function introduced by Bermúdez *at al.* is recalled [170]:

$$f_x(x) = -\ln\left(1 - \frac{x - x_{\mathrm{int}}}{d}\right). \tag{5.9}$$

- The modified logarithm function established by Modave *et al.*, such that its derivative is also continuous at the interface between the physical domain and the PML, reads [176]:

$$f_x(x) = -\ln\left(1 - \frac{x - x_{\mathrm{int}}}{d}\right) - \frac{x - x_{\mathrm{int}}}{d}. \tag{5.10}$$

- The third stretching function is the one proposed in Equation 4.51, which accounts for the mean flow effects and cancels out the oscillations in the propagation direction in the PML (with $a_\mathrm{r} = \left(1 - M_x^2\right)/k_0$):

$$f_x(x) = -\left(1 - M_x^2\right)\ln\left(1 - \frac{x - x_{\mathrm{int}}}{d}\right) - \mathrm{j}k_0(x - x_{\mathrm{int}}). \tag{5.11}$$

Acoustic Duct Modes

Figure 5.13 and 5.14 represent the errors in the physical domain against the number of degrees of freedom per shortest acoustic wavelength d_{λ_a}, for the first two acoustic duct modes respectively. Since the y-momentum is zero and the pressure is proportional to the density, only the errors on the density and on the x-momentum are displayed for the acoustic plane wave. The three stretching functions provide convergence of the error but present different features. The convergence in the asymptotic region ceases with Modave's PML and some stagnation is observed: this plateau corresponds to the same stagnation in the error in the PML. This seems to indicate that Modave's PML is less adapted to low

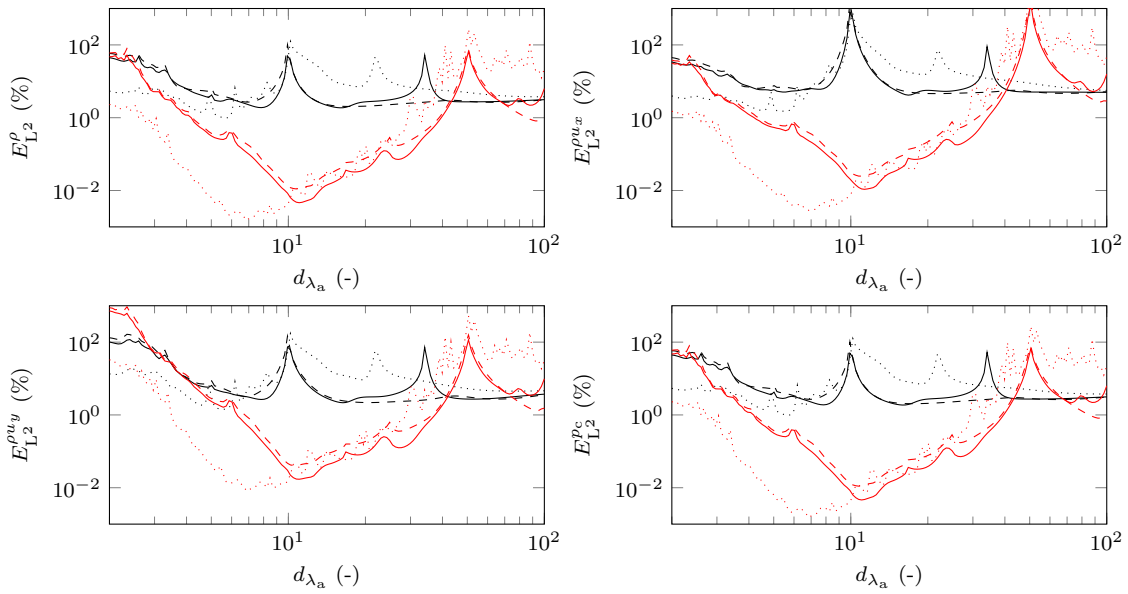

Figure 5.14: L^2-norm error in the physical domain against the number of degrees of freedom per shortest acoustic wavelength, for the first non-plane acoustic duct mode. $h = 0.1$, $d = 0.5$, $M_x = 0.6$, $m = 1$. Solid line: Bermúdez. Dashed line: Modave. Dotted line: proposed stretching function. Black: $p = 1$. Red: $p = 5$. Top left: ρ. Top right: ρu_x. Bottom left: ρu_y. Bottom right: p_c.

frequencies. The proposed stretching function shows promising results: the overall level of error is lower than for the other two PMLs. The accuracy benefit is up to a factor 100 with respect to the error obtained with Bermúdez's PML, even for the first cut-on non-plane acoustic mode. Moreover, the convergence is about one order higher for the proposed PML with respect to Bermúdez's PML, in the low-frequency range.

For cut-off modes (visible on Figure 5.14 for high values of d_{λ_a}), all PML models present a monotonous increase of the error as the frequency decreases (or as d_{λ_a} increases). The error in the physical domain is bounded by the reflection error (see Equation 4.47), which depends on the length of the domain and of the PML: a longer domain or PML would provide a larger convergence range. A major drawback of the proposed PML for cut-off modes is that the imaginary part of the stretching function cancels out the evanescent part of the wave in the PML, where the evanescent waves are therefore not absorbed. The waves damping must be efficient enough in the physical domain to avoid reflections in the PML. Large domains may overcome that issue, since cut-off modes amplitudes would be insignificant when entering the PML. However, in comparison with the other two PMLs, it seems that there is no major difference in the error in the physical domain, and the main issue seems to be the domain length.

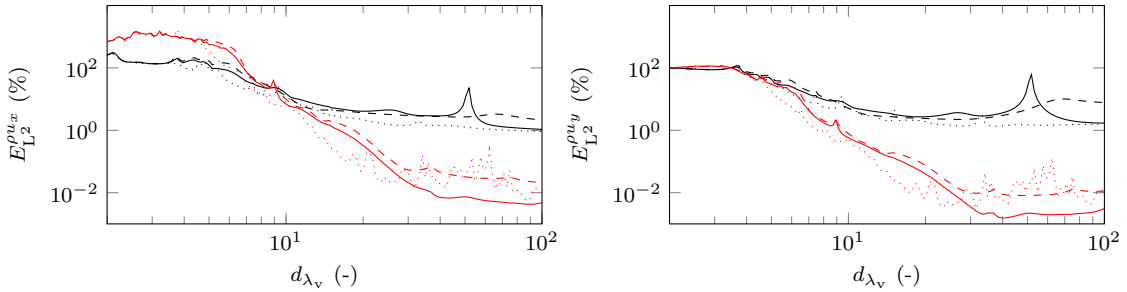

Figure 5.15: L^2-norm error in the physical domain against the number of degrees of freedom per hydrodynamic wavelength, for the first vorticity duct mode. $h = 0.1$, $d = 0.5$, $M_x = 0.6$. Solid line: Bermúdez. Dashed line: Modave. Dotted line: proposed stretching function. Black: $p = 1$. Red: $p = 5$. Left: ρu_x. Right: ρu_y.

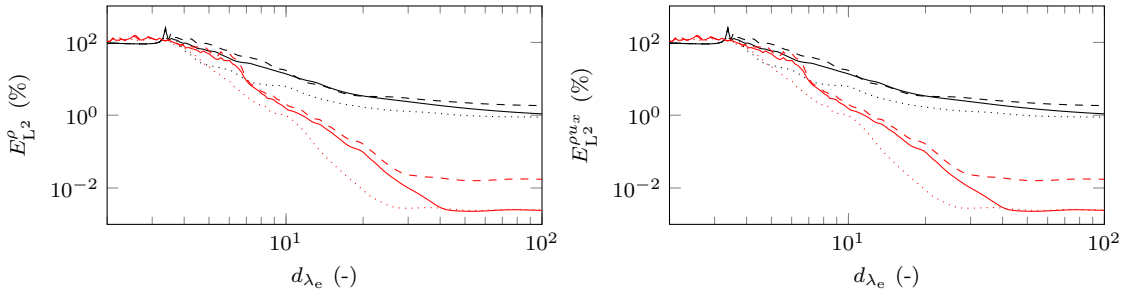

Figure 5.16: L^2-norm error in the physical domain against the number of degrees of freedom per hydrodynamic wavelength, for the first entropy duct mode. $h = 0.1$, $d = 0.5$, $M_x = 0.6$. Solid line: Bermúdez. Dashed line: Modave. Dotted line: proposed stretching function. Black: $p = 1$. Red: $p = 5$. Left: ρ. Right: ρu_x.

Vorticity and Entropy Duct Modes

Figures 5.15 and 5.16 represent the errors of the variables for the first vorticity and entropy duct modes. Different regimes are observed: an under-resolved region for $d_{\lambda_\mathrm{v}} = d_{\lambda_\mathrm{e}} < 6$, an intermediate regime for $6 < d_{\lambda_\mathrm{v}} < 30$ where the numerical model converges, and a plateau in the very low-frequency range. The three PMLs present similar results. However, the proposed stretching function lowers the error level in the intermediate region, and reaches the plateau for a lower resolution than Bermúdez's PML, especially for the entropy mode. Modave's PML plateau level is higher than for the other PMLs. In practice, aeracoustic models solve problems where the acoustic waves dominate the vorticity/entropy waves. The PMLs are preferably designed to absorb acoustic waves.

5.5 Summary

In this chapter, the implementation and the performance of the proposed high-order finite element model for the LEE have been verified. The propagation of uncoupled acoustic, vorticity and entropy waves has been checked through two test cases: wave propagation

in free field and duct modes propagation. The mean flow effects, with either uniform or non-uniform velocity, have been assessed. The numerical model convergence has been verified, for both mesh refinement and polynomial order increase. The performance of the model has been assessed in terms of different performance metrics (numerical errors with respect to analytic solutions, system matrix condition number and number of non-zeros, and number of degrees of freedom per wavelength.). Finally, the efficiency of the Perfectly Matched Layer has been confirmed for the different types of waves. A comparison of stretching functions has shown that the proposed PML yields more accurate results than PMLs already existing in the literature for propagating acoustic, entropy and vorticity waves. The proposed formulation is however less efficient for evanescent waves, to which no extra absorption can be provided.

Chapter 6

Numerical Stabilisation

The classical Galerkin finite element formulation is known to suffer from stability issues for convection-dominated problems. In this chapter, some alternative variational formulations are investigated for the Linearised Euler Equations. In a first section, the different sources of numerical errors are presented. In the second section, a one-dimensional dispersion analysis is performed in order to evaluate the dispersion properties of the high-order Finite Element Method. A stabilisation method is then introduced in the third section. Finally, in the fourth section, the stabilised formulation is assessed, with a particular emphasis on the choice of the stabilisation parameters.

6.1 Sources of Numerical Error

6.1.1 Pollution Effect

The following error bound has been derived in the H^1-norm for the *hp*-FEM and the Helmholtz equation in one dimension [98, 105]:

$$E_{\mathrm{H}^1} \leq C_1 \left(\frac{kh}{2p}\right)^p + C_2 k \left(\frac{kh}{2p}\right)^{2p}, \tag{6.1}$$

where C_1 and C_2 are weak functions of p, independent of ω and h. This expression highlights the different sources of error: the first term is linked with the interpolation error which dominates in the high-resolution regime, whereas the second term represents the dispersion error and the pollution effect which prevail in the low-resolution regime. From this expression, it is also clear that the error decreases exponentially when the polynomial

order p is increased, while it converges only algebraically when the mesh resolution h is decreased. This highlights the superiority of p-refinement over classical h-refinement. Beriot *et al.* have demonstrated that this expression is also valid in the context of the convected Helmholtz equation [51].

The dispersion error is defined as the relative difference between the exact and numerical wavenumbers, for a given frequency. For the high-order Finite Element Method and the Helmholtz equation, the following error estimator has been derived [140]:

$$E_{\mathrm{d}} = \frac{1}{2}\left(\frac{p!}{(2p)!}\right)^2 \frac{(kh)^{2p}}{2p+1} + \mathcal{O}\left((kh)^{2p+2}\right), \tag{6.2}$$

where E_{d} is the dispersion error. This estimator is derived for $kh \ll 1$, but it also tends to apply for low resolutions. In the presence of mean flow, this estimator is corrected by a factor $1 - M$, with the wavenumber also taking the Mach number M into consideration through: $k = k_0/(1 + M)$ [51]. The dispersion error is a local phenomenon which accumulates as the wave propagates through the computational domain, turning into the pollution effect. This numerical behaviour scales with kL which is proportional to the number of wavelengths in the domain, where the domain length L is contained in the weak function C_2 in the second term in Equation 6.1. This effect is illustrated in Figure 6.1 which shows a one-dimension wave propagation over a domain such that the phase error due to dispersion has accumulated in the finite elements over the computational domain. This results in a significant difference in phase between the numerical and exact solutions. The pollution effect reduces the performance of the conventional low order Finite Element Method at high frequencies. For large values of p, the phase errors become negligible. The high-order Finite Element Method is therefore seen as an efficient approach to circumvent the pollution effect [51]. As a consequence, the p-FEM allows to reduce the memory and time requirements by several orders of magnitude compared to the linear or quadratic FEM for a fixed accuracy in large-scale problems [52].

6.1.2 Convection-Related Instabilities

The standard Galerkin formulation suffers from unstable spurious oscillations in convection-dominated problems [92]. For the convective-diffusive transport equation, the Péclet number expresses the convective to diffusive transport ratio and is defined as: $\mathrm{Pe} = uh/(2\nu)$, where h is the mesh size, u is the convection velocity and ν is a diffusivity coefficient. It indicates that non-physical oscillations are present in the numerical solution for Pé-

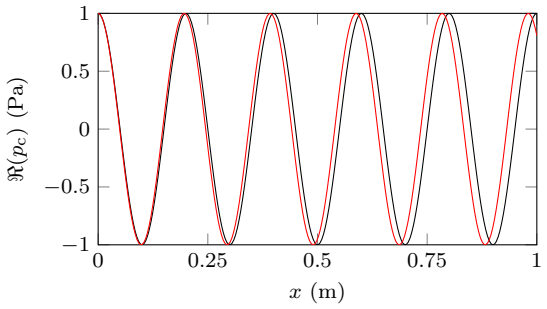

Figure 6.1: Dispersion error in one dimension. Black solid line: analytic solution. Red solid line: numerical solution.

clet numbers higher than 1, for which convection dominates over diffusion. For linear shape functions, the spurious node-to-node oscillations are due to a lack of diffusion in the Galerkin scheme with respect to the exact solution scheme. As an illustration, Figure 6.2 shows the acoustic propagation in a simplified aeroengine exhaust with uniform mean flow. This test case will be investigated in detail in Section 8.2. The left-hand side picture represents a typical Linearised Euler Equations solution as obtained with the classical linear finite element formulation. On the right hand side, the analytic solution is presented. The overall pressure distribution obtained with the linear FEM is correct, however some spurious oscillations deteriorate the solution accuracy. This lack of stability, also referred to as the locking phenomenon, has been first reported for the LEE in 1980 by Astley and Eversman in [177]. Cai *et al.* have demonstrated that these effects also hold for higher orders, still for the convection–diffusion transport problem [178]. They have observed that depending on the polynomial order parity, the difference between the exact and numerical diffusivity coefficients changes sign: this indicates that the high-order Galerkin formulation adds or subtracts diffusion to the numerical model, according to the parity of p. However, they have shown that incrementing the polynomial order helps to limit the spurious oscillations. In addition, exponential convergence is still found when p is increased. The polynomial order required for a given Péclet number is analytically derived to achieve nodally stable solutions.

In order to counterbalance the negative diffusion introduced by the Galerkin approach with linear elements, a solution consists in adding a diffusion term. This amounts to introducing a decentered upwind approximation of the convective term, where the classical Galerkin formulation is equivalent to a centered scheme. Petrov-Galerkin-type generalised methods use weighting functions which do not coincide with the interpolation functions space. In upwind approximations for finite element methods the element upstream of a node is heavily weighted with respect to the element downstream. The first upwind finite element

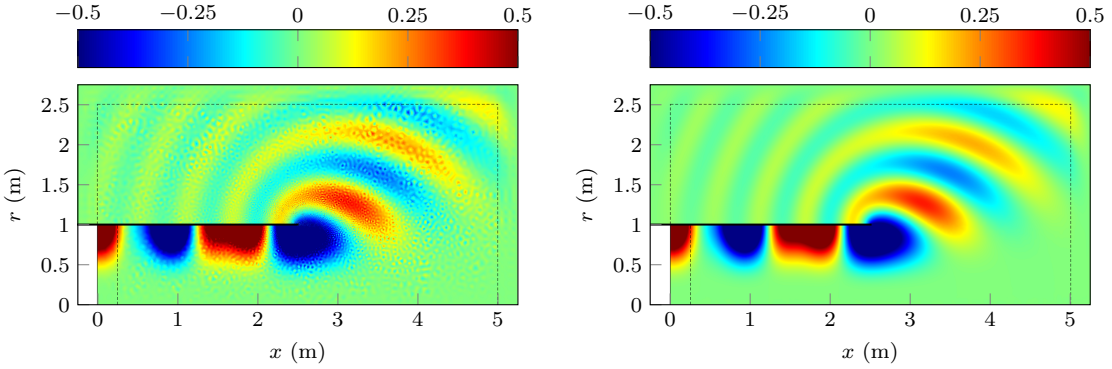

(a) Linear FEM.

(b) Exact solution.

Figure 6.2: Convection-related spurious oscillations in two dimensions. Real part of the modified pressure.

formulations used modified weighting functions which weighted upstream elements more heavily than downstream elements, with respect to a given node [92]. Despite its stability, this method has been observed to introduce excessive numerical dissipation [179, 180]. The main stabilisation techniques rely on the addition of a stabilisation term in the formulation of the form [92]:

$$\int_{\Omega} \boldsymbol{w}^{\mathrm{T}} \mathfrak{L}(\boldsymbol{q}) \mathrm{d}\Omega + \int_{\Omega} \mathfrak{D}(\boldsymbol{w}) \boldsymbol{\tau} \mathfrak{L}(\boldsymbol{q}) \mathrm{d}\Omega = \mathbf{0}, \tag{6.3}$$

where $\mathfrak{D}$ is the stabilisation operator and $\boldsymbol{\tau}$ is a stabilisation parameter. Note that in this equation the residual $\mathfrak{R}$ is equal to the differential operator $\mathfrak{L}(\boldsymbol{q})$ in the absence of external source. The stabilisation operator defines the stabilisation technique: the Streamline-Upwind Petrov-Galerkin (SUPG), Galerkin/Least-Squares (GLS) and SubGrid-Scale (SGS) methods are the main ones. These methods and others have been compared for the diffusion-convection-reaction equation with a finite element approach [181]. Reviews on classical approaches can be found in [182], and in [183] for high-order methods. An overview of stabilised finite element methods is also available for the advective-diffusive equation in [184].

Several authors have studied the SUPG method. A finite element SUPG-based approach has been used to solve multidimensional advective-diffusive systems [88, 185]. Carette *et al.* have applied a linear finite element SUPG formulation to solve the multi-dimensional compressible Euler equations. They have provided a definition of the stabilisation parameter matrix, as well as a shock-capturing term [186]. The stabilisation parameter computation has been investigated by Tezduyar and Osawa for the unsteady incompressible Navier-Stokes equations [187]. These parameters are based on the local length-scales. For high-order finite elements, Bause and Schwegler have recently studied the SUPG stabilisation together with anisotropic shock capturing in order to treat the crosswind direction, per-

pendicular to the propagation direction [188]. Applied to unsteady non-linear convection-diffusion-reaction models with small diffusion, the method reduces spurious oscillations in crosswind direction and improves the simulations accuracy.

The Algebraic Subgrid Scale (ASGS) method has been applied by Codina to stabilise the Finite Element Method for the diffusion-convection-reaction equation [189]. A stabilisation matrix has been proposed as an extension of a one-dimensional study. Guasch and Codina have used this approach to solve the two-dimensional convected Helmholtz equation, using a stabilisation parameter which has been derived from a dispersion analysis [143]. They indicate that the formulation is equivalent to the GLS method and demonstrate the benefits of the approach. Conceptually simpler and more general than the SUPG method, the GLS technique has been introduced by Hughes *et al.* and is applicable to a wide range of problem classes [190].

In the framework of the Linearised Euler Equations, Rao and Morris have used the SUPG stabilisation method in the frequency domain using nodal polynomials and unstructured triangular meshes [64]. They use a simple stabilisation parameter matrix, similar to the one used by Beau *et al.* for the compressible Euler equations and which depends on the coefficient matrices spectral radii [191]. Similarly, Iob *et al.* have used the ASGS approach together with the stabilisation parameter introduced by Guasch and Codina for the two-dimensional convected Helmholtz equation [59].

In this work, the dispersion properties of the Linearised Euler Equations are investigated with high-order finite elements and dedicated stabilisation techniques are studied. Unlike most of the aforementioned studies which considered time-domain approaches, here the formulation in frequency domain gives an additional parameter to account for the unsteadiness of the equations and which is the angular frequency of the time-harmonic solutions. Thus, the dispersion/stabilisation analysis developed in this chapter involves the following specific parameters: the angular frequency, the convection velocity, the element size and the polynomial order.

6.2 One-Dimensional Analysis

In this section, the one-dimensional Linearised Euler Equations are studied through a dispersion analysis. An equivalent problem is defined, involving a one-dimensional advection equation. A dispersion relation is derived to provide the numerical wavenumber. The dispersion and amplitude errors are evaluated, and the effects of the high orders are assessed.

6.2.1 Advection Equation

The one-dimensional Linearised Euler Equations with uniform mean flow can be written:

$$\mathrm{j}\omega \boldsymbol{q} + \boldsymbol{A}_x \frac{\partial \boldsymbol{q}}{\partial x} = \boldsymbol{0}. \tag{6.4}$$

The perturbations variables vector $\boldsymbol{q}$ and the flux matrix $\boldsymbol{A}_x$ read:

$$\boldsymbol{q} = \left\{ \begin{array}{c} \rho \\ \rho u_x \\ p_\mathrm{c} \end{array} \right\} \text{ and } \boldsymbol{A}_x = \left[\begin{array}{ccc} 0 & 1 & 0 \\ -u_{0_x}^2 & 2u_{0_x} & \dfrac{\rho_0 c_0^2}{p_{\mathrm{c}_0}} \\ -\dfrac{p_{\mathrm{c}_0}}{\rho_0} u_{0_x} & \dfrac{p_{\mathrm{c}_0}}{\rho_0} & u_{0_x} \end{array} \right]. \tag{6.5}$$

The flux matrix can be diagonalised as: $\boldsymbol{A}_x = \boldsymbol{W}_x \boldsymbol{\Lambda}_x \boldsymbol{W}_x^{-1}$, with $\boldsymbol{\Lambda}_x$ the eigenvalues diagonal matrix and $\boldsymbol{W}_x$ the eigenvectors matrix as in Section 4.2. The amplitude vector $\hat{\boldsymbol{q}} = \boldsymbol{W}_x^{-1}\boldsymbol{q} = \{\hat{q}_\mathrm{e}, \hat{q}_{\mathrm{a}^-}, \hat{q}_{\mathrm{a}^+}\}^\mathrm{t}$ contains the entropy ($\hat{q}_\mathrm{e}$), the incoming acoustic ($\hat{q}_{\mathrm{a}^-}$) and the outgoing acoustic ($\hat{q}_{\mathrm{a}^+}$) characteristic waves. After diagonalisation of the flux terms, the one-dimensional Linearised Euler Equations read:

$$\mathrm{j}\omega \hat{\boldsymbol{q}} + \boldsymbol{\Lambda}_x \frac{\partial \hat{\boldsymbol{q}}}{\partial x} = \boldsymbol{0}. \tag{6.6}$$

Since the matrix $\boldsymbol{\Lambda}_x$ is diagonal, the system can be broken down into three independent one-dimensional scalar equations. These are time-harmonic advection equations with the phase velocities λ_{i_x}:

$$\mathrm{j}\omega \hat{q}_i + \lambda_{i_x} \frac{\partial \hat{q}_i}{\partial x} = 0 \ \forall i \in \{1, 2, 3\}. \tag{6.7}$$

Investigating the dispersion problem for the one-dimensional Linearised Euler Equations with uniform mean flow is therefore equivalent to studying the scalar advection equation 6.7. This particular equation will be examined in the following sections.

6.2.2 Dispersion Analysis

Considering Equation 6.7, the following scalar one-dimensional advection problem is examined:

$$\mathrm{j}\omega q(x) + u \frac{\partial q(x)}{\partial x} = 0 \ \forall x \in [0, L], \tag{6.8}$$

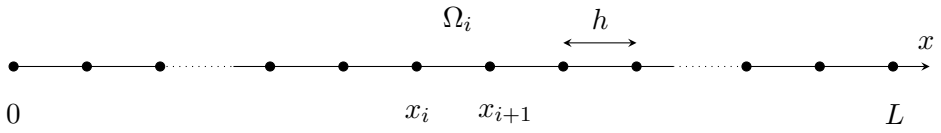

Figure 6.3: One-dimensional domain periodic discretisation for the dispersion analysis.

where $q(x)$ is a scalar quantity and $u \neq 0$ is a uniform convection velocity. Applying the standard Galerkin formulation to Equation 6.8 leads to:

$$\int_0^L \left(\mathrm{j}\omega \overline{w} q - u \frac{\partial \overline{w}}{\partial x} q \right) \mathrm{d}x = - \left[u \overline{w} q \right]_0^L , \tag{6.9}$$

where w is the scalar test function and the overline denotes the complex conjugate. The domain $[0, L]$ is subdivided into n_e elements $\Omega_i = [x_i, x_{i+1}]$, with $i \in \{0, 1, ..., n_\mathrm{e} - 1\}$ and $x_i = ih$ the nodes locations. The element size h is considered uniform. The periodic structure of the mesh in shown in Figure 6.3. Within each interior element, the discrete model can be written as follows:

$$\left(\mathrm{j}\omega \int_{x_i}^{x_{i+1}} \boldsymbol{N}^\mathrm{T} \boldsymbol{N} \mathrm{d}x - u \int_{x_i}^{x_{i+1}} \frac{\mathrm{d}\boldsymbol{N}^\mathrm{T}}{\mathrm{d}x} \boldsymbol{N} \mathrm{d}x \right) \left\{ \begin{array}{c} \alpha_i^\mathrm{v} \\ \alpha_{2,i}^\mathrm{b} \\ \vdots \\ \alpha_{P,i}^\mathrm{b} \\ \alpha_{i+1}^\mathrm{v} \end{array} \right\} = \left\{ \begin{array}{c} 0 \\ \vdots \\ 0 \end{array} \right\}, \tag{6.10}$$

where $\boldsymbol{N}$ is the vector of shape functions and $\{\alpha_i^\mathrm{v},\, \alpha_{2,i}^\mathrm{b},\, \cdots,\, \alpha_{p,i}^\mathrm{b}; \alpha_{i+1}^\mathrm{v}\}^\mathrm{t}$ are the degrees of freedom associated with the element Ω_i. The superscript $^\mathrm{v}$ denotes the degrees of freedom of the exterior nodes, i.e. associated with the nodal vertex shape functions. The superscript $^\mathrm{b}$ denotes the degrees of freedom of the interior nodes associated with the bubble shape functions. In this dispersion analysis, the classical Lagrange shape functions are used because of their nodal property which gives an easy access to the values of the degrees of freedom, as explained in Section 2.4.3. Since all the elements of the discretisation are identical, the mesh is periodic and the equations satisfied by the degrees of freedom of element i are the same as those satisfied by the degrees of freedom of element $i + 1$.

Harmonic solutions of the form $\mathrm{e}^{-\mathrm{j}kx}$ are sought, where k is the wavenumber. The exterior nodal degrees of freedom are defined by $q_i(x_i) = \alpha_i^\mathrm{v}$ and $q_i(x_{i+1}) = \alpha_{i+1}^\mathrm{v}$. It follows that:

$$\alpha_i^\mathrm{v} = \mathrm{e}^{-\mathrm{j}kih} = Q^i, \tag{6.11}$$

where $Q = \mathrm{e}^{-\mathrm{j}kh}$ is the Floquet multiplier [192]. This definition is also valid for the interior nodal degrees of freedom inside the element. Considering the complex amplitude vector $\boldsymbol{\Phi}_0 = \{\Phi_0^{(1)}, \Phi_0^{(2)}, \cdots, \Phi_0^{(p)}\}^{\mathrm{t}}$, any degree of freedom of the vector $\boldsymbol{\Phi}_i = \{\alpha_i^{\mathrm{v}}, \alpha_{2,i}^{\mathrm{b}}, \cdots, \alpha_{p,i}^{\mathrm{b}}, \alpha_{i+1}^{\mathrm{v}}\}^{\mathrm{t}}$ satisfies:

$$\Phi_i^{(l)} = \Phi_0^{(l)} Q^i \ \forall l \in \{1, ..., p\}. \tag{6.12}$$

After assembly, the discrete system written in matrix form yields:

$$\boldsymbol{R}\boldsymbol{\Phi}_0 = \mathbf{0}, \tag{6.13}$$

where $\boldsymbol{R}$ is a coefficient matrix. This system contains the numerical model dispersion relation for the following fixed parameters: the angular frequency ω, the convection velocity u and the mesh size h. In practice, the numerical Floquet multiplier $Q_{\mathrm{n}} = \mathrm{e}^{-\mathrm{j}k_{\mathrm{n}}h}$ is obtained by solving Equation 6.13 relating the contributions at the nodes (after expressing the contributions of the interior nodes in terms of the contributions of the exterior nodes). The numerical discrete wavenumber k_{n} is then obtained from the expression of Q_{n} by:

$$k_{\mathrm{n}} = -\frac{1}{\mathrm{j}h} \ln Q_{\mathrm{n}} + \frac{2n\pi}{h}, \tag{6.14}$$

where the second term accounts for the infinite number of possible solutions and $n \in \mathbb{Z}$. The wavenumber which best approximates the exact solution is considered.

6.2.3 Dispersion and Amplitude Errors

For a fixed value of ω, the exact wavenumber for the one-dimensional time-harmonic advection equation is: $k_{\mathrm{e}} = \omega/u$. This corresponds to a wave propagating with the flow at the velocity u. The relative difference between the exact and discrete wavenumbers defines the dispersion error E_{d}:

$$E_{\mathrm{d}} = \left| \frac{k_{\mathrm{n}} - k_{\mathrm{e}}}{k_{\mathrm{e}}} \right|. \tag{6.15}$$

In addition, the numerical eigenvector $\boldsymbol{\Phi}_0$ provides some information about the numerical model local error. The solution approximation is evaluated within an element, by combination of the nodally exact vertex values and of the numerical eigenvector $\boldsymbol{\Phi}_{0_{\mathrm{n}}}$ for the

interior nodal functions:

$$q_{\mathrm{n}}(x) = \Phi_{0_{\mathrm{e}}}^{(1)} N_0(x) + \Phi_{0_{\mathrm{e}}}^{(1)} \mathrm{e}^{-\mathrm{j}k_{\mathrm{e}}h} N_1(x) + \sum_{i=2}^{p} \Phi_{0_{\mathrm{n}}}^{(i)} N_i(x), \tag{6.16}$$

where N_0 and N_1 are the vertex linear shape functions, and N_i are the interior nodal shape functions for $i \in \{2, \cdots, p\}$. The L^2-norm amplitude error E_{a} measures the relative difference between the numerical approximation q_{n} and the exact solution q_{e}:

$$E_{\mathrm{a}} = \frac{\|q_{\mathrm{n}} - q_{\mathrm{e}}\|_{\mathrm{L}^2}}{\|q_{\mathrm{e}}\|_{\mathrm{L}^2}}, \text{ with } \|\chi\|_{\mathrm{L}^2} = \sqrt{\int_{x_i}^{x_{i+1}} |\chi|^2 \, \mathrm{d}x}. \tag{6.17}$$

This error is evaluated in an element Ω_i. The convection velocity and the mesh size are fixed to $u_0 = 1$ and $h = 1$. The shape functions polynomial order p varies from 1 to 6. The dispersion relation (6.13) is solved for several values of the number of degrees of freedom per wavelength $d_\lambda^{(p)}$. In this section, the following definition is used:

$$d_\lambda^{(p)} = \frac{2\pi p u}{\omega h}. \tag{6.18}$$

The dispersion and amplitude errors are plotted against the number of degrees of freedom per wavelength, in Figure 6.4. Three regions emerge: a pre-convergence regime, a low-resolution regime where the dispersion error dominates and a high-resolution regime where the interpolation error prevails. The relative difference between the exact and discrete wavenumbers increases for low numbers of degrees of freedom per wavelength, which corresponds to large wavenumbers. The effects of the high orders are also visible: for a fixed value of $d_\lambda^{(1)}$, increasing the polynomial order improves the model accuracy and the dispersion error. For a fixed value of $d_\lambda^{(p)} = p d_\lambda^{(1)}$, the p-FEM improves significantly the performance in the high-resolution regime and decreases the interpolation error. However, the p-convergence is not regular. The convergence rate in $d_\lambda^{(p)}$ for the dispersion error is $2p$ for even orders and $2(p+1)$ for odd orders.

Regarding the amplitude error, the convergence rate in $d_\lambda^{(p)}$ is p for even orders and $p+1$ for odd orders. Even orders have the same convergence rate as the immediately preceding odd orders, which means that for a given problem the convergence is faster when increasing the order from an even value to the immediately following odd order. The dispersion and amplitude errors exhibit some peaks in the low-resolution regime, corresponding to the so-called aliasing effect [193]. In practice, they represent the poor conditioning of the condensed system matrix due to the bubble functions [51]. This is observed for $p \geq 2$.

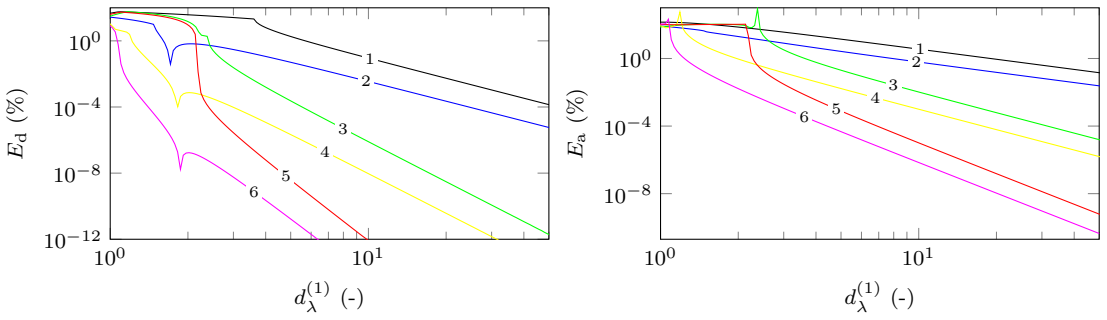

(a) Dispersion error.

(b) Amplitude error.

Figure 6.4: Dispersion and amplitude errors against $d_\lambda^{(1)}$ for the one-dimensional advection problem 6.8.

6.3 Stabilisation

In order to limit the dispersion effects with flow, stabilisation techniques may be applied. A stabilisation term is added to the classical Galerkin formulation. This term depends on a stabilisation operator and on a stabilisation parameter. In the following, alternative formulations are examined. An investigation of the stabilisation parameters is also performed.

6.3.1 Stabilised Formulation

A hyperbolic problem $\mathfrak{L}(\boldsymbol{q}) = \boldsymbol{0}$ is considered, where $\mathfrak{L}$ is the differential operator applied to the unknown variable $\boldsymbol{q}$. The general form of the stabilised formulation is given in Equation 6.3, where the stabilisation operator $\mathfrak{D}$ is applied to the test function $\boldsymbol{w}$ and the stabilisation parameter $\boldsymbol{\tau}$ is a matrix. These two terms define the type of stabilisation assigned to the system and the amount of artificial diffusion. They are computed within each element. For the one-dimensional advection problem, the formulation 6.9 transforms into the following stabilised formulation after integration by parts:

$$\int_0^L \left(\mathrm{j}\omega w^\mathrm{T} q - u\frac{\partial w^\mathrm{T}}{\partial x} q\right) \mathrm{d}x + \sum_{i=1}^{n_\mathrm{e}} \int_{x_i}^{x_{i+1}} \mathfrak{D}(w)^\mathrm{T} \tau \left(\mathrm{j}\omega q + u\frac{\partial q}{\partial x}\right) \mathrm{d}x = -\left[u w^\mathrm{T} q\right]_0^L, \quad (6.19)$$

with $\mathfrak{D}(w) = \mathfrak{L}(w)$, within the Galerkin/Least-Squares (GLS) stabilisation scheme [190]. In one dimension, the stabilisation matrix $\boldsymbol{\tau}$ reduces to a scalar parameter τ. For the

two-dimensional Linearised Euler Equations, the formulation 4.2 becomes:

$$\int_{\Omega} \mathrm{j}\omega \boldsymbol{w}^{\mathrm{T}}\boldsymbol{q} - \frac{\partial \boldsymbol{w}^{\mathrm{T}}}{\partial x}\boldsymbol{A}_x\boldsymbol{q} - \frac{\partial \boldsymbol{w}^{\mathrm{T}}}{\partial y}\boldsymbol{A}_y\boldsymbol{q}\mathrm{d}\Omega + \sum_{i=1}^{n_{\mathrm{e}}} \int_{\Omega_i} \mathfrak{D}(\boldsymbol{w})^{\mathrm{T}}\boldsymbol{\tau}\left(\mathrm{j}\omega q + \boldsymbol{w}^{\mathrm{T}}\frac{\partial \boldsymbol{A}_x\boldsymbol{q}}{\partial x} + \boldsymbol{w}^{\mathrm{T}}\frac{\partial \boldsymbol{A}_y\boldsymbol{q}}{\partial y}\right)\mathrm{d}\Omega_i = -\int_{\Gamma} \boldsymbol{w}^{\mathrm{T}}\left(n_x\boldsymbol{A}_x + n_y\boldsymbol{A}_y\right)\boldsymbol{q}\mathrm{d}\Gamma. \quad (6.20)$$

The GLS stabilisation operator reads:

$$\mathfrak{D}(\boldsymbol{w}) = \mathrm{j}\omega q + \boldsymbol{w}^{\mathrm{T}}\frac{\partial \boldsymbol{A}_x^{\mathrm{T}}\boldsymbol{q}}{\partial x} + \boldsymbol{w}^{\mathrm{T}}\frac{\partial \boldsymbol{A}_y^{\mathrm{T}}\boldsymbol{q}}{\partial y}, \quad (6.21)$$

where the matrices Hermitian transposes are used, providing better results, as observed for solving the Euler equations [191]. Here the GLS stabilisation scheme is used since it considers the whole components of the differential operator. The SUPG stabilisation method, which involves only the convective parts of the differential operator, has also been tested and has provided results with similar conclusions to those observed with the GLS operator.

6.3.2 Stabilisation Parameter

The performance of the stabilisation scheme depends on the choice of the stabilisation parameter τ. The objective of this section is to find optimal values for the stabilisation parameter, so as to cancel out the nodal error for the following given parameters: the polynomial order p, the angular frequency ω,the convection velocity u and the characteristic mesh size h. This novel approach should provide values of τ which improve the numerical model in the low-resolution regime.

One-Dimensional Study

As in Section 6.2.2, the dispersion relation is written for the stabilised formulation 6.19 which includes the stabilisation parameter τ. After assembly, the discrete system within an element reads: $\boldsymbol{R}_\tau\boldsymbol{\Phi}_0 = \boldsymbol{0}$, where $\boldsymbol{R}_\tau$ is a coefficient matrix which depends on τ. Unlike in the dispersion analysis, the objective is not to determine the numerical wavenumber k_{n}. On the contrary, the exact solution wavenumber k_{e} is enforced in the system through the exact Floquet multiplier $Q_{\mathrm{e}} = \mathrm{e}^{-\mathrm{j}k_{\mathrm{e}}h}$. This procedure is equivalent to suppressing the nodal error in the system, by taking advantage of the additional degree of freedom τ introduced

in the system. The stabilisation parameter optimal value is then obtained, as a function of $d_\lambda^{(p)}$ and ω. For the linear shape functions, its analytic expression reads:

$$\tau_{\text{opt,1D}}^{(1)} = \frac{\nu}{\mathrm{j}\omega} \frac{\nu\,(2+\cos\nu) - 3\sin\nu}{\nu^2\,(2+\cos\nu) + 6\,(1-\cos\nu) - 6\nu\sin\nu}, \tag{6.22}$$

where $\nu = 2\pi/d_\lambda^{(1)} = kh$ is the Helmholtz number associated with the wavenumber $k = \omega/u_0$ and the characteristic mesh size h. Equation 6.22 shows the dependency in ω: it indicates that τ can be understood as a time parameter [92]. The optimal stabilisation parameters $\tau_{\text{opt,1D}}^{(2)}$ and $\tau_{\text{opt,1D}}^{(3)}$, respectively for the quadratic and cubic shape functions are also obtained. The expression for $p = 2$ reads:

$$\begin{aligned}
\tau_{\text{opt,1D}}^{(2)} = \frac{\nu}{\mathrm{j}\omega}\Bigg[& -60\sin\nu + 12\nu\,(1+4\cos\nu) + 12\nu^2\sin\nu + \nu^3\,(3-\cos\nu) \\
& + 2\mathrm{j}\Bigg(-2250 + 2400\cos\nu - 150\cos 2\nu + 120\nu\,(17\sin\nu - \sin 2\nu) \\
& - \nu^2\,(54 - 888\cos\nu + 42\cos 2\nu) + \nu^3\,(194\sin\nu + 7\sin 2\nu) \\
& + \nu^4\left(\frac{39}{2} + 20\cos\nu - \frac{\cos 2\nu}{2}\right)\Bigg)^{1/2}\Bigg] \\
\Big/ \Big[& 240\,(1-\cos\nu) - 240\nu\sin\nu + 24\nu^2\,(1+4\cos\nu) + 16\nu^3\sin\nu + \nu^4\,(3-\cos\nu)\Big].
\end{aligned} \tag{6.23}$$

For $p = 3$, the expression is particularly lenghty and is not written here. It can be noted that the three stabilisation parameters are purely imaginary. For the odd orders 1 and 3, the imaginary part of $\tau_{\text{opt,1D}}^{(\bullet)}$ is strictly negative. On the contrary, the imaginary part of $\tau_{\text{opt,1D}}^{(2)}$ is negative for low numbers of degrees of freedom per wavelength and positive for $d_\lambda^{(1)} > 1.7$. It shows that depending on the order parity, the artificial numerical diffusion created by the stabilisation term is either added or subtracted. This is consistent with the results observed by Cai *et al.* on the stabilisation effects on the high-order Finite Element Method for convection-dominated problems [178], where the dependency on the parity of the polynomial degree is also noticed. One specificity of our study is to consider the transport equation in the frequency domain. This allows to find relations between the stabilisation properties and the additional parameter that is the frequency.

The optimal stabilisation parameters are plotted in Figure 6.5, against the number of degrees of freedom per wavelength $d_\lambda^{(1)}$. The odd orders behave in a similar way, with a monotonous decrease with $d_\lambda^{(1)}$. This indicates that odd orders are well behaved, because the stabilisation is not required anymore when the mesh is sufficiently refined. Surprisingly, the evolution of the optimal parameter is very different for the second order: in the low-

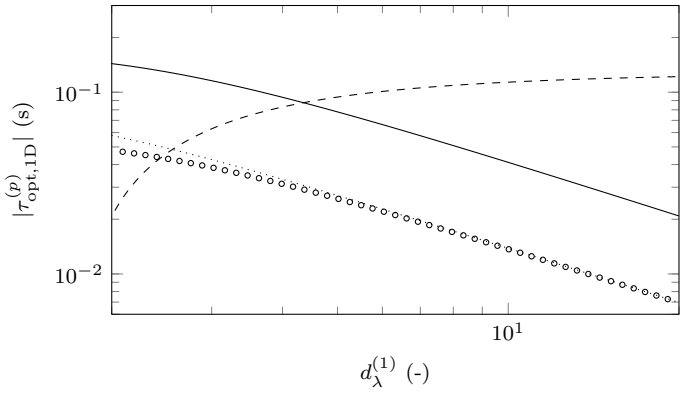

Figure 6.5: Absolute value of the one-dimensional optimal stabilisation parameter against $d^{(1)}_{\lambda}$. Solid line: $p = 1$. Dashed line: $p = 2$. Dotted line: $p = 3$. $\circ$ marker: $|\tau^{(1)}_{\mathrm{opt,1D}}/3|$.

resolution regime $\tau^{(2)}_{\mathrm{opt,1D}}$ increases notably and tends to reach a non-zero asymptotic value in the high-resolution regime. This indicates that, unlike the odd orders, the numerical scheme based on quadratic shape functions does not converge to the exact solution and still requires a stabilisation as the mesh is refined. A similar tendency has been found numerically for $p = 4$. This particular behaviour of the even orders has also been observed by Cai *et al.* [178].

The following relation can be found between $\tau^{(1)}_{\mathrm{opt,1D}}$ and $\tau^{(3)}_{\mathrm{opt,1D}}$, in the high-resolution regime: $\tau^{(3)}_{\mathrm{opt,1D}} \approx \tau^{(1)}_{\mathrm{opt,1D}}/3$. This approximation is valid for $d^{(1)}_{\lambda} > 10$ with an absolute error lower than 1% which decreases when $d^{(1)}_{\lambda}$ increases. It can be found numerically that the relation $\tau^{(p)}_{\mathrm{opt,1D}} \approx \tau^{(1)}_{\mathrm{opt,1D}}/p$ can be generalised for higher odd orders, in the high-resolution regime. This result is consistent with the stabilisation parameter value classically used in the literature for steady problems [92], which reads:

$$\tau^{(p)}_{\mathrm{s,1D}} = \alpha \frac{h}{2u_0 p} = \alpha \frac{\pi}{\omega d^{(1)}_{\lambda} p} = \frac{\alpha}{2} \frac{\nu}{\omega p}, \tag{6.24}$$

where $\alpha > 0$ is a coefficient to adapt to the problem to be solved. This expression is derived from the analysis of the one-dimensional steady convective-diffusive equation, in which $\alpha = 1$ [92]. It shows the analogy with the time-harmonic advection equation, by expressing the steady parameter in terms of ω and $d^{(1)}_{\lambda}$. Since $d^{(p)}_{\lambda} = p d^{(1)}_{\lambda}$, it is quite remarkable to notice that this expression can be written as:

$$\tau^{(p)}_{\mathrm{s,1D}} = \alpha \frac{\pi}{\omega d^{(p)}_{\lambda}}. \tag{6.25}$$

This stabilisation parameter is significantly different from the optimal stabilisation param-

eters, as it is a strictly positive real number. This difference comes from the time-derivative in the equation of the time-harmonic problem, that translates into the factor $\mathrm{j}\omega$ in the frequency domain. At a given frequency, this steady parameter tends to zero when the number of degrees of freedom per wavelength increases, which corresponds to a mesh refinement and/or an increase of the interpolation order p. This indicates that no stabilisation is necessary for a fine mesh and/or for high-orders [92, 178]. Our study shows a slightly different result: overall, p-refinement does bring the stabilisation parameters values down closer to zero, as seen in Figure 6.5, but h-refinement shows that stabilisation is still needed for even orders, which optimal stabilisation parameter tends to a non-zero asymptotic value.

Two-Dimensional Study

In two dimensions, the Linearised Euler Equations are coupled and the decomposition leading to the advection equations 6.7 is not possible. Considering the flux matrices diagonalisations ($\boldsymbol{A}_{x_i} = \boldsymbol{W}_{x_i}\boldsymbol{\Lambda}_{x_i}\boldsymbol{W}_{x_i}^{-1}$), the two-dimensional Linearised Euler Equations with uniform mean flow can be written for the characteristics vector $\hat{\boldsymbol{q}}$:

$$\mathrm{j}\omega\hat{\boldsymbol{q}} + \boldsymbol{\Lambda}_x\frac{\partial\hat{\boldsymbol{q}}}{\partial x} + \boldsymbol{W}_x^{-1}\boldsymbol{W}_y\boldsymbol{\Lambda}_y\boldsymbol{W}_y^{-1}\boldsymbol{W}_x\frac{\partial\hat{\boldsymbol{q}}}{\partial y} = \boldsymbol{0}. \tag{6.26}$$

The coupling is observed through the third term. In this case, the study performed in the previous paragraph cannot be reduced to a scalar equation. However, it can be replicated by considering the two-dimensional Linearised Euler Equations written for the variables vector $\boldsymbol{q}$. The optimal stabilisation matrix which cancels out the dispersion error is sought for a given wavenumber and a fixed mesh. Harmonic plane wave solutions of the form $\boldsymbol{q}_\mathrm{e} \equiv \mathrm{e}^{\mathrm{j}(k_x x + k_y y)}$ are sought, with a uniform mean flow u_{0_x} in the x-direction. The mesh is quadrangular with dimension $h_x \times h_y$. This study is similar to the one performed by Guasch and Codina for the convected Helmholtz equation in two dimensions [143]. For bilinear shape functions, the following optimal stabilisation matrix is found for a wave propagating in the x-direction:

$$\boldsymbol{\tau}^{(1)}_{\mathrm{opt,2D}} = \frac{\mu}{\mathrm{j}\omega}\frac{\mu\left(2+\cos\mu\right) - 3\sin\mu}{\mu^2\left(2+\cos\mu\right) + 6\left(1-\cos\mu\right) - 6\mu\sin\mu}\boldsymbol{I}, \tag{6.27}$$

where $\mu = k_x h_x$ is the Helmholtz number associated with the wavenumber $k_x = \omega/(u_{0_x} + c_0)$, the characteristic length h_x in the propagation direction and the phase velocity $u_{0_x} + c_0$ of the right-propagating acoustic wave. This stabilisation parameter is a 4×4 diagonal matrix, whose coefficients are identical. Their expression is the same as the one obtained for the scalar one-dimensional time-harmonic advection problem in Equation 6.22, with

the difference that μ is used instead of ν.

This example confirms the possibility to find optimal stabilisation parameters, even for the two-dimensional Linearised Euler Equations. However, obtaining this parameter becomes costly on more complicated problems and may quickly become prohibitive especially for high polynomial orders. Also, this parameter is derived out for a structured mesh and depends on the type of elements and their topology. Contrarily to what is observed by Guasch and Codina for the convected Helmholtz equation [143], this parameter does not seem to lead to significant improvements for unstructured meshes.

In the following, the steady parameter used in the literature for solving hyperbolic problems is assessed [64, 191]. It is defined as:

$$\boldsymbol{\tau}_{\mathrm{s,2D}}^{(p)} = \frac{\alpha}{p} \max\left(\frac{h_x}{2\mu_x}, \frac{h_y}{2\mu_y}\right) \boldsymbol{I}. \tag{6.28}$$

The spectral radii (μ_x, μ_y) of the flux matrices $(\boldsymbol{A}_x, \boldsymbol{A}_y)$ respectively correspond to the phase velocities associated with these matrices. α is the coefficient controlling the stability and accuracy of the scheme. This expression is similar to the one-dimensional steady stabilisation parameter $\tau_{\mathrm{s,1D}}^{(p)} = \alpha h/(2u_0 p)$ introduced in Equation 6.24. Note that Hughes and Mallet found another definition of the parameter for multi-dimensional cases [88]. The results obtained with this parameter are quite similar to those with $\boldsymbol{\tau}_{\mathrm{s,2D}}^{(p)}$, for our application cases, therefore it is not considered in the following.

6.4 Numerical Results

In this section, several numerical examples are presented in order to examine the performance of the stabilisation parameters. First, numerical results for the scalar one-dimensional time-harmonic advection problem are presented. Then, the numerical stabilisation is investigated for acoustic wave propagation in a two-dimensional straight duct.

6.4.1 One-Dimensional Test Case

The scalar one-dimensional time-harmonic advection equation is implemented and solved through the p-FEM model presented in Chapter 4. A wave propagates in the domain with unit amplitude. The system is non-dimensionalised. The convection velocity is $u = 1$. The mesh size is constant over the domain and set to $h = 1$. The simulations are performed

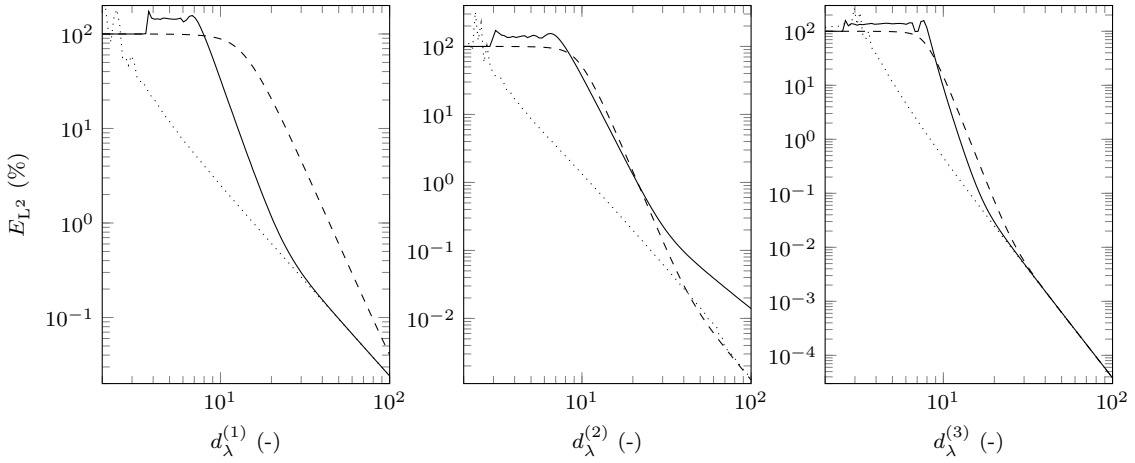

Figure 6.6: L^2-norm error against $d_\lambda^{(p)}$, for the one-dimensional time-harmonic advection problem. $n_e = 1000$. Left: $p = 1$. Middle: $p = 2$. Right: $p = 3$. Solid line: $\tau = 0$. Dashed line: $\tau = \tau_{\mathrm{s,1D}}^{(p)}$, with $\alpha = 1$. Dotted line: $\tau = \tau_{\mathrm{opt,1D}}^{(p)}$.

with $n_\mathrm{e} = 1000$ elements in the domain, in order to observe some significant dispersion error. The numerical simulation output is the L^2-norm relative error E_{L^2} between the numerical solution and the analytic solution. The numerical results compare different methods: the standard Galerkin formulation with no stabilisation, the Galerkin/Least-Squares method with the standard stabilisation parameter $\tau_{\mathrm{s,1D}}^{(p)}$ defined in Equation 6.25 and the Galerkin/Least-Squares method with the optimal parameters $\tau_{\mathrm{opt,1D}}^{(1)}$, $\tau_{\mathrm{opt,1D}}^{(2)}$ and $\tau_{\mathrm{opt,1D}}^{(3)}$.

Figure 6.6 shows the L^2-norm error against the number of degrees of freedom per wavelength for the linear, quadratic and cubic shape functions. Without stabilisation, two regions are observed: in the low-resolution regime ($d_\lambda^{(p)} < 30$), the dispersion error is significant and dominates over the interpolation error which is prevailing in the high-resolution regime ($d_\lambda^{(p)} > 30$). Stabilisation with the steady parameter $\tau_{\mathrm{s,1D}}^{(P)}$ does not improve the model accuracy in the dispersion region. Note that these curves are obtained with $\alpha = 1$. For $p = 2$, the convergence rate in the high-resolution regime is increased, which verifies the correction brought by the stabilisation parameter as discussed in Figure 6.5. As expected, the dispersion error is cancelled out by the optimal stabilisation parameters $\tau_{\mathrm{opt,1D}}^{(p)}$ which are built to suppress the nodal error. The dispersion error is also cancelled out for the high-order shape functions, although the stabilisation parameters do not enforce the exact wavenumber at the internal nodes of the elements. The convergence rates observed in the high-resolution regime are extended to the low-resolution regime: they are of order 2 for $p = 1$ and 2, and of order 4 for $p = 3$, which are the same as those observed in the dispersion analysis. Like the steady stabilisation parameter, the convergence rate in the asymptotic regime is increased by 1 for the quadratic shape functions. This confirms the

correction needed by the standard Galerkin formulation for even orders and observed in Figure 6.5.

Although the optimal stabilisation parameters perform as expected, obtaining their analytic expressions soon becomes prohibitive for high orders. Nevertheless, some additional investigation may help in finding more convenient ways for determining the optimal values of τ. Using the steady stabilisation parameter accounting for high orders should provide a reliable alternative, at least for a sufficient number of degrees of freedom per wavelength.

6.4.2 Two-Dimensional Test Case

To examine the impact of the stabilisation in two dimensions, the following test case is introduced: an acoustic plane wave propagates inside an infinite straight duct with a uniform mean flow $\boldsymbol{u}_0 = (u_{0_x}, 0)$. Hard-wall and characteristic boundary conditions are applied. The L^2-norm error is measured with respect to the analytic solution, for the mass density and the x-momentum: in this case the flow is homentropic, and the pressure and the mass density are linked by a constant factor. The errors are plotted against the number of degrees of freedom per hydrodynamic wavelength, which is analogous to the one defined in Equation 6.18:

$$d_{\lambda_\mathrm{v}}^{(p)} = \frac{2\pi p |u_{0_x}|}{\omega h}, \tag{6.29}$$

where h is the typical mesh size. The computational domain extends from $x = 0$ to $L = 1.5\,\mathrm{m}$ and from $y = 0$ to $H = 1\,\mathrm{m}$. The standard wavenumber is given by: $k_0 = 10\,\mathrm{m}^{-1}$, with $\omega = 3402.7\,\mathrm{rad\,s}^{-1}$ and $c_0 = 340.27\,\mathrm{m\,s}^{-1}$. The mean flow density is $\rho_0 = 1.225\,\mathrm{kg\,m}^{-3}$ and the specific heats ratio is $\gamma = 1.4$. In order to better observe the stabilisation effects, two mean flow configurations are investigated: an upstream propagation with Mach number $M = u_{0_x}/c_0 = -0.6$ and a downstream propagation with $M = 0.6$. The respective acoustic wavelengths are: $\lambda_\mathrm{u} \approx 0.25\,\mathrm{m}$ and $\lambda_\mathrm{d} \approx 1\,\mathrm{m}$, which correspond respectively to 6 and 1.5 wavelengths in the domain. The study is performed for $d_{\lambda_\mathrm{v}}^{(p)}$ varying from 2 to 30, with $p = 1$. The polynomial order, the angular frequency and the flow velocity being fixed, the mesh size is varied. An unstructured triangular mesh is used.

Figures 6.7 and 6.8 represent the L^2-norm errors with $p = 1$, for the downstream and upstream cases. The stabilisation scheme improves the model accuracy with respect to the case without stabilisation, in most of the cases. The dispersion region is more visible on the plot related to the upstream propagation, whereas the interpolation error is evidenced in the plot linked with the downstream propagation. In fact, for a given value of $d_{\lambda_\mathrm{v}}^{(p)}$, the

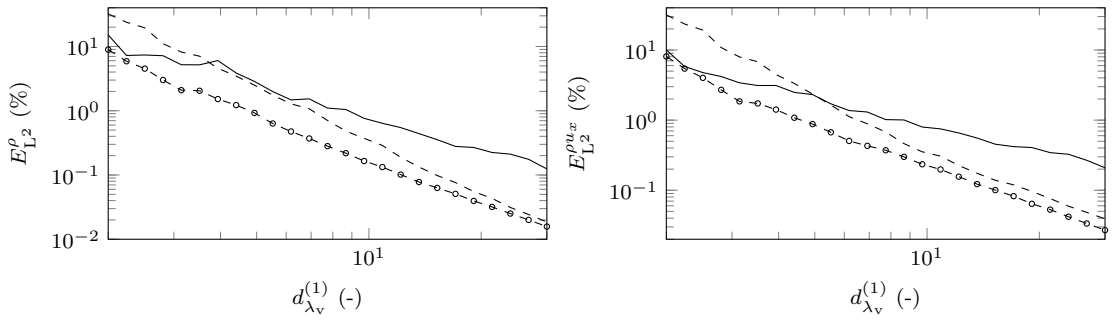

(a) Error on ρ. (b) Error on ρu_x.

Figure 6.7: L^2-norm error against $d^{(1)}_{\lambda_\mathrm{v}}$, for an acoustic plane wave in a two-dimensional infinite straight duct. $p = 1$, $k_0 = 10\,\mathrm{m}^{-1}$, $M = 0.6$. Solid line: $\boldsymbol{\tau} = \mathbf{0}$. Dashed line: $\boldsymbol{\tau} = \boldsymbol{\tau}^{(1)}_{\mathrm{s,2D}}$. No marker: $\alpha = 1$. $\circ$ marker: $\alpha = 0.1$.

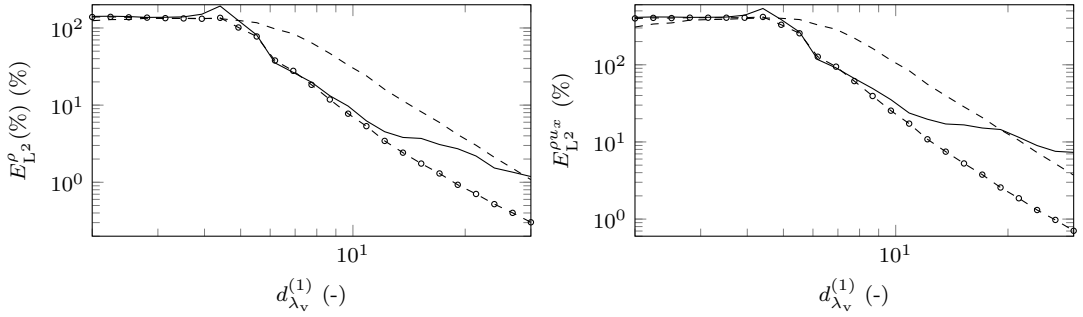

(a) Error on ρ. (b) Error on ρu_x.

Figure 6.8: L^2-norm error against $d^{(1)}_{\lambda_\mathrm{v}}$, for an acoustic plane wave in a two-dimensional infinite straight duct. $p = 1$, $k_0 = 10\,\mathrm{m}^{-1}$, $M = -0.6$. Solid line: $\boldsymbol{\tau} = \mathbf{0}$. Dashed line: $\boldsymbol{\tau} = \boldsymbol{\tau}^{(1)}_{\mathrm{s,2D}}$. No marker: $\alpha = 1$. $\circ$ marker: $\alpha = 0.1$.

corresponding number of degrees of freedom per acoustic wavelength is:

$$d^{(p)}_{\lambda_\mathrm{a}} = \frac{2\pi p(1+M)}{k_0 h} = \frac{1+M}{|M|} d^{(p)}_{\lambda_\mathrm{v}}, \tag{6.30}$$

and therefore $d^{(p)}_{\lambda_\mathrm{a}}(-|M|) < d^{(p)}_{\lambda_\mathrm{a}}(|M|)$, for a given value of the Mach number. This indicates that for a fixed value of $d^{(p)}_{\lambda_\mathrm{v}}$, there are less degrees of freedom for solving the case with $M = -0.6$ than for $M = 0.6$. In the downstream case, the lowest error is achieved with the steady parameter for $\alpha = 0.1$. It is observed that with $p = 2$ and 3, the steady parameter with $\alpha = 1$ is the most efficient. In the upstream case, the steady parameter gives the best performance at higher numbers of degrees of freedom per wavelength ($d^{(p)}_{\lambda_\mathrm{v}} > 10$). For fixed mesh and polynomial order, the angular frequency is low in the high-resolution regime. Asymptotically, this tends to solving a quasi-steady case for which the steady stabilisation parameter is optimal.

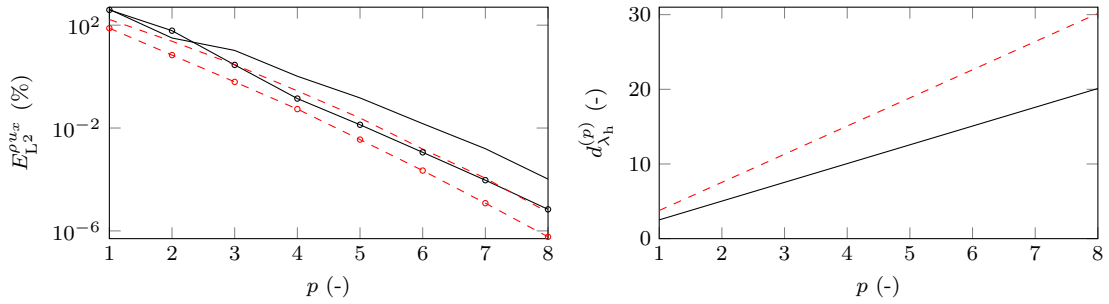

(a) Error on ρu_x.

(b) $d^{(p)}_{\lambda_\mathrm{v}}$.

Figure 6.9: Acoustic plane wave and first hydrodynamic mode in a two-dimensional infinite straight duct. $k_0 = 10$, $M = -0.6$. Solid line: acoustic plane wave. Dashed line: first hydrodynamic mode. No marker: $\boldsymbol{\tau} = 0$. $\circ$ marker: $\boldsymbol{\tau} = \boldsymbol{\tau}^{(p)}_{\mathrm{s},2D}$, with $\alpha = 1$.

6.4.3 Discussion

From these one- and two-dimensional studies, a few conclusions are drawn. The dispersion error is dominant for low orders and the optimal parameter $\boldsymbol{\tau}_x$ performs well. For high orders, the interpolation error is dominant and the time-harmonic case is close to a steady case: the steady parameter is more efficient. The indication on which parameter to use should be given by the problem to solve: within each element, a test on the number of degrees of freedom per wavelength should indicate whether using the optimal stabilisation parameter or the steady one. The proposed optimal stabilisation parameter may be useful for solving problems using the linear Finite Element Method. But the classical steady parameter should be more efficient when resorting to the high-order Finite Element Method. As an illustration of this last statement, Figure 6.9 shows the L^2-norm error on the x-momentum for the acoustic plane wave and for the first hydrodynamic mode with $M = -0.6$ and $h = 0.1\,\mathrm{m}$, against the polynomial order p. The plots are obtained without stabilisation and with the classical steady parameter. For both modes, the error is decreased by about an order of magnitude with the steady stabilisation parameter. The plot on the right-hand side shows the corresponding values of the numbers of degrees of freedom per acoustic wavelength and per hydrodynamic wavelength.

In the application test cases presented in Chapter 8, the classical Galerkin/Least-Squares stabilisation operator is used, with the two-dimensional stabilisation parameter introduced in Equation 6.28. The coefficient controlling the stability is set to $\alpha = 1$.

Chapter 7

Coupling Two Propagation Models

In this chapter, a novel method is introduced to couple the Linearised Euler Equations (LEE) with the Linearised Potential Equation (LPE) in order to reduce the final global matrix size. The motivations for this improvement and the coupling method basic ideas are discussed in the first section. The Linearised Potential Equation is presented in the second section, along with its variational formulation. In the third section, the coupling procedure is described. The method is verified in the fourth section through acoustic propagation in duct. Finally, the coupling method performances are assessed.

7.1 Motivations

Realistic aeroengine exhaust noise problems involve different physical area in the computational domain. The jet region presents strong shear layers, whereas the mean flow is generally uniform or potential outside the shear layer and in the far field. Subdividing the computational domain into smaller subdomains is therefore useful in order to optimise the computational costs, for instance in terms of memory requirements and of computational time. In this context, the Linearised Euler Equations may be solved in the strong mean flow gradient regions such as the shear layer. In the remaining domain where the mean flow can be approximated as potential, the Linearised Potential Equation may be used to solve the acoustic propagation. Solving this scalar equation is beneficial since it has only one unknown. The Linearised Euler Equations involve up to five unknowns for axisymmetric or three-dimensional problems, which means that solving the Linearised Potential Equation in adequate regions of the computational domain would scale by a factor 1/5 the number of unknowns.

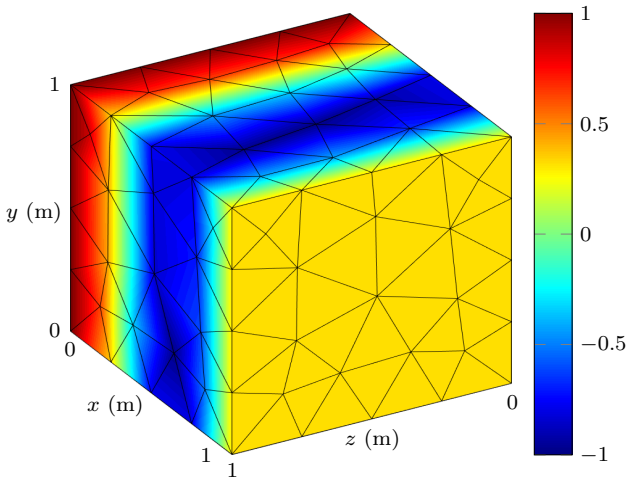

Figure 7.1: Modified pressure real part contour for an acoustic plane wave propagating in a three-dimensional unit duct. $k_0 = 5\,\mathrm{m}^{-1}$, $M = 0$, $m = 0$, $h = 0.25\,\mathrm{m}$, $p = 5$.

To illustrate the relative costs of both formulations, a three-dimensional problem is solved on the one hand with the Linearised Euler Equations and on the other hand with the Linearised Potential Equation. An acoustic plane wave propagates in a unit cube, in a medium at rest. The acoustic wavenumber is $k_0 = 5\,\mathrm{m}^{-1}$ and the characteristic mesh size is 0.25 m. Figure 7.1 displays the contours of the modified pressure real part, together with the mesh on the faces of the cube. The numerical model performances are studied in Figure 7.2, where the factorisation time and memory usage of the two mathematical models are plotted against the L^2-norm error on the pressure field. These plots have been obtained by varying the polynomial order of the shape functions from 1 to 6. The numerical solutions produced by the two models are similar. For instance at order 6, the accuracy reached on the pressure is similar for both schemes with $E^{p_c}_{\mathrm{L}^2} \approx 1.2 \times 10^{-5}\%$. However, the cost for solving the LEE is about 46 times higher. In terms of memory usage, the LEE requires 25 times more memory, which is considerable. These numbers emphasize the difficulty of applying LEE solvers to large scale three-dimensional problems, and this justifies the investigation of a hybrid LEE/LPE approach.

In this approach, the LEE would be applied in regions of strongly sheared flows and the LPE elsewhere. The challenge lies in the coupling of the two different mathematical models. Continuity conditions are applied at the interface in order to transmit the correct fluxes from a subdomain to the other. One additional difficulty lies in the fact that the Linearised Euler Equations convey vorticity and entropy waves which are not supported by the Linearised Potential Equation. Therefore, the coupling interface should be located in a region where only acoustic waves propagate so that no spurious reflections are generated.

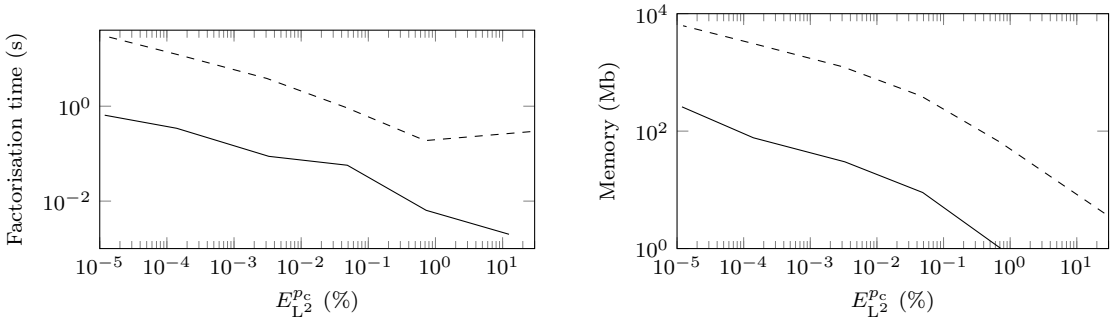

(a) Factorisation time.

(b) Memory usage.

Figure 7.2: Factorisation time and memory usage against the L^2-norm error on the modified pressure, for the three-dimensional test case. $k_0 = 5\,\mathrm{m}^{-1}$, $M = 0$, $m = 0$, $h = 0.25\,\mathrm{m}$, $p \in \{1, \cdots, 6\}$. Solid line: LPE solution. Dashed line: LEE solution.

7.2 Linearised Potential Formulation

7.2.1 Linearised Potential Equation

The basic steps to obtain the Linearised Potential Equation are presented here. In this theory, the base flow velocity component and the perturbation velocity component are both irrotational. This condition means that they can be written as: $\boldsymbol{u}_0 = \boldsymbol{\nabla}\phi_0$ and $\boldsymbol{u}' = \boldsymbol{\nabla}\phi'$, where ϕ is the velocity potential of a fluid element travelling along a streamline. As an alternative to the momentum conservation equation, Bernoulli's equation indicates that the sum of the kinetic and potential energies remains constant along a streamline. For an unsteady, compressible, homentropic, inviscid, irrotational flow that is steady at infinity, Bernoulli's equation evaluated along any streamline reads [144]:

$$H = \frac{\partial \phi}{\partial t} + \frac{1}{2}\boldsymbol{u}\cdot\boldsymbol{u} + \frac{c^2}{\gamma - 1}, \tag{7.1}$$

where H is a constant. After decomposition between the base flow and perturbation components, and linearisation, the linearised Bernoulli equation provides the density fluctuations:

$$\rho' = -\frac{\rho_0}{c_0^2}\frac{\mathrm{d}_0\phi'}{\mathrm{d}t}. \tag{7.2}$$

The fluctuations of the squared sound speed have been used for homentropic flow and perturbations with $p' = c_0^2\rho'$, such that:

$$\left(c^2\right)' = (\gamma - 1)\frac{\rho'}{\rho_0}c_0^2. \tag{7.3}$$

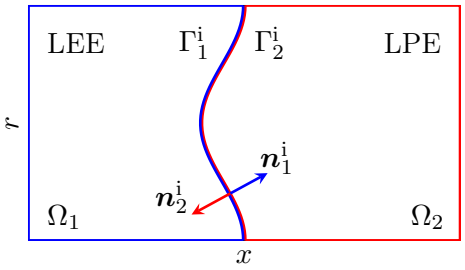

Figure 7.3: Coupling configuration between two subdomains.

Substituting the density and velocity expressions in the mass conservation equation in the Linearised Euler Equations 3.13, the Linearised Potential Equation is obtained:

$$\rho_0 \frac{\mathrm{d}_0}{\mathrm{d}t}\left(\frac{1}{c_0^2}\frac{\mathrm{d}_0\phi'}{\mathrm{d}t}\right) - \boldsymbol{\nabla}\cdot\left(\rho_0\boldsymbol{\nabla}\phi'\right) = 0. \tag{7.4}$$

7.2.2 Weighted Residual Formulation

The variational formulation of the Linearised Potential Equation 7.4 written for the velocity potential is derived on the same model as the one used to obtain the weak formulation of the Linearised Euler Equations in Section 4.1. The two-dimensional formulation reads:

$$\begin{aligned}\int_\Omega \left[-\frac{\rho_0}{c_0^2}\frac{\overline{\mathrm{d}_0 w}}{\mathrm{d}t}\frac{\mathrm{d}_0\phi}{\mathrm{d}t} + \rho_0\boldsymbol{\nabla}\overline{w}\cdot\boldsymbol{\nabla}\phi\right]\mathrm{d}x\mathrm{d}y \\ = -\int_\Gamma \frac{\rho_0}{c_0^2}\overline{w}\left[\mathrm{j}\omega\boldsymbol{u}_0\cdot\boldsymbol{n}\phi + \left((\boldsymbol{u}_0\cdot\boldsymbol{n})^2 - c_0^2\right)\frac{\partial\phi}{\partial n} + (\boldsymbol{u}_0\cdot\boldsymbol{n})(\boldsymbol{u}_0\cdot\boldsymbol{\tau})\frac{\partial\phi}{\partial\tau}\right]\mathrm{d}\Gamma,\end{aligned} \tag{7.5}$$

where w is the weighting function and $\boldsymbol{\tau}$ is the unit tangential vector to the boundary Γ. The velocity potential gradients along the normal and tangential directions are noted: $\partial\phi/\partial n = \boldsymbol{\nabla}\phi\cdot\boldsymbol{n}$ and $\partial\phi/\partial\tau = \boldsymbol{\nabla}\phi\cdot\boldsymbol{\tau}$. The superscript notation has been dropped from the velocity potential, and from here onwards ϕ represents the velocity potential perturbations.

7.3 Coupling Procedure

A computational domain composed of two non-overlapping subdomains Ω_1 and Ω_2, respectively for solving the Linearised Euler Equations and the Linearised Potential Equation, is considered. Figure 7.3 shows the two subdomains as well as the interface where the boundaries Γ_1^{i} and Γ_2^{i} are geometrically identical, although they respectively belong to each subdomain. The superscript $^{\mathrm{i}}$ denotes the interface. The normal vectors $\boldsymbol{n}_1^{\mathrm{i}}$ and $\boldsymbol{n}_2^{\mathrm{i}}$ to the interface boundaries point toward their respective domain exterior. Along the

interface, the transmission conditions must provide the correct source term within each boundary integral of the variational formulations. These coupling conditions are discussed in the following paragraphs.

7.3.1 Robin Boundary Conditions

Choosing the boundary conditions at the interface is crucial for the transmission condition. The characteristic boundary conditions are used here, which are equivalent to Robin boundary conditions. Considering a given subdomain, the incoming waves imposed through the characteristics are given by the solution from the other domain. As explained in Section 4.2, the numerical solution is split between incoming and outgoing waves. Imposing the incoming waves while letting the outgoing waves free inside the domain properly sets the system. The acoustic characteristics propagate along the normal vector $\boldsymbol{n}$ to the boundary with velocities: $\lambda_{\pm} = \pm c_0 + \boldsymbol{u}_0 \cdot \boldsymbol{n}$. This one-dimensional approximation with a uniform mean flow leads to the generalised Robin boundary condition which reads:

$$\frac{\partial \phi}{\partial n} + \mathrm{j} k_{+}^{\mathrm{c}} \phi = g_n, \tag{7.6}$$

where g_n is the source term denoting the characteristic travelling along $\boldsymbol{n}$, and $k_{+}^{\mathrm{c}} = \omega/(c_0 + \boldsymbol{u}_0 \cdot \boldsymbol{n})$ is the outgoing acoustic wavenumber. The final formulation for the Linearised Potential Equation reads:

$$\begin{aligned} \int_{\Omega} \left[-\frac{\rho_0}{c_0^2} \overline{\frac{\mathrm{d}_0 w}{\mathrm{d}t}} \frac{\mathrm{d}_0 \phi}{\mathrm{d}t} + \rho_0 \boldsymbol{\nabla} \overline{w} \cdot \boldsymbol{\nabla} \phi \right] \mathrm{d}x\mathrm{d}y \\ + \int_{\Gamma} \frac{\rho_0}{c_0^2} \overline{w} \left[\mathrm{j}\omega \boldsymbol{u}_0 \cdot \boldsymbol{n} \phi - \mathrm{j} k_{+}^{\mathrm{c}} \left((\boldsymbol{u}_0 \cdot \boldsymbol{n})^2 - c_0^2 \right) \phi + (\boldsymbol{u}_0 \cdot \boldsymbol{n}) (\boldsymbol{u}_0 \cdot \boldsymbol{\tau}) \frac{\partial \phi}{\partial \tau} \right] \mathrm{d}\Gamma \\ = - \int_{\Gamma} \frac{\rho_0}{c_0^2} \left((\boldsymbol{u}_0 \cdot \boldsymbol{n})^2 - c_0^2 \right) \overline{w} g_n \mathrm{d}\Gamma, \end{aligned} \tag{7.7}$$

where only the right-hand side boundary integral contributes as a source term through the characteristic g_n. Within the coupling technique, this term needs to be specified at the interface in terms of the variables in the interfacing subdomain.

7.3.2 Coupling Terms

First, subdomain 2 is considered. In that domain, the Linearised Potential Equation is solved. Along the interface, the boundary integral which contributes to the application of

the incoming waves can be written:

$$\mathrm{B}^{\mathrm{i}}_{\mathrm{LPE}} = -\int_{\Gamma^{\mathrm{i}}_2} \frac{\rho_0}{c_0^2}\left(\left(\boldsymbol{u}_0 \cdot \boldsymbol{n}^{\mathrm{i}}_2\right)^2 - c_0^2\right)\overline{w}_2 g_{n_{1\to2}} \mathrm{d}\Gamma^{\mathrm{i}}_2, \tag{7.8}$$

where $g_{n_{1\to2}}$ is the source term imposed from the solution in the Linearised Euler Equations domain. From Equation 7.6, the source term along Γ^{i}_2 is written:

$$g_{n_{1\to2}} = \frac{\partial \phi_1}{\partial n^{\mathrm{i}}_2} + \mathrm{j}k^{\mathrm{c}}_+ \phi_1, \tag{7.9}$$

where the velocity potential ϕ_1 is the contribution from domain 1 (Linearised Euler Equations), which must be expressed in terms of the variables available in domain 1. From the velocity potential definition and the density expression in Equation 7.2, an expression of the velocity potential in terms of the velocity and the density can be derived:

$$\phi = -\frac{1}{\mathrm{j}\omega}\left(\frac{c_0^2}{\rho_0}\rho + \boldsymbol{u}_0 \cdot \boldsymbol{u}\right). \tag{7.10}$$

In this work, the Linearised Euler Equations are solved for the conservative variables. In terms of these variables, the velocity potential reads:

$$\phi = \frac{1}{\mathrm{j}\omega\rho_0}\left(\left(u_0^2 - c_0^2\right)\rho - \boldsymbol{u}_0 \cdot (\rho\boldsymbol{u})\right), \tag{7.11}$$

where $u_0 = \|\boldsymbol{u}_0\|$ is the mean flow velocity vector norm.

From the perspective of domain 1, the interface boundary integral is split between the contributions from the incoming and outgoing waves. This is performed by decomposing the flux matrix like: $\boldsymbol{F}_1 = \boldsymbol{F}_1^+ + \boldsymbol{F}_1^-$, where the flux matrices $\boldsymbol{F}_1^\pm$ depend on the diagonal eigenvalues matrix $\boldsymbol{\Lambda}_1^\pm$ and on the eigenvectors matrix $\boldsymbol{W}_1$ (see Section 4.2.1). The boundary integral involving the incoming characteristics is then:

$$\mathrm{B}^{\mathrm{i}}_{\mathrm{LEE}} = -\int_{\Gamma^{\mathrm{i}}_1} \boldsymbol{w}_1^{\mathrm{T}} \boldsymbol{F}_1^- \boldsymbol{q}_{2\to1} \mathrm{d}\Gamma^{\mathrm{i}}_1, \tag{7.12}$$

where the flux matrix $\boldsymbol{F}_1^- = \boldsymbol{W}_1 \boldsymbol{\Lambda}_1^- \boldsymbol{W}_1^{-1}$ depends on the negative eigenvalues and is such that only the incoming characteristics are selected. The variable vector $\boldsymbol{q}_{2\to1}$ is built from the numerical solution in domain 2 (Linearised Potential Equation). From the expressions of the velocity, density and pressure fields in terms of the velocity potential given in Section

7.2.1, the variable vector reads:

$$\boldsymbol{q}_{2\to1} = \left\{ \begin{array}{lcl} & - & \dfrac{\rho_0}{c_0^2}\dfrac{\mathrm{d}_0\phi_2}{\mathrm{d}t} \\ \rho_0\dfrac{\partial\phi_2}{\partial x} & - & \dfrac{\rho_0}{c_0^2}\dfrac{\mathrm{d}_0\phi_2}{\mathrm{d}t}u_{0_x} \\ \rho_0\dfrac{\partial\phi_2}{\partial y} & - & \dfrac{\rho_0}{c_0^2}\dfrac{\mathrm{d}_0\phi_2}{\mathrm{d}t}u_{0_y} \\ & - & \dfrac{p_{\mathrm{c}_0}}{c_0^2}\dfrac{\mathrm{d}_0\phi_2}{\mathrm{d}t} \end{array} \right\}. \tag{7.13}$$

This coupling method combines two mathematical models which do not support the exact same waves: while the Linearised Potential Equation only supports the right- and left-propagating acoustic waves, the Linearised Euler Equations also contain the vorticity and entropy waves. For that reason and in order to avoid spurious reflections, the interface boundary should be placed in a region where the vorticity and entropy waves amplitude is not significant with respect to the acoustic waves. In the framework of aeroengine noise, the vorticity waves develop along the jet shear layer as a vortex shedding: the interface boundary should therefore not be placed in that region.

7.3.3 Requirements

The proposed coupling technique is quite general and may be applied to several mathematical models. However, a few requirements need to be considered. First, the coupling procedure relies on the ability to directly express the variables in each subdomain in terms of the variables in the interfacing subdomain. In other words, there should exist operator matrices $\boldsymbol{U}_{1\to2}$ and $\boldsymbol{U}_{2\to1}$ such that: $\boldsymbol{q}_1 = \boldsymbol{U}_{2\to1}\boldsymbol{q}_2$ and $\boldsymbol{q}_2 = \boldsymbol{U}_{1\to2}\boldsymbol{q}_1$, where $\boldsymbol{q}_1$ and $\boldsymbol{q}_2$ are the variable vectors in each domain. In the framework of the Linearised Potential Equation coupled with the Linearised Euler Equations, the variable vectors are: $\boldsymbol{q}_1 = \{\rho,\, \rho u_x,\, \rho u_y,\, p_{\mathrm{c}}\}^{\mathrm{t}}$ and $\boldsymbol{q}_2 = \phi$. From Equations 7.11 and 7.13, the transformation operator matrices read:

$$\boldsymbol{U}_{2\to1} = \rho_0 \left\{ \begin{array}{c} 0 \\ \dfrac{\partial}{\partial x} \\ \dfrac{\partial}{\partial y} \\ 0 \end{array} \right\} - \frac{\rho_0}{c_0^2} \left\{ \begin{array}{c} 1 \\ u_{0_x} \\ u_{0_y} \\ p_{\mathrm{c}} \end{array} \right\} \frac{\mathrm{d}_0}{\mathrm{d}t}, \tag{7.14}$$

and $\boldsymbol{U}_{1\to 2} = \dfrac{1}{\mathrm{j}\omega\rho_0}\begin{bmatrix}(u_0^2 - c_0^2) & -u_{0_x} & -u_{0_y} & 0\end{bmatrix}$.

Regarding the numerical method, the static condensation introduced in Section 4.3.5 cannot be applied on the elements along the interface. Since the degrees of freedom, including the interior degrees of freedom, are coupled along the interface, between both domains, no direct expression of the bubble degrees of freedom can be found in terms of the remaining degrees of freedom. Static condensation remains applicable on the rest of the domain.

7.4 Verification

In order to verify the coupling method, several test cases are considered. First, the code implementation is verified for the Linearised Potential Equation, as well as the coupling conditions between two subdomains solving that equation. Then, the coupling technique is verified between two subdomains solving the Linearised Euler Equations. Finally, the coupling technique between the Linearised Potential Equation and the Linearised Euler Equations is validated.

7.4.1 Linearised Potential Equation

A two-dimensional infinite straight duct is considered with characteristic boundary conditions, where the Linearised Potential Equation is solved. An acoustic plane wave propagates in the duct in the positive x-direction, with an axial uniform mean flow. In the following, the mean flow Mach number is: $M = 0.6$. The duct is 1 m large and high, and the typical mesh size is 0.5 m such that 4 triangular elements compose the mesh, as seen in Figure 7.4. Hard-wall boundary conditions are applied at $y = 0$ and $y = 1\,\mathrm{m}$. The coupling interface is placed vertically in the middle of the duct at $x = 0.5\,\mathrm{m}$, in such a way that the plane wave is orthogonal to the interface. A single domain with no interface is also considered for comparison with the coupled subdomains. The same mesh is used for that single domain.

The relative error between the numerical and analytic solutions is measured on the velocity potential. The L^2- and H^1-norm errors are plotted against the Helmholtz number $k_0 h$ in Figure 7.5, where h is fixed and k_0 is varied from $0.01\,\mathrm{m}^{-1}$ to $100\,\mathrm{m}^{-1}$. The polynomial order varies from 1 to 9. It is observed that the L^2-norm convergence in the high-resolution regime is of order p for the coupling technique, whereas it is of order $p+1$ for the single domain. On the other hand, the H^1-norm convergence is of order p for both cases. This is explained by the gradient component present in the source term $g_{n_{1\to 2}}$ (see Equation 7.9)

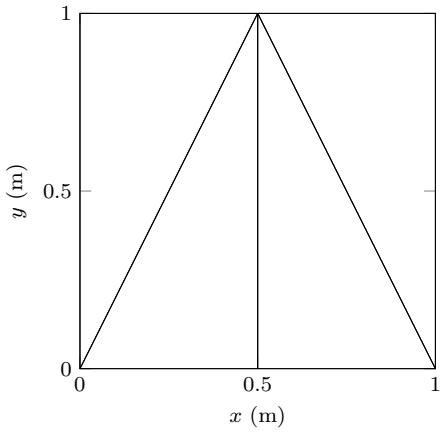

Figure 7.4: Mesh for coupling verification with the Linearised Potential Equation (interface at $x = 0.5\,\mathrm{m}$).

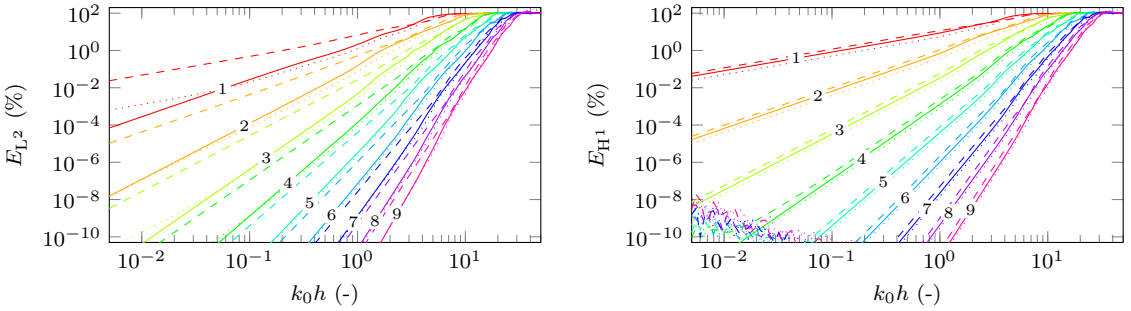

(a) L^2-norm.

(b) H^1-norm.

Figure 7.5: Error against the Helmholtz number, for an acoustic plane wave in a two-dimensional duct, solving the Linearised Potential Equation. $h = 0.5\,\mathrm{m}$, $M = 0.6$. Solid line: no coupling, one single domain. Dashed line: coupling, with $p_{\mathrm{int}} = p$. Dotted line: coupling, with $p_{\mathrm{int}} = p + 1$.

introduced along the interface (as shown by Equation 7.8) and which must be evaluated within the coupling scheme, unlike the no-coupling case. This term is such that the numerical scheme looses one accuracy order along the interface. For the H^1-norm error, the gradient term is integrated in the norm computation which makes the errors without and with coupling similar.

In order to circumvent this loss of accuracy, the polynomial order p_{int} in the elements along the interface is incremented by 1. This is applied both to the triangular elements along the interface and to each of their three edges. The dotted curves show the errors obtained with this procedure: with coupling, the accuracy becomes similar to the one obtained without coupling. If the plane wave propagation direction is parallel to the interface, it is observed that no additional error is introduced by the coupling: in that case, the solution gradient in the propagation direction is zero. Increasing the polynomial order along the interface translates into a slight increase of the number of degrees of freedom, which should not be

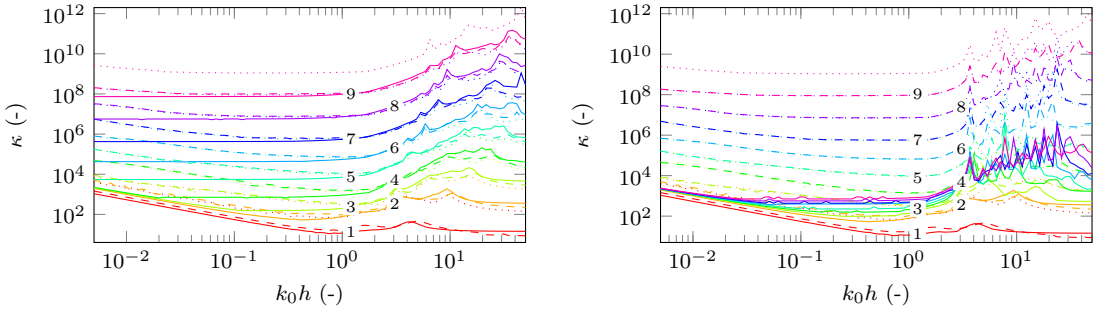

(a) No condensation.

(b) With condensation.

Figure 7.6: Condition number against the Helmholtz number, for an acoustic plane wave in a two-dimensional duct, solving the Linearised Potential Equation. $h = 0.5\,\mathrm{m}$, $M = 0.6$. Solid line: no coupling, one single domain. Dashed line: coupling, with $p_{\mathrm{int}} = p$. Dotted line: coupling, with $p_{\mathrm{int}} = p + 1$.

significant when solving real test cases. The H^1-norm error oscillations observed for the high orders are due to the low error and high condition number which are such that the machine precision is reached.

Figure 7.6 shows the condition number κ measured in the L^1-norm (see Equation 5.4) against the Helmholtz number, with and without condensation. The coupling technique with $p_{\mathrm{int}} = p$ is such that the condition number is similar to the case with a single domain and no condensation, except in the very high-resolution regime where the condition number increases more with coupling. Using $p_{\mathrm{int}} = p + 1$ along the interface significantly increases the condition number, up to a factor 20 for $p = 9$. In the lower resolution regime, this factor is of order 7, still for $p = 9$. This difference increases with p. With condensation, the condition number improvement is significant with the single domain solution where its value is drastically reduced with respect to the case without condensation. Since no condensation is applied in the elements along the interface, the coupled solution is less efficient in terms of condition number which remains similar to the case without condensation and increases in the very-high resolution regime. However, in practical applications the mid-resolution regime is more of interest and the condition number increase due to the absence of condensation in the elements along the interface should not be an issue.

7.4.2 Linearised Euler Equations

The test case is now applied with the Linearised Euler Equations. The stabilised formulation is used to solve the acoustic plane wave propagation in the two-dimensional infinite straight duct. The L^2- and H^1-norm errors are plotted against the Helmholtz number in Figures 7.7 and 7.8 respectively, both for the density and the x-momentum. For the

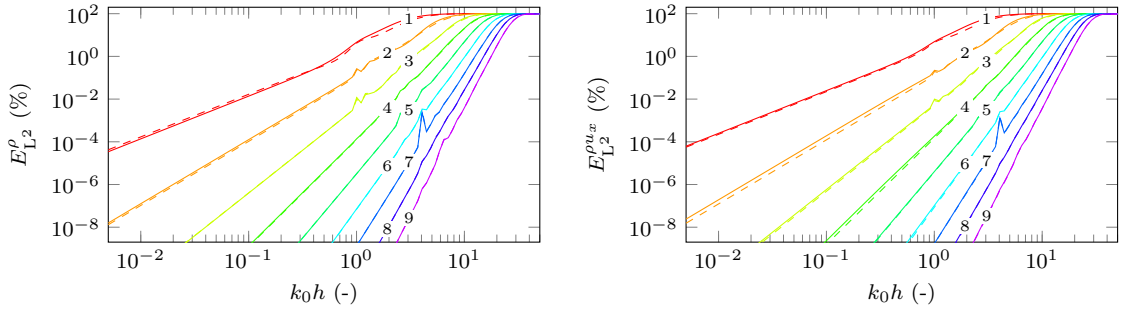

(a) Error on ρ.

(b) Error on ρu_x.

Figure 7.7: L^2-norm error against the Helmholtz number, for an acoustic plane wave in a two-dimensional duct, solving the Linearised Euler Equations. $h = 0.5\,\mathrm{m}$, $M = 0.6$. Solid line: no coupling, one single domain. Dashed line: coupling, with $p_{\mathrm{int}} = p$.

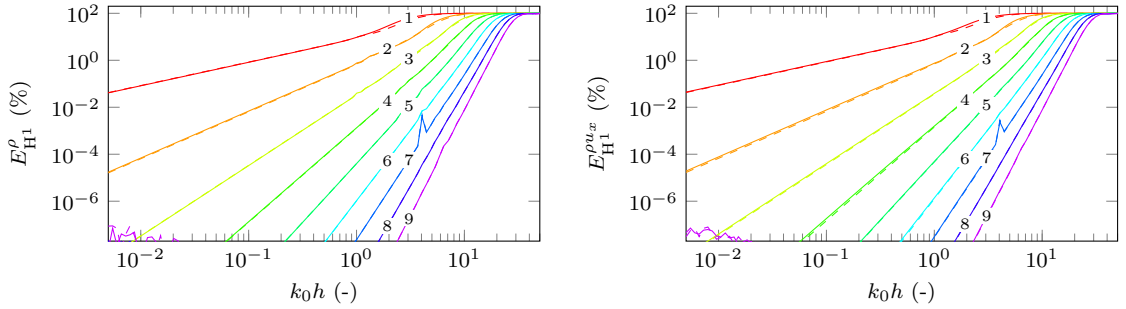

(a) Error on ρ.

(b) Error on ρu_x.

Figure 7.8: H^1-norm error against the Helmholtz number, for an acoustic plane wave in a two-dimensional duct, solving the Linearised Euler Equations. $h = 0.5\,\mathrm{m}$, $M = 0.6$. Solid line: no coupling, one single domain. Dashed line: coupling, with $p_{\mathrm{int}} = p$.

acoustic plane wave with uniform mean flow, the density and pressure are proportional and the y-momentum equals zero. For both variables and for both error measures, the numerical model accuracy is similar between the single domain solution and the coupled solution. This is explained by the form of the boundary integral along the interface for the Linearised Euler Equations. Unlike the Linearised Potential Equation, it does not involve any variable derivative and the gradient terms are not explicitly present in the integral. Therefore, no additional error is made through the transmission conditions across the interface. The propagation of vorticity and entropy waves inside the duct gives similar results, and the same accuracy between the single domain solution and the coupled solution is observed. For the sake of completeness, the same conclusions also apply to higher mode numbers ($m \geq 1$) for all types of waves (acoustic, vorticity and entropy).

Figure 7.9 shows that the coupling interface does not increase the global matrix system condition number in the case without condensation. On the contrary, in comparison to the single domain solution with condensation, the condensed coupled solution presents higher

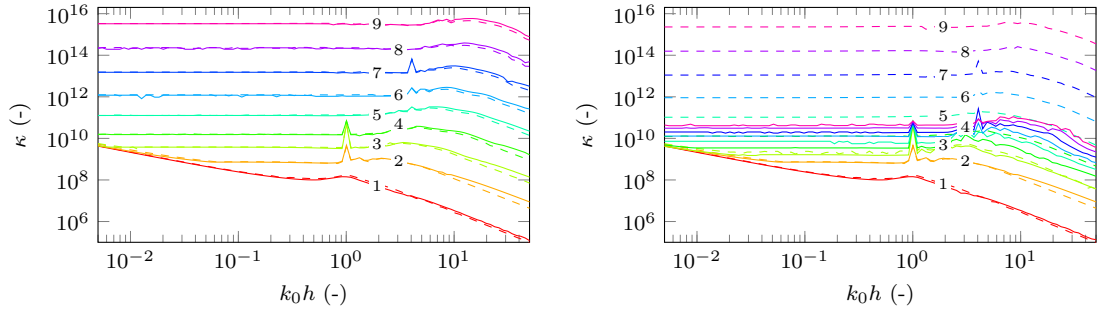

(a) No condensation.

(b) With condensation.

Figure 7.9: Condition number against the Helmholtz number, for an acoustic plane wave in a two-dimensional duct, solving the Linearised Euler Equations. $h = 0.5\,\mathrm{m}$, $M = 0.6$. Solid line: no coupling, one single domain. Dashed line: coupling, with $p_{\mathrm{int}} = p$.

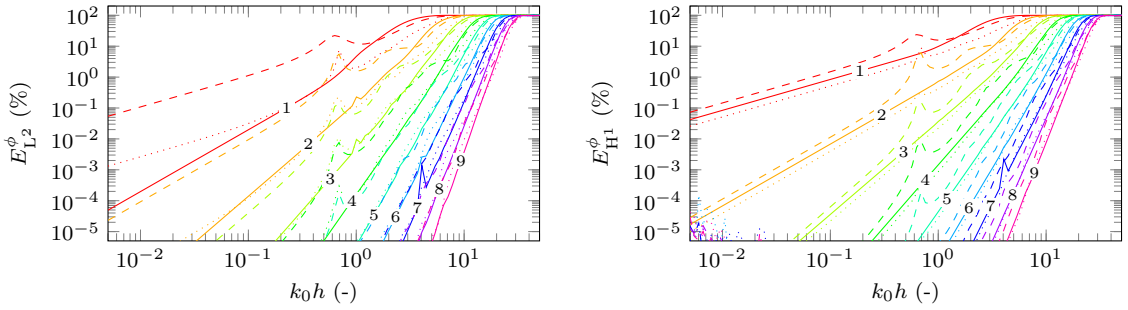

(a) L^2-norm.

(b) H^1-norm.

Figure 7.10: Error against the Helmholtz number, for an acoustic plane wave in a two-dimensional duct, solving the Linearised Euler Equations coupled with the Linearised Potential Equation. $h = 0.5\,\mathrm{m}$, $M = 0.6$. Solid line: no coupling, one single domain. Dashed line: coupling, with $p_{\mathrm{int}} = p$. Dotted line: coupling, with $p_{\mathrm{int}} = p + 1$.

levels of condition number. This indicates that the absence of condensation along the interface has some dominant effect on the global system matrix condition number.

7.4.3 Coupling Between the Linearised Euler Equations and the Linearised Potential Equation

The coupling between the Linearised Euler Equations and the Linearised Potential Equation is now verified. The acoustic plane wave propagates in the same two-dimensional infinite straight duct, where the Linearised Euler Equations are solved in the left-hand side subdomain and the Linearised Potential Equation is solved in the right-hand side subdomain. The mesh is the same as the one used for the previous cases (see Figure 7.4), and the coupling transmission conditions are applied along the interface at $x = 0.5\,\mathrm{m}$. The L^2- and H^1-norm errors on the velocity potential are plotted in Figure 7.10 The L^2-norm error on the coupled solution with $p_{\mathrm{int}} = p$ converges in the asymptotic regime with one

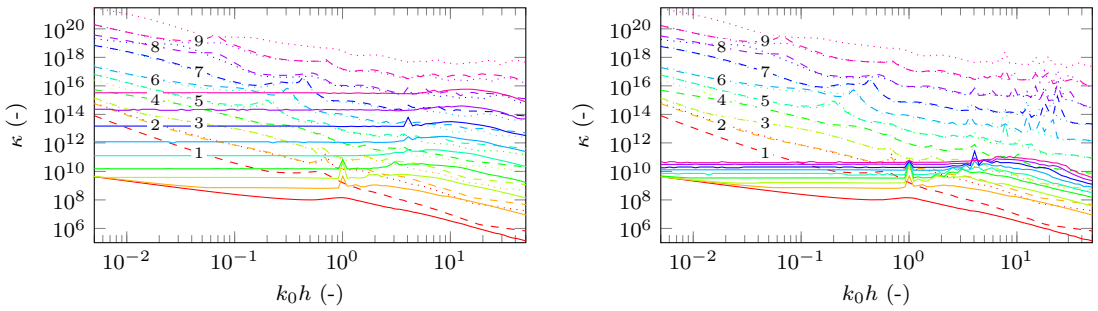

(a) No condensation.

(b) With condensation.

Figure 7.11: Condition number against the Helmholtz number, for an acoustic plane wave in a two-dimensional duct, solving the Linearised Euler Equations coupled with the Linearised Potential Equation. $h = 0.5\,\mathrm{m}$, $M = 0.6$. Solid line: no coupling, one single domain. Dashed line: coupling, with $p_{\mathrm{int}} = p$. Dotted line: coupling, with $p_{\mathrm{int}} = p + 1$.

order less than the single domain solution. On the contrary, the coupled solution with $p_{\mathrm{int}} = p + 1$ retrieves the convergence rate of the single domain solution and is as accurate. Regarding the H^1-norm error, the convergence rates are equal for all solutions and the error levels are similar. These observations are consistent with the conclusions from the previous sections. Moreover, some peaks are visible in the error curves and are emphasized with the coupling. These peaks may be due to some aliasing effects: the bubble functions are the cause for possible singular or poorly conditioned global system matrices [51]. In terms of condition number, the same conclusions as those described in the previous sections can be drawn. Figure 7.11 shows that the coupling procedure increases the condition number, and this increase grows in the high-resolution regime. The use of static condensation does not improve the condition number for the coupled solution, unlike the single domain solution.

Coupling with Non-Uniform Mean Flow

In order to further assess the accuracy of the coupling method, another test case is considered. An acoustic duct mode propagates in a straight duct where the mean flow has boundary layers along the duct hard-walls and is constant in the center part of the duct. Like in Section 3.4.1, the mean flow velocity field is expressed as: $\boldsymbol{u}_0 = u_{0_x} f_{\mathrm{bl}}(y) \boldsymbol{e}_x$. The analytic expression of the boundary layer mean flow velocity profile f_{bl} is:

$$f_{\mathrm{bl}}(y) = \begin{cases} -\left(\dfrac{y}{\delta}\right)^2 + 2\dfrac{y}{\delta} & , \text{if } 0 \leq y \leq \delta \\ 1 & , \text{if } \delta < y < H - \delta \\ -\left(\dfrac{y}{\delta}\right)^2 + 2\dfrac{H-\delta}{\delta}\dfrac{y}{\delta} - \dfrac{H-2\delta}{\delta}\dfrac{H}{\delta} & , \text{if } H - \delta \leq y \leq H \end{cases}, \tag{7.15}$$

where H is the duct height and δ is the boundary layer thickness. In the following the duct height is $H = 1\,\mathrm{m}$ and its length is $L = 0.5\,\mathrm{m}$, while the characteristic mesh size

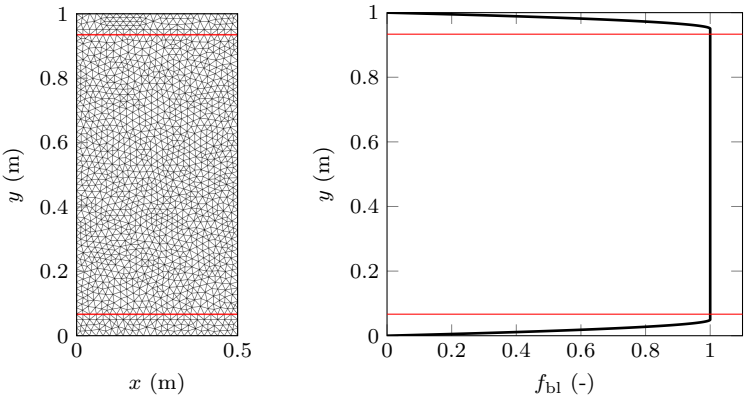

(a) Mesh. (b) Velocity profile.

Figure 7.12: Unstructured triangular mesh for coupling and non-uniform flow profile.

is $h = 0.02\,\mathrm{m}$ in the whole computational domain. The boundary layer thickness is $\delta = H/20 = 0.05\,\mathrm{m}$, i.e. two to three elements discretise the boundary layer in the transverse direction. Figure 7.12 shows the computational domain with the unstructured triangular mesh and the mean flow velocity profile. The red lines indicate the position of the coupling interfaces, along the x-axis at $y = H/15 = 0.067\,\mathrm{m}$ and at $y = 14H/15 = 0.933\,\mathrm{m}$. They are deliberately placed one mesh element outside the boundary layers in order to allow a proper coupling. The Linearised Euler Equations are solved in the boundary layer regions ($0 \leq y \leq \delta$ and $H - \delta \leq y \leq H$) while the Linearised Potential Equation is solved between these two non-uniform regions ($\delta < y < H - \delta$). 388 triangular elements compose the subdomains where the LEE are solved, and 2410 elements compose the subdomain where the LPE is solved. The mean flow Mach number at the center of the duct is $M = 0.5$, and the second non-plane acoustic mode propagates in the duct ($m = 2$) with the standard wavenumber $k_0 = 100\,\mathrm{m}^{-1}$. Figure 7.13 shows the contours of the real parts of the momentum components for this configuration. The L^2-norm errors measured against the semi-analytic solutions obtained like in Section 3.4 are shown in Figure 7.14 against the polynomial order which varies from 1 to 10. Two types of curves are plotted: the solid lines correspond to the full LEE solution while the dashed lines correspond to the coupled solution. The convergence is observed and no major difference in the error is found between the two configurations. This confirms the ability of the proposed coupling technique to handle propagation in non-uniform mean flows. The plateau in the convergence for $p \geq 8$ is due to the error introduced by the mean flow interpolation in the boundary layer, as discussed in Section 5.3.2. The benefits introduced by the coupling procedure are illustrated in Figure 7.15 where the computational times and the memory usage are plotted against the polynomial order. For the range of orders where the problem is accurately solved

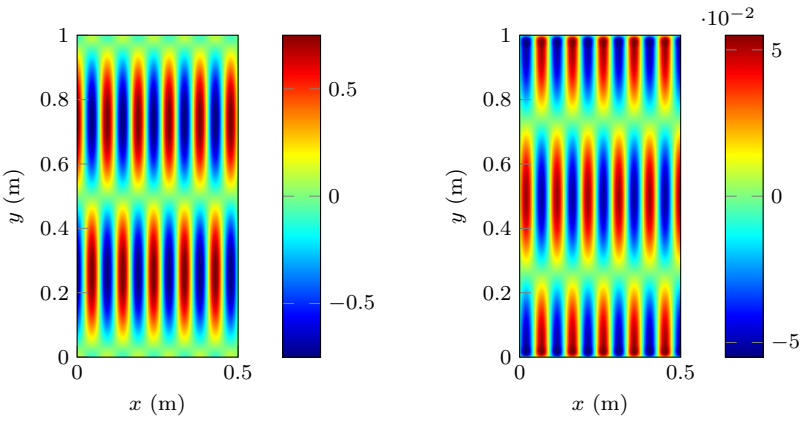

(a) $\Re(\rho u_x)$. (b) $\Re(\rho u_y)$.

Figure 7.13: Momentum real part contours for the coupling test case with non-uniform mean flow. $k_0 = 100\,\mathrm{m}^{-1}$, $M = 0.5$, $m = 2$, $h = 0.02\,\mathrm{m}$, $p = 5$.

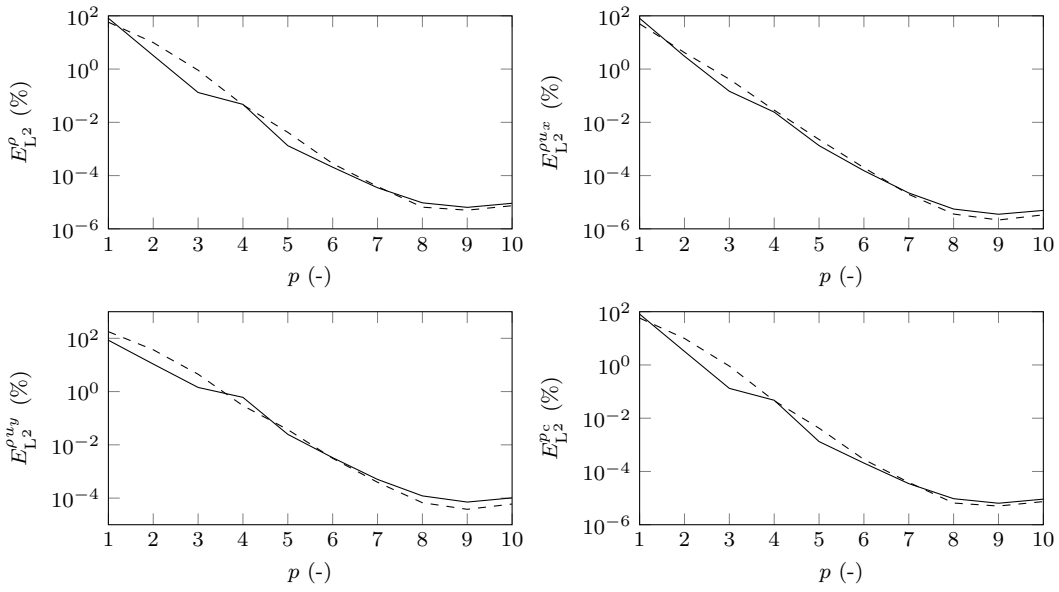

Figure 7.14: L^2-norm error against the polynomial order, for the coupling test case with non-uniform mean flow. $k_0 = 100\,\mathrm{m}^{-1}$, $M = 0.5$, $m = 2$, $h = 0.02\,\mathrm{m}$, $p \in \{1, \cdots, 10\}$. Solid line: full LEE solution. Dashed line: coupled solution. Top left: ρ. Top right: ρu_x. Bottom left: ρu_y. Bottom right: p_c.

($E_{\mathrm{L}^2} < 1\,\%$ for $p \geq 4$), the factorisation time with coupling is about 10 times lower than for the full LEE. This factor is around 7 for the total time. In terms of memory usage, the requirements for the coupled solution are about 6 times lower than for the full LEE solution. These results show the profit that can be earned from the coupling technique. Some more comments on the coupling performance and benefits are discussed in the following section.

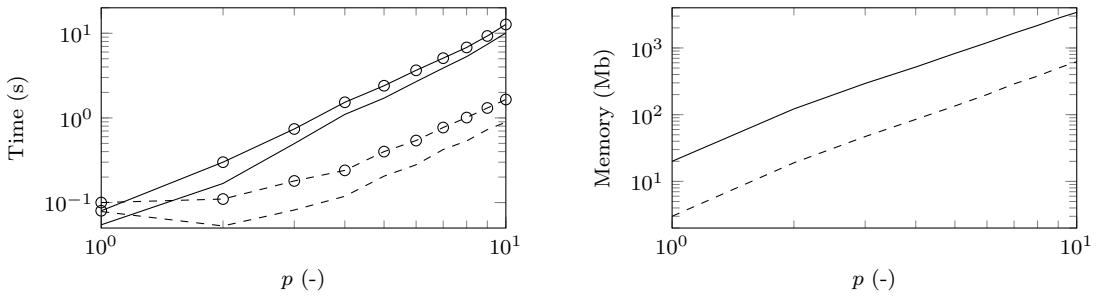

(a) Factorisation (no marker) and total (∘ marker) solving times.

(b) Memory usage.

Figure 7.15: Computational time and memory usage against the polynomial order, for the coupling test case with non-uniform mean flow. $k_0 = 100\,\mathrm{m}^{-1}$, $M = 0.5$, $m = 2$, $h = 0.02\,\mathrm{m}$, $p \in \{1, \cdots, 10\}$. Solid line: full LEE solution. Dashed line: coupled solution.

7.5 Performance of the Coupling Method

The main objective of the coupling method is to further reduce the computational costs in terms of computational time and memory requirements. These performances are assessed in this section. As an example, the coupling method performance is shown on the following test case, with a high wavenumber. The acoustic mode $m = 1$ propagates in a two-dimensional squared infinite straight duct of length 1 m. The wave propagates upstream with the standard wavenumber $k_0 = 50\,\mathrm{m}^{-1}$, in a mean flow with Mach number $M = -0.6$. The wavenumber in the propagation direction is: $k_x = 124.9\,\mathrm{m}^{-1}$. This configuration is such that about 20 waves are present in the domain. The typical mesh size is: $h = 0.05\,\mathrm{m}$, which is the same dimension as one acoustic wavelength. The coupling interface is placed at $x = h$, and the hard-wall boundary conditions are imposed at $y = 0$ and 1 m. The computational domain is composed of 722 structured triangular elements, of which 38 elements are in the subdomain where the Linearised Euler Equations are solved and 684 elements where the Linearised Potential Equation is solved. With these parameters, about 5.3 % of the domain is solved with the Linearised Euler Equations, while 94.3 % is solved with the Linearised Potential Equation. Figure 7.16 shows the mesh and the modified pressure field in the duct.

Solving this problem with $p = 7$ and with condensation gives the following results. The full Linearised Euler Equations solution involves 28504 degrees of freedom and requires 376 Mb to store the system matrix. The L^2-norm error on the velocity potential is: $E^{\phi}_{\mathrm{L}^2} = 0.49\,\%$. The coupled solution with $p_{\mathrm{int}} = p$ involves 10191 degrees of freedom, i.e. almost 3 times less than the full Linearised Euler Equations. The memory usage is 47 Mb and the L^2-norm error is $E^{\phi}_{\mathrm{L}^2} = 0.92\,\%$, which is not as accurate as the single domain solution. Considering

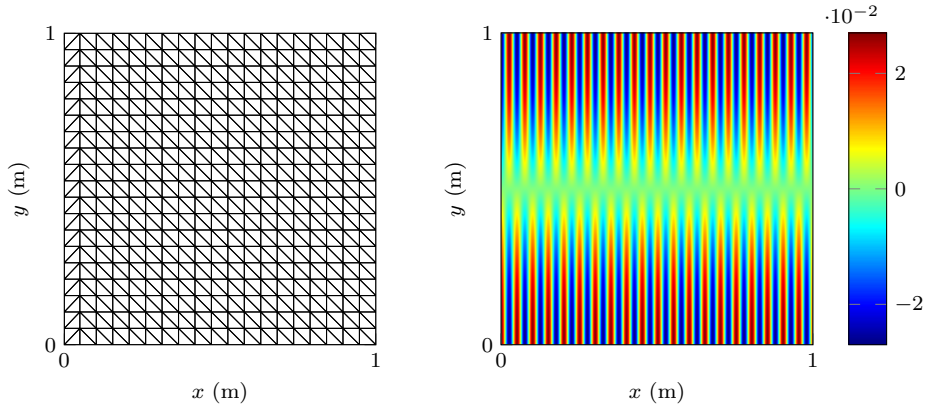

(a) Mesh. (b) $\Re(p_c)$.

Figure 7.16: Mesh and real part of the modified pressure, for the first non-plane acoustic mode in a two-dimensional duct with axial uniform mean flow, solving the Linearised Euler Equations coupled with the Linearised Potential Equation. $k_0 = 50\,\mathrm{m}^{-1}$, $h = 0.05\,\mathrm{m}$, $M = 0.6$.

the coupled solution with $p_{\mathrm{int}} = p + 1$, 11046 degrees of freedom compose the system. The memory usage is 55 Mb, which is slightly more than the coupled solution with $p_{\mathrm{int}} = p$ but still about 7 times lower than the full Linearised Euler Equations. In terms of accuracy, the L^2-norm error is: $E^{\phi}_{\mathrm{L}^2} = 0.35\,\%$.

In order to better assess the benefit of the coupling procedure in terms of memory usage, the test case is ran for several values of the ratio $\tau^{n_\mathrm{e}}_{\mathrm{LEE/LPE}}$. This ratio is defined like:

$$\tau^{n_\mathrm{e}}_{\mathrm{LEE/LPE}} = \frac{n_\mathrm{e}^{\mathrm{LEE}}}{n_\mathrm{e}^{\mathrm{LEE}} + n_\mathrm{e}^{\mathrm{LPE}}}, \tag{7.16}$$

where $n_\mathrm{e}^{\mathrm{LEE}}$ is the number of triangular elements in the subdomain where the Linearised Euler Equations are solved, and $n_\mathrm{e}^{\mathrm{LPE}}$ is the number of triangular elements in the subdomain where the Linearised Potential Equation is solved. This ratio is varied from 5.26 % to 94.74 %. As an output, the ratio $\tau^{\mathrm{mem}}_{\mathrm{LEE/LPE}}$ between the benefit in memory usage with the coupled solution and the memory usage with the full Linearised Euler Equations solution is calculated. Figure 7.17 shows the L^2-norm error on the velocity potential on the left-hand side and the memory usage ratio on the right-hand side, both against the ratio of elements in the Linearised Euler Equations domain for $p = 3$ and 6. The parameters for these simulations are: $k_0 = 10\,\mathrm{m}^{-1}$, $h = 0.05\,\mathrm{m}$ and $M = 0.6$. For $p = 3$, the error obtained with the coupled solution with $p_{\mathrm{int}} = p + 1$ is of the same order as the error obtained with the full Linearised Euler Equations solution, all over the range of values of $\tau^{n_\mathrm{e}}_{\mathrm{LEE/LPE}}$. With $p_{\mathrm{int}} = p$, the coupled solution is one order less accurate. For $p = 6$, both coupled solutions are about two orders less accurate than the non-coupled solution. This may be

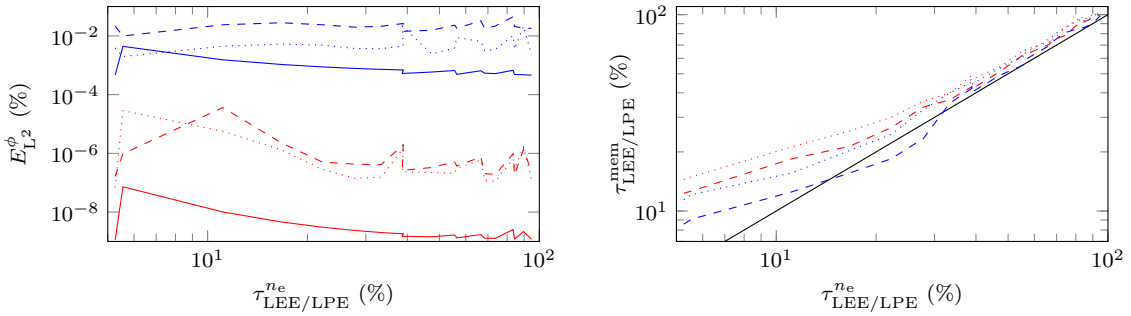

(a) L^2-norm error.

(b) Memory usage ratio.

Figure 7.17: Comparison of the full Linearised Euler Equations solution and the coupled solution, against the ratio of elements in the Linearised Euler Equations domain. $k_0 = 10\,\mathrm{m}^{-1}$, $h = 0.05\,\mathrm{m}$, $M = 0.6$. Solid line: no coupling, one single domain. Dashed line: coupling, with $p_{\mathrm{int}} = p$. Dotted line: coupling, with $p_{\mathrm{int}} = p + 1$. Blue line: $p = 3$. Red line: $p = 6$. Black line: $\tau^{\mathrm{mem}}_{\mathrm{LEE/LPE}} = \tau^{n_\mathrm{e}}_{\mathrm{LEE/LPE}}$.

due to the condition number which is much higher with the coupled solution in the very-high resolution regime. In terms of memory, the benefit of the coupled solution follows the rule: $\tau^{\mathrm{mem}}_{\mathrm{LEE/LPE}} = \varepsilon\tau^{n_\mathrm{e}}_{\mathrm{LEE/LPE}}$, especially for $\tau^{n_\mathrm{e}}_{\mathrm{LEE/LPE}} > 30\,\%$ with $\varepsilon \approx 1.1$. The advantage is less in terms of memory percentage for low ratios of elements in the Linearised Euler Equations, especially for $p = 6$ which means in the high-resolution regime.

The proposed coupled solution offers the possibility to drastically reduce the number of degrees of freedom for solving a given problem. This technique is based on the ability to reciprocally relate the variables of each mathematical model, the proper definition of subdomains with respect to the physical phenomena, and the application of proper coupling boundary conditions along the subdomains interfaces. Here, characteristic boundary conditions are applied. They are able to transmit the fluxes between two subdomains, but the absence of condensation in the interface elements makes the system condition number larger. The use of Lagrange multipliers may be a suitable alternative to improve the transmission conditions with the gradient evaluation at the interface, and to improve the overall condition number. It would also help avoid the loss of accuracy along the interface due to the gradient interpolation. This technique consists in hiding the gradient terms inside additional degrees of freedom, the Lagrange multipliers, and solves an additional system [194, 195]. The additional equations are built such that the local solution continuity is satisfied across the subdomains interface. This technique is not investigated in this work, but may be a way to further improve the proposed coupling technique.

Chapter 8

Applications

In this chapter, the high-order finite element model is used to solve various aeroengine noise radiation applications. An engine air intake is first investigated in the presence of potential mean flow, and the solution is verified against a generic commercial software solution. An ideal exhaust problem is then studied, and the solution is compared against an analytic solution available in the literature. In the last section, the sound field produced by a small-scale realistic aeroengine exhaust is computed. The numerical model accuracy is assessed, and its performance is compared against a standard finite element approach.

8.1 Intake

In this section, the numerical model is applied to an aeroengine intake. The test case is first presented: the complex nacelle geometry is described, as well as the non-uniform mean flow. The reference solution computed with a commercial software is introduced. Finally, the results obtained with the high-order finite element model are analysed and further discussed.

8.1.1 Test Case

As a first application test case, the Pratt & Whitney JT15D is considered in a static configuration with hard walls. This test case is useful to verify the applicability of the model to a non-straight geometry and in the presence of mean flow. NASA conducted experiments in the late 1970's and early 1980's to understand static and flight condition effects on fan noise. The experimental results provided a database for CAA prediction

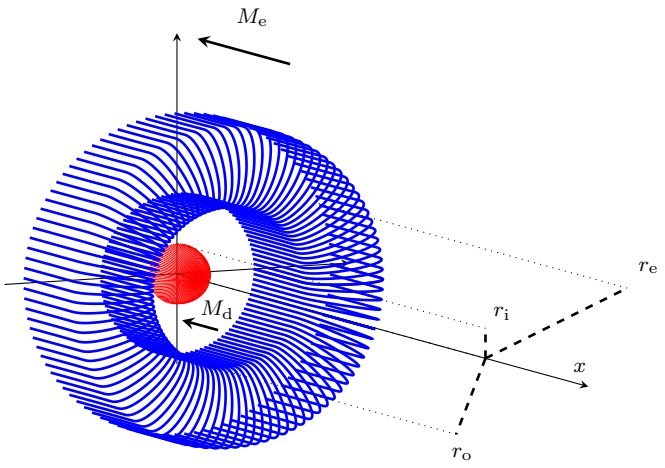

Figure 8.1: Intake geometry.

tools validation. In particular, this problem has been used to solve the Linearised Euler Equations in the frequency domain on a curvilinear mesh by means of the optimised 4^{th}-order dispersion-relation-preserving (DRP) scheme [196].

The JT15D fan rig is composed of 28 fan blades and 41 fan bypass stator vanes. Its bypass ratio is of 3.3. A strong acoustic mode with azimuthal order $m = -13$ and radial order $n = 1$ is generated by rods in front of the fan blades. The mode propagates inside the duct and radiates to the far field. The annular duct inner radius is $r_i = 9.98\,\text{cm}$ and its outer radius is $r_o = 26.7\,\text{cm}$. The exterior radius is $r_e = 53.4\,\text{cm}$. The sketch is shown in Figure 8.1. The mean flow is characterised by a velocity inside the annular duct with Mach number M_d. The medium outside the fan rig is at rest ($M_e = 0$).

8.1.1.1 Geometry

Since the intake has an axial symmetry along x the computational domain is an axisymmetric section of the intake, extending from $x = 0$ to $1.5\,\text{m}$ and from $r = 0$ to $1\,\text{m}$, as seen in Figure 8.2. The acoustic duct mode is injected through a PML of width d_d. The outgoing waves are absorbed by a PML surrounding the computational domain and of width d_e. The duct walls are completely reflective and no impedance condition is applied. Axisymmetric boundary conditions are applied along the symmetry axis. The domain is discretised with unstructured triangular elements, refined along the duct walls to represent accurately the geometry. In the PMLs, quadrangle elements are used. Field points are located on the circle centred at $(0.6, 0)$ and of radius $0.6\,\text{m}$.

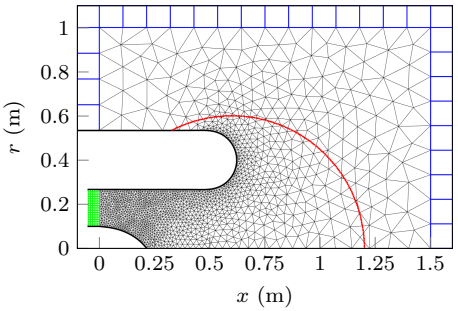

(a) Computational domain, mesh and control points (red dots).

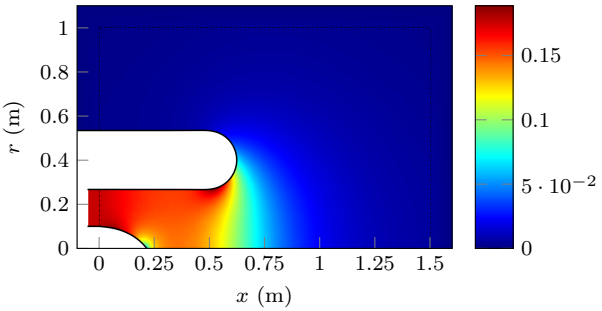

(b) $M_\mathrm{d} = 0.175$.

Figure 8.2: Intake computational domain and mean flow Mach number contours.

8.1.1.2 Mean Flow Properties

For this test case, the mean flow is incompressible and irrotational, as introduced in Section 7.2. The mean flow density, sound speed and specific heats ratio are uniform over the domain: $\rho_0 = 1.225\,\mathrm{kg/m^3}$, $c_0 = 340.27\,\mathrm{m/s}$ and $\gamma = 1.4$. Under these assumptions, the conservation equations simplify and the Laplace equation is obtained for the mean flow velocity potential ϕ_0:

$$\boldsymbol{\Delta}\phi_0 = 0. \tag{8.1}$$

In this work, the Laplace equation is solved numerically using the high-order finite element model together with the following axisymmetric variational formulation:

$$\int_\Omega r\boldsymbol{w}\cdot\boldsymbol{\phi}_0 \mathrm{d}\Omega = \int_\Gamma rw\boldsymbol{u}_0\cdot\boldsymbol{n}\mathrm{d}\Gamma, \tag{8.2}$$

where the mean flow normal velocity is specified along the boundary in the duct and the mean flow velocity potential is set to zero along the outlet boundary. The resulting mean flow velocity potential solution ϕ_0 is then used to obtain the mean flow velocity $\boldsymbol{u}_0$ and pressure p_0 through the following relationships: $\boldsymbol{u}_0 = \boldsymbol{\nabla}\phi_0$ and $p_0 = p_\infty + \rho_0\left(u_\infty^2 - u_0^2\right)$, where $p_\infty = \rho_0 c_0^2/\gamma$ and $u_\infty = 0$ are the reference pressure and velocity. The mean flow is then interpolated linearly at each node of the acoustic mesh shown in Figure 8.2(a) for the noise propagation computation. The mean flow nodal values surrounding each acoustic node are used for this estimation.

In the original work, five fan tip speeds were tested, between low subsonic and supersonic conditions [196]. In this work, two conditions are tested for different values of the fan axial Mach number M_d and of the blade pass frequency BPF. In the first condition, the fan axial Mach number is $M_\mathrm{d} = 0.175$, for a blade pass frequency of 3150 Hz and the Helmholtz

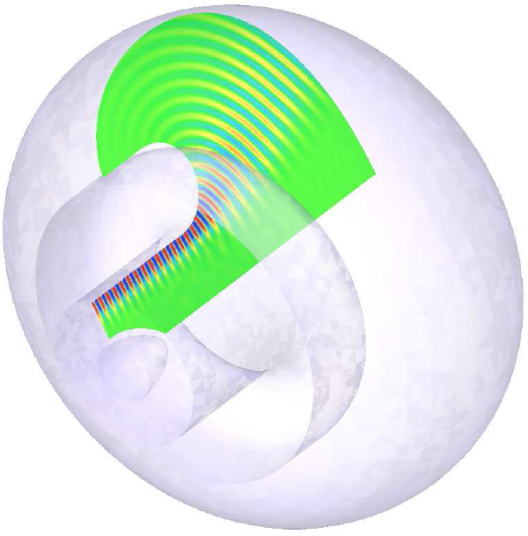

Figure 8.3: Intake reference solution with control plane in the nacelle.

number based on the intake exterior radius is $k_0 r_e = 31$. In the second condition, the fan axial Mach number is $M_d = 0.275$ and BPF $= 4480\,\text{Hz}$. The corresponding Helmholtz number based on the intake exterior radius is $k_0 r_e = 44$. The Mach number contours are plotted in Figure 8.2(b) for condition 1.

8.1.2 Reference Solution

In the literature, several solutions have been developed for this test case, including both experimental and computational results [196, 197]. In this work, the numerical results are compared with the solution obtained from the commercial software Virtual.Lab Acoustics. This reference solution solves the three-dimensional Linearised Potential Equation using an adaptive high-order finite element approach [52]. This mathematical model is described in the coupling procedure, in Section 7.2. The reference and numerical solutions are compared by calculating the Sound Pressure Level (SPL) at the field points introduced above. The reference pressure for the SPL is: $p_{ref} = 20\,\mu\text{Pa}$. Figure 8.3 shows an example of the three dimensional reference solution with a control plane.

8.1.3 Numerical Results

For this problem, the full Linearised Euler Equations are solved with the high-order finite element model. The computational domain is discretised with linear elements of characteristic size $h_w = 0.01\,\text{m}$ along the duct walls and $h = 0.1\,\text{m}$ elsewhere. The mesh is shown in Figure 8.2(a). The outer PML is one-element wide, while 5 elements are used in the

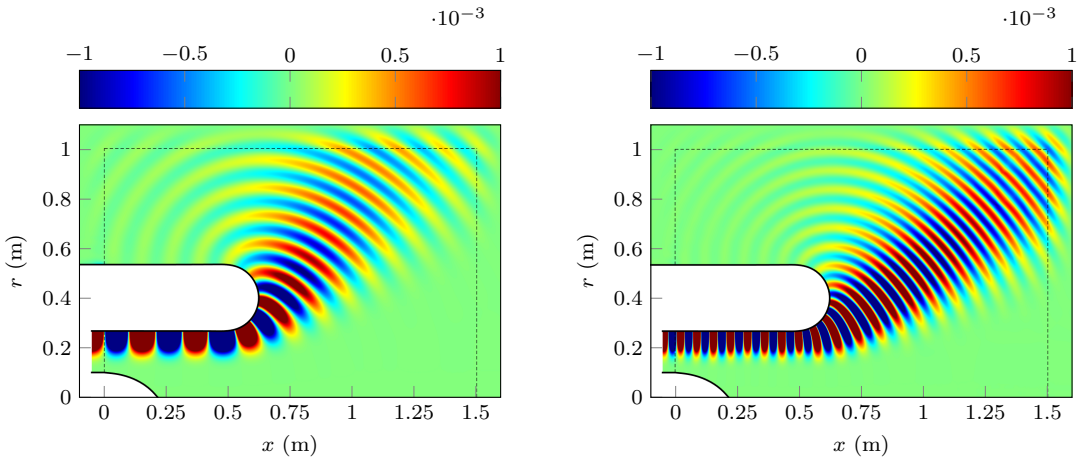

(a) Condition 1: $f = 3150\,\text{Hz}$, $M_\text{d} = 0.175$.

(b) Condition 2: $f = 4480\,\text{Hz}$, $M_\text{d} = 0.275$.

Figure 8.4: Intake modified pressure real part contours. $p = 6$.

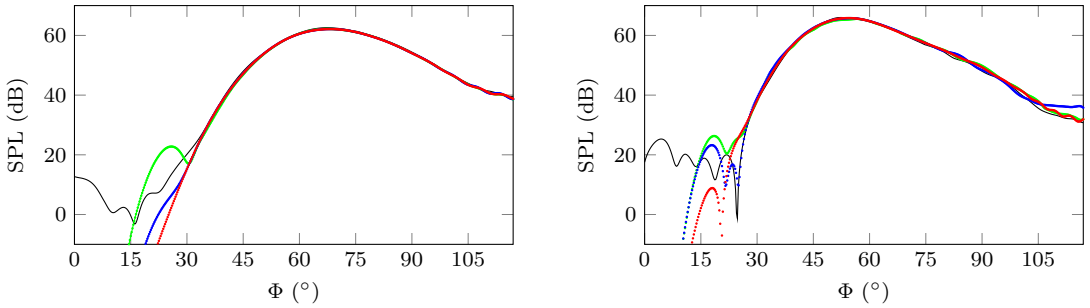

(a) Condition 1: $f = 3150\,\text{Hz}$, $M_\text{d} = 0.175$.

(b) Condition 2: $f = 4480\,\text{Hz}$, $M_\text{d} = 0.275$.

Figure 8.5: Intake Sound Pressure Level along the control circle. Black line: reference solution. Dots: numerical solution. Green: $p = 4$. Blue: $p = 5$. Red: $p = 6$.

in-duct PML: $d_\text{e} = 0.1\,\text{m}$ and $d_\text{d} = 0.05\,\text{m}$. For the first condition, the mean flow Mach number varies between 0 in the exterior region and a maximum value of 0.189. The shortest acoustic wavelength is 0.0876 m for waves propagating upstream, whereas the longest one is 0.128 m for waves propagating downstream. For the second condition, the mean flow Mach number varies between 0 in the exterior region and a maximum value of 0.296. The shortest acoustic wavelength is 0.0534 m, whereas the longest acoustic wavelength is 0.0984 m.

Figure 8.4 shows the contours of the modified pressure real part for both conditions. The results are obtained with a polynomial order $p = 6$. The acoustic duct mode propagates and radiates to the far field in front of the aeroengine intake. The directivity pattern is further observed in Figure 8.5 where the Sound Pressure Level is plotted against the position along the near-field control circle. The position angle Φ is measured from the positive x-direction. The numerical solution is compared with the reference solution, for p ranging from 4 to 6. The agreement between the solutions is verified for $\Phi > 30°$, in the

region where the Sound Pressure Level is the highest. With this mesh, the convergence is already observed with $p = 4$. The discrepancy in the range $\Phi < 30°$ is not relevant here since the maximum Sound Pressure Level in this region is about 40 dB lower than the overall maximum SPL. The convergence of the numerical model is observed in that region and the acoustic pressure tends to zero nearby the symmetry axis. The main sound directivity is observed at $\Phi = 67°$ for condition 1 and at $\Phi = 54°$ for condition 2.

8.1.4 Discussion

This test case shows that the high-order finite element code is able to handle non-straight geometries for acoustic propagation with potential mean flow. A good compromise must be found for the mesh size definition. On the one hand, the geometry complexity requires a fine mesh in order to accurately describe the duct boundaries. Without this proper geometrical representation, the numerical solution would converge to a solution different from the reference solution. On the other hand, the high-order elements approach is optimum with coarse elements since it relies on high-order polynomials. In order to optimise the computational costs, particular care should be taken to the mesh construction. In addition, improvements may be obtained by using coarse curved elements and/or an adaptive order scheme where lower polynomial orders would be used in the small elements. The efficiency of the high-order polynomials is also seen with the convergence of the numerical solution in the low-angle range along the axis ($\Phi < 30°$), where the acoustic pressure tends to zero.

8.2 Straight Duct Radiation

8.2.1 Test Case

Let us now examine the noise propagating by a straight semi-infinite circular duct [63]. The duct radius is $r_\mathrm{d} = 1\,\mathrm{m}$. The duct wall is infinitely thin and hard-wall boundary conditions are applied on both sides. The mean flow velocity is axial, with Mach number M_d in the duct and M_e in the exterior region. These velocities may be different, and a shear layer transitions continuously from one velocity to the other. The mean flow density, sound speed and specific heats ratio have the same values as those defined in Section 8.1.1.2. Figure 8.6 shows the test case configuration. Acoustic duct modes are generated and propagate inside the duct. From the duct exit plane, the acoustic modes radiate to the far field. The geometrical singularity at the duct trailing edge is responsible for the generation of

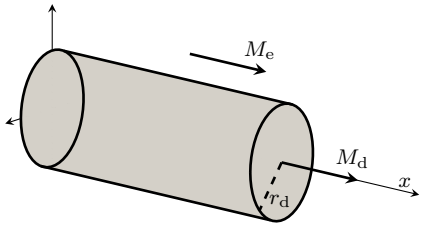

Figure 8.6: Straight duct geometry.

vorticity waves which are convected by the mean flow. In addition, shear layers may trigger Kelvin-Helmholtz instabilities. Below a critical Strouhal number St, these instabilities will grow exponentially [30, 56]: $\mathrm{St} = f\theta/(c_0(M_\mathrm{d} - M_\mathrm{e}))$, where f is the frequency and θ is the shear layer momentum thickness. After a certain distance from the duct trailing edge, the shear layer thickness is large enough for the Strouhal number to exceed this critical value: the exponential growth stops and the instability decays. Furthermore, the presence of a shear layer is responsible for the acoustic field refraction. These physical phenomena are further discussed in the following sections.

The computational domain extends from $x = 0$ to 5 m and from $r = 0$ to 2.5 m. The duct exit plane is located at $x_\mathrm{d} = 2.5\,\mathrm{m}$ (see Figure 8.7). Acoustic modes are injected inside the duct through a PML of length d_d. In the outer region, the computational domain is surrounded by a PML of width d_e. Axisymmetric boundary conditions are applied along the axis at $r = 0$. The discretisation uses triangular elements, with a structured mesh inside the PMLs and an unstructured mesh elsewhere. The mesh is refined at the duct trailing edge in order to take the geometric singularity into account. Furthermore, in order to take the vorticity shedding into account with mean flow, the refinement is extended along the duct wake. Three configurations are investigated: the no-flow condition, the uniform flow condition and the non-uniform flow condition. These effects are shown in the numerical results in Section 8.2.3.

8.2.2 Reference Solution

The numerical solution is compared to the solution by Gabard and Astley [198]. In this analytic model the mean flow is discontinuous across the vortex sheet, with different jet and ambient velocities. Since the streamline at the trailing edge is continuous, the vortex sheet displacement is zero at the trailing edge and the Kutta condition states that the normal velocity at the trailing edge also vanishes. Within the analytic reference model,

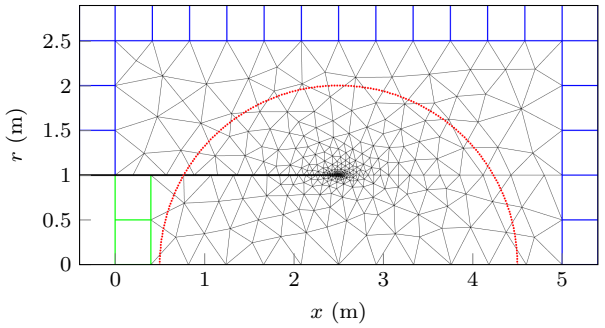

Figure 8.7: Straight duct computational domain, mesh and control field points (red dots). No-flow condition.

this condition is enforced at the duct trailing edge through a complex parameter which can control the amount of vorticity shedding added to the system [199]. This analytic model reproduces the mean flow effects on the sound field, as seen and discussed in Sections 8.2.3.2 and 8.2.3.3: the refraction through the shear layer, the vortex sheet instability wave and its interaction with the acoustic field. The solutions are compared on a 2 m-radius circle centred on the point $(x_\mathrm{d}, 0)$, along which the angle Φ is measured from the positive x-direction.

8.2.3 Numerical Results

8.2.3.1 No-Flow

An acoustic wave propagates in the straight infinite duct and radiates to the far field, with no flow: $M_\mathrm{d} = M_\mathrm{e} = 0$. The incoming acoustic wave is the time-harmonic duct mode $(m, n) = (10, 1)$ with the angular frequency $\omega = 5785\,\mathrm{rad/s}$, corresponding to the Helmholtz number $k_0 r_\mathrm{d} = 17$. The acoustic wavelength is: $\lambda_\mathrm{a} = 0.37\,\mathrm{m}$. The duct mode amplitude is $A_{p_{0,1}} = 1$, as defined in Section 3.3. The characteristic mesh size is 0.4 m inside the duct and in the outer region, which corresponds to less than 1 element per wavelength. At the duct trailing edge, the mesh is refined in order to account for the geometrical singularity: the element size there is 0.1 mm. The PMLs are one-element wide, both in the outer region and inside the duct ($d_\mathrm{d} = d_\mathrm{e} = 0.4\,\mathrm{m}$). Figure 8.7 shows the computational domain, the mesh and the control circle where the numerical solution is compared with the reference solution.

Figure 8.8 displays some numerical results with the variables fluctuations contours: the real parts of the modified pressure, the axial momentum, the radial momentum and the azimuthal momentum. These results are obtained with the maximum polynomial order

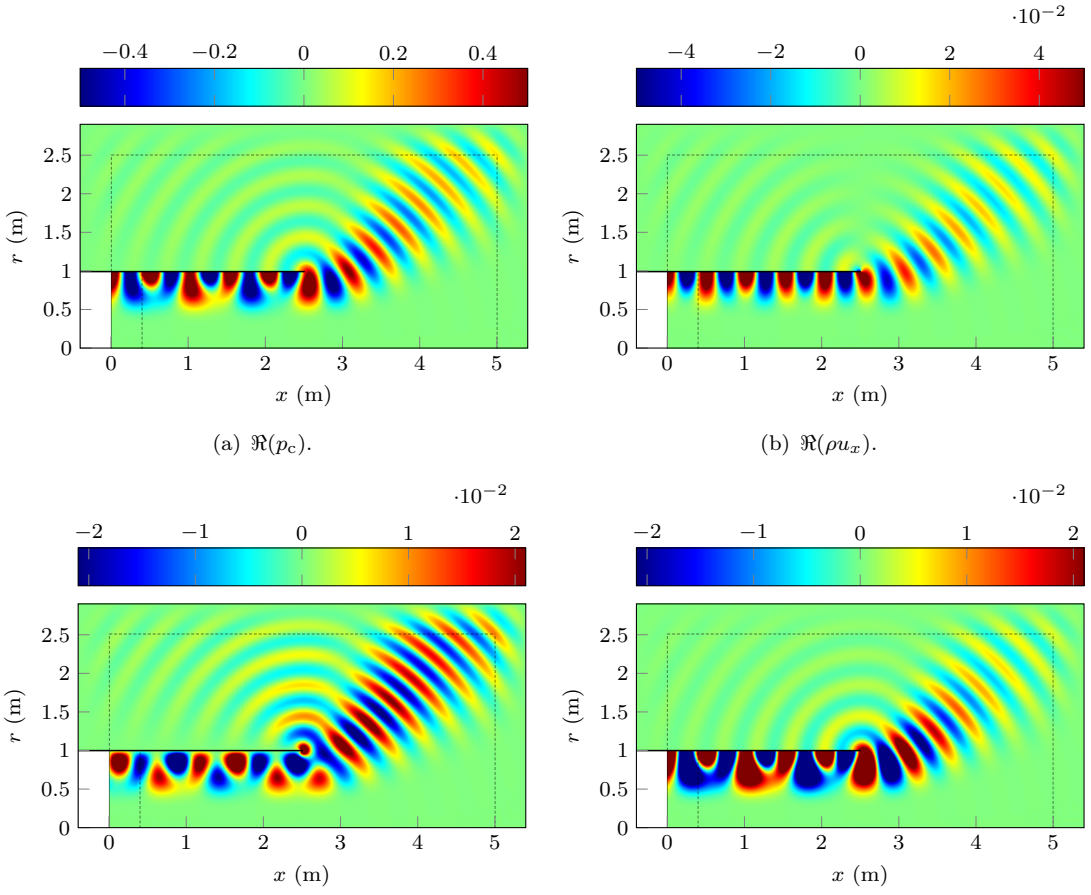

Figure 8.8: Straight duct variables perturbations real part contours, for the no-flow condition. $(m, n) = (10, 1)$, $k_0 r_\mathrm{d} = 17$, $M_\mathrm{d} = M_\mathrm{e} = 0$, $p = 10$.

available in the implementation, namely $p = 10$. The solution shows the acoustic wave propagating inside the duct and radiating to the far field. The main direction of propagation from the duct trailing edge is observed. The outgoing waves are properly absorbed inside the PML, with no noticeable reflections.

The numerical and reference analytic solutions are compared at the control field points. Figure 8.9 shows the Sound Pressure Level against the position angle along the control circle. The agreement is excellent. The maximum SPL is reached inside the duct with about 120 dB, while outside the duct the maximum is about 110 dB in the direction $\Phi \approx 50°$. To further verify the numerical solution, the nodal error between the numerical and analytic solutions is integrated over the control circle and measured in the L^2-norm. For $p = 10$, the numerical errors are: $E^{p_\mathrm{c}}_{\mathrm{L}^2} = 1.5\,\%$, $E^{\rho u_x}_{\mathrm{L}^2} = 0.63\,\%$ and $E^{\rho u_r}_{\mathrm{L}^2} = 2.4\,\%$, which confirms the accuracy of the model. For SPL > 20 dB, the maximum difference between the numerical and analytic SPL at each angle along the control circle is 0.56 dB.

Since the numerical model uses high-order polynomials, their impact is assessed in Figure

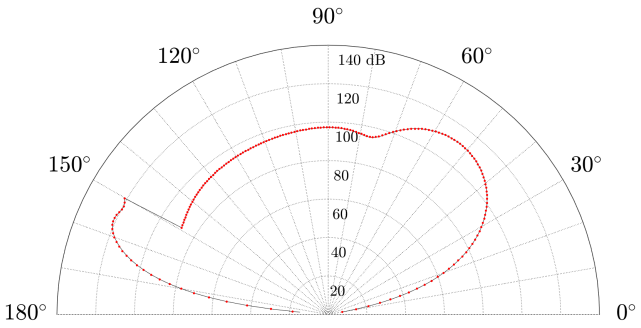

Figure 8.9: Straight duct Sound Pressure Level along the control circle, for the no-flow condition. $(m, n) = (10, 1)$, $k_0 r_\mathrm{d} = 17$, $M_\mathrm{d} = M_\mathrm{e} = 0$, $p = 10$. Black solid line: reference solution. Red dots: numerical solution.

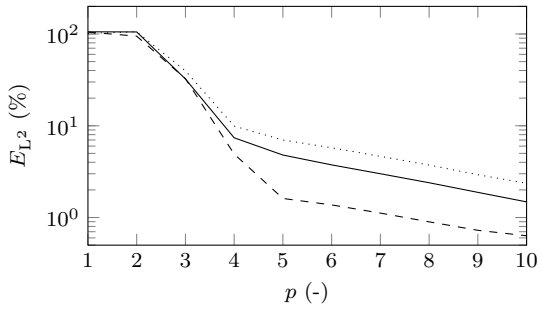

Figure 8.10: Straight duct relative error along the control circle against the polynomial order, for the no-flow condition. $(m, n) = (10, 1)$, $k_0 r_\mathrm{d} = 17$, $M_\mathrm{d} = M_\mathrm{e} = 0$. Solid line: $E^{p_\mathrm{c}}_{\mathrm{L}^2}$. Dashed line: $E^{\rho u_x}_{\mathrm{L}^2}$. Dotted line: $E^{\rho u_r}_{\mathrm{L}^2}$.

8.10. The errors along the control circle are plotted against the polynomial order. The low orders $p = 1$ and 2 are unable to solve the problem because the mesh is too coarse. The numerical accuracy increases with the polynomial order, from $p = 2$ to 9. Two stages are observed in that convergence: from $p = 2$ to 4, the convergence rate is about 0.6 whereas it is only of order 0.1 for p from 4 to 10. The difference in the convergence rate can be explained by the accuracy in the PML which controls the error in the computational domain, and by the mesh refinement at the duct wall singularity which controls the geometrical accuracy. Moreover, the accuracy levels differ from one variable to the other. The error on the x-momentum is about 4 times lower than the error on the r-momentum.

Concerning the numerical model performance, the run times and memory usage are plotted in Figure 8.11 against the polynomial order. The model is implemented in Matlab [200], on a Windows laptop with 4 cores and 16 Gb of RAM, and MUMPS is used to solve the matrix system [173]. The total solving time is about 1.5 times larger than the factorisation time needed for the LU decomposition of the system matrix. The factorisation time, the total solving time, and the memory usage are quadratic functions of the polynomial order, for a given mesh. The results with $p = 8$ are now considered. The corresponding numerical solution gives the following errors: $E^{p_\mathrm{c}}_{\mathrm{L}^2} = 2.4\,\%$, $E^{\rho u_x}_{\mathrm{L}^2} = 0.9\,\%$ and $E^{\rho u_r}_{\mathrm{L}^2} = 3.7\,\%$.

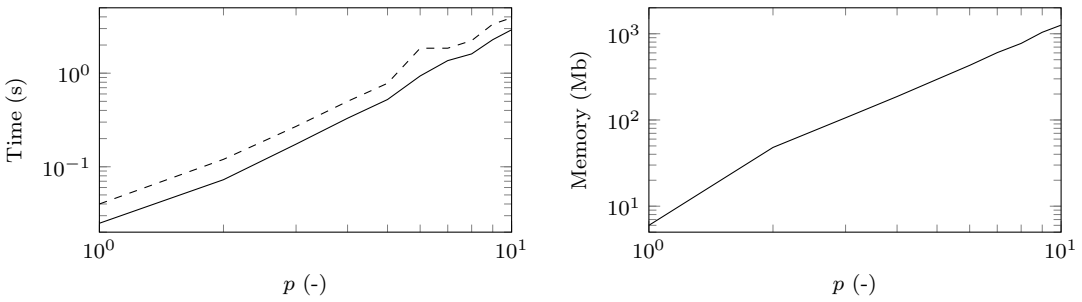

(a) Factorisation (solid line) and total (dashed line) solving times.

(b) Memory usage.

Figure 8.11: Straight duct computational performance, for the no-flow condition. $(m, n) = (10, 1)$, $k_0 r_\mathrm{d} = 17$, $M_\mathrm{d} = M_\mathrm{e} = 0$.

Similar errors are obtained with quadratic polynomials and a refined mesh: $E_{\mathrm{L}^2}^{p_\mathrm{c}} = 2.2\,\%$, $E_{\mathrm{L}^2}^{\rho u_x} = 0.87\,\%$ and $E_{\mathrm{L}^2}^{\rho u_r} = 3.4\,\%$. For this simulation with $p = 2$, the characteristic mesh size is 0.05 m inside the duct and in the outer region, and the PMLs are five-element wide in order to account for the low polynomial order. This mesh corresponds to 61285 triangular elements and 1025 quadrangle elements in the PMLs, which translates into 632815 degrees of freedom. The memory usage is 6.5 Gb and the total solving time is 20.9 s. In comparison, the high-order solution with $p = 8$ is obtained with 800 triangular elements and 24 quadrangle elements: 48445 degrees of freedom compose the final system, which represents a reduction of a factor 13 as compared to the standard quadratic solution. In terms of memory usage, this high-order solution uses 773 Mb which is only $1/8^{\mathrm{th}}$ of the memory required by the solution with $p = 2$. The total solving time is almost divided by a factor 10, with 2.23 s.

8.2.3.2 Uniform Flow

In the second mean flow configuration, the incoming duct mode $(10, 1)$ still propagates at the angular frequency $\omega = 5785\,\mathrm{rad/s}$ and the Helmholtz number is $k_0 r_\mathrm{d} = 17$. Unlike the previous case, a uniform mean flow is now present in the whole domain and its Mach number is: $M_\mathrm{d} = M_\mathrm{e} = 0.5$. The mean flow is responsible for the generation of a vorticity shed from the duct trailing edge. The shortest acoustic wavelength is 0.18 m and the largest acoustic wavelength is 0.55 m. The vorticity wave and the shortest acoustic wave have the same length. As seen in Figure 8.12, the mesh is refined in order to capture both effects: the characteristic mesh size is 0.4 m inside the duct and in the outer region, and the element size along the duct wake is 0.01 m. This refinement is necessary to capture the small oscillations of the vorticity wave along the duct wake. Again, the PMLs are

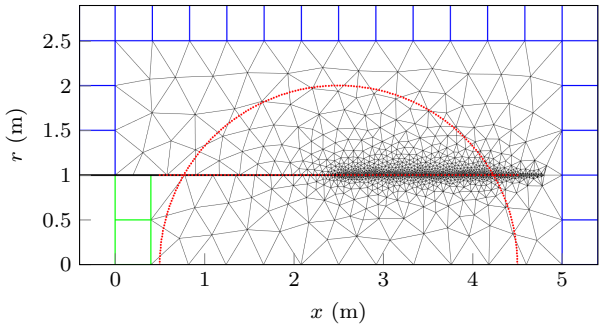

Figure 8.12: Straight duct computational domain, mesh and control points (red dots). Uniform flow condition.

one-element wide with quadrangle elements, both in the outer region and inside the duct ($d_\mathrm{d} = d_\mathrm{e} = 0.4\,\mathrm{m}$). In addition to those located along the 2 m-radius circle, control points are placed along the duct wall and its wake.

The variables perturbations contours are shown in Figure 8.13, for $p = 9$. The momentum fluctuations contours reveal the vortex sheet which develops from the duct trailing edge. The vortices are generated at the duct lip and are convected by the mean flow. The axial and azimuthal momentum present a very steep gradient across the vortex sheet, which requires a significant mesh refinement along the duct wake. The pressure and radial momentum perturbations are plotted along the control line located at $r = 1\,\mathrm{m}$. Figure 8.14 represents the real parts of these perturbations with $p = 9$. Along the duct wall ($x < 2.5\,\mathrm{m}$), the normal velocity is proportional to the vanishing momentum radial component. Along the duct wake ($x > 2.5\,\mathrm{m}$), the vorticity waves are observed and the envelope of the acoustic field is also visible. The continuity of both variables is verified at the duct trailing edge, indicating that the Kutta condition is well represented by the numerical model, without specific treatment. The numerical solution is in excellent agreement with the reference solution, which incorporates the Kutta condition: the normal acoustic velocity vanishes at the duct trailing edge and the solution is continuous at the trailing edge. This condition indicates that the acoustic pressure vanishes like $\sqrt{x}$ at the trailing edge, where x is the distance from the trailing edge. If the Kutta condition was not satisfied, a singularity at the trailing edge would be observed in the acoustic pressure which would behave like $p \equiv 1/\sqrt{x}$. Here the numerical solution naturally verifies the Kutta condition, which is implicitly imposed inside the numerical model. The Linearised Euler Equations support the acoustic, vorticity and entropy waves which compose the density, velocity and pressure fields, and the shape functions continuity is ensured in the discretisation over the computational domain.

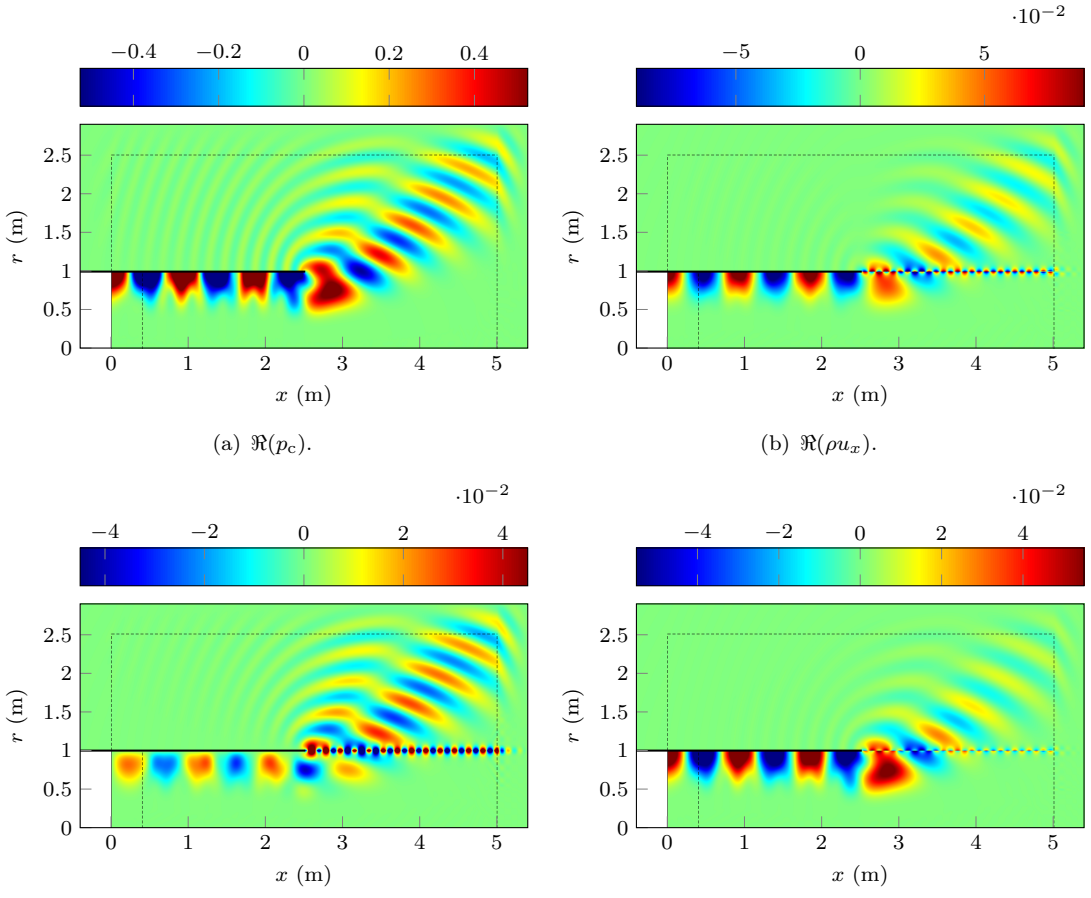

(a) $\Re(p_c)$. (b) $\Re(\rho u_x)$.

(c) $\Re(\rho u_r)$. (d) $\Re(\rho u_\theta)$.

Figure 8.13: Straight duct variables perturbations real part contours, for the uniform flow condition. $(m, n) = (10, 1)$, $k_0 r_d = 17$, $M_d = M_e = 0.5$, $p = 9$.

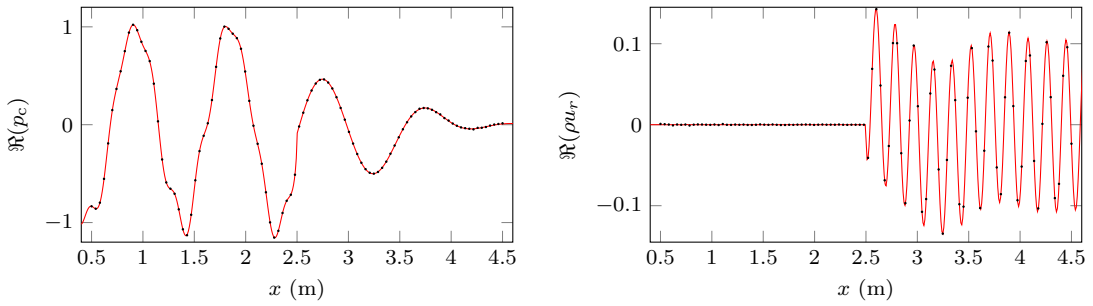

(a) $\Re(p_c)$. (b) $\Re(\rho u_r)$.

Figure 8.14: Straight duct variables perturbations along the duct wall and its wake, for the uniform flow condition. $(m, n) = (10, 1)$, $k_0 r_d = 17$, $M_d = M_e = 0.5$, $p = 9$. Black dots: analytic solution. Red line: numerical solution.

The Sound Pressure Level along the control circle also shows the comparison between the numerical and analytic solutions. The sound directivity is seen in Figure 8.15 and the agreement between the solutions is very good. The nodal errors with $p = 9$ confirm the numerical accuracy: $E^{p_c}_{L^2} = 0.26\,\%$, $E^{\rho u_x}_{L^2} = 1.6\,\%$ and $E^{\rho u_r}_{L^2} = 0.77\,\%$. The difference between the numerical and analytic SPL does not exceed 0.27 dB, for SPL $\geq$ 60 dB.

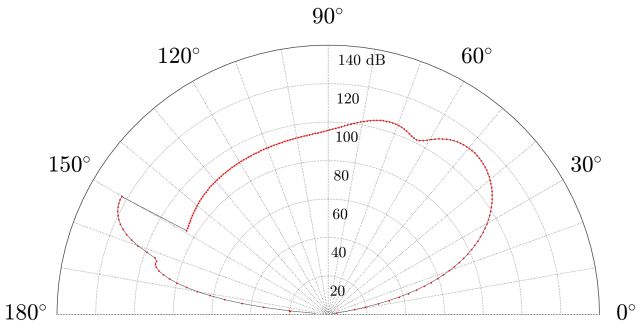

Figure 8.15: Straight duct Sound Pressure Level along the control circle, for the uniform flow condition. $(m, n) = (10, 1)$, $k_0 r_\mathrm{d} = 17$, $M_\mathrm{d} = M_\mathrm{e} = 0.5$, $p = 9$. Black solid line: analytic solution. Red dots: numerical solution.

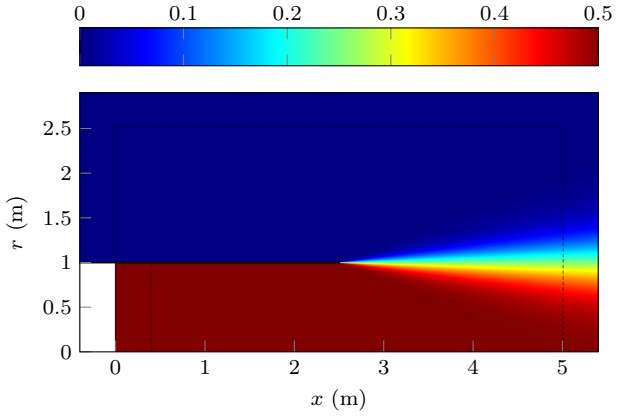

Figure 8.16: Straight duct mean flow Mach number contours, for the non-uniform flow condition. $M_\mathrm{d} = 0.5$, $M_\mathrm{e} = 0$.

8.2.3.3 Non-Uniform Flow

The final configuration focuses on the non-uniform flow condition, characterised by mean flow shear layers with strong gradients. In order to reproduce these features, an analytic mean flow shear layer is considered. The Mach number flow profile outside the duct is taken to be:

$$M(r, x) = \overline{M} \left(1 + \tanh \left(\frac{r_\mathrm{d} - |r|}{\zeta \delta(x)} \right) \right), \tag{8.3}$$

where $\overline{M} = (M_\mathrm{d} + M_\mathrm{e})/2$, $\zeta = 2/5 \cos^2(\beta/2)$ is a parameter that controls the shear layer profile, β is the spreading angle and δ is the shear layer thickness. The latter reads:

$$\delta(x) = 2\,(x - x_\mathrm{d}) \tan(\beta/2). \tag{8.4}$$

The medium outside the duct is at rest ($M_\mathrm{e} = 0$) and the following parameters are chosen: $M_\mathrm{d} = 0.5$ and $\beta = 20°$. Within each finite element, the mean flow velocity is imposed directly at each Gauss point of the quadrature. Figure 8.16 shows the mean flow Mach number contours. The duct mode $(10, 1)$ is injected at the fan plane and the angular fre-

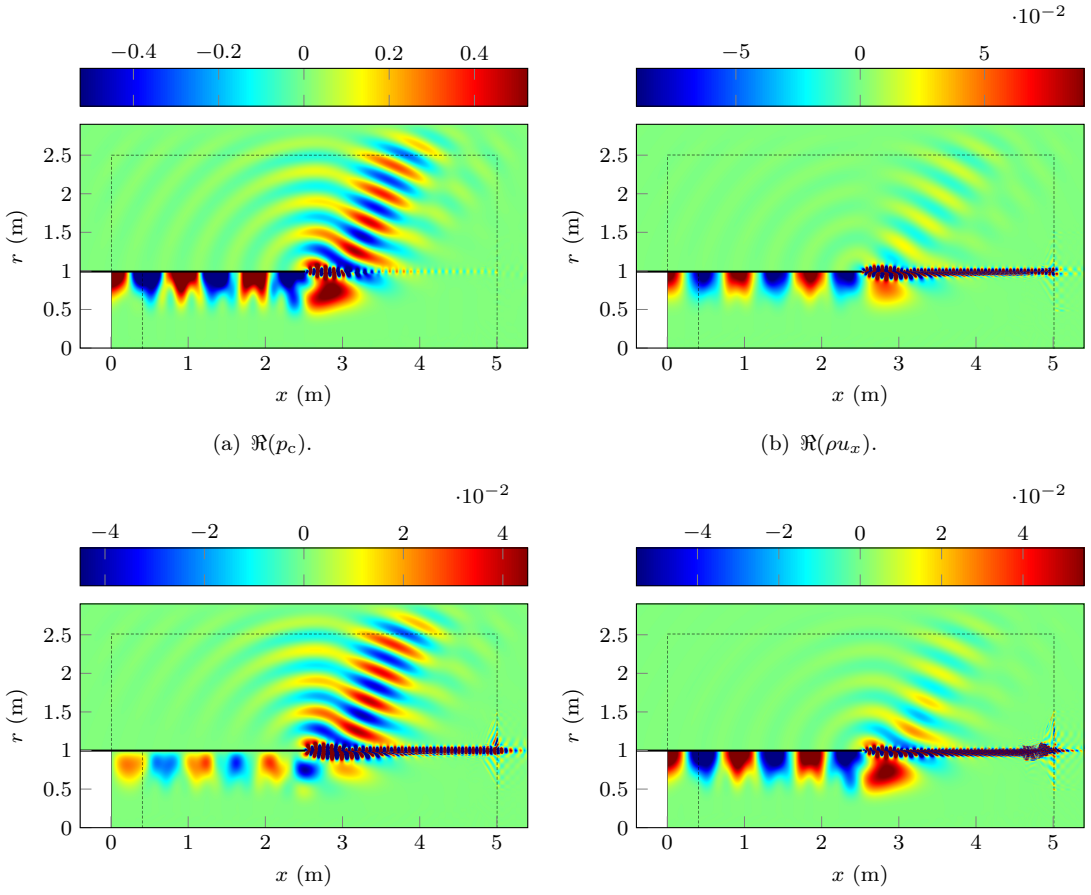

(a) $\Re(p_c)$. (b) $\Re(\rho u_x)$.

(c) $\Re(\rho u_r)$. (d) $\Re(\rho u_\theta)$.

Figure 8.17: Straight duct variables perturbations real part contours, for the non-uniform flow condition. $(m, n) = (10, 1)$, $k_0 r_\mathrm{d} = 17$, $M_\mathrm{d} = 0.5$, $M_\mathrm{e} = 0$, $p = 10$.

quency is set to $\omega = 5785\,\mathrm{rad/s}$. The Helmholtz number is $k_0 r_\mathrm{d} = 17$. The computational domain is discretised with the same mesh as the one depicted in Figure 8.12 for the uniform mean flow condition.

The solutions are shown in Figure 8.17 for the modified pressure, the axial momentum, the radial momentum and the azimuthal momentum with $p = 10$. In comparison to the uniform flow solution, the refraction of the sound field through the shear layer is visible, and the main directivity is around $\Phi = 64°$ instead of 46°. Spurious reflections are observed on the momentum contour plots, from the PML along the duct wake. They may be explained by the fact that the PML is tuned to absorb acoustic waves, and not vorticity waves which wavenumber is of the form k_0/M and may not be consistent with the chosen PML stretching function (see Section 5.4). This should be further investigated in order for the PML to better damp both acoustic and vorticity waves. Though, these reflections do not impact the numerical solution in the range of interest, i.e. for $x < 4.5\,\mathrm{m}$, where the mesh is refined. The Sound Pressure Level along the control circle is shown in Figure 8.18. The

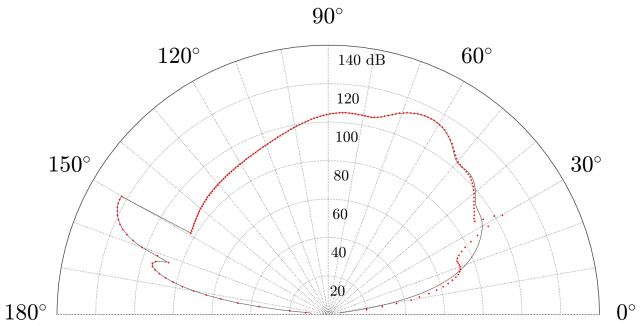

Figure 8.18: Straight duct Sound Pressure Level along the control circle, for the non-uniform flow condition. $(m, n) = (10, 1)$, $k_0 r_\mathrm{d} = 17$, $M_\mathrm{d} = 0.5$, $M_\mathrm{e} = 0$, $p = 10$. Black solid line: reference solution. Red dots: numerical solution.

analytic solution available without vorticity shedding is also represented, as an element of reference. It shows that the numerical solution is very similar. Around the angle $\Phi = 30°$, a peak corresponding to the vortex sheet is observed which is not included in the reference solution. The non-uniform mean flow is responsible for the wave refraction outside the duct.

The solution convergence is assessed in Figure 8.19 which displays the variables real parts along the duct wall and its wake, for $p = 4, 9$ and 10. Along the duct wall, the solution has already converged with $p = 4$: the oscillations are visible on the pressure and axial momentum plots, while the normal velocity along the hard wall is verified to be zero on the radial momentum plot. There, the analytic solution obtained with no vorticity shedding is identical to the numerical solution. At the duct trailing edge, a Kelvin-Helmholtz instability wave is generated: it grows exponentially and then decreases since the shear layer thickness keeps increasing [56, 201]. This instability is not included in the analytic solution. A vorticity wave with constant amplitude is visible in the momentum plots, but its effect on the pressure field is less significant. These small oscillations are not well represented by the orders $p < 8$. Since the mean flow is non-uniform, the contributions of the acoustic and vorticity waves supported by the Linearised Euler Equations are visible on the pressure plot.

Numerical Solution with Coupling

The numerical solutions presented in the previous sections were obtained using a full Linearised Euler Equations model, i.e. the LEE were solved in the whole computational domain. Five variables are solved for in large regions of the computational domain where the mean flow is potential: the Linearised Potential Equation could be successfully applied in these regions. Therefore, this test case is appropriate for applying the coupling method

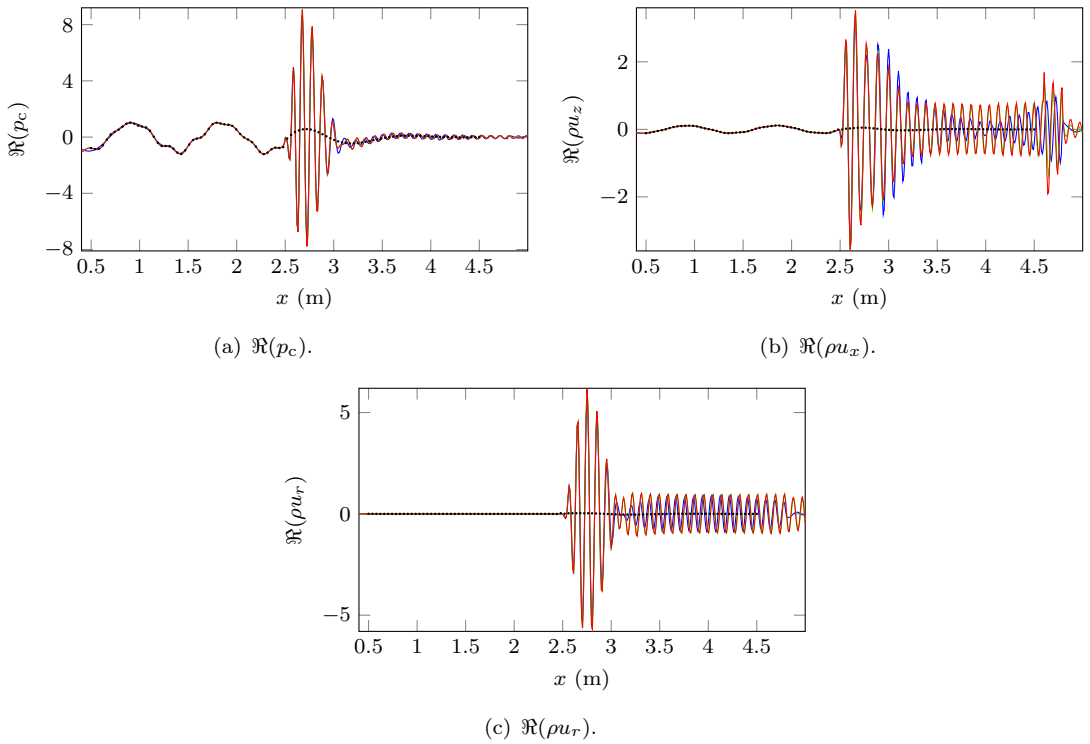

(a) $\Re(p_c)$.

(b) $\Re(\rho u_x)$.

(c) $\Re(\rho u_r)$.

Figure 8.19: Straight duct variables perturbations along the duct wall and its wake, for the non-uniform flow condition. $(m, n) = (10, 1)$, $k_0 r_d = 17$, $M_d = 0.5$, $M_e = 0$, $p = 10$. Black dots: reference solution (no vorticity shedding). Solid line: numerical solution. Blue: $p = 4$. Green: $p = 9$. Red: $p = 10$.

introduced in Chapter 7. A new computational domain which contains several subdomains is used. Figure 8.20 shows the new configuration with the computational domain and the mean flow Mach number: the subdomains are marked out by the interfaces which surround the mean flow shear layer. The subdomain containing the shear layer is solved using the Linearised Euler Equations. Outside this region for $r < 1\,\text{m}$, the mean flow is uniform with $M = 0.5$ and the Linearised Potential Equation is used. The LPE is also used outside the shear layer where the medium is at rest ($r > 1\,\text{m}$). The transmission conditions developed in Section 7.3 are applied along the interface boundaries. Around the trailing edge, the interface is deliberately placed at a distance 0.2 m from the geometrical singularity in order to avoid spurious reflections due to the vortex sheet generated there. In fact, the Linearised Potential Equation only supports acoustic waves and is not able to propagate vorticity waves. Vorticity waves of significant amplitude which would reach the interface boundaries would be reflected back into the LEE domain and pollute the solution. The typical mesh size is $h = 0.2\,\text{m}$ in the computational domain, with the following refinements: 0.1 m along the interface boundaries and 0.01 m along the duct wake.

The coupling method produces results similar to the full Linearised Euler Equations solution, as seen in Figure 8.21 where the pressure field contours are plotted. The solution

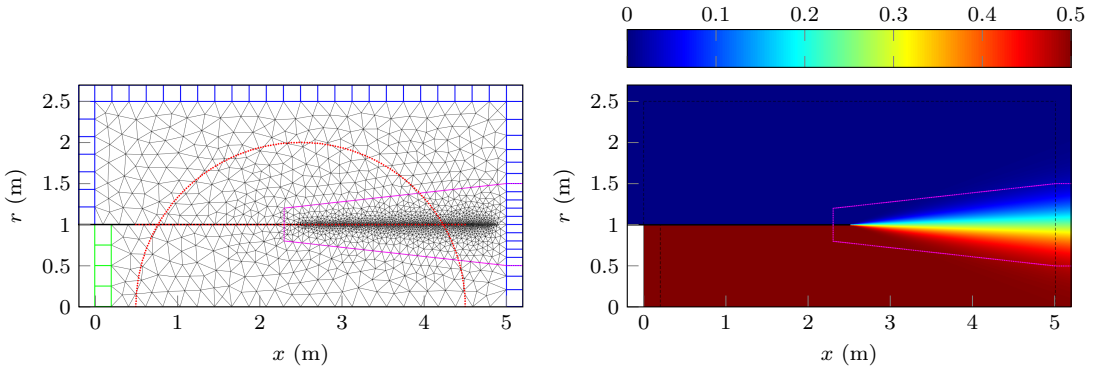

(a) Computational domain, mesh, control points (red dots) and coupling interface (magenta dotted lines).

(b) Mean flow Mach number.

Figure 8.20: Straight duct computational domain and mean flow Mach number contours. Non-uniform flow condition with coupling.

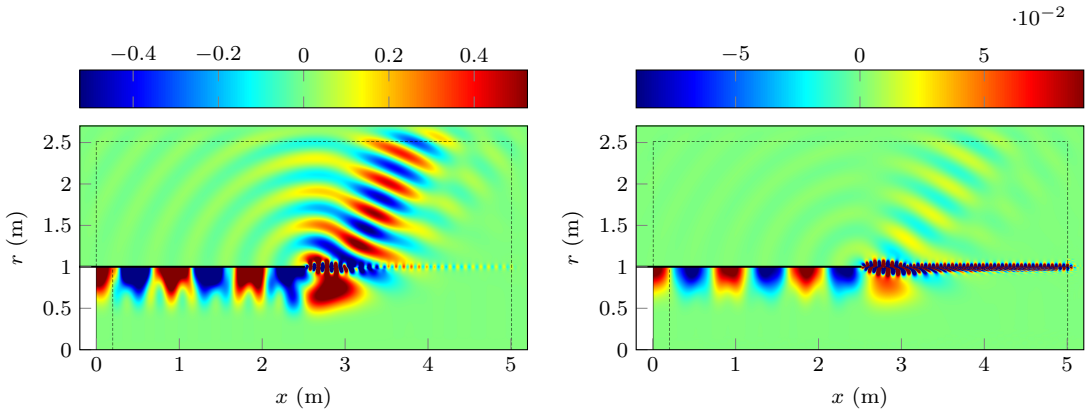

(a) $\Re(p_c)$.

(b) $\Re(\rho u_x)$.

Figure 8.21: Straight duct coupled solution, for the non-uniform flow condition. $(m, n) = (10, 1)$, $k_0 r_d = 17$, $M_d = 0.5$, $M_e = 0$, $p = 9$.

continuity along the coupling interfaces is verified and the pressure field is similar to the one obtained in Figure 8.17 with the full Linearised Euler Equations. The Sound Pressure Level along the control circle depicted in Figure 8.22 also shows the good behaviour of the coupled model, which corresponds to the reference Linearised Euler Equations solution. Some discrepancies are observed near the symmetry axis for $\Phi < 20°$ where the SPL is lower than 80 dB, i.e. about 60 dB below the maximum SPL. They may be explained by some spurious reflections from the PML or along the coupling interface. This needs to be further investigated.

The grid contains $n_e^{\text{LEE}} = 3381$ elements in the Linearised Euler Equations subdomain and $n_e^{\text{LPE}} = 942$ elements in the Linearised Potential Equation subdomain. This configuration corresponds to the following ratio: $\tau^{n_e}_{\text{LEE/LPE}} = 78.2\,\%$, i.e. 78.2 % of the elements in the domain are solved with the Linearised Euler Equations and 21.8 % of the elements are

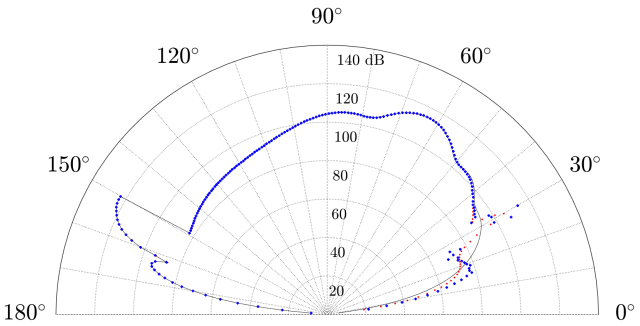

Figure 8.22: Straight duct Sound Pressure Level along the control circle, for the non-uniform flow condition, with coupling. $(m, n) = (10, 1)$, $k_0 r_\mathrm{d} = 17$, $M_\mathrm{d} = 0.5$, $M_\mathrm{e} = 0$, $p = 9$. Black solid line: reference solution. Red dots: full Linearised Euler Equations numerical solution. Blue + marker: coupling numerical solution.

solved with the Linearised Potential Equation. The memory usage for the full Linearised Euler Equations is 7.39 Gb with $p = 9$, while it is 5.93 Gb for the coupled solution with the same polynomial order. The corresponding memory usage ratio is: $\tau^{\mathrm{mem}}_{\mathrm{LEE/LPE}} = 80.2\,\%$, i.e. the coupled solution uses 80.2 % of the memory used for solving the full Linearised Euler Equations solution. This confirms the observations in Section 7.5: the benefit in memory usage with respect to the full Linearised Euler Equations solution corresponds to the ratio of elements in the Linearised Potential Equation subdomains.

8.3 Aeroengine Exhaust

The study of noise propagation by a straight duct has shown that the high-order numerical model performs well with a simple geometry and is able to represent the physical features in the presence of a non-uniform mean flow. These aspects are now considered on a turbofan exhaust involving a realistic sheared mean flow together with a complex geometry.

8.3.1 Test Case

This turbofan exhaust test case has been developed within the European Union project TURNEX [202] in 2008, and used by several authors to benchmark Computational AeroAcoustics methods [58, 59]. The aeroengine exhaust is composed of a bypass duct and a core duct. Figure 8.23 shows the exhaust geometry. The bypass duct exterior radius at the exit plane is $r_{\mathrm{bpde}} = 0.126\,\mathrm{m}$. Within the TURNEX project, the results obtained by Iob and Arina with conventional linear finite elements are considered [59]. Since the reference values are not available, a qualitative comparison of the acoustic field contours is performed.

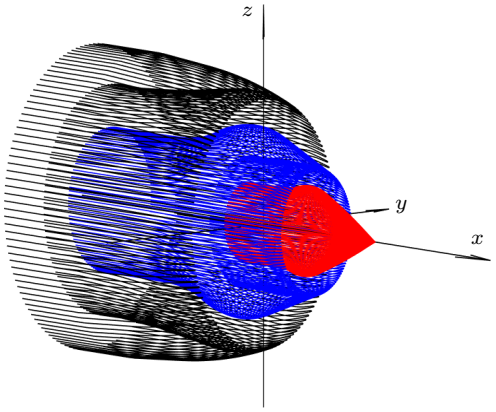

Figure 8.23: Aeroengine exhaust geometry.

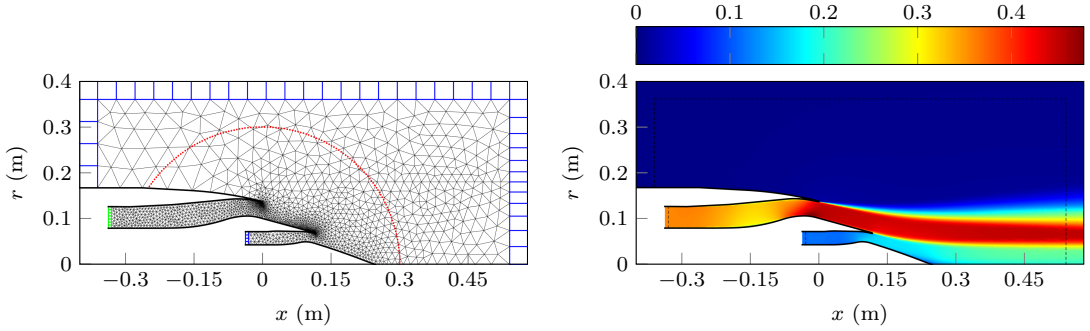

(a) Computational domain, mesh and control points (red dots).

(b) Mean flow Mach number.

Figure 8.24: Aeroengine exhaust computational domain and mean flow Mach number contours.

8.3.1.1 Geometry

An axisymmetric section of the turbofan exhaust forms the computational domain, which extends from $x = -0.36\,\mathrm{m}$ to $0.54\,\mathrm{m}$ and from $r = 0$ to $0.36\,\mathrm{m}$. In order to properly represent the geometry, a fine mesh size h_w is applied along the duct walls with $h_\mathrm{w} = 6.5\,\mathrm{mm}$. The mesh size at the ducts trailing edges is $0.5\,\mathrm{mm}$. In the rest of the domain, the typical mesh size is $h = 0.04\,\mathrm{m}$. Figure 8.24 shows the computational domain, as well as the control field points where the numerical solution is assessed. These field points are located on the circle centred on the point $(0, 0)$ and of radius $0.3\,\mathrm{m}$. A Perfectly Matched Layer is used to impose the incoming acoustic mode in the bypass duct, with a unit intensity. The computational domain is surrounded by a PML, and axisymmetric boundary conditions are applied along the axis at $r = 0$. The grid is composed of unstructured triangular elements, and structured quadrangle elements in the PMLs. Acoustic modes are generated in the bypass duct, propagate along the duct and radiate to the far field.

8.3.1.2 Fluid Properties

In this study, the medium is at rest at infinity. The mean flow Mach number in the bypass duct is $M_{\text{bpd}} = 0.447$, while it is $M_{\text{bpd}} = 0.223$ in the core duct. Figure 8.24 shows the mean flow Mach number contours. For the static-approach condition, the fluid density is: $\rho_{0_{\text{bpd}}} = 1.177\,\text{kg/m}^3$ in the bypass duct and $\rho_{0_{\text{cd}}} = 0.509\,\text{kg/m}^3$ in the core duct. The sound speed is: $c_{0_{\text{bpd}}} = 347.19\,\text{m/s}$ in the bypass duct and $c_{0_{\text{cd}}} = 527.62\,\text{m/s}$ in the core duct. The mean flow description has been obtained within the TURNEX project solving the Reynolds-Averaged Navier-Stokes equations with a k-ε turbulence model on a very fine mesh. These nodal values are interpolated on the acoustic mesh. Two approaches are investigated: in the first one, the mean flow data are interpolated on the nodes of the acoustic mesh, whereas in the second one, they are interpolated at the Gauss points of the numerical quadrature. The mean flow interpolation effects are discussed in Section 8.3.3.

8.3.2 Numerical Results

The numerical results are presented for the static-approach condition. First, the full Linearised Euler Equations solution is investigated. Then, the coupled solution results are shown. Finally, the mean flow interpolation effects are considered.

8.3.2.1 Full Linearised Euler Equations Solution

An acoustic duct mode is injected in the bypass duct with the Helmholtz number $k_0 r_{\text{bpde}} = 17.5$. Two modes are considered: the plane wave $(0, 1)$, and the mode $(9, 1)$. Figure 8.25 shows the modified pressure real part for both modes, with $p = 9$. These colormaps illustrate the complexity of the physics with the presence of multiple-scale wavelengths. Vorticity sheddings develop along the shear layer from the ducts trailing edges. A qualitative comparison with the reference solution from Iob and Arina [59] indicates that the solutions are similar.

The acoustic waves pressure fields along the control circle are plotted in Figure 8.26 for polynomial orders ranging from 2 to 9. The position angle Φ is measured from the positive x-direction. The numerical model convergence is observed. With $p = 5$ the solution has already converged in most of the domain, with the exception of the region close to the symmetry axis where the shear layer is located.

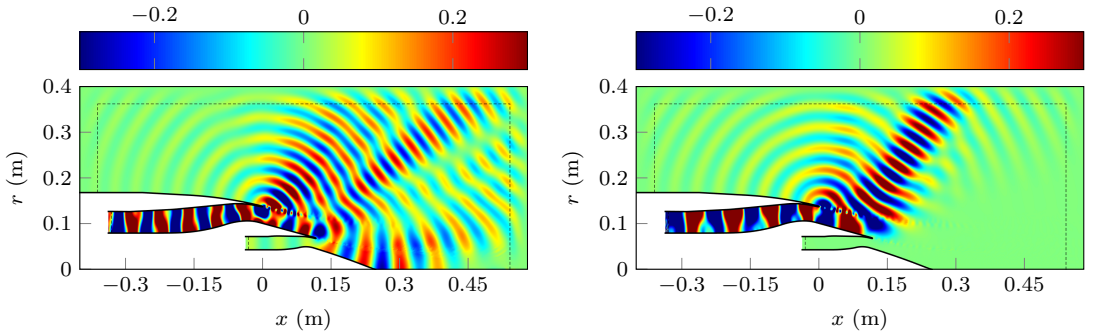

(a) $(m, n) = (0, 1)$. (b) $(m, n) = (9, 1)$.

Figure 8.25: Aeroengine exhaust contours of the modified pressure perturbations real part. $k_0 r_{\text{bpde}} = 17.5$, $p = 9$.

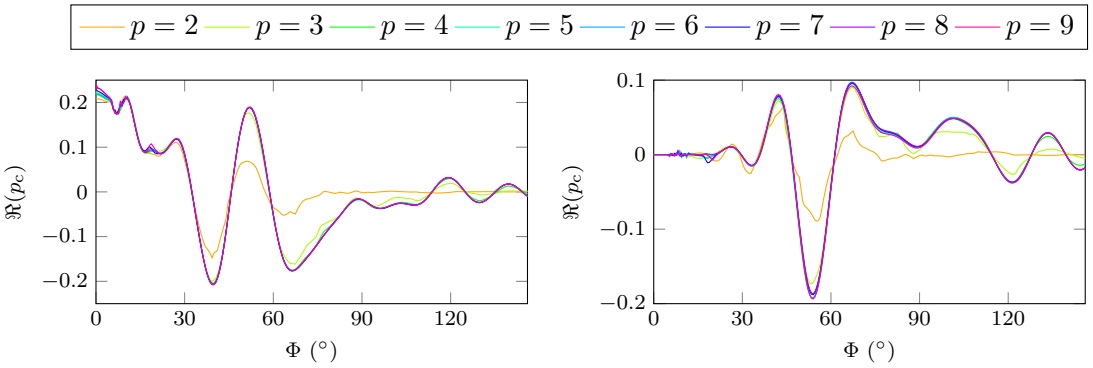

(a) $(m, n) = (0, 1)$. (b) $(m, n) = (9, 1)$.

Figure 8.26: Aeroengine exhaust modified pressure field along the control circle.

8.3.2.2 Coupled Solution

The coupled solution is now studied. The computational domain is the same as for the full Linearised Euler Equations solution, except that the domain is now split between LEE and LPE regions and coupling interfaces are introduced. Figure 8.27 shows the mesh and the mean flow Mach number with the coupling interfaces. In the shear layer region, delimited by the magenta dotted lines, the Linearised Euler Equations are solved. Outside that region, the Linearised Potential Equation is solved, i.e. inside the bypass and core ducts and above the aeroengine. In each of these regions, the mean flow is relatively uniform and the velocity potential assumption is valid. The numerical results obtained with the coupled solution are in good agreement with the ones obtained from the Linearised Euler Equations. The comparison of the solutions along the control circle is plotted in Figure 8.28 for the two acoustic modes. The black dashed line placed at $\Phi = 37°$ indicates the position of the coupling interface: values of Φ lower than 37° correspond to the Linearised Euler Equations subdomain, while values of Φ higher than 37° correspond to the Linearised Potential Equation subdomain. The coupled solution reproduces the same features as

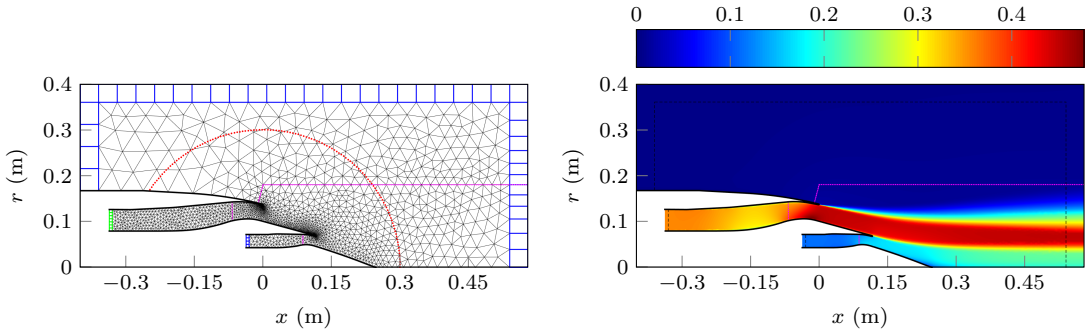

(a) Computational domain, mesh, control points (red dots) and coupling interface (magenta dotted lines).

(b) Mean flow Mach number.

Figure 8.27: Aeroengine exhaust computational domain and mean flow Mach number contours, with coupling.

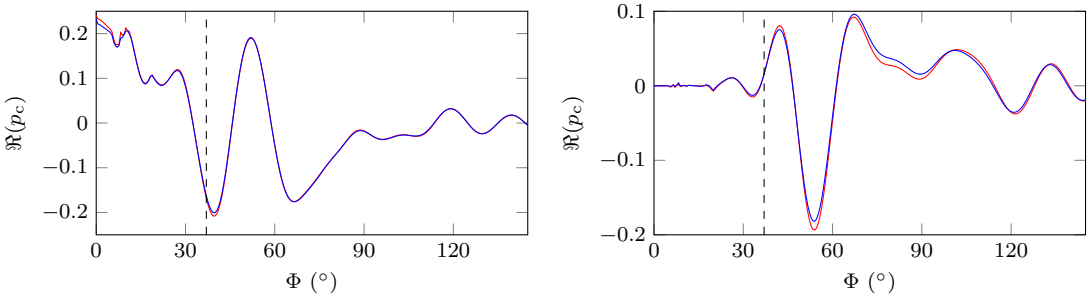

(a) $(m, n) = (0, 1)$.

(b) $(m, n) = (9, 1)$.

Figure 8.28: Aeroengine exhaust Sound Pressure Level along the control circle. $p = 9$. Red line: full Linearised Euler Equations solution. Blue line: coupled solution.

the full Linearised Euler Equations, especially with the acoustic plane wave. The mode $(9, 1)$ shows a larger difference between the two solutions. However, the difference of the corresponding Sound Pressure Levels does not exceed 1.45 dB. For the acoustic plane wave, that difference is lower than 0.46 dB all along the control circle. Note that for this coupled solution the polynomial order has not been increased along the interface, which could explain the slight difference with the full LEE solution. Further investigations should be performed to better understand these changes.

The computational domain is composed of $n_{\mathrm{e}}^{\mathrm{LEE}} = 2452$ elements in the Linearised Euler Equations subdomain, and $n_{\mathrm{e}}^{\mathrm{LPE}} = 1272$ elements in the Linearised Potential Equation subdomain. 65.8 % of the elements in the computational domain are solved with the Linearised Euler Equations, and 34.2 % are solved with the Linearised Potential Equation. With $p = 9$, the memory usage for the full Linearised Euler Equations solution is 5.14 Mb, while it is 3.67 Mb for the coupled solution. This means that the coupled solution uses 71.4 % of the memory used for the full Linearised Euler Equations solution.

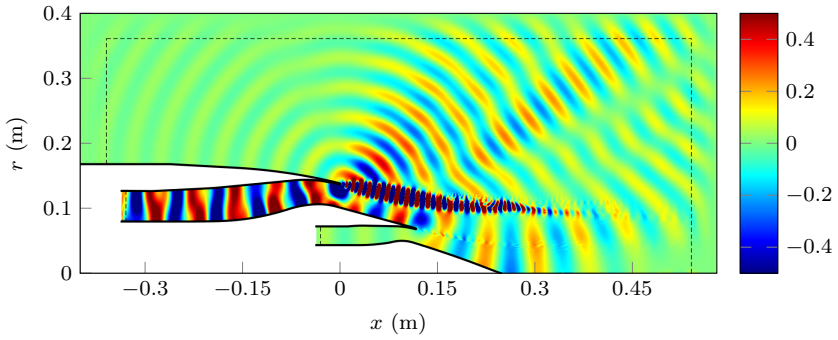

Figure 8.29: Aeroengine exhaust contours of the modified pressure perturbations real part, with Gauss points CFD interpolation. $(m, n) = (0, 1)$, $k_0 r_{\text{bpde}} = 17.5$, $p = 9$.

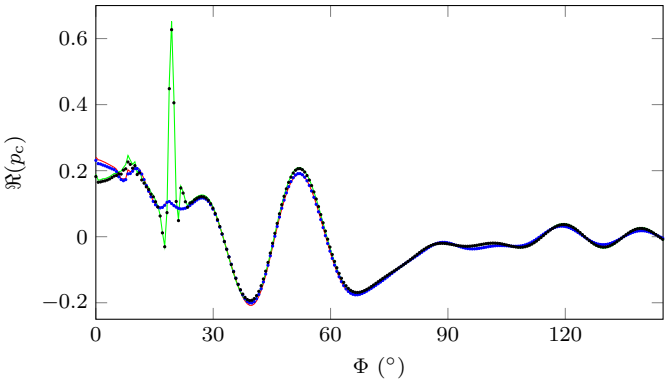

Figure 8.30: Aeroengine exhaust Sound Pressure Level along the control circle, with Gauss points CFD interpolation. $(m, n) = (0, 1)$, $p = 9$. Solid lines: full Linearised Euler Equations solutions. Dots: coupled solutions. Red, blue: nodal mean flow interpolation. Green, black: Gauss points mean flow interpolation.

Mean Flow Interpolation

In this test case, the numerical solutions have been obtained with a linear interpolation of the mean flow data at each node of the acoustic mesh. Each acoustic node is localised in the CFD mesh. Then the nodal mean flow values of the corresponding CFD element surrounding the acoustic node are linearly interpolated to provide the mean flow values at the acoustic node. The interpolated values at the acoustic nodes of each element are then used to interpolate the mean flow values at each Gauss point of the element. In that case, some additional error may be introduced on the mean flow values used inside each element. As an alternative, the mean flow data are now directly interpolated at the Gauss points of the numerical quadrature within each element in the acoustic simulation. Figure 8.29 displays the contours of the modified pressure real part for that configuration, for the incoming acoustic plane wave. The impact of the mean flow interpolation at the Gauss points is clearly visible: the amplitude of the vorticity shedding is much higher than in the configuration with nodal interpolation. However, outside the shear layer, the acoustic field is in good agreement with the one obtained with a nodal interpolation of the mean

flow data. The plot given in Figure 8.30 gives a more precise insight into those effects, and shows how the mean flow interpolation affects the pressure field along the control circle. As discussed in the previous section, the full LEE solution and the coupled solution match well. The impact of the mean flow interpolation is significant in the shear layer region ($\Phi < 30°$), where the amplitude of the acoustic field is amplified because of the interaction with the vorticity and entropy waves. By contrast, the impact outside the shear layer region is very limited and the lobes of main acoustic amplitude remain unaffected by the mean flow interpolation method.

8.3.3 Discussion

With the aeroengine exhaust test case, the applicability of the high-order finite element model has been investigated. It has been shown that the model converges to a given solution, which is qualitatively in excellent agreement with the reference solution available in the literature. The LEE/LPE coupling approach also proved successful by providing accurate results while allowing a significant reduction of the computational cost. Enhancements may be considered: the use of Lagrange multipliers at the interface may improve the coupling conditions by hiding the derivative terms which introduce some error. The transmission conditions at the coupling interface depend on the derivatives of the velocity potential, on the LEE side, and on the derivatives of the density and velocity, on the LPE side. These derivatives could be hidden inside additional degrees of freedom, the so-called Lagrange multipliers, to solve additionally in the global system, which would avoid to explicitly approximate the derivatives in the model. This would cancel the additional error created at the coupling interface.

Regarding the mean flow interpolation, its effects have been discussed and showed that a Gauss point interpolation modifies the solution in the shear layer region with respect to a nodal interpolation. In that region, the amplitude of the field is much higher using the interpolation at the Gauss points. This modification may be seen as an improvement, in the sense that it implicates a more accurate interpolation of the mean flow values at each Gauss point. Outside the shear layer, the impact of the mean flow interpolation does not seem to be very significant. The acoustic field does not seem to be largely influenced, whereas the hydrodynamic field is. Interpolating at the Gauss points also directly links the numerical solution to the CFD interpolation. These effects would require some more dedicated studies [175].

In addition, the exhaust complex geometry requires a specific mesh refinement along the aeroengine ducts in order to properly represent the geometry. This constraint translates into a large increase in the number of degrees of freedom when using high orders. Using adaptive order rules should also drastically improve the computational performance of the model. Adaptive order schemes can be based on a-priori or a-posteriori estimators [52, 203] which help in improving the computational efficiency of the model by setting some criteria to choose the polynomial order within each element. Lower polynomial orders may be used in the refined region, allowing a significant reduction of the computational effort. Such schemes should be able to take into account not only the effects of the acoustic waves, but also the vorticity and entropy waves supported by the Linearised Euler Equations.

Chapter 9

Conclusion

In this work, a novel high-order finite element model has been developed to solve the Linearised Euler Equations in the frequency domain for aeroengine exhaust noise applications. This numerical method combines a high-order Finite Element Method associated with a Galerkin/Least-Squares stabilisation technique. The boundary conditions have been imposed through the method of characteristics, while Perfectly Matched Layers have been applied around the computational domain to inject duct modes and absorb outgoing waves. A coupling procedure with the Linearised Potential Equation has been developed to further reduce the computational costs. The key contributions of this work, which have been introduced in Section 1.2 are first summarised, and some insight on future work is given in a second section.

9.1 Key Contributions

The main contribution of this work is the application of a high-order finite element method to solve the Linearised Euler Equations in the frequency domain. The problem formulation has been developed in two dimensions, in three dimensions and for axisymmetric problems, with the use of the method of characteristics to define the boundary conditions. This method presents several advantages with respect to existing techniques which solve the LEE in the frequency domain, and in particular compared to the classical FEM: since the dispersion error and the pollution effect can be treated by increasing the polynomial order instead of refining the mesh, this results in improved accuracy and lower memory requirements for a given problem. For acoustic, vorticity, and entropy waves, the p-FEM code has been verified on simple test cases such as plane wave propagation in free field, and

duct mode propagation with uniform and non-uniform flow. The numerical results have been compared with reference analytic solutions, showing the convergence of the numerical scheme by h- and p-refinement. The L^2-norm error has been found to converge with an order $p+1$ with respect to the Helmholtz number kh. The effects of mean flow interpolation have also been assessed: the mean flow interpolation error is responsible for a stagnation in the error convergence which level is equal to about one order of magnitude higher than the mean flow interpolation error.

As absorbing boundary conditions for outgoing waves, the Perfectly Matched Layer has been applied around the computational domain. It has been found that the PML efficiency highly depends on the stretching function, which is responsible for the wave envelope inside the layer where two sources of error have been identified: the truncation or reflection error, and the discretisation or interpolation error. An existing logarithmic stretching function has been modified with an imaginary part in order to improve the PML damping properties. This new PML has been built to generate linear absorption profiles inside the layer for one-dimensional acoustic waves, and to cancel out the natural oscillations in the PML in the direction of propagation. The proposed stretching function has been shown to provide improved convergence results for two-dimensional duct mode propagation with respect to two existing stretching functions in the literature: lower levels of error have been reached over a large range of degrees of freedom per wavelength, not only for acoustic waves but also for vorticity and entropy waves.

In order to treat the dispersion problem and the convection-related spurious oscillations, numerical stabilisation has been investigated. Unlike steady analyses for time-domain problems which have been studied in the literature, the high-order finite element formulation for the LEE involves two additional variables which are the angular frequency ω and the polynomial order p. Novel optimal stabilisation parameters which are able to cancel the dispersion error have been derived analytically, for the first three polynomial orders. These unsteady parameters are purely imaginary numbers which vary with the frequency, the convection velocity and the characteristic mesh size, unlike the steady stabilisation parameter found in the literature which is real and only depends on the convection velocity and the characteristic mesh size. Although the optimal parameters are very efficient in cancelling out the dispersion error, obtaining them for high orders appears to be expensive. The effects of high orders have also been assessed. It has been observed that even orders introduce an artificial diffusion in the model which is responsible for lowering the convergence rate of the dispersion error for these orders. Stabilisation has been shown to

correct the asymptotic convergence of these orders.

In the framework of aeroengine exhaust noise, the mean flow distribution is highly heterogeneous with regions of complex rotational mean flows and regions of quasi-uniform mean flows. Therefore, a novel technique has been developed to couple the Linearised Euler Equations with the Linearised Potential Equation in order to optimise the acoustic simulation while taking into account the mean flow configuration: in this model the LEE are solved in the rotational flow regions while the LPE are solved in the potential flow regions. Characteristic transmission conditions have been used along the interfaces between the mathematical models. The coupling procedure has been tested for several test cases. It has been found that the coupling procedure provides accurate results, with one accuracy order lower than the full Linearised Euler Equations solution. The approximation of the solution gradients at the coupling interface explains this difference, which may be treated by increasing the polynomial order in the interface elements. A performance study has shown that the memory requirements can be improved by a factor of the same order as the ratio of elements solved with the Linearised Euler Equations.

The numerical model has been applied to several test cases in Chapter 8. First, noise propagation has been solved for the JT15D aeroengine intake to verify the method with a non-straight geometry and a potential flow: the results match the reference solution obtained with the company software Virtual.Lab which solves the Linearised Potential Equation. Second, a simplified aeroengine exhaust with straight duct has been investigated with different mean flow configurations: the high-order finite element model is in good agreement with the available analytic solution, and is able to capture the vorticity shedding that develops from the duct trailing edge singularity. It has been observed that the Kutta condition at the duct trailing edge is supported by the numerical model without additional treatment, which may be explained by the continuous discretisation of the pressure and velocity fields inherent to the finite element method. Third, a realistic aeroengine exhaust combining a complex geometry and a complex sheared mean flow has been studied: the solution convergence has been observed by increasing the polynomial order, and the coupling solution has been shown to provide results similar to the full Linearised Euler Equations solution with lower memory requirements. It has been seen that the mean flow interpolation has significant impact on the acoustic field in the shear layer region, but very low effects outside that region. The physical phenomena linked with acoustic propagation in non-uniform media have been observed: propagation in duct, wave reflection, wave refraction through shear layer, vorticity/entropy waves interaction with acoustic field

and vorticity shedding from duct trailing edge.

9.2 Future Work

In this three-year-and-a-half work, the capability of the proposed high-order finite element model has been demonstrated to solve the Linearised Euler Equations with reduced computational costs with respect to classical finite elements. However, much further research remains to be conducted on this subject. Here are a few aspects that are considered of interest for additional investigation. Since the coupling technique introduces an additional error along the subdomains interface, the use of Lagrange multipliers instead of characteristic transmission conditions should be a valid improvement. In practice, the gradient terms at the interface would be hidden in supplementary variables, the Lagrange multipliers, which would be added to the global system. This would therefore cancel out the additional error and provide a solution with the same accuracy as the full Linearised Euler Equations solution. The benefits of the coupling technique should be even more noticeable on large scale problems involving installation effects for instance, where the LEE region could be reduced to the relevant area.

Another amelioration regards the geometry representation. It has been seen that complex geometries require local mesh refinement to properly represent their profile. This may translate into an excessive number of degrees of freedom when dealing with high-order polynomials. Two solutions could be applied. The first one would consist in using curved elements along the boundaries, which would allow the use of large elements and high-order polynomial interpolation shape functions. Some initial tests have been carried out and have provided promising results, showing that quadratic and cubic elements could be used together with high-order shape functions for the applications studied in this work. The second one relies on *hp*-adaptivity rules: depending on the local element size, a suitable polynomial order may be used. Typically, for a given wavelength, small elements would require low orders while large elements would require high orders.

This adaptivity scheme would also help for treating the multiple wavelengths present when solving the Linearised Euler Equations: the polynomial order in an element should be selected with respect to the local mesh size and the local dominant wavelength. Existing a-priori and a-posteriori adaptivity rules may be applied to the scheme, but they should account for the vorticity and entropy waves. For instance, Prinn developed an a-priori estimator for solving the Linearised Potential Equation based on one-dimensional acoustic

waves [46]. This estimator has been applied to the Linearised Euler Equations in this work, and it has been observed that it is not able to take into account the interaction with the vorticity and entropy waves. Some research on a-posteriori adaptivity schemes may be of interest. A combination of all the aforementioned features with automatically processed decision within the model would provide a more complete, computationally efficient, solver for complex acoustic problems.

In addition, to further assess the numerical model developed in this work, it should be applied to solving complete large scale industrial problems involving aeroengine exhaust noise for several frequencies. Tests should also determine the maximum frequency resolvable with this high-order finite element method, considering the computational resources currently available. The method could also be used for other applications involving for instance swirling mean flows with azimuthal components. Finally, the method has been shown to provide efficient and accurate results with less computational cost than classical finite element methods; it would be appropriate to compare this approach with other techniques such as domain decomposition methods or Discontinuous Galerkin Methods. Lieu *et al.* have for instance compared the p-FEM to the wave-based DGM for the Helmholtz equation, showing that both methods present some advantages and inconvenients. Such comparisons should be interesting to look at in order to keep developing efficient CAA solvers.

Appendix A

Entropy Equation

In this appendix, the mathematical procedure to obtain the entropy equation is detailed. The first law of thermodynamics in Equation 3.4 expresses the energy total differential in terms of the entropy and mass density total differentials. Substituting its expression into the energy conservation equation 3.3, it yields:

$$\rho T\frac{\mathrm{d}s}{\mathrm{d}t}+\boldsymbol{u}\cdot\left(\rho\frac{\partial\boldsymbol{u}}{\partial t}+\frac{1}{2}\rho\boldsymbol{\nabla}u^2\right)+\left(e+\frac{1}{2}u^2+\frac{p}{\rho}\right)\left(\frac{\partial\rho}{\partial t}+\boldsymbol{\nabla}\cdot(\rho\boldsymbol{u})\right) - \boldsymbol{\nabla}\cdot(\boldsymbol{\sigma}\boldsymbol{u})-p\boldsymbol{\nabla}\cdot\boldsymbol{u}=\boldsymbol{f}\cdot\boldsymbol{u}-\boldsymbol{\nabla}\cdot\boldsymbol{Q}. \quad \text{(A.1)}$$

Since the term $\boldsymbol{\nabla}u^2$ expands into: $2\left((\boldsymbol{u}\cdot\boldsymbol{\nabla})\boldsymbol{u}+\boldsymbol{u}\times(\boldsymbol{\nabla}\times\boldsymbol{u})\right)$, Equation A.1 becomes:

$$\rho T\frac{\mathrm{d}s}{\mathrm{d}t}+\boldsymbol{u}\cdot\left(\rho\frac{\partial\boldsymbol{u}}{\partial t}+\rho(\boldsymbol{u}\cdot\boldsymbol{\nabla})\boldsymbol{u}\right)+\left(e+\frac{1}{2}u^2+\frac{p}{\rho}\right)\left(\frac{\partial\rho}{\partial t}+\boldsymbol{\nabla}\cdot(\rho\boldsymbol{u})\right) + \boldsymbol{u}\cdot(\rho\boldsymbol{u}\times(\boldsymbol{\nabla}\times\boldsymbol{u}))-\boldsymbol{\nabla}\cdot(\boldsymbol{\sigma}\boldsymbol{u})-p\boldsymbol{\nabla}\cdot\boldsymbol{u}=\boldsymbol{f}\cdot\boldsymbol{u}-\boldsymbol{\nabla}\cdot\boldsymbol{Q}. \quad \text{(A.2)}$$

On the left-hand side of Equation A.2, the first term is proportional to the entropy material derivative. The second term is part of the momentum conservation equation 3.2 since that equation can be written like:

$$\rho\frac{\partial\boldsymbol{u}}{\partial t}+\rho(\boldsymbol{u}\cdot\boldsymbol{\nabla})\boldsymbol{u}-\boldsymbol{\nabla}\cdot\boldsymbol{\sigma}=\boldsymbol{f}. \quad \text{(A.3)}$$

In the second parenthesis of the third term, the mass conservation equation 3.1 is found and that term is exactly equal to zero. In the fourth term, $\boldsymbol{u}\cdot(\rho\boldsymbol{u}\times(\boldsymbol{\nabla}\times\boldsymbol{u}))$ also happens to be zero. The fifth term expands like: $\boldsymbol{\nabla}\cdot(\boldsymbol{\sigma}\boldsymbol{u})=\boldsymbol{\sigma}:\boldsymbol{\nabla}\boldsymbol{u}+\boldsymbol{u}\cdot(\boldsymbol{\nabla}\cdot\boldsymbol{\sigma})$. Thus, Equation

A.2 simplifies to:

$$\rho T \frac{\mathrm{d}s}{\mathrm{d}t} - \boldsymbol{\sigma} : \boldsymbol{\nabla u} - p \boldsymbol{\nabla} \cdot \boldsymbol{u} = -\boldsymbol{\nabla} \cdot \boldsymbol{Q}, \tag{A.4}$$

Using the constitutive equation 3.6, the entropy equation is finally obtained:

$$\rho T \frac{\mathrm{d}s}{\mathrm{d}t} - \boldsymbol{\tau} : \boldsymbol{\nabla u} = -\boldsymbol{\nabla} \cdot \boldsymbol{Q}. \tag{A.5}$$

Appendix B

Linearised Euler Equations

B.1 Three Dimensions

In conservative form, the three-dimensional Linearised Euler Equations read:

$$\mathrm{j}\omega\boldsymbol{q} + \frac{\partial \boldsymbol{A}_x \boldsymbol{q}}{\partial x} + \frac{\partial \boldsymbol{A}_y \boldsymbol{q}}{\partial y} + \frac{\partial \boldsymbol{A}_z \boldsymbol{q}}{\partial z} = \boldsymbol{0}, \tag{B.1}$$

where $\boldsymbol{q} = \{\rho', (\rho u_x)', (\rho u_y)', (\rho u_z)', p_\mathrm{c}'\}^\mathrm{t}$. The flux matrices are:

$$\boldsymbol{A}_x = \begin{bmatrix} 0 & 1 & 0 & 0 & 0 \\ -u_{0_x}^2 & 2u_{0_x} & 0 & 0 & \dfrac{\rho_0 c_0^2}{p_{\mathrm{c}_0}} \\ -u_{0_x}u_{0_y} & u_{0_y} & u_{0_x} & 0 & 0 \\ -u_{0_z}u_{0_x} & u_{0_z} & 0 & u_{0_x} & 0 \\ -\dfrac{p_{\mathrm{c}_0}}{\rho_0}u_{0_x} & \dfrac{p_{\mathrm{c}_0}}{\rho_0} & 0 & 0 & u_{0_x} \end{bmatrix}, \boldsymbol{A}_y = \begin{bmatrix} 0 & 0 & 1 & 0 & 0 \\ -u_{0_x}u_{0_y} & u_{0_y} & u_{0_x} & 0 & 0 \\ -u_{0_y}^2 & 0 & 2u_{0_y} & 0 & \dfrac{\rho_0 c_0^2}{p_{\mathrm{c}_0}} \\ -u_{0_y}u_{0_z} & 0 & u_{0_z} & u_{0_y} & 0 \\ -\dfrac{p_{\mathrm{c}_0}}{\rho_0}u_{0_y} & 0 & \dfrac{p_{\mathrm{c}_0}}{\rho_0} & 0 & u_{0_y} \end{bmatrix},$$

$$\boldsymbol{A}_z = \begin{bmatrix} 0 & 0 & 0 & 1 & 0 \\ -u_{0_z}u_{0_x} & u_{0_z} & 0 & u_{0_x} & 0 \\ -u_{0_y}u_{0_z} & 0 & u_{0_z} & u_{0_y} & 0 \\ -u_{0_z}^2 & 0 & 0 & 2u_{0_z} & \dfrac{\rho_0 c_0^2}{p_{\mathrm{c}_0}} \\ -\dfrac{p_{\mathrm{c}_0}}{\rho_0}u_{0_z} & 0 & 0 & \dfrac{p_{\mathrm{c}_0}}{\rho_0} & u_{0_z} \end{bmatrix}. \tag{B.2}$$

B.2 Cylindrical Coordinates

In cylindrical coordinates (r, θ, x), the Linearised Euler Equations read:

$$\mathrm{j}\omega \boldsymbol{q} + \frac{1}{r}\boldsymbol{A}_\mathrm{c}\boldsymbol{q} + \frac{1}{r}\frac{\partial r \boldsymbol{A}_r \boldsymbol{q}}{\partial r} + \frac{1}{r}\frac{\partial \boldsymbol{A}_\theta \boldsymbol{q}}{\partial \theta} + \frac{\partial \boldsymbol{A}_x \boldsymbol{q}}{\partial x} = \boldsymbol{0}, \tag{B.3}$$

with $\boldsymbol{q} = \{\rho', (\rho u_r)', (\rho u_\theta)', (\rho u_x)', p'_\mathrm{c}\}^\mathrm{t}$. The flux matrices $\boldsymbol{A}_r$, $\boldsymbol{A}_\theta$, $\boldsymbol{A}_x$ and the matrix $\boldsymbol{A}_\mathrm{c}$ read:

$$\boldsymbol{A}_r = \begin{bmatrix} 0 & 1 & 0 & 0 & 0 \\ -u_{0_r}^2 & 2u_{0_r} & 0 & 0 & \frac{\rho_0 c_0^2}{\pi_0} \\ -u_{0_r}u_{0_\theta} & u_{0_\theta} & u_{0_r} & 0 & 0 \\ -u_{0_x}u_{0_r} & u_{0_x} & 0 & u_{0_r} & 0 \\ -\frac{\pi_0}{\rho_0}u_{0_r} & \frac{\pi_0}{\rho_0} & 0 & 0 & u_{0_r} \end{bmatrix}, \boldsymbol{A}_\theta = \begin{bmatrix} 0 & 0 & 1 & 0 & 0 \\ -u_{0_r}u_{0_\theta} & u_{0_\theta} & u_{0_r} & 0 & 0 \\ -u_{0_\theta}^2 & 0 & 2u_{0_\theta} & 0 & \frac{\rho_0 c_0^2}{\pi_0} \\ -u_{0_\theta}u_{0_x} & 0 & u_{0_x} & u_{0_\theta} & 0 \\ -\frac{\pi_0}{\rho_0}u_{0_\theta} & 0 & \frac{\pi_0}{\rho_0} & 0 & u_{0_\theta} \end{bmatrix},$$

$$\boldsymbol{A}_x = \begin{bmatrix} 0 & 0 & 0 & 1 & 0 \\ -u_{0_x}u_{0_r} & u_{0_x} & 0 & u_{0_r} & 0 \\ -u_{0_\theta}u_{0_x} & 0 & u_{0_x} & u_{0_\theta} & 0 \\ -u_{0_x}^2 & 0 & 0 & 2u_{0_x} & \frac{\rho_0 c_0^2}{\pi_0} \\ -\frac{\pi_0}{\rho_0}u_{0_x} & 0 & 0 & \frac{\pi_0}{\rho_0} & u_{0_x} \end{bmatrix} \text{ and } \boldsymbol{A}_\mathrm{c} = \begin{bmatrix} 0 & 0 & 0 & 0 & 0 \\ 0 & 0 & 0 & 0 & -\frac{\rho_0 c_0^2}{\pi_0} \\ 0 & 0 & 0 & 0 & 0 \\ 0 & 0 & 0 & 0 & 0 \\ 0 & 0 & 0 & 0 & 0 \end{bmatrix}. \tag{B.4}$$

For axisymmetric problems, $\boldsymbol{q} \equiv \mathrm{e}^{-\mathrm{j}m\theta}$ where m is the azimuthal order. Equation B.3 simplifies to:

$$\mathrm{j}\omega \boldsymbol{q} + \frac{1}{r}\boldsymbol{A}_\mathrm{c}\boldsymbol{q} + \frac{1}{r}\frac{\partial r \boldsymbol{A}_r \boldsymbol{q}}{\partial r} - \mathrm{j}\frac{m}{r}\boldsymbol{A}_\theta \boldsymbol{q} + \frac{\partial \boldsymbol{A}_x \boldsymbol{q}}{\partial x} = \boldsymbol{0}. \tag{B.5}$$

Appendix C

Analytic Solutions

Rectangular Cross-Section Duct

For a rectangular cross-section duct in Cartesian coordinates with axial uniform mean flow, the variables analytic expressions are:

$$\begin{cases} \rho &= \dfrac{A_p}{c_0^2} & \cos(k_y y)\cos(k_z z)\mathrm{e}^{-\mathrm{j}k_x x} &+ & B_\rho \mathrm{e}^{-\mathrm{j}\frac{k_0}{M_x}x} \\ u_x &= \dfrac{A_p}{\rho_0 c_0}\dfrac{k_x}{k_0 - M_x k_x} & \cos(k_y y)\cos(k_z z)\mathrm{e}^{-\mathrm{j}k_x x} &+ & B_x \mathrm{e}^{-\mathrm{j}\frac{k_0}{M_x}x} \\ u_y &= \dfrac{A_p}{\rho_0 c_0}\dfrac{-\mathrm{j}k_y}{k_0 - M_x k_x} & \sin(k_y y)\cos(k_z z)\mathrm{e}^{-\mathrm{j}k_x x} &+ & B_y \mathrm{e}^{-\mathrm{j}\frac{k_0}{M_x}x} \\ u_z &= \dfrac{A_p}{\rho_0 c_0}\dfrac{-\mathrm{j}k_z}{k_0 - M_x k_x} & \cos(k_y y)\sin(k_z z)\mathrm{e}^{-\mathrm{j}k_x x} &+ & B_z \mathrm{e}^{-\mathrm{j}\frac{k_0}{M_x}x} \\ p &= A_p & \cos(k_y y)\cos(k_z z)\mathrm{e}^{-\mathrm{j}k_x x} & & \end{cases} , \tag{C.1}$$

where A_p and $B_\bullet$ are constant amplitudes. Note that the subscript $_{m,n}$ and the superscript $^{\pm}$ are dropped to facilitate the reading. These expressions are modal and for waves propagating in one direction. Contributions to the acoustic field are found in all the variables, whereas the vorticity contributions appear only in the velocity field through the constant amplitudes B_x, B_y and B_z. The entropy wave is supported by the density component through the constant amplitude B_ρ.

Circular Cross-Section Duct

For circular and annular cross-section ducts in cylindrical coordinates with axial uniform mean flow, each variable depends on the azimuthal and radial orders (m, n) and on the amplitude $U(r)$ in the radial direction. The subscript $_{m,n}$ and the superscript $^{\pm}$ are also

dropped here. The variables analytic expressions are:

$$\begin{cases} \rho &= \dfrac{A_p}{c_0^2} & U(r)\mathrm{e}^{-\mathrm{j}m\theta}\mathrm{e}^{-\mathrm{j}k_x x} &+ & B_\rho \mathrm{e}^{-\mathrm{j}\frac{k_0}{M_x}x} \\ u_r &= \dfrac{A_p}{\rho_0 c_0}\dfrac{\mathrm{j}}{k_0 - M_x k_x} & U'(r)\mathrm{e}^{-\mathrm{j}m\theta}\mathrm{e}^{-\mathrm{j}k_x x} &+ & B_r \mathrm{e}^{-\mathrm{j}\frac{k_0}{M_x}x} \\ u_\theta &= \dfrac{A_p}{\rho_0 c_0}\dfrac{1}{k_0 - M_x k_x}\dfrac{m}{r} & U(r)\mathrm{e}^{-\mathrm{j}m\theta}\mathrm{e}^{-\mathrm{j}k_x x} &+ & B_\theta \mathrm{e}^{-\mathrm{j}\frac{k_0}{M_x}x} \\ u_x &= \dfrac{A_p}{\rho_0 c_0}\dfrac{k_x}{k_0 - M_x k_x} & U(r)\mathrm{e}^{-\mathrm{j}m\theta}\mathrm{e}^{-\mathrm{j}k_x x} &+ & B_x \mathrm{e}^{-\mathrm{j}\frac{k_0}{M_x}x} \\ p &= A_p & U(r)\mathrm{e}^{-\mathrm{j}m\theta}\mathrm{e}^{-\mathrm{j}k_x x} & & \end{cases} , \tag{C.2}$$

where A_p and $B_\bullet$ are constant amplitudes.

Appendix D

Flux Matrices and Characteristics

The matrices of change of basis for the flux matrix $\boldsymbol{F} = n_x \boldsymbol{A}_x + n_y \boldsymbol{A}_y + n_z \boldsymbol{A}_z$ (valid for $n_x \neq 0$) are given in three dimensions for the Cartesian coordinate systems. The matrix of eigenvalues $\boldsymbol{\Lambda}$ is:

$$\boldsymbol{\Lambda} = \begin{bmatrix} \boldsymbol{u}_0 \cdot \boldsymbol{n} & 0 & 0 & 0 & 0 \\ 0 & \boldsymbol{u}_0 \cdot \boldsymbol{n} & 0 & 0 & 0 \\ 0 & 0 & \boldsymbol{u}_0 \cdot \boldsymbol{n} & 0 & 0 \\ 0 & 0 & 0 & \boldsymbol{u}_0 \cdot \boldsymbol{n} - c_0 & 0 \\ 0 & 0 & 0 & 0 & \boldsymbol{u}_0 \cdot \boldsymbol{n} + c_0 \end{bmatrix}, \tag{D.1}$$

The matrices of change of basis $\boldsymbol{W}$ and $\boldsymbol{W}^{-1}$ read:

$$\boldsymbol{W} = \begin{bmatrix} 0 & 0 & 1 & 1 & 1 \\ -n_y & -n_z & u_{0_x} & u_{0_x} - n_x c_0 & u_{0_x} + n_x c_0 \\ n_x & 0 & u_{0_y} & u_{0_y} - n_y c_0 & u_{0_y} + n_y c_0 \\ 0 & n_x & u_{0_z} & u_{0_z} - n_z c_0 & u_{0_z} + n_z c_0 \\ 0 & 0 & 0 & \dfrac{p_{c_0}}{\rho_0} & \dfrac{p_{c_0}}{\rho_0} \end{bmatrix}, \boldsymbol{W}^{-1} = \begin{bmatrix} \dfrac{n_y \boldsymbol{u}_0 \cdot \boldsymbol{n} - u_{0_y}}{n_x} & -n_y & \dfrac{1 - n_y^2}{n_x} & -\dfrac{n_y n_z}{n_x} & 0 \\ \dfrac{n_z \boldsymbol{u}_0 \cdot \boldsymbol{n} - u_{0_z}}{n_x} & -n_z & -\dfrac{n_y n_z}{n_x} & \dfrac{1 - n_z^2}{n_x} & 0 \\ 1 & 0 & 0 & 0 & -\dfrac{\rho_0}{p_{c_0}} \\ \dfrac{\boldsymbol{u}_0 \cdot \boldsymbol{n}}{2c_0} & -\dfrac{n_x}{2c_0} & -\dfrac{n_y}{2c_0} & -\dfrac{n_z}{2c_0} & \dfrac{\rho_0}{2p_{c_0}} \\ -\dfrac{\boldsymbol{u}_0 \cdot \boldsymbol{n}}{2c_0} & \dfrac{n_x}{2c_0} & \dfrac{n_y}{2c_0} & \dfrac{n_z}{2c_0} & \dfrac{\rho_0}{2p_{c_0}} \end{bmatrix}. \tag{D.2}$$

These expressions are valid for $n_x \neq 0$. For $n_x = 0$, they read:

$$\boldsymbol{W} = \begin{bmatrix} 0 & 0 & 1 & 1 & 1 \\ 1 & 0 & u_{0_x} & u_{0_x} & u_{0_x} \\ 0 & -n_z & u_{0_y} & u_{0_y} - n_y c_0 & u_{0_y} + n_y c_0 \\ 0 & n_y & u_{0_z} & u_{0_z} - n_z c_0 & u_{0_z} + n_z c_0 \\ 0 & 0 & 0 & \dfrac{p_{c_0}}{\rho_0} & \dfrac{p_{c_0}}{\rho_0} \end{bmatrix}, \boldsymbol{W}^{-1} = \begin{bmatrix} -u_{0_x} & 1 & 0 & 0 & 0 \\ n_z u_{0_y} - n_y u_{0_z} & 0 & -n_z & n_y & 0 \\ 1 & 0 & 0 & 0 & -\dfrac{\rho_0}{p_{c_0}} \\ \dfrac{\boldsymbol{u}_0 \cdot \boldsymbol{n}}{2c_0} & 0 & -\dfrac{n_y}{2c_0} & -\dfrac{n_z}{2c_0} & \dfrac{\rho_0}{2p_{c_0}} \\ -\dfrac{\boldsymbol{u}_0 \cdot \boldsymbol{n}}{2c_0} & 0 & \dfrac{n_y}{2c_0} & \dfrac{n_z}{2c_0} & \dfrac{\rho_0}{2p_{c_0}} \end{bmatrix}. \tag{D.3}$$

Bibliography

[1] K. Hamiche, G. Gabard, and H. Bériot. A High-Order Finite Element Method for the Linearised Euler Equations. In 26$^{\text{th}}$ *International Conference on Noise and Vibration ISMA2014*, Leuven, Belgium, 2014. 7

[2] K. Hamiche, H. Bériot, and G. Gabard. Application of a High-Order FEM Solver to Aeroengine Exhaust Noise Radiation. In 10$^{\text{th}}$ *European Congress and Exposition on Noise Control Engineering EuroNoise 2015*, Maastricht, Netherlands, 2015.

[3] K. Hamiche, H. Bériot, and G. Gabard. A Stabilised High-Order Finite Element Model for the Linearised Euler Equations. In 21$^{\text{st}}$ *AIAA/CEAS Aeroacoustics Conference*, Dallas, TX, USA, 2015.

[4] K. Hamiche, H. Bériot, and G. Gabard. Application of a High-Order FEM Solver to Realistic Aeroengine Exhaust Noise Radiation. In 22$^{\text{nd}}$ *International Congress on Sound and Vibration ICSV22*, Florence, Italy, 2015.

[5] K. Hamiche, G. Gabard, and H. Bériot. A High-Order Finite Element Method for the Linearised Euler Equations. *Acta Acustica United With Acustica*, 2016. Accepted 27 April 2016. 7

[6] L. Fritschi, A. Lex Brown, R. Kim, D. Schwela, and S. Kephalopoulos. *Burden of Disease from Environmental Noise: Quantification of Healthy Life Years Lost in Europe*. WHO Regional Office for Europe, Copenhagen, Denmark, 2011. 1, 2.1

[7] ICAO. Environmental Protection - Volume 1 - Aircraft Noise. Technical report, International Civil Aviation Organization, Montréal, Quebec, Canada, 2011. 1

[8] H. E. Laszlo, E. S. McRobie, S. A. Stansfeld, and A. L. Hansell. Annoyance and Other Reaction Measures to Changes in Noise Exposure - A Review. *Science of the Total Environment*, 435:551–562, 2012. 2.1

[9] R. N. Lawton and D. Fujiwara. Living with Aircraft Noise: Airport Proximity,

Aviation Noise and Subjective Wellbeing in England. *Transportation Research Part D: Transport and Environment*, 42:104–118, 2016. 2.1

[10] J. A. Benfield, P. A. Bell, L. J. Troup, and N. C. Soderstrom. Aesthetic and Affective Effects of Vocal and Traffic Noise on Natural Landscape Assessment. *Journal of Environmental Psychology*, 30(1):103–111, 2010. 2.1

[11] J. R. Barber, K. R. Crooks, and K. M. Fristrup. The Costs of Chronic Noise Exposure for Terrestrial Organisms. *Trends in Ecology and Evolution*, 25(3):180–189, 2010. 2.1

[12] ICAO. Environmental Report. Technical report, International Civil Aviation Organization, Montréal, Quebec, Canada, 2010. 2.1

[13] European Commission. Flightpath 2050: Europe's Vision for Aviation. Technical report, European Union, Luxembourg, 2011. 2.1

[14] R. J. Astley, R. Sugimoto, and P. Mustafi. Computational Aero-Acoustics for Fan Duct Propagation and Radiation. Current Status and Application to Turbofan Liner Optimisation. *Journal of Sound and Vibration*, 330(26):3832–3845, 2011. 2.1

[15] D. P. Lockard and G. M. Lilley. The Airframe Noise Reduction Challenge. Technical report, NASA Langley Research Center, Hampton, 2004. 2.1

[16] G. M. Lilley. The Prediction of Airframe Noise and Comparison with Experiment. *Journal of Sound and Vibration*, 239(4):849–859, 2001. 2.1

[17] F. C. Sgard, N. Atalla, and C. K. Amedin. Vibro-Acoustic Behaviour of a Cavity Backed by a Plate Coated with a Meso-Heterogeneous Porous Material. *Acta Acustica United with Acustica*, 93(1):106–114, 2007. 2.1

[18] D. Lafarge and A. Duclos. Acoustic Non-Local Permittivities in Rigid-Framed Porous Metamaterials. In *International Conference Days on Diffraction*, St. Petersbourg, Russia, 2008. 2.1

[19] T. Elnady, A. Elsabbagh, W. Akl, O. Mohamady, V. M. Garcia-Chocano, D. Torrent, F. Cervera, and J. Sánchez-Dehesa. Quenching of Acoustic Bandgaps by Flow Noise. *Applied Physics Letters*, 94(13):134104, 2009. 2.1

[20] J. C. Hardin and S. L. Lamkin. Computational Aeroacoustics - Present Status and Future Promise. In *Aero- and Hydro-Acoustics*, Lyon, France, 1986. 2.2

[21] R. D. Sandberg. Direct Numerical Simulations for Flow and Noise Studies. *Procedia Engineering*, 61:356–362, 2013. 2.2, 2.3

[22] B. A. Singer, D. P. Lockard, and M. Lilley. Hybrid Acoustic Predictions. *Computers and Mathematics with Applications*, 46(4):647–669, 2003. 2.2

[23] J. C. Hardin and S. L. Lamkin. Aeroacoustic Computation of Cylinder Wake Flow. *AIAA Journal*, 22(1):51–57, 1984. 2.2

[24] C. K. W. Tam and J. C. Webb. Dispersion-Relation-Preserving Finite Difference Schemes for Computational Acoustics. *Journal of Computational Physics*, 107(2): 262–281, 1993. 2.2, 2.3, 2.4.3, 2.5

[25] C. K. W. Tam. Recent Advances in Computational Aeroacoustics. *Fluid Dynamics Research*, 38(9):591–615, 2006. 2.2

[26] G. Bao, G. W. Wei, and S. Zhao. Numerical Solution of the Helmholtz Equation with High Wavenumbers. *International Journal for Numerical Methods in Engineering*, 59(3):389–408, 2004. 2.2

[27] A. Deraemaeker, I. M. Babuŝka, and P. Bouillard. Dispersion and Pollution of the FEM Solution for the Helmholtz Equation in One, Two and Three Dimensions. *International Journal for Numerical Methods in Engineering*, 46(4):471–499, 1999. 2.2, 2.4.3

[28] K. W. Thompson. Time-Dependent Boundary Conditions for Hyperbolic Systems II. *Journal of Computational Physics*, 89(2):439–461, 1990. 2.2, 2.5, 4.2.1

[29] D. P. Lockard. An Overview of Computational Aeroacoustic Modeling at NASA Langley. In *The Tenth Thermal and Fluids Analysis Workshop*, Huntsville, AL, USA, 2001. 2.2

[30] R. J. Astley. Numerical Methods for Noise Propagation in Moving Flows, with Application to Turbofan Engines. *Acoustical Science and Technology*, 30(4):227–239, 2009. 2.2, 2.3, 2.4.1, 3.1.3, 8.2.1

[31] S. W. Rienstra and A. Hirschberg. *An Introduction to Acoustics*. Eindhoven University of Technology, Eindhoven, Netherlands, 2013. 2.3, 3.1.2, 3.1.3, 3.2

[32] S. A. Orszag. Analytical Theories of Turbulence. *Journal of Fluid Mechanics*, 41(2): 363–386, 1970. 2.3

[33] C. A. Wagner, T. Hüttl, and P. Sagaut. *Large-Eddy Simulation for Acoustics*. Cambridge University Press, Cambridge, United-Kingdom, 2007. 2.3

[34] A. N. Kolmogorov. On the Local Structure of Turbulence in Incompressible Viscous Fluid at Very Large Reynolds Number. *Comptes Rendus de l'Académie des Sciences de l'URSS*, 30:301–305, 1941. 2.3

[35] D. J. Bodony and S. K. Lele. Current Status of Jet Noise Predictions Using Large-Eddy Simulation. *AIAA Journal*, 46(2):364–380, 2008. 2.3

[36] M. J. Lighthill. *An Introduction to Fourier Analysis and Generalised Functions*. Cambridge University Press, Cambridge, United-Kingdom, 1958. 2.3

[37] R. Ewert. The Fast Random Particle-Mesh Method to Realize Unsteady Turbulent Sound Sources and Velocity Fields for CAA Applications. In 13$^{\text{th}}$ *AIAA/CEAS Aeroacoustics Conference*, Rome, Italy, 2007. 2.3

[38] T. Toulorge. *Efficient Runge-Kutta Discontinuous Galerkin Methods Applied to Aeroacoustics*. PhD thesis, Katholieke Universiteit Leuven, 2012. 2.3, 2.4.3

[39] A. Kierkegaard. *Frequency Domain Linearized Navier-Stokes Equations Methods for Low Mach Number Internal Aeroacoustics*. PhD thesis, Royal Institute of Technology Stockholm, 2011. 2.3

[40] J. Tournadre, P. Martinez-Lera, and W. Desmet. Numerical Study of the Acoustic Response of a Single Orifice with Turbulent Mean Flow. In 22$^{\text{nd}}$ *International Congress on Sound and Vibration ICSV22*, Florence, Italy, 2015. 2.3

[41] C. Bailly and D. Juvé. Numerical Solution of Acoustic Propagation Problems Using Linearized Euler Equations. *AIAA Journal*, 38(1):22–29, 2000. 2.3, 2.4.1

[42] C. Bogey, C. Bailly, and D. Juvé. Computation of Flow Noise Using Source Terms in Linearized Euler Equations. *AIAA Journal*, 40(2):235–243, 2002. 2.3, 2.4.1

[43] R. Ewert and W. Schröder. Acoustic Perturbation Equations Based on Flow Decomposition via Source Filtering. *Journal of Computational Physics*, 188(2):365–398, 2003. 2.3

[44] A. Agarwal, P. J. Morris, and R. Mani. The Calculation of Sound Propagation in Nonuniform Flows: Suppression of Instability Waves. *AIAA Journal*, 42(1):80–88, 2004. 2.3, 2.4.1, 2.4.1

[45] A. Angeloski, M. Discacciati, C. Legendre, G. Lielens, and A. Huerta. Challenges for Time and Frequency Domain Aeroacoustic Solvers. In 11^{th} *World Congress on Computational Mechanics*, Barcelona, Spain, 2014. 2.3, 2.4.1, 2.4.1, 3.1.3

[46] A. G. Prinn. *Efficient Finite Element Methods for Aircraft Engine Noise Prediction.* PhD thesis, University of Southampton, 2014. 2.3, 2.4.3, 9.2

[47] A. D. Pierce. Wave Equation for Sound in Fluids with Unsteady Inhomogeneous Flow. *Journal of the Acoustical Society of America*, 87:2292–2299, 1990. 2.3

[48] A. Prinn, G. Gabard, and H. Bériot. Finite Element Simulation of Noise Radiation Through Shear Layers. In *Acoustics 2012 Nantes Conference*, Nantes, France, 2012. 2.3

[49] D. C. Pridmore-Brown. Sound Propagation in a Fluid Flowing Through an Attenuating Duct. *Journal of Fluid Mechanics*, 4(4):393–406, 1958. 2.3

[50] E. Bécache, A.-S. Bonnet-Ben Dhia, and G. Legendre. Perfectly Matched Layers for the Convected Helmholtz Equation. *SIAM Journal on Numerical Analysis*, 42(1): 409–433, 2004. 2.3, 2.5, 3.3, 4.4.1, 4.4.3, 4.4.3

[51] H. Bériot, G. Gabard, and E. Perrey-Debain. Analysis of High-Order Finite Elements for Convected Wave Propagation. *International Journal for Numerical Methods in Engineering*, 96(11):665–688, 2013. 2.3, 2.4.3, 2.6, 5.1.2, 6.1.1, 6.1.1, 6.2.3, 7.4.3

[52] H. Bériot, A. Prinn, and G. Gabard. Efficient Implementation of High-Order Finite Elements for Helmholtz Problems. *International Journal for Numerical Methods in Engineering*, 106(3):213–240, 2016. 2.3, 2.4.3, 2.6, 6.1.1, 8.1.2, 8.3.3

[53] O. Labbé, C. Peyret, G. Rahier, and M. Huet. A CFD/CAA Coupling Method Applied to Jet Noise Prediction. *Computer & Fluids*, 86:1–13, 2013. 2.4.1

[54] S. W. Rienstra. Impedance Models in Time Domain, Including the Extended Helmholtz Resonator Model. In 12^{th} *AIAA/CEAS Aeroacoustics Conference*, Cambridge, MA, USA, 2006. 2.4.1

[55] G. Gabard and E. J. Brambley. A Full Discrete Dispersion Analysis of Time-Domain Simulations of Acoustic Liners with Flow. *Journal of Computational Physics*, 273 (15):310–326, 2014. doi: 10.1016/j.jcp.2014.05.004. 2.4.1

[56] A. Michalke. On Spatially Growing Disturbances in an Inviscid Shear Layer. *Journal of Fluid Mechanics*, 23(3):521–544, 1965. 2.4.1, 8.2.1, 8.2.3.3

[57] Y. Özyörük. Numerical Prediction of Aft Radiation of Turbofan Tones through Exhaust Jets. *Journal of Sound and Vibration*, 325(1-2):122–144, 2009. 2.4.1, 2.4.3, 4.4.2

[58] Y. Özyörük and B. J. Tester. Application of Frequency-Domain Linearized Euler Solutions to the Prediction of Aft Fan Tones and Comparison with Experimental Measurements on Model Scale Turbofan Exhaust Nozzles. *Journal of Sound and Vibration*, 330(16):3846–3858, 2011. 2.4.1, 2.4.3, 8.3.1

[59] A. Iob, R. Arina, and C. Schipani. Frequency-Domain Linearized Euler Model for Turbomachinery Noise Radiation Through Engine Exhaust. *AIAA Journal*, 48(4): 848–858, 2010. 2.4.1, 4.4.2, 6.1.2, 8.3.1, 8.3.1, 8.3.2.1

[60] A. Iob, R. Della Ratta Rinaldi, and R. Arina. A Frequency-Domain Linearized Euler Model for Noise Radiation. In Prof. Max Mulder, editor, *Aeronautics and Astronautics*, ISBN: 978-953-307-473-3. InTech, 2011. 2.4.1

[61] W. Eversman and R. J. Astley. Acoustic Transmission in Non-Uniform Ducts with Mean Flow - Part I: The Method of Weighted Residuals. *Journal of Sound and Vibration*, 74(1):89–101, 1981. 2.4.1

[62] R. J. Astley and W. Eversman. Acoustic Transmission in Non-Uniform Ducts with Mean Flow - Part II: The Finite Element Method. *Journal of Sound and Vibration*, 74(1):103–121, 1981. 2.4.1

[63] R. M. Munt. The Interaction of Sound with a Subsonic Jet Issuing from a Semi-Infinite Cylindrical Pipe. *Journal of Fluid Mechanics*, 83(4):609–640, 1977. 2.4.1, 8.2.1

[64] P. P. Rao and P. J. Morris. Use of Finite Element Methods in Frequency Domain Aeroacoustics. *AIAA Journal*, 44(7):1643–1652, 2006. 2.4.1, 2.4.3, 6.1.2, 6.3.2

[65] M. Billson, L.-E. Eriksson, and L. Davidson. Acoustic Source Terms for the Linearized Euler Equations in Conservative Form. *AIAA Journal*, 43(4):752–759, 2005. 2.4.1

[66] S. K. Richards, X. X. Chen, X. Huang, and X. Zhang. Computation of Fan Noise Radiation Through an Engine Exhaust Geometry with Flow. *International Journal of Aeroacoustics*, 6(3):223–241, 2007. 2.4.1

[67] Z. Rarata. *Application and Assessment of Time-Domain DGM for Intake Acoustics Using 3D Linearized Euler Equations*. PhD thesis, University of Southampton, 2014. 2.4.1, 2.4.3

[68] K. Ho-Le. Finite Element Mesh Generation Methods: A Review and Classification. *Computer-Aided Design*, 20(1):27–38, 1988. 2.4.2

[69] P. J. Frey and P.-L. George. *Mesh Generation, Application to Finite Elements*. John Wiley & Sons, Inc., Hoboken, NJ, USA, 2008. 2.4.2

[70] V. S. Schmid, H. Bériot, O. Atak, and G. Gabard. High-Order Curved Mesh Generation by Using a Fine Linear Target Mesh. In *VII European Congress on Computational Methods in Applied Sciences and Engineering*, Crete Island, Greece, 2016. 2.4.2

[71] G. Desquesnes, M. Terracol, E. Manoha, and P. Sagaut. On the Use of High-Order Overlapping Grid Methods for Coupling in CFD/CAA. *Journal of Computational Physics*, 220(1):355–382, 2006. 2.4.3

[72] L. Yuang and C.-W. Shu. Discontinuous Galerkin Method Based on Non-Polynomial Approximation Spaces. *Journal of Computational Physics*, 218(1):295–323, 2006. 2.4.3

[73] D. Stanescu, M. Y. Hussaini, and F. Farassat. Aircraft Engine Noise Scattering by Fuselage and Wings: A Computational Approach. *Journal of Sound and Vibration*, 263(2):319–333, 2003. 2.4.3

[74] R. Della Ratta Rinaldi, A. Iob, and R. Arina. An Efficient Discontinuous Galerkin Method for Aeroacoustic Propagation. *International Journal for Numerical Methods in Fluids*, 69(9):1473–1495, 2012.

[75] M. Williamschen, G. Gabard, and H. Bériot. Performance of the DGM for the Linearized Euler Equations with Non-Uniform Mean Flow. In 21st *AIAA/CEAS Aeroacoustics Conference*, Dallas, TX, USA, 2015. 2.4.3

[76] H. L. Atkins and C.-W. Shu. Quadrature-Free Implementation of Discontinuous Galerkin Method for Hyperbolic Equations. *AIAA Journal*, 36(5):775–782, 1998. 2.4.3

[77] R. D. Ciskowski and C. A. Brebbia. *Boundary Element Methods in Acoustics*. Elsevier Applied Science, Southampton, United-Kingdom, 1991. 2.4.3

[78] S. W. Herrin, T. W. Wu, and A. F. Seybert. *Handbook of Noise and Vibration Control*, chapter 8. Boundary Element Modelling, pages 116–127. John Wiley & Sons, Inc., Hoboken, NJ, USA, 2007. 2.4.3

[79] P. K. Banerjee and R. Butterfield. *Boundary Element Methods in Engineering Science*. McGraw-Hill, London, United-Kingdom, 1981. 2.4.3

[80] C. A. Brebbia, J. C. F. Telles, and L. C. Wrobel. *Boundary Element Techniques: Theory and Applications in Engineering*. Springer-Verlag, Berlin, Germany, 1984. 2.4.3

[81] L. Greengard and V. Rokhlin. A Fast Algorithm for Particle Simulations. *Journal of Computational Physics*, 73(2):325–348, 1987. 2.4.3

[82] W. Hackbusch. A Sparse Matrix Arithmetic Based on H-Matrices. Part I: Introduction to H-Matrices. *Computing*, 62(2):89–108, 1999. 2.4.3

[83] W. Hackbusch and B. N. Khoromskij. A Sparse H-Matrix Arithmetic. Part II: Application to Multi-Dimensional Problems. *Computing*, 64(1):21–47, 2000. 2.4.3

[84] E. Perrey-Debain. Analysis of Convergence and Accuracy of the DRBEM for Axisymmetric Helmholtz-Type Equation. *Engineering Analysis with Boundary Elements*, 23 (8):703–711, 1999. 2.4.3

[85] S. Mancini, R. J. Astley, S. Sinayoko, G. Gabard, and M. Tournour. An Integral Formulation for Wave Propagation on Weakly Non-Uniform Potential Flows. *Journal of Sound and Vibration*, 2016. Submitted. 2.4.3

[86] R. H. Lyon and R. G. DeJong. *Theory and Application of Statistical Energy Analysis*. Butterworth-Heinemann, Newton, MA, USA, 1995. 2.4.3

[87] A. M. Ondet and J. L. Barbry. Modeling of Sound Propagation in Fitted Workshops Using Ray Tracing. *Journal of the Acoustical Society of America*, 85(2):787–796, 1989. 2.4.3

[88] T. J. R. Hughes, L. P. Franca, and M. Mallet. A New Finite Element Formulation for Computational Fluid Dynamics: VI. Convergence Analysis of the Generalized SUPG Formulation for Linear Time-Dependent Multidimensional Advective-Diffusive Systems. *Computer Methods in Applied Mechanics and Engineering*, 63(1):97–112, 1987. 2.4.3, 6.1.2, 6.3.2

[89] K.-J. Bathe. *Finite Element Procedures.* Prentice-Hall, Inc., Upper Saddle River, NJ, USA, 1996. 5.2.2

[90] O. C. Zienkiewicz and R. L. Taylor. *The Finite Element Method, Volume 1, The Basis.* Butterworth-Heinemann, Oxford, United-Kingdom, 2000. 2.4.3, 4.1

[91] G. M. L. Gladwell. A Finite Element Method for Acoustics. In *Fifth International Conference on Acoustics*, Liège, Belgium, 1965. 2.4.3

[92] J. Donea and A. Huerta. *Finite Element Methods for Flow Problems.* John Wiley & Sons, Ltd, Chichester, United-Kingdom, 2003. 2.4.3, 6.1.2, 6.1.2, 6.3.2, 6.3.2, 6.3.2, 6.3.2

[93] I. Harari. A Survey of Finite Element Methods for Time-Harmonic Acoustics. *Computer Methods in Applied Mechanics and Engineering*, 195(13–16):1594–1607, 2006. 2.4.3

[94] L. L. Thompson. A Review of Finite-Element Methods for Time-Harmonic Acoustics. *Journal of the Acoustical Society of America*, 119(3):1315–1330, 2006. 2.4.3

[95] I. Harari and T. J. R. Hughes. Finite Element Methods for the Helmholtz Equation in an Exterior Domain: Model Problems. *Computer Methods in Applied Mechanics and Engineering*, 87(1):59–96, 1991. 2.4.3

[96] I. M. Babuŝka, F. Ihlenburg, E. T. Paik, and S. A. Sauter. A Generalized Finite Element Method for Solving the Helmholtz Equation in Two Dimensions with Minimal Pollution. *Computer Methods in Applied Mechanics and Engineering*, 128(3–4): 325–359, 1995.

[97] A. A. Oberai and P. M. Pinsky. A Residual-Based Finite Element Method for the Helmholtz Equation. *International Journal for Numerical Methods in Engineering*, 49(3):399–419, 2000. 2.4.3

[98] F. Ihlenburg and I. M. Babuŝka. Finite Element Solution of the Helmholtz Equation with High Wave Number, Part I: The *h*-Version of the FEM. *Computers & Mathematics with Applications*, 30(9):9–37, 1995. 2.4.3, 2.6, 6.1.1

[99] I. M. Babuŝka and S. A. Sauter. Is the Pollution Effect of the FEM Avoidable for the Helmholtz Equation Considering High Wave Numbers? *SIAM Journal on Numerical Analysis*, 34(6):2392–2423, 1997. 2.4.3

[100] J. M. Melenk and I. M. Babuŝka. The Partition of Unity Finite Element Method: Basic Theory and Applications. *Computer Methods in Applied Mechanics and Engineering*, 139(1):289–314, 1996. 2.4.3

[101] B. Després. Sur une Formulation Variationnelle de Type Ultra-Faible. *Comptes Rendus de l'Académie des Sciences*, 318(1):939–944, 1994. 2.4.3

[102] O. Cessenat and B. Després. Application of an Ultra-Weak Variational Formulation of Elliptic PDEs to the Two-Dimensional Helmholtz Problem. *SIAM Journal on Numerical Analysis*, 35(1):255–299, 1998. 2.4.3

[103] C. Farhat, I. Harari, and L. P. Franca. The Discontinuous Enrichment Method. *Computer Methods in Applied Mechanics and Engineering*, 190(48):6455–6479, 2001. 2.4.3

[104] I. M. Babuŝka and B. Q. Guo. The h, p and $h-p$ Version of the Finite Element Method; Basis Theory and Applications. *Advances in Engineering Software*, 15(3–4): 159–174, 1992. 2.4.3

[105] F. Ihlenburg and I. M. Babuŝka. Finite Element Solution of the Helmholtz Equation with High Wave Number, Part II: The *hp*-Version of the FEM. *SIAM Journal on Numerical Analysis*, 34(1):315–358, 1997. 2.4.3, 2.6, 5.2.2, 6.1.1

[106] W. Rachowicz, D. Pardo, and L. Demkowicz. Fully Automatic *hp*-Adaptivity in Three Dimensions. *Computer Methods in Applied Mechanics and Engineering*, 195 (37):4816–4842, 2006. 2.4.3

[107] H. Bériot, A. Prinn, and G. Gabard. On the Performance of High-Order FEM for Solving Large-Scale Industrial Acoustic Problems. In 20^{th} *International Congress on Sound & Vibration ICSV20*, Bangkok, Thailand, 2013. 2.4.3, 4.3.4, 5.1.2

[108] P. Šolín, K. Segeth, and I. Doležel. *Higher-Order Finite Element Methods*. CRC Press, Boca Raton, FL, USA, 2004. 2.4.3, 4.3.3, 4.3.4, 4.3.5

[109] S. Petersen, D. Dreyer, and O. von Estorff. Assessment of Finite and Spectral Element Shape Functions for Efficient Iterative Simulations of Interior Acoustics. *Computer Methods in Applied Mechanics and Engineering*, 195(44):6463–6478, 2006. 2.4.3

[110] J. Biermann, O. von Estorff, S. Petersen, and C. Wenterodt. Higher Order Finite and Infinite Elements for the Solution of Helmholtz Problems. *Computer Methods in Applied Mechanics and Engineering*, 198(13–14):1171–1188, 2009. 2.4.3

[111] R. J. Astley. Infinite Elements for Wave Problems: A Review of Current Formulations and an Assessment of Accuracy. *International Journal for Numerical Methods in Engineering*, 49(7):951–976, 2000. 2.5

[112] B. Engquist and A. Majda. Absorbing Boundary Conditions for the Numerical Simulation of Waves. *Mathematics of Computation*, 31(139):629–651, 1977. 2.5

[113] J.-P. Bérenger. A Perfectly Matched Layer for the Absorption of Electromagnetic Waves. *Journal of Computational Physics*, 114(2):184–200, 1994. 2.5, 4.4.1

[114] F. Farassat, K. Brentner, and M. H. Dunn. A Study of Supersonic Surface Sources - The Ffowcs Williams–Hawkings Equation and Kirchhoff Formula. In 4$^{\text{th}}$ *AIAA/CEAS Aeroacoustics Conference*, Toulouse, France, 1998. 2.5

[115] H.-O. Kreiss. Initial Boundary Value Problems for Hyperbolic Systems. *Communications on Pure and Applied Mathematics*, 23(3):277–298, 1970. 2.5

[116] R. L. Higdon. Initial-Boundary Value Problems for Linear Hyperbolic Systems. *SIAM Review*, 28(2):177–217, 1986. 2.5, 4.2, 4.2.1

[117] K. W. Thompson. Time Dependent Boundary Conditions for Hyperbolic Systems. *Journal of Computational Physics*, 68:1–24, 1987. 2.5, 4.2.1

[118] M. B. Giles. Non-Reflecting Boundary Conditions for Euler Equation Calculations. *AIAA Journal*, 28(12):2050–2058, 1990. 2.5

[119] R. Mankbadi, R. Hixon, S.-H. Shih, and L. A. Povinelli. Use of Linearized Euler Equations for Supersonic Jet Noise Prediction. *AIAA Journal*, 36(2):140–147, 1998. 2.5

[120] A. Bayliss and E. Turkel. Radiation Boundary Conditions for Wave-Like Equations. *Communications on Pure and Applied Mathematics*, 33(6):707–725, 1980. 2.5

[121] A. Bayliss and E. Turkel. Far Field Boundary Conditions for Compressible Flows. *Journal of Computational Physics*, 48(2):182–199, 1982. 2.5

[122] F. Q. Hu. Absorbing Boundary Conditions. *International Journal of Computational Fluid Dynamics*, 18(6):513–522, 2004. 2.5

[123] D. J. Bodony. Analysis of Sponge Zones for Computational Fluid Mechanics. *Journal of Computational Physics*, 212(2):681–702, 2006. 2.5

[124] M. Israeli and S. A. Orszag. Approximation of Radiation Boundary Conditions. *Journal of Computational Physics*, 41(1):115–135, 1981. 2.5

[125] S. Ta'asan and D. M. Nark. An Absorbing Buffer Zone Technique for Acoustic Wave Propagation. In 33rd *Aerospace Sciences Meeting and Exhibit*, Reno, NV, USA, 1995. 2.5

[126] S. K. Richards, X. Zhang, X. X. Chen, and P. A. Nelson. The Evaluation of Non-Reflecting Boundary Conditions for Duct Acoustic Computation. *Journal of Sound and Vibration*, 270(3):539–557, 2004. 2.5

[127] F. Q. Hu. On Absorbing Boundary Conditions for Linearized Euler Equations by a Perfectly Matched Layer. *Journal of Computational Physics*, 129(1):201–219, 1996. 2.5

[128] C. K. W. Tam, L. Auriault, and F. Cambuli. Perfectly Matched Layer as Absorbing Boundary Condition for the Linearized Euler Equations in Open and Ducted Domains. *Journal of Computational Physics*, 144(1):213–234, 1998. 2.5

[129] A. Abarbanel, D. Gottlieb, and J. S. Hesthaven. Well-Posed Perfectly Matched Layers for Advective Acoustics. *Journal of Computational Physics*, 154(2):266–283, 1999. 2.5

[130] F. Q. Hu. A Stable, Perfectly Matched Layer for Linearized Euler Equations in Unsplit Physical Variables. *Journal of Computational Physics*, 173(2):455–480, 2001. 2.5

[131] F. Q. Hu. A Perfectly Matched Layer Absorbing Boundary Condition for Linearized Euler Equations with a Non-Uniform Mean Flow. *Journal of Computational Physics*, 208(2):469–492, 2005. 2.5, 4.4.1

[132] D. Xue and L. Demkowicz. Control of Geometry Induced Error in *hp* Finite Element (FE) Simulations - I. Evaluation of FE Error for Curvilinear Geometries. *International Journal of Numerical Analysis and Modeling*, 2(3):283–300, 2005. 2.6

[133] D. Moxey, M. D. Green, S. J. Sherwin, and J. Peiró. An Isoparametric Approach to High-Order Curvilinear Boundary-Layer Mesh. *Computer Methods in Applied Mechanics and Engineering*, 283:636–350, 2015. 2.6

[134] T. J. R. Hughes, J. A. Cottrell, and Y. Bazilevs. Isogeometric Analysis: CAD, Finite

Elements, NURBS, Exact Geometry and Mesh Refinement. *Computer Methods in Applied Mechanics and Engineering*, 194(39):4135–4195, 2005. 2.6

[135] R. Sevilla, S. Fernández-Méndez, and A. Huerta. NURBS-Enhanced Finite Element Method. *International Journal for Numerical Methods in Engineering*, 76(1):56–83, 2008. 2.6

[136] M. Muriel Gracia, B. Vanelderen, W. De Roeck, and W. Desmet. Accurate Interfacing Schemes for the Coupling of CFD Data with High Order DG Methods for Aeroacoustic Propagation. In 26$^{\text{th}}$ *International Conference on Noise and Vibration ISMA2014*, Leuven, Belgium, 2014. 2.6

[137] M. Muriel Gracia, W. De Roeck, and W. Desmet. Efficient Interfacing Scheme for Using Source Terms in a High-Order DG Aeroacoustics Propagation Solver. In 22$^{\text{nd}}$ *International Congress on Sound and Vibration ICSV22*, Florence, Italy, 2015. 2.6

[138] A. Bayliss, C. I. Goldstein, and E. Turkel. On Accuracy Conditions for the Numerical Computation of Waves. *Journal of Computational Physics*, 59(3):396–404, 1985. 2.6

[139] F. Ihlenburg. *Finite Element Analysis of Acoustic Scattering*. Springer-Verlag, New York, NY, USA, 1998. 2.6

[140] M. Ainsworth. Discrete Dispersion Relation for *hp*-Version Finite Element Approximation at High Wave Number. *SIAM Journal on Numerical Analysis*, 42(2):553–575, 2004. 2.6, 6.1.1

[141] G. Gabard, R. J. Astley, and M. Ben Tahar. Stability and Accuracy of Finite Element Methods for Flow Acoustics - I: General Theory and Application to One-Dimensional Propagation. *International Journal for Numerical Methods in Engineering*, 63(7): 947–973, 2005. 2.6

[142] G. Gabard, R. J. Astley, and M. Ben Tahar. Stability and Accuracy of Finite Element Methods for Flow Acoustics - II: Two-Dimensional Effects. *International Journal for Numerical Methods in Engineering*, 63(7):974–987, 2005. 2.6

[143] O. Guasch and R. Codina. An Algebraic Subgrid Scale Finite Element Method for the Convected Helmholtz Equation in Two Dimensions with Application in Aeroacoustics. *Computer Methods in Applied Mechanics and Engineering*, 196(45–48): 4672–7689, 2007. 2.6, 6.1.2, 6.3.2, 6.3.2

[144] G. K. Batchelor. *An Introduction to Fluid Dynamics.* Cambridge University Press, Cambridge, United-Kingdom, 1967. 3.1.1, 3.1.1, 3.1.2, 7.2.1

[145] A. L. Lavoisier. *Traité Élémentaire de Chimie.* Cuchet, Paris, France, 1789. 3.1.1

[146] O. Louisnard. *Cours de Mécanique des Fluides.* Creative Commons, San Francisco, CA, USA, 2012. 3.1.1

[147] I. G. Currie. *Fundamental Mechanics of Fluids, Third Edition.* Marcel Dekker, Inc., New York, NY, USA, 2003. 3.1.1

[148] R. B. Bird, W. E. Stewart, and E. N. Lightfoot. *Transport Phenomena.* John Wiley & Sons, Inc., New York, NY, USA, 1960. 3.1.1, 3.1.2

[149] F. M. White. *Fluid Mechanics.* McGraw-Hill, New York, NY, USA, 2011. 3.1.1

[150] H. Devoe. *Thermodynamics and Chemistry.* Prentice-Hall, Inc., Upper Saddle River, NJ, USA, 2001. 3.1.1, 3.1.2

[151] L. M. B. C. Campos. On 36 Forms of the Acoustic Wave Equation in Potential Flows and Inhomogeneous Media. *Applied Mechanics Reviews*, 60:149–171, 2007. 3.1.2

[152] M. E. Goldstein. An Exact Form of Lilley's Equation with a Velocity Quadrupole / Temperature Dipole Source Term. *Journal of Fluid Mechanics*, 443:231–236, 2001. 3.1.3

[153] M. Abramowitz and I. A. Stegun. *Handbook of Mathematical Functions.* National Bureau of Standards, New York, NY, USA, 1964. 3.3

[154] G. N. Watson. *A Treatise on the Theory of Bessel Functions.* Cambridge University Press, Cambridge, United-Kingdom, 1966. 3.3

[155] L. Brillouin. *Wave Propagation and Group Velocity.* Academic Press, New York, NY, USA, 1960. 3.3

[156] R. J. LeVeque. *Finite Difference Methods for Ordinary and Partial Differential Equations.* SIAM, Philadelphia, PA, USA, 2007. 3.4

[157] G. Kooijman. *Acoustical Response of Shear Layers.* PhD thesis, Technische Universiteit Eindhoven, 2007. 3.4

[158] H. R. Lewis and P. M. Bellan. Physical Constraints on the Coefficients of Fourier

Expansions in Cylindrical Coordinates. *Journal of Mathematical Physics*, 31(11): 2596–2596, 1990. 3.4.2

[159] Y. W. Kwon and H. Bang. *The Finite Element Method Using Matlab*. CRC Press, Boca Raton, FL, USA, 2000. 4.1

[160] R. Hixon. Radiation and Wall Boundary Conditions for Computational Aeroacoustics: A Review. *International Journal of Computational Fluid Dynamics*, 18(6): 523–531, 2004. 4.2, 4.2.1

[161] G. B. Whitham. *Linear and Nonlinear Waves*. John Wiley & Sons, Inc., New York, NY, USA, 1974. 4.2.1

[162] M. K. Myers. On the Acoustic Boundary Condition in the Presence of Flow. *Journal of Sound and Vibration*, 71(3):429–434, 1980. 4.2.3, 4.2.3

[163] W. Eversman. The Boundary Condition at an Impedance Wall in a Non-Uniform Duct with Potential Mean Flow. *Journal of Sound and Vibration*, 246(1):63–69, 2001. 4.2.3, 4.2.3

[164] C. Geuzaine and J.-F. Remacle. Gmsh: A Three-Dimensional Finite Element Mesh Generator with Built-In Pre- and Post-Processing Facilities. *International Journal for Numerical Methods in Engineering*, 79(11):1309–1331, 2009. 4.3.1

[165] D. A. Dunavant. High Degree Efficient Symmetrical Gaussian Quadrature Rules for the Triangle. *International Journal for Numerical Methods in Engineering*, 21(6): 1129–1148, 1985. 4.3.2

[166] A. M. Turing. Rounding-Off Errors in Matrix Processes. *The Quarterly Journal of Mechanics and Applied Mathematics*, 1(3):287–308, 1948. 4.3.2

[167] W. Desmet and D. Vandepitte. Finite Element Modeling for Acoustics. In *Lecture Notes of the ISAAC21 Course*, Leuven, Belgium, 2010. 4.3.2

[168] G. E. Karniadakis and S. Sherwin. *Spectral/hp Element Methods for Computational Fluid Dynamics*. Oxford University Press, Oxford, United-Kingdom, 2013. 4.3.5

[169] A. Lieu, G. Gabard, and H. Bériot. A Performance Study of High-Order Finite Elements and Wave-Based Discontinuous Galerkin Methods for a Convected Helmholtz Problem. In 22$^{\text{nd}}$ *International Congress on Sound and Vibration ICSV22*, Florence, Italy, 2015. 4.3.5

[170] A. Bermúdez, L. Hervella-Nieto, A. Prieto, and R. Rodríguez. An Optimal Perfectly Matched Layer with Unbounded Absorbing Function for Time-Harmonic Acoustic Scattering Problems. *Journal of Computational Physics*, 223(2):469–488, 2007. 4.4.3, 4.4.3, 5.4.2

[171] R. Cimpeanu, A. Martinsson, and M. Heil. A Parameter-Free Perfectly Matched Layer Formulation for the Finite-Element-Based Solution of the Helmholtz Equation. *Journal of Computational Physics*, 296(C):329–347, 2015. 4.4.3, 4.4.3

[172] W. W. Hager. Condition Estimates. *SIAM Journal on Scientific and Statistical Computing*, 5(2):311–316, 1984. 5.1.2

[173] MUMPS Team. MUMPS 4.10.0: User's Guide. Technical report, 2011. 5.1.2, 8.2.3.1

[174] G. Gabard. Discontinuous Galerkin Methods with Plane Waves for Time-Harmonic Problems. *Journal of Computational Physics*, 225(2):1961–1984, 2007. 5.1.2

[175] M. Williamschen, G. Gabard, and H. Bériot. Impact of the Mean Flow Representation on DGM Simulations of Flow Acoustics. In 22$^{\text{nd}}$ *AIAA/CEAS Aeroacoustics Conference*, Lyon, France, 2016. 5.3.2, 8.3.3

[176] A. Modave, E. Delhez, and C. Geuzaine. Optimizing Perfectly Matched Layers in Discrete Contexts. *International Journal for Numerical Methods in Engineering*, 99 (6):410–437, 2014. 5.4.2

[177] R. J. Astley and W. Eversman. The Finite Element Duct Eigenvalue Problem: An Improved Formulation with Hermitian Elements and No-Flow Condensation. *Journal of Sound and Vibration*, 69(4):509–518, 1980. 6.1.2

[178] Q. Cai, S. Kollmannsberger, E. Sala-Lardies, A. Huerta, and E. Rank. On the Natural Stabilization of Convection Dominated Problems Using High-Order Bubnov-Galerkin Finite Elements. *Computers and Mathematics with Applications*, 66(12):2545–2558, 2014. 6.1.2, 6.3.2, 6.3.2

[179] I. Christie, D. F. Griffiths, A. R. Mitchell, and O. C. Zinkiewicz. Finite Element Methods for Second Order Differential Equations with Significant First Derivatives. *International Journal for Numerical Methods in Engineering*, 10(6):1389–1396, 1976. 6.1.2

[180] J. C. Heinrich, P. S. Huyakorn, O. C. Zinkiewicz, and R. Mitchell. An 'Upwind' Finite

Element Scheme for Two-Dimensional Convective Transport Equation. *International Journal for Numerical Methods in Engineering*, 11(1):131–143, 1977. 6.1.2

[181] R. Codina. Comparison of Some Finite Element Methods for Solving the Diffusion-Convection-Reaction Equation. *Computational Methods in Applied Mechanics and Engineering*, 156(1):185–210, 1998. 6.1.2

[182] A. Quarteroni. *Numerical Models for Differential Problems.* Springer-Verlag, Milan, Italy, 2009. 6.1.2

[183] E. Burman, A. Quarteroni, and B Stamm. Stabilization Strategies for High Order Methods for Transport Dominated Problems. *Bollettino U.M.I.*, 1(1):57–77, 2008. 6.1.2

[184] L. P. Franca, G. Hauke, and A. Masud. Revisiting Stabilized Finite Element Methods for the Advective-Diffusive Equation. *Computer Methods in Applied Mechanics and Engineering*, 195(13):1560–1572, 2006. 6.1.2

[185] T. J. R. Hughes and M. Mallet. A New Finite Element Formulation for Computational Fluid Dynamics: III. The Generalized Streamline Operator for Multidimensional Advective-Diffusive Systems. *Computer Methods in Applied Mechanics and Engineering*, 58(3):305–328, 1986. 6.1.2

[186] J.-C. Carette, H. Deconinck, H. Paillère, and P. L. Roe. Multidimensional Upwinding: Its Relation to Finite Elements. *International Journal for Numerical Methods in Fluids*, 20(8–9):935–955, 1995. 6.1.2

[187] T. E. Tezduyar and Y. Osawa. Finite Element Stabilization Parameters Computed from Element Matrices and Vectors. *Computer Methods in Applied Mechanics and Engineering*, 190(3–4):411–430, 2000. 6.1.2

[188] M. Bause and K. Schwegler. Analysis of Stabilized High-Order Finite Element Approximation of Nonstationary and Nonlinear Convection-Diffusion-Reaction Equations. *Computer Methods in Applied Mechanics and Engineering*, 209–212:184–196, 2012. 6.1.2

[189] R. Codina. On Stabilized Finite Element Methods for Linear Systems of Convection-Diffusion-Reaction Equations. *Computer Methods in Applied Mechanics and Engineering*, 188(1–3):61–82, 2000. 6.1.2

[190] T. J. R. Hughes, L. P. Franca, and G. M. Hulbert. A New Finite Element Formula-

tion for Computational Fluid Dynamics: VII. The Galerkin/Least-Squares Method for Advective-Diffusive Equations. *Computer Methods in Applied Mechanics and Engineering*, 73(2):173–186, 1989. 6.1.2, 6.3.1

[191] G. J. Le Beau, S. E. Ray, S. K. Aliabadi, and T. E. Tezduyar. SUPG Finite Element Computation of Compressible Flows with the Entropy and Conservation Variables Formulations. *Computer Methods in Applied Mechanics and Engineering*, 104(3): 397–422, 1993. 6.1.2, 6.3.1, 6.3.2

[192] G. Floquet. Sur les Equations Différentielles Linéaires à Coefficients Périodiques. *Annales Scientifiques de l'E.N.S.*, 2(12):47–88, 1883. 6.2.2

[193] W. A. Mulder. Spurious Modes in Finite-Element Discretizations of the Wave Equation May Not Be All That Bad. *Applied Numerical Mathematics*, 30(4):425–445, 1999. 6.2.3

[194] A. de la Bourdonnaye, C. Farhat, A. Macedo, F. Magoulès, and F.-X. Roux. A Non Overlapping Domain Decomposition Method for the Exterior Helmholtz Problem. Technical Report RR-3271, INRIA, 1997. 7.5

[195] C. Farhat, A. Macedo, M. Lesoinne, F.-X. Roux, F. Magoulès, and A. de La Bourdonnaye. Two-Level Domain Decomposition Methods with Lagrange Multipliers for the Fast Iterative Solution of Acoustic Scattering Problems. *Computer Methods in Applied Mechanics and Engineering*, 184(24):213–239, 2000. 7.5

[196] J. H. Lan, Y. Guo, and C. Bréard. Validation of Acoustic Propagation Code with JT15D Static and Flight Test Data. In 10^{th} *AIAA/CEAS Aeroacoustics Conference*, Manchester, United-Kingdom, 2004. 8.1.1, 8.1.1.2, 8.1.2

[197] J. H. Lan and C. Bréard. Validation of 3D Acoustic Propagation Code with Analytical and Experimental Results. In 11^{th} *AIAA/CEAS Aeroacoustics Conference*, Monterey, CA, USA, 2005. 8.1.2

[198] G. Gabard and R. J. Astley. Theoretical Model for Sound Radiation from Annular Jet Pipe: Far- and Near-Field Solutions. *Journal of Fluid Mechanics*, 549(1):315–341, 2006. 8.2.2

[199] S. W. Rienstra. Acoustic Radiation from a Semi-Infinite Annular Duct in a Uniform Subsonic Mean Flow. *Journal of Sound and Vibration*, 94(2):267–288, 1984. 8.2.2

[200] *MATLAB R2013a*. The MathWorks Inc., Natick, MA, USA, 2014. 8.2.3.1

[201] P. G. Drazin. *Introduction to Hydrodynamic Stability*. Cambridge University Press, Cambridge, United-Kingdom, 2002. 8.2.3.3

[202] B. J. Tester, F. Arnold, S. Caro, and S. Lidoine. TURNEX: Turbomachinery Noise Radiation Through the Engine Exhaust. Publishable Final Activity Report. Technical report, E.U. Project 516079, 2008. 8.3.1

[203] M. Ainsworth and J. T. Oden. A Procedure for A Posteriori Error Estimation for $h-p$ Finite Element Methods. *Computer Methods in Applied Mechanics and Engineering*, 101(1–3):73–96, 1992. 8.3.3